TECHNISCHE UNIVERSITÄT WIEN

DISSERTATION

Development and optimization of novel large area silicon pad sensors for the CMS High Granularity Calorimeter

ausgeführt zum Zwecke der Erlangung des akademischen Grades eines Doktors der Naturwissenschaften unter der Leitung von

Univ.Prof. Dipl.-Phys. Dr.rer.nat. Jochen SCHIECK
und
Univ.Lektor Dipl.-Ing. Dr.techn. Thomas BERGAUER

Institut für Hochenergiephysik (HEPHY)
der Österreichischen Akademie der Wissenschaften
und
E141 Atominstitut der Technischen Universität Wien

eingereicht an der Technischen Universität Wien
Fakultät für Physik

von

Ing. Dipl.-Ing. Peter PAULITSCH, BSc BSc
Matrikelnummer: 1127072

Wien, am 22.10.2024

Kurzfassung

Der Large Hadron Collider (LHC) ist zur Zeit (2024) unter den Speicherringen sowohl der größte (27 km Umfang) als auch der mit der höchsten Kollisionsenergie (13.6 TeV). Während seine Beiträge zur Hochenergiephysik weiterhin substanziell sind, wird mehr Luminosität benötigt, um in angemessener Zeit genügend experimentelle Daten für neue physikalische Entdeckungen zu erhalten. Um die Rolle des LHC für die Zukunft zu sichern, plant das CERN ein Upgrade zur Erhöhung der Luminosität um den Faktor 10, genannt „High-Luminosity LHC" (HL-LHC). Diese Aufrüstung wird die Fähigkeit der Maschine verbessern, seltene Prozesse zu entdecken und die statistische Präzision zu erhöhen. Bei höherer Luminosität benötigen die Experimente aber eine bessere räumliche und zeitliche Auflösung, sowie eine verbesserte Strahlenhärte.

Diese Arbeit konzentriert sich auf die Siliziumdetektoren für das Compact Muon Solenoid (CMS) Experiment. CMS wird während des HL-LHC Upgrades wegen den oben erwähnten höheren Anforderungen auch die Sensoren aufrüsten. Dies wird als „CMS Phase-2-Upgrade" bezeichnet, das Upgrade der neuen Endkappen-Kalorimeter heißt „High Granularity Calorimeter" (HGCAL). CMS plant das HGCAL als Sandwich-Kalorimeter, bestehend aus Siliziumsensoren für den elektromagnetischen Subdetektor und für Teile des hadronischen Subdetektors. Eine weitere Motivation für das HGCAL ist die Teilchenflussanalyse, die die Identifizierung einzelner Teilchen in Jets ermöglicht.

CMS muss diese Anforderungen zu vertretbaren Kosten erfüllen, daher werden große hexagonale p-Typ Sensoren verwendet, die in einem 8"-Verfahren hergestellt werden. 8"-Sensoren wurden bisher noch nicht in großen Teilchenphysikexperimenten eingesetzt, stellen also ein Novum, ein First-of-a-kind (FOAK) dar. Demnach ist diese Forschung notwendig, um die Eignung dieser Technik für Hochenergie-Teilchenphysikexperimente zu verifizieren. Diese 8"-Sensoren wurden vom Autor, basierend auf Vorarbeiten, designt und in iterativen Prototyping-Zyklen verbessert. Für die Bestrahlungsstudien wurden die vom Autor designten Ministrip-Sensoren genutzt, die aufgrund ihrer kleinen Abmessungen deutlich flexibler einzusetzen, zu kontaktieren und handzuhaben sind.

Als Vorbereitung auf die Studien wurde eine bereits existierende Teststation weiter verbessert, und zur Qualifizierung des Testsystems wurden Eingangskontrollen auf mechanische Schäden durchgeführt, sowie die elektrische Charakterisierung wie Leckströme, Kapazitäten, Interpad-Isolation, Interpad-Kapazität und Hochspannungs-Stabilität getestet und mit den Anforderungen des CMS-Experiments abgeglichen. Analysemethoden wie Spreading Resistance Profiling (SRP), Sekundärionen-Massenspektrometrie (SIMS), Rasterelektronenmikroskopie (SEM), und konfokale Lasermikroskopie ergänzen die oben genannten elektrischen Methoden. Dabei zeigte sich von 11 getesteten Sensoren ein Yield von etwa 36 %.

Ein wesentlicher Punkt dieser Arbeit ist der Einfluss von Strahlenschäden auf die elektrischen Eigenschaften. Die Neutronenfluenz der bestrahlten Sensoren und Teststrukturen reicht bis zu $10^{16}\,\mathrm{n_{eq}cm^{-2}}$, so dass wegen des Anstiegs des Leckstroms für elektrische Messungen an bestrahlten Sensoren niedrige Temperaturen (−30 to −20 °C) und das Einblasen von Trockenluft erforderlich sind.

Das Kernelement der Bestrahlungsstudien sind die Annealing-Studien, genauer gesagt, das Verhalten der Sensoren nach definierter Erwärmung. Bezüglich Strahlenhärte hat sich in dieser Studie gezeigt, dass die neuen 8"-Sensoren durchaus mit bereits etablierten und umfassend in der Literatur beschriebenen Siliziumsensortechnologien wie 6" und n-Typ vergleichbare Ergebnisse bieten. In einem Punkt, bei der Verringerung der damage function α durch Annealing, zeigten die fünf untersuchten Ministrip-Sensoren ein deutlich besseres Annealing-Verhalten als bisher etablierte Siliziumsensortechnologien im n-Typ und auf 6"-Wafern. Wenn diese Resultate in zukünftigen Studien bestätigt werden, sind diese neuen Sensoren als durchaus qualifiziert für das Phase-2 Upgrade des HGCAL zu betrachten, und CMS wird die endgültigen Sensordesigns für die Serienproduktion nutzen und die Sensoren schließlich im HGCAL implementieren. Insgesamt würden bei HGCAL etwa 30 000 Siliziumsensoren mit einer Gesamtfläche von etwa 620 $\mathrm{m^2}$ verbaut.

Abstract

The Large Hadron Collider (LHC) is currently (2024) the largest (27 km in circumference) storage ring and has the highest collision energy (13.6 TeV). While its contributions to high-energy physics remain substantial, more luminosity is needed to obtain sufficient experimental data for new physical discoveries in a reasonable time. To secure the role of the LHC for the future, CERN is planning an upgrade to increase the luminosity by a factor of 10, called "High-Luminosity LHC" (HL-LHC). This upgrade will improve the machine's ability to detect rare processes and increase statistical precision. However, the experiments require better spatial and temporal resolution and improved beam hardness at higher luminosity.

This work focuses on the silicon detectors for the Compact Muon Solenoid (CMS) experiment. CMS will also upgrade the sensors during the HL-LHC upgrade due to the higher requirements mentioned above. It is called the "CMS Phase-2 Upgrade". The upgrade to the new endcap calorimeters is called "High Granularity Calorimeter" (HGCAL). CMS plans the HGCAL as a sandwich calorimeter consisting of silicon sensors for the electromagnetic sub-detector and for parts of the hadronic sub-detector. A further motivation for the HGCAL is particle flow analysis, which allows the identification of individual particles in jets.

CMS must meet these requirements at a reasonable cost, so large hexagonal p-type sensors manufactured in an 8" process are used. Large particle physics experiments did not employ 8" sensors yet, so they represent a first-of-a-kind (FOAK) novelty. Accordingly, this research is necessary to verify the suitability of this technique for high-energy particle physics experiments. These 8" sensors were designed by the author based on preliminary work and improved in iterative prototyping cycles. For the irradiation studies, the author designed and used Ministrip sensors, which are much more flexible to use, contact, and handle due to their small dimensions.

The author further improved an existing test station and carried out initial inspections for mechanical damage in preparation for the studies and to qualify the test system. The electrical properties, such as leakage current, capacitance, and high-voltage stability, were tested and compared with the requirements of the CMS experiment. Analysis methods such as spreading resistance profiling (SRP), secondary ion mass spectrometry (SIMS), scanning electron microscopy (SEM), and confocal laser microscopy complement the electrical methods mentioned above. The 11 tested sensors showed a yield of around 36 %.

An essential point of this work is the evaluation of radiation hardness in terms of electrical characterization, such as leakage current, pad capacitance, interpad isolation through ohmic resistance, and interpad capacitance.The neutron fluence of the irradiated sensors and test structures ranges up to $10^{16}\,n_{eq}cm^{-2}$ so that low temperatures (−30 to −20 °C) and the blowing of dry air are required for electrical measurements on irradiated sensors.

The core element of the irradiation studies is the test series of annealing, or more precisely, the behavior of the sensors after defined heating. Regarding radiation hardness, this study has shown that the new 8" sensors offer comparable results to silicon sensor technologies already established and comprehensively described in the literature, such as 6" and n-type sensors. At one point, when reducing the damage function α through annealing, the five Ministrip sensors examined showed significantly better annealing behavior than already established silicon sensor technologies in n-type and on 6" wafers. The author suggests future examinations to verify these results. In that case, these new sensors should be considered well qualified for the Phase-2 Upgrade of the HGCAL, and CMS will use the final sensor designs for series production, and the sensors eventually implemented in the HGCAL. In total, around 30.000 silicon sensors with a total area of around 620 m^2 will be installed in HGCAL.

Contents

List of abbreviations

ALICE	A Large Ion Collider Experiment
ARRAY	switching mAtRix pRobecArd sYstem
ATI	Atominstitut
ATLAS	A Toroidal LHC ApparatuS
CAD	computer-aided design
CE-E	Calorimeter Endcap - Electronic
CE-H	Calorimeter Endcap - Hadronic
CERN	Conseil européen pour la recherche nucléaire
CLSM	confocal laser scanning microscopy
CMS	Compact Muon Solenoid
CSC	cathode strip chambers
CV	capacitance versus voltage measurement
CVD	chemical vapor deposition
Cz	Czochralski process
DAQ	data acquisition
DM	Dark Matter
DT	drift tubes
DUT	device under test
ECAL	Electromagnetic Calorimeter
ER	Edge ring
FOAK	First-of-a-kind
FZ	Float-Zone process
GCD	gate-controlled diode
GEM	gas electron multiplier
GR	Guard ring
HCAL	Hadronic Calorimeter
HD	High-density design
HEPHY	Institute of High Energy Physics
HGCAL	High Granularity Calorimeter
HL-LHC	High-Luminosity Large Hadron Collider
IV	current versus voltage measurement
LCR	inductivity/capacitance/resistance meter
LD	Low-density design
LHC	Large Hadron Collider
LHCb	Large Hadron Collider beauty
MBE	molecular beam epitaxy
MCz	magnetic applied field Czochralski process
MIP	minimum ionizing particle
MOCVD	metalorganic chemical vapor deposition
MOS	metal-oxide semiconductor
NIEL	non-ionizing energy loss
PQC	Process Quality Control
RINSC	Rhode Island Nuclear Science Center
RPC	resistive plate chambers
SEM	scanning electron microscopy
SIMS	secondary-ion mass spectrometry
SM	Standard Model of particle physics
SNR	signal-to-noise ratio
SRP	spreading resistance profiling
TRIGA	Training, Research, Isotopes, General Atomic

"Science is a way of thinking much more than it is a body of knowledge."

Carl Sagan

1 Introduction and Background

1.1 Current status of particle physics: The Standard Model

The Standard Model (SM) of particle physics is the fundamental theory about the known particles in the universe. It encompasses the three known fundamental forces (strong, weak, and electromagnetic) carried by corresponding gauge bosons, as well as the Higgs boson (see Figure 1.1). The other group of particles, the fermions, are the known fundamental building blocks of matter. The SM is one of the results of evolved quantum field theory, explaining the emergence of particles by spontaneous symmetry breaking. Over time, there have been numerous proofs of the SM, from discovering the predicted top quark [10] to the Higgs boson [18], completing the model, and raising its credence.

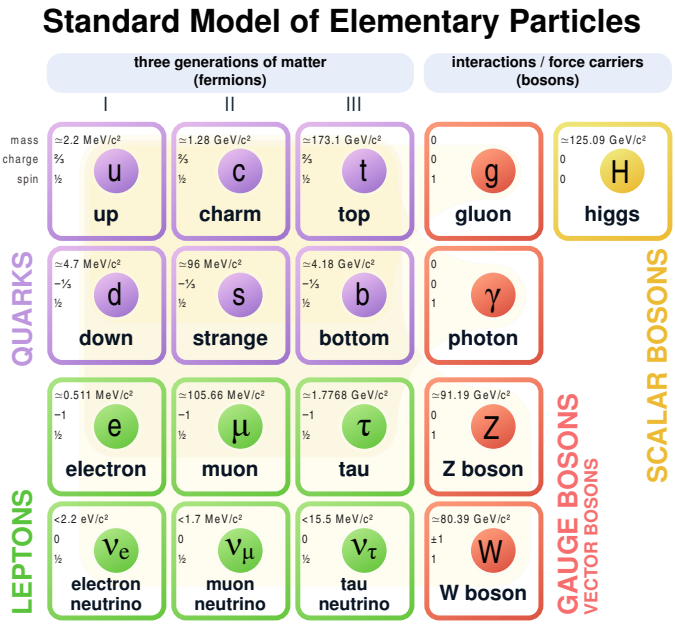

Figure 1.1: The Standard Model of particle physics. The fundamental particles separate into three generations of fermions, which are the building blocks of matter. Further, fermions split up into quarks and leptons. The SM completes by the mediators of force, the gauge bosons, and the Higgs boson. Image from [81].

Despite its successes in the past, the SM still cannot explain all phenomena in particle physics and cosmology. To name a few topics not sufficiently described within the framework of the SM:

- *Baryon asymmetry*: The SM predicts that the Big Bang should have formed equal amounts of matter and antimatter baryons. However, observation shows a vast imbalance between matter and antimatter in the observable universe, having a ratio of 6.14×10^{10} in favor of matter [23].
- *Neutrino oscillations and their non-zero masses*: Neutrino oscillation is the phenomenon that neutrinos can change their lepton flavor during propagation in vacuum. Consequently, the mass eigenstates of neutrinos cannot be identical to their particle eigenstates, so there must be a neutrino mixing. This means that at least two neutrino types must have a non-zero mass [69]. The SM does not naturally include such a mechanism.
- *Gravity and Dark Energy*: The Standard Model does not contain a complete theory of gravitation, and it especially does not describe phenomena like the observed accelerated expansion of the Universe by Dark Energy.
- *Dark Matter* (discussed in Section 1.2)

1.2 Beyond the Standard Model: The search for Dark Matter

Dark Matter (DM) is a postulated form of matter which is not interacting with "luminous" matter, by hypothesis, maybe just via the weak force, hence the term "Dark". However, its gravitational influence has a variety of impacts on the structure formation in the Universe. The Lambda-CDM model is the current model of cosmology, where DM is an integral part of it. Measurements of the Planck space telescope[63] show that DM constitutes 84 % of the total mass and 26 % of the total energy content of the Universe (see Figure 1.2). Since the first hints for the existence of DM emerged more than 100 years ago [76][86], this hypothesis gained more and more observational support, especially in the last decades [33].
As no particle of the Standard Model features the postulated attributes of Dark Matter particles, the search for a new underlying theory is ongoing. Complementary, the experimental discovery of DM particles, direct or indirect, is one of the goals of modern physics.

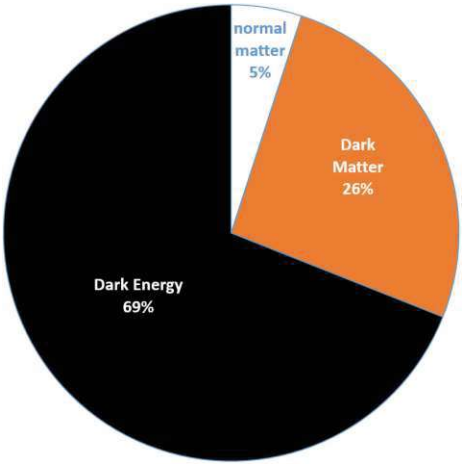

Figure 1.2: Constituents of the Universe. Our ordinary matter, described by the Standard Model, represents only a tiny fraction (5 %) of total energy content. According to recent data, Dark Matter occupies 26 % and Dark Energy 69 % [63].

By fundamental principles, there are three orthogonal approaches for Dark Matter searches (see Figure 1.3):

- *Direct detection*: Current Dark Matter hypotheses claim that the earth must be exposed to a flux of cosmic DM particles. Consequently, the direct detection searches for the recoil of (baryonic) nuclei when colliding with a DM particle. The recoil itself may be proven by the release of thermal energy [70] or other forms of energy dissipation, like scintillation [6].
- *Indirect detection*: This search type aims for detectable Standard Model particles coming from products of Dark Matter reactions in outer space. These may be either DM annihilation

reactions or products of DM decay. For indirect detection, all SM particles can act as a decay product, charged or neutral. Typically, multi-purpose experiments like IceCube [41] and Fermi Gamma-ray Space Telescope [2] also take part in indirect Dark Matter searches.

- *Production*: Production of Dark Matter particles in collider experiments is orthogonal to direct and indirect detection. Collisions in the Large Hadron Collider (LHC) (see Section 1.3) could produce DM particles [34]. These do not leave any signature in the detectors so that they may be detected indirectly as missing energy and momentum. Production has good sensitivity for low-mass Dark Matter particles.

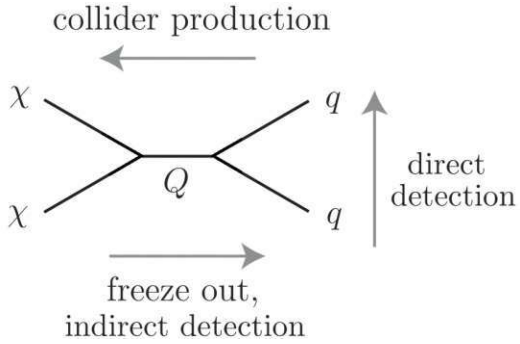

Figure 1.3: Feynman diagram representing non-gravitational Dark Matter searches. χ stands for a Dark Matter particle, q for a Standard Model quark. The arrow marks the time coordinate. Rotating the diagram by 90° shows three different approaches: *Direct detection* aims to record nuclei recoil events by interacting with Dark Matter particles. *Indirect detection* intends to work via self-annihilation of Dark Matter particles, for example, resulting in characteristic signatures in cosmic radiation. The opposite is *production in colliders*, two Standard Model particles annihilating into a Dark Matter particle pair. Figure from [13].

1.3 The Large Hadron Collider (LHC)

Located in underground caverns at CERN near Geneva, the Large Hadron Collider (LHC) is currently (2024) the world's largest collider, with a circumference of 27 km. It also exceeds all other accelerators by its center of mass energy $\sqrt{s} = 13.6\,\text{TeV}$ for protons and 5.12 TeV/nucleon for Pb^{82+} ions. The design value is $\sqrt{s} = 14\,\text{TeV}$ for protons and will be reached in the HL-LHC upgrade (see Section 1.4). The purpose of the LHC is to find answers to fundamental open questions in particle physics (see Section 1.2). Figure 1.4 shows a schematic of pre-accelerators, storage rings, and experiments at CERN. The LHC has been instrumental in several breakthrough discoveries, including the discovery [18] of the Higgs boson in 2012, which confirmed the existence of the Higgs field, a field of energy that permeates all of space and gives particles mass [25][36].
Besides breakthroughs in fundamental physics, accelerator science and the developed technology at CERN provided other advantageous improvements for science, medicine, and society: The World Wide Web, grid computing, and medical treatment technology like hadron therapy [51].

There are four interaction points where the beams cross, bringing the particles to collisions. At each of these points, there is an experiment located to analyze reaction products: The ATLAS[a] experiment, CMS[b], ALICE[c], and LHCb[d]. ATLAS and CMS are general-purpose detectors, studying the Higgs boson and looking for new physics. ALICE examines quark-gluon plasmas and gives significant input to cosmology. LHCb focuses on b-physics experiments using b-hadrons to measure CP-violation. This can help to explain the baryon asymmetry in the Universe.

[a] A Toroidal LHC ApparatuS
[b] Compact Muon Solenoid
[c] A Large Ion Collider Experiment
[d] Large Hadron Collider beauty

Table 1.1: Parameters of the Large Hadron Collider [11]

circumference	26 659 m
energy per particle	6.8 TeV (protons), 2.56 TeV/nucleon (ions)
luminosity	$1.2 \times 10^{34}\,\mathrm{cm}^{-2}\,\mathrm{s}^{-1}$
bunches/beam	2808
protons/bunch	1.2×10^{11}
bunch spacing	25 ns or 7.5 m
average/peak bunch crossing rate	31.6 MHz / 40 MHz
average collisions per crossing	20
circulating current/beam	540 mA
stored beam energy	360 MJ
number of magnets	9593
number of main dipoles	1232
number of main quadrupoles	392
peak dipole field	8.33 T

1.4 The High Luminosity Upgrade

In collider physics, (instantaneous) luminosity is, aside from collision energy (which sets an upper limit for the rest mass of produced new particles), the most critical parameter of a storage ring. It defines as the number of collisions per time and bunch overlap area:

$$L\ (\mathrm{cm}^{-2}\mathrm{s}^{-1}) = \frac{f\ n\ N_1\ N_2}{A} = \frac{f\ n\ N_1\ N_2}{4\pi\sigma_x\sigma_y} \tag{1.1}$$

where f is the revolution frequency, n the number of particle bunches in the storage ring, N_1 and N_2 the number of particles per bunch, and A the area of bunch overlap, as a product of σ_x and σ_y. Usually the beam profile follows a Gaussian distribution with $\sigma_{x,y}$.
The integrated luminosity L_{int} determines the number of produced particles N with a reaction cross section σ over the lifetime T of an experiment:

$$N = \sigma L_{\mathrm{int}} = \sigma \int_0^T L\,dt \tag{1.2}$$

Reaching higher luminosities is the main driver for upgrading the LHC to the so-called "High-Luminosity-LHC", increasing the instantaneous luminosity by a factor of five and the integrated luminosity by a factor of ten [1]. This will allow intensified search for rare events like Dark Matter particles (see Section 1.2).
A way to increase detector resolution is downsizing sensing elements to reduce spatial and temporal error margins and suppress pileups[e]. However, reducing the sensing elements size leads to new challenges such as weaker signals, which have to be mitigated by electronics. By implication, both approaches (increasing spatial resolution and luminosity) are common strategies to improve modern high energy physics experiments. Not only does the detector layout have to be improved, but also its material properties. Since the primary intention of colliding beam experiments is to produce particles (in large part at high energies), the detector elements are in a harsh radiation environment. Particle flux increases linear with luminosity, so higher integrated luminosities lead to elevated radiation doses for the surrounding material. Detectors for higher radiation levels, therefore, have to be more radiation hardened. In addition, the designed collision energy will be reached with a center of mass energy of $\sqrt{s} = 14$ TeV for protons. Consequently, future accelerators such as the HL-LHC and its experiments (see Section 1.5) need primary research for new materials and detector structures [60].

1.5 The Compact Muon Solenoid (CMS) experiment

At the LHC, there are two large general-purpose particle detectors: ATLAS and CMS. These general-purpose experiments aim to examine a wide range of physics like preciser measurements of the Higgs

[e] multiple hits on the same segment resulting in signal pulse overlap

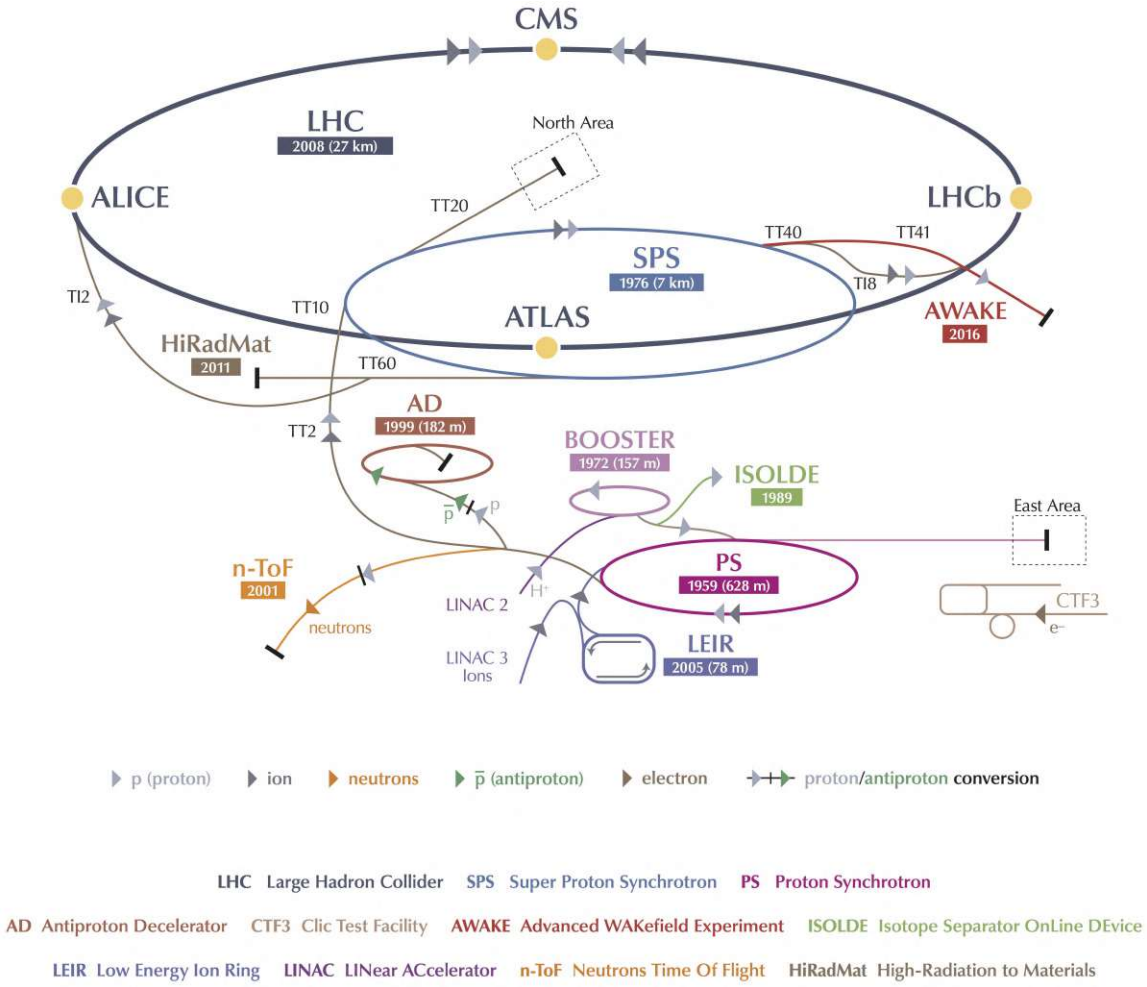

Figure 1.4: Accelerator complex at CERN. This schematic shows injectors, pre-accelerators, storage rings, as well as experiments. The detectors described in this thesis will be integrated into the upgraded CMS experiment [12].

boson (already discovered 2012 by ATLAS and CMS) and physics beyond the Standard Model like extra dimensions, Supersymmetry, and Dark Matter (see Section 1.2). Besides proton collisions, ATLAS and CMS also take part in the studies of heavy ion collisions. This thesis focuses on detectors for the CMS Phase-2 Upgrade, so the following paragraphs will solely deal with the design of CMS [16].

As seen in Figure 1.5, the core structure of CMS is a huge solenoid magnet capable of producing a magnetic field of 3.8 T. A steel yoke in the outer layers of the detector confines the magnetic field. This magnetic field bends the tracks of charged particles, determining the charge sign and the curvature of the bent track. By design, CMS subsystems measure the momentum from the bent track and energy deposition in the calorimeters of hadrons and charged leptons. To achieve this, CMS has a multi-staged structure with different detecting layers:

- **Layer 1**: The innermost layer, the Tracker [17], measures the tracks of particles to determine momentum. It is essential to have as little influence as possible to minimize energy loss. This means that reduction of the material budget is crucial. Therefore the inner part includes thin, high-resolution silicon pixel detectors, whereas the Outer Tracker consists of silicon strip detectors. In the inner region, the high particle flux of $10^7\,\mathrm{cm}^{-2}\,\mathrm{s}^{-1}$ requires a high granularity of 66 million pixels, covering an area of $16\,\mathrm{m}^2$. The microstrip detectors in the outer region have 9.6 million channels and an area of $200\,\mathrm{m}^2$. The total area of the silicon sensors in the Tracker is $216\,\mathrm{m}^2$ (see Figure 1.5), making it currently (2024) the largest silicon tracker on earth.

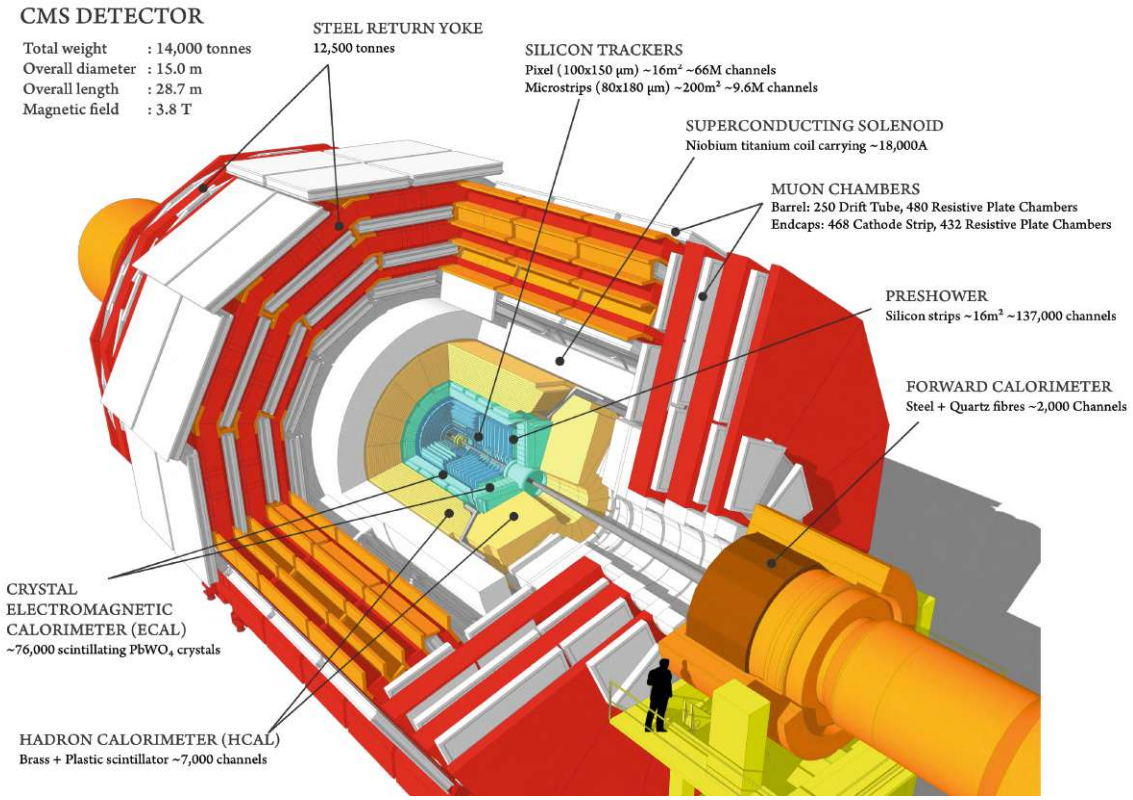

Figure 1.5: Current (2024) schematic of the CMS experiment [67].

The transverse momentum p_t of a particle deduces from the equation:

$$p_t = q\, r\, B \tag{1.3}$$

where q is the particle's electric charge, r is the radius of its bent track, and B is the magnetic field.

- **Layer 2**: Next follows the calorimeter, in this position, the electromagnetic calorimeter (ECAL). An ECAL measures the energy of particles by completely absorbing them via electromagnetic interaction. A calorimeter has two essential features which are advantageous at high energies: First, because a calorimeter counts particles, the count probability follows a Poisson distribution. As a result, the relative energy resolution of a calorimeter improves at higher energies as more particles N are counted:

$$\frac{\Delta E}{E} \propto \sqrt{N^{-1}} \tag{1.4}$$

Second, the length of a shower in a calorimeter is proportional to just the logarithm of the energy, allowing to have compact calorimeters even at the highest energies:

$$L_{\text{shower}} \propto \log E \tag{1.5}$$

In the case of CMS, a scintillating material, lead tungstate ($PbWO_4$), scintillates when electromagnetically interacting particles pass it. This highly transparent material conducts the scintillating light, picked up by silicon avalanche photodiodes for readout. In this electromagnetic calorimeter, the amount of light is proportional to the deposited energy of the particle.
The ECAL structure consists of a barrel section and two bases, the "endcaps", containing 76 200 lead tungstate crystals. To increase spatial precision, the ECAL contains preshower detectors in front of both endcaps. These preshower detectors discriminate single high-energy photons, which are more interesting than a pair of low-energy photons in many physics scenarios.

- **Layer 3**: After the ECAL, a hadronic calorimeter (HCAL) measures the energy of hadrons via by producing jets of hadronic particles created by the strong nuclear interaction. In contrast to the ECAL, it is a sandwich calorimeter, layers of high-density materials (brass and steel) interleaved with plastic scintillators. Wavelength-shifting fibers guide the scintillation light to hybrid photodiodes.

- **Layer 4**: As seen in Equation 1.3, a magnetic field is needed to bend the paths of charged particles. In CMS, a superconducting solenoid produces this field of 3.8 T. The current through the niobium-titanium coils is 18 160 A, corresponding to 2.3 GJ of stored energy. It was essential to install such a large and powerful magnet, to effectively bend the paths of high momentum particles to a measurable radius.
  The magnet itself is also the core structure, serving as a mounting point for the detector constructions. The magnet's return yoke surrounds the magnet coils. It performs as a field containment and guidance as its secondary role is to act as an absorber for the muon system.

- **Layer 5**: Detecting muons (see Figure 1.1) is, as the name "Compact Muon Solenoid" suggests, a primary goal of the CMS experiment. Detecting muons is of vital interest because one of the most evident signatures of the Higgs boson decay is: $H^0 \rightarrow 4\mu$ [22]. Muons have very little stopping power so that they can penetrate meters of dense material. This means that the CMS's calorimeters cannot stop high energy muons, so CMS has an extra muon system installed as the final layer. As the previous layers stop all other particles, the only remaining particles detected in the muon systems will be muons. The magnet's return yoke plays a crucial role in stopping all other particles.
  The muon system relies on four different detector types for tracking: fast resistive plate chambers (RPC) for triggering, used at the barrel and the endcaps. Drift tubes (DT) measure muon positions in the barrel, cathode strip chambers (CSC) are in the endcaps. As a complement to the other detector types, gas electron multiplier (GEM) detectors provide additional spatial information to improve resolution and increase coverage.

1.6 The CMS Phase-2 Upgrade

During the Long Shutdown 3 (see Figure 1.6), projected to be from 2026 to 2028, the CMS experiment will be adapted to the requirements of the High-Luminosity-LHC (see Section 1.4). This project is called CMS Phase-2 Upgrade [19]. This upgrade concerns most components, including detectors, readout electronics, and the triggering system, because of the increased need for trigger performance and higher data rates [9]. The current detectors already suffer from substantial radiation damage because they are already near their projected lifetime limits. The new detectors for the Phase-2 Upgrade have to withstand these new conditions on multiple levels:
First, the increased integrated luminosity leads to higher demands on radiation hardness (see Chapter 4). Radiation damage is widely linear to integrated luminosity, which will be 3000 fb^{-1} or 4000 fb^{-1} in the ultimate scenario. This is about ten times higher than the projected 350 fb^{-1} at the end of the lifetime of current detectors, increasing the demand for radiation hardness for Phase-2 detectors by ten.
Second, the increased instantaneous luminosity leads to an increased pile-up. Currently, the pile-up is at about 50 collisions per bunch crossing. For the HL-LHC, this will increase to 200 collisions per bunch crossing, raising the demands on spatial (granularity) and temporal resolution to allow shower separation and to implement methods like particle flow analysis[f].
Third, the Trigger system will be improved to allow Tracker information for decision logic. The so-called track-trigger-concept will implement a stub-logic to filter low-momentum particles already at the module level [21].
Fourth, mechanical considerations about the material budget in the substructures will minimize the influence on particle momenta and energies. The modularity will be improved to allow faster replacement of faulty modules.

[f] sensor fusion technology to exploit detector capabilities by using the best energy/momentum resolution for individual particles in a jet

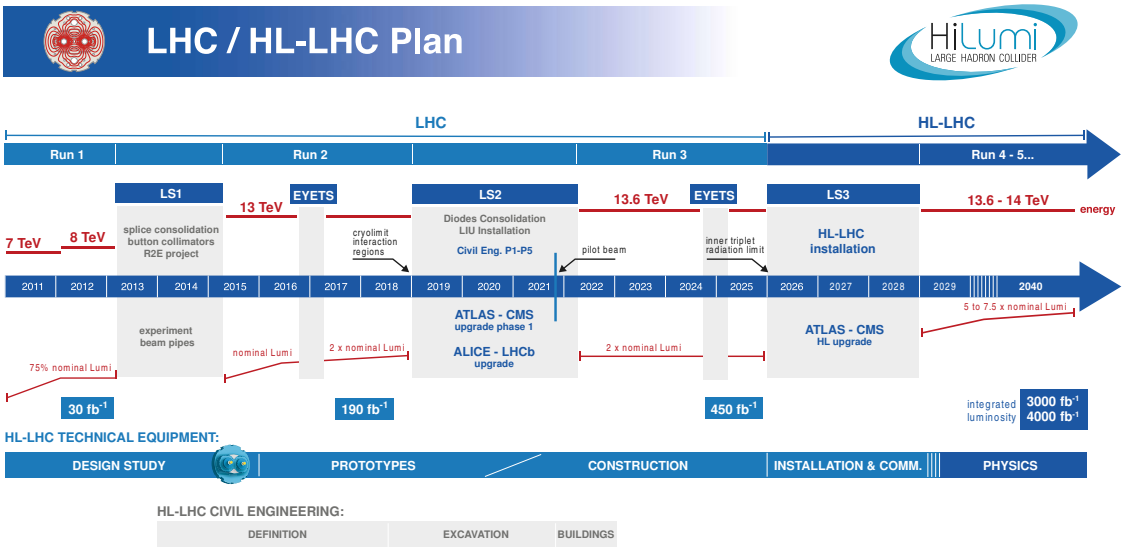

Figure 1.6: Project schedule of the LHC and its experiments. Run 3 is operating since 2022, which projects to the end of 2025. Then the Long Shutdown 3 will follow, upgrading the LHC and CMS and ATLAS experiments. In 2026, the HL-LHC installation will start and be accompanied by upgrading the ATLAS and CMS experiments (see Section 1.6) [37].

1.7 The High Granularity Calorimeter (HGCAL)

In contrast to CMS' other subsystems where only minor upgrades will be applied, the Tracker and the calorimeters will widely change, including replacing whole systems and technologies (see Section 1.6) to meet these demands. Especially the forward region of the calorimeters will have to endure from fluences up to $10^6\,n_{eq}cm^{-2}$and ionization doses around 2 MGy (see Figure 1.7). While the radiation-damaging particle flux through the tracker is mainly caused by charged hadrons, neutral hadrons (neutrons) are dominant in the HGCAL. Because of the required radiation tolerance and the demands on resolution, electronics, and mechanics mentioned before, the CMS Collaboration will upgrade the forward calorimeters to the High Granularity Calorimeter (HGCAL) during Phase-2.
The HGCAL design features a modular structure consisting of hexagonal base elements, denoted as "modules". One module is an integrated stack of readout electronics, a silicon sensor, a Kapton sheet for high voltage insulation, and a copper/tungsten base plate for CO_2 cooling at -30 °C. The layers are held together via glue. These modules combine into wedge-shaped cassettes, which feature superordinate components like power supply, cooling structures, and absorber plates, completing its setup as a sampling calorimeter. The cassettes, on their part, assemble into discs, which build the endcaps in layers. A cross section of one HGCAL segment is shown in Figure 1.8. The HGCAL divides into an electronic calorimeter (Calorimeter Endcap - Electronic, CE-E) consisting of silicon sensors and a hadronic calorimeter (Calorimeter Endcap - Hadronic, CE-H) consisting of bot silicon sensors and scintillating tiles. The scintillating tiles in the outer regions of CE-H, are not the topic of this work and will not be explained in detail here. Thermal insulation will enclose the whole calorimeter, which allows its operation at -30 °C [20].

Extensive inter-cell calibration is required to maintain the performance of the HGCAL over the entire projected lifetime. This is defined by whether the sensitivity is sufficient for minimum-ionizing particles (MIPs), which corresponds to the smallest expected signal-to-noise ratio (SNR). This must also be maintained at the end of the runtime, at 3000 fb^{-1}. This requires cells with low electrical capacitance, which automatically translates to the requirement for a small cell area (0.1 to 1.3 cm^2) given the small cell thickness of 120 to 300 µm. The required fine lateral and longitudinal granularity leads to a high number of cells (up to 444 per sensor). These are the summarized basic requirements for the silicon sensors of the HGCAL [20]:

- *Radiation tolerance*: The energy resolution must be guaranteed even after 3000 fb^{-1}; this

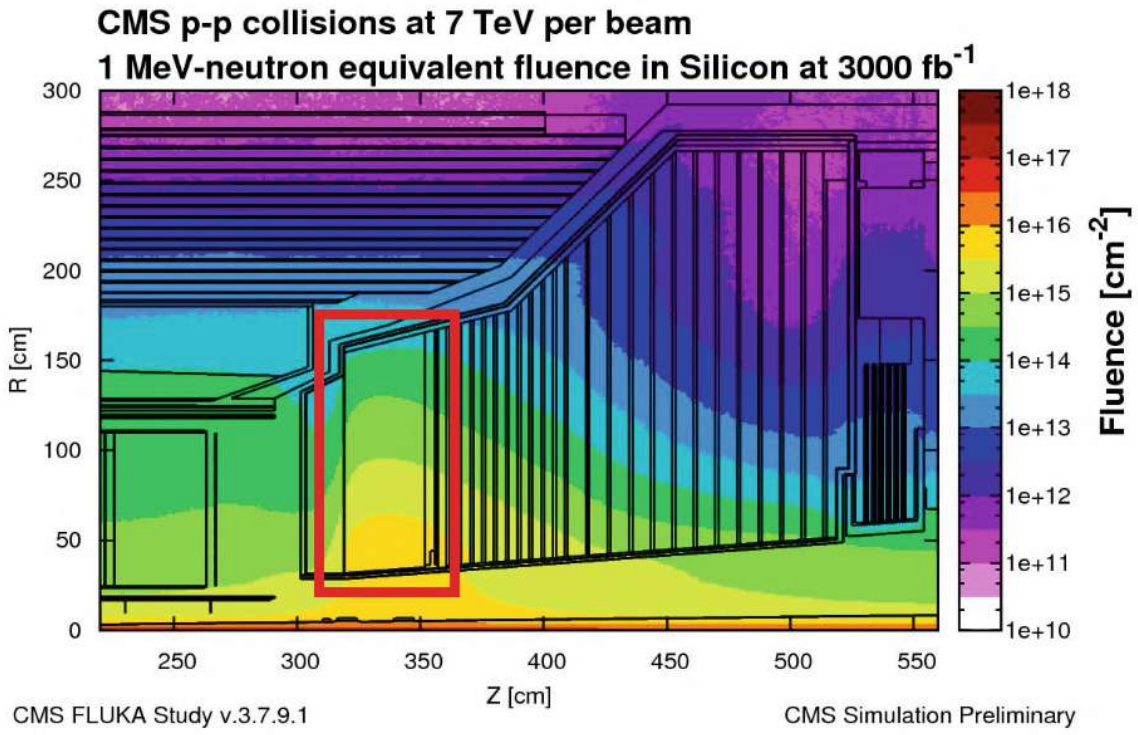

Figure 1.7: FLUKA simulation of the expected total fluence of the HGCAL after an integrated luminosity of 3000 fb^{-1}. The fluence is normalized to 1 MeV equivalent neutrons. The beam axis is horizontal, parallel to the text direction. The bunch crossing point is located at the bottom left. The red square marks the electromagnetic calorimeter (CE-E) [20].

requires good inter-cell calibration of 3 % [20] using minimum ionizing particles. According to simulations (Figure 1.7) the maximum obtained fluence is 10^{16} cm^{-2} over the planned lifetime. In this region with the highest radiation exposure, the HD sensors (Section 5.4) with 120 µm active thickness are used, which was also considered in the tests of the Ministrip sensors (Section 6.4).

- *Dense calorimeter*: This keeps the lateral dimensions of the shower small, which is the prerequisite for compactness of the calorimeter.
- *Fine lateral granularity*: To keep the electronic noise low, to obtain the required signal-to-noise ratio to perform the MIP calibration finally, to accomplish the two shower separation, to detect narrow jets, as well as to limit the region in which the energy measurement is performed, which is necessary to suppress pileup effects.
- *Fine longitudinal granularity*: This allows fine sampling of the shower length, which increases the electromagnetic energy resolution (for example $H^0 \to \gamma\gamma$), for pattern recognition, and discrimination against pileup effects.
- *precision timing measurement*: To obtain precise timing information from each cell while maintaining a significant amount of deposited energy, to suppress pileup effects, and for the identification of triggering vertices.
- *ability to contribute to the Level-1 trigger decision*: results from the preceding requirements.

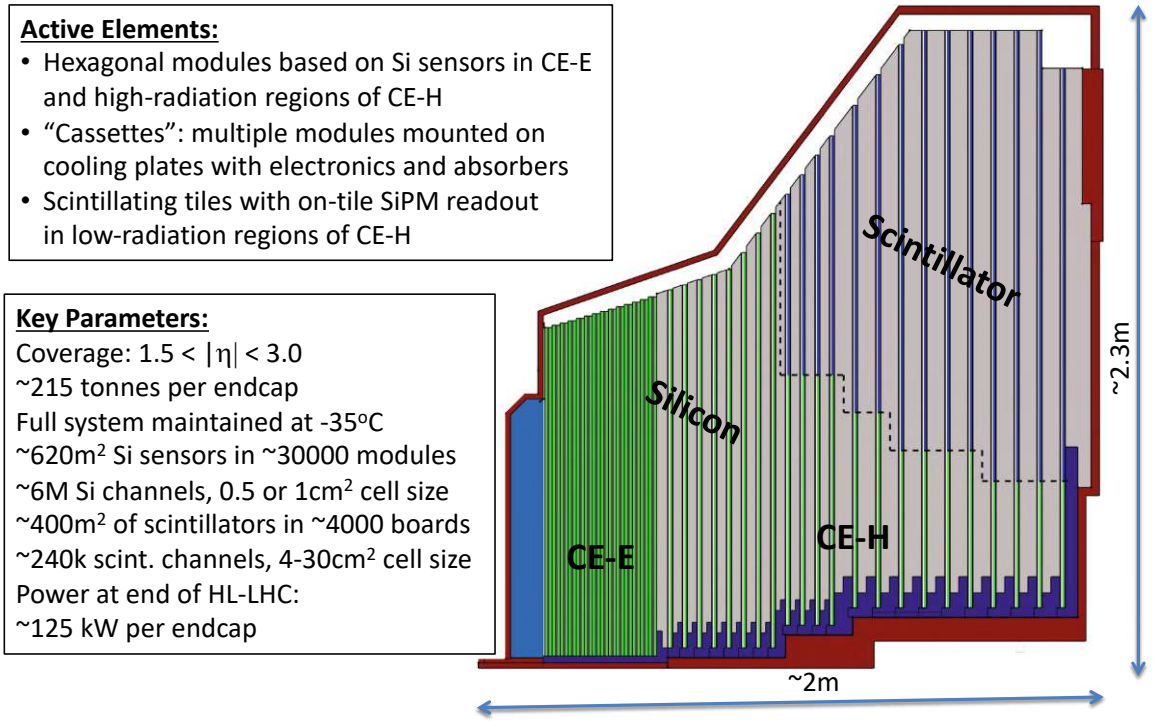

Figure 1.8: Cross section of one sector of the HGCAL. This thesis focuses on the silicon part as sensing elements, marked as green slices. The beam axis is horizontal, parallel to the text direction. The bunch crossing point is located at the bottom left. The HGCAL divides into an electronic calorimeter (Calorimeter Endcap - Electronic, CE-E) consisting of silicon sensors and a hadronic calorimeter (Calorimeter Endcap - Hadronic, CE-H) consisting of bot silicon sensors (green) and scintillator tiles (blue). Figure from [5].

"The best that most of us can hope to achieve in physics is to misunderstand at a deeper level."

Wolfgang Pauli

2 Theory of semiconductor particle detectors

2.1 Fundamentals of semiconductors

Semiconductors have shaped our modern civilization like no other technology. Of course, this also applies to high-energy physics, not only in terms of high-performance clusters for data analysis, but also fundamentally in terms of new technologies for the detection of particles. This chapter deals with the physical fundamentals and thus provides an introduction and basis for understanding the following chapters. Many parts of this chapter are considered textbook knowledge and are not referenced separately.

Solids divide into three groups based on their electrical conductivity: Conductors, semiconductors, and insulators. As one might suspect, the conductivity of semiconductors lies between those of conductors and insulators. The boundary regions of these three groups overlap, so there are other specifics to define semiconductors: The negative temperature coefficient for resistivity[a] and the bandgap. Table 2.1 provides an overview of the properties of these three classes.

2.1.1 Band model

It is known from quantum mechanics that the energy levels of bound electrons in atoms are discrete. In single atoms, these energy levels are also sharply defined within the uncertainty relation. However, in many-particle systems, the potentials of neighboring atoms perturb the previously sharp energy levels and split them into different sub-levels. In many-particle systems, such as current-technology semiconductors, this smearing is so advanced that the energy levels are grouped into energy bands (Figure 2.1). The lower energy bands ($\approx$ meV) are still strictly bound to the respective atomic nucleus. Higher energy ($\approx$ eV) bands, which are not bound to atomic nuclei, are, therefore, quasi-free and can be modeled with the help of the Fermi gas. These bands are grouped under the term "conduction band". Between the conduction band and the energy band of the localized electrons,

[a] The conductivity of semiconductors, unlike metals, increases with increasing temperature. This is because more charge carriers enter the conduction band as the temperature rises.

Table 2.1: Distinction between conductors, semiconductors and insulators. Typical values at 300 K [45].

Type	Conductivity	Band gap	Mobile charge carrier density
Conductors	$>10^3$ S/cm	0	$10^{22}\,\mathrm{cm}^{-3}$
Semiconductors		0.1 to 4 eV	10^6 to $10^{13}\,\mathrm{cm}^{-3}$
Insulators	$<10^{-8}$ S/cm	>4 eV	~ 0

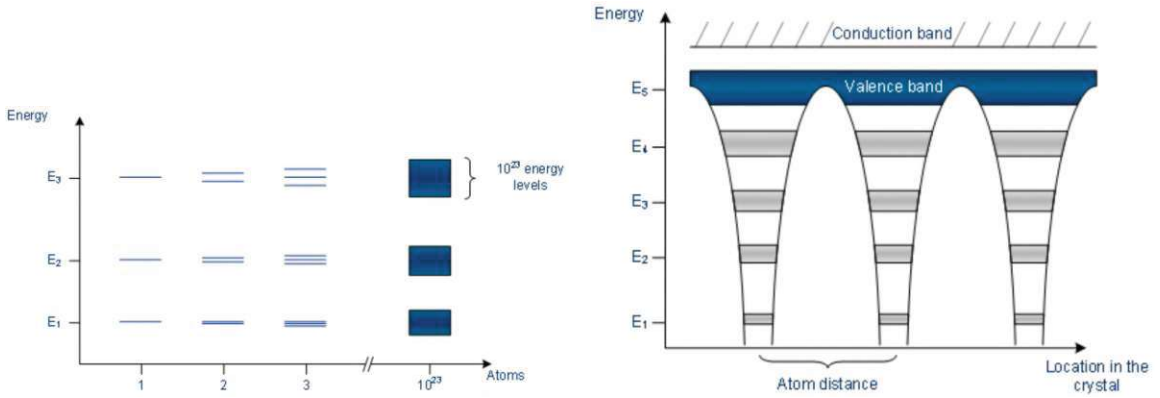

(a) The transition from single-particle systems ($n = 1$, discrete energy levels) via multi-particle systems with split energy levels to many-particle systems. The energy levels are finely granulated so that they form a banded structure.

(b) If one considers the potential wells of the individual atoms, the separation into valence and conduction bands can be understood. The energy difference between the valence and conduction bands is called the "band gap".

Figure 2.1: Formation of energy bands in semiconductors. Images from [47].

there is an energy band in which the electrons can jump from atom to atom. This is called the valence band. The distance between the valence band and the conduction band is called "bandgap" and is the central characteristic of semiconductors (see Table 2.1).

Since in semiconductors, the bandgap is comparatively narrow, 0.1 to 4 eV, there are already single electrons in the conduction band at room temperature (Fermi-Dirac statistics), but not yet so many to achieve the high conductivity of conductors. With increasing temperature, more and more electrons enter the conduction band, and the conductivity of semiconductors increases. This essentially explains the effect of the negative temperature coefficient on the resistivity of semiconductors.

Direct and indirect semiconductors

For a complete picture of the band structure, the electrons' energy-momentum (E-k) relationship must be considered a crystal direction function. In 'indirect' semiconductors (such as Si or Ge, see Figure 2.2b), the electrons in the sinks of the conduction band (in momentum space) have a different crystal momentum k than the holes in the maxima of the valence band. Therefore, for a transition to occur, momentum transfer to the crystal lattice must occur. This is not the case for gallium arsenide (GaAs), a 'direct' semiconductor, see Figure 2.2a. The generation of e/h pairs and recombination can occur without momentum transfer to the lattice. Light generation by recombination is thus more efficient, which is why GaAs are one of the preferred base materials for LED manufacturing [45].

Intrinsic semiconductors

This subsection discusses the conduction properties of semiconductors, mainly using silicon as an example, without special doping. An intrinsic semiconductor is entirely pure, with no significant doping species present. Intrinsic semiconductors are, therefore, also called pure semiconductors or i-semiconductors. At $T > 0$K, bonds can break in semiconductors; Valence electrons are released, leaving holes. As expressed in the band model, the valence electrons are lifted from the valence band into the conduction band and contribute thus contribute to the current flow (electron conduction). Analogously, a hole can be occupied by a valence electron, which leaves a free hole elsewhere; this is called hole conduction. Electrons and holes behave like free particles with different effective masses [45].

Therefore, in intrinsic semiconductors, the concentration of excited electrons in the valence band and the concentration of holes are equal: $c_n = c_p$. It is even possible that a doped semiconductor is nevertheless an intrinsic semiconductor: This is precisely the case if the doping is composed of equal

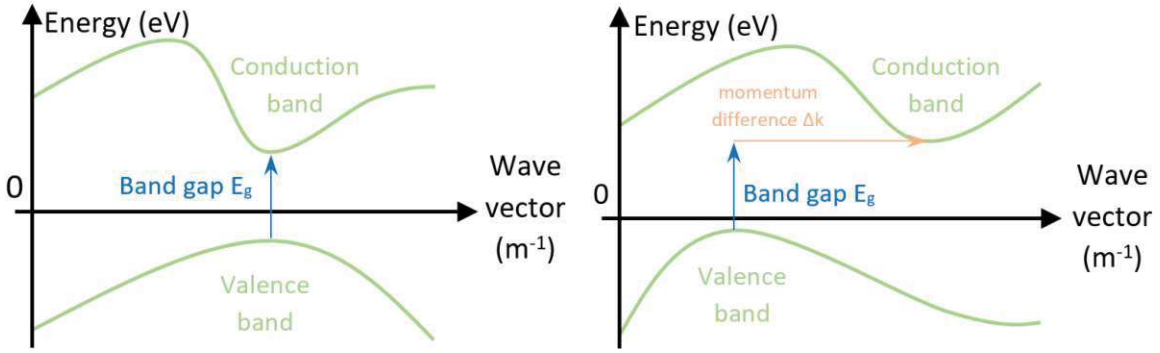

(a) In a direct semiconductor, the minimum of the conduction band is precisely above the maximum of the valence band. The difference of the wave vectors is zero, so the energy transfer can be direct, for example, by the emission of a photon.

(b) In an indirect semiconductor, no photon can be emitted directly because the energy-transferring electron must first go into an intermediate state and transfer momentum to the crystal lattice (momentum difference Δk).

Figure 2.2: Sketched dispersion relation of direct and indirect semiconductors. The energy is plotted vertically, and the crystal momentum (k-vector) in the Brillouin zone (momentum space) is plotted horizontally.

proportions of donors and acceptors, i.e., the concentration of the additionally generated charge carriers also balances electrically, so $c_n = c_p$ still applies.

2.1.2 Doping

Doping is the introduction of foreign atoms into a semiconductor crystal lattice to change the conductivity in a targeted and controlled manner. The doping elements are subsequently introduced into the semiconductor material from the outside using various processes (ion implantation, diffusion) or are already added to the melt when the ingot is drawn. The number of valence electrons of the doping element determines the doping type. Elements with 3 valence electrons are used for p-doping, 5-valent elements for n-doping. The conductivity of a specifically impure exemplary silicon crystal can thus be increased by a factor of 10^6. Two essential substances silicon can be doped with are boron (3 valence electrons = 3-valent, Group III in the periodic table of elements) and phosphorus (5 valence electrons = 5-valent, Group V), see Figure 2.3.

n-doping

The 5-valent doping element has one more valence electron than the silicon atoms. 4 outer electrons can bind with one silicon atom each; the fifth is free to move and serves as a charge carrier. This unbound electron requires much less energy to be lifted from the valence band to the conduction band than the electrons that cause the intrinsic conductivity of silicon. The dopant element that donates an electron is called an electron donor.

The dopant elements become positively charged by emitting negative charge carriers and are more or less fixed in the lattice; only the electrons move in a first approximation. Doped semiconductors whose conductivity is based on free electrons (= **n**egative charges) are n-conducting or n-doped. While holes (and just as many electrons) can be spontaneously generated in the crystal at any time, the number of free electrons is now outweighed by the donors introduced, which is why these are called majority charge carriers. Holes, on the other hand, are called minority charge carriers.

p-doping

In contrast to the free electron in n-doping, 3-valent dopants have exactly the opposite effect: they can accept an additional outer electron and thus leave a hole in the valence band of the silicon atoms. As a result, the electrons in the valence band become mobile. The holes naturally move in the opposite direction to the electron movement.

By accepting an electron, the dopant element becomes negatively charged; such dopant atoms are called electron acceptors. Again, the dopant element is more or less fixed in the crystal lattice; only the positive charge moves. P-conducting or p-doped semiconductors are called such because

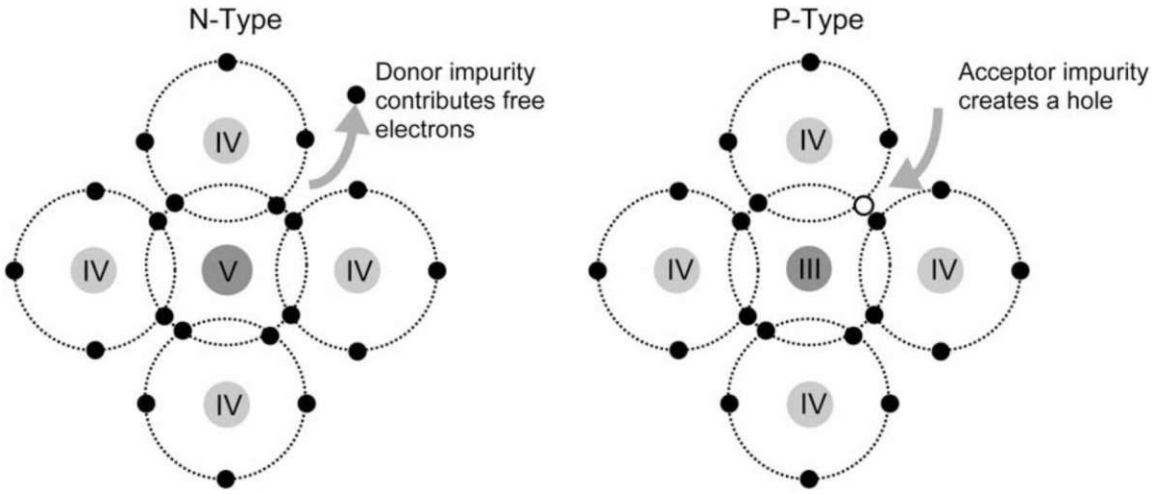

Figure 2.3: Comparison of n- and p-doping. If a 5-valent atom is introduced into the crystal lattice, which consists of 4-valent atoms, there is an excess electron with a negative charge. This results in n-doping (left graph). The reverse is true when a 3-valent atom is introduced into the crystal lattice. A missing electron can be filled by neighboring electrons, where in turn, an electron is missing. This is called a p-doping (right graph). Image from [15].

the conductivity is based on **p**ositive holes so to say, a "missing" electron. Analogous to n-doped semiconductors, the holes are the majority charge carriers, and free electrons are the minority charge carriers.

2.2 p-n junctions and electrical characteristics of diodes

As described in Section 2.1.2, there are free charge carriers in doped semiconductors, and the number of these is much higher than the number created by the incidence of high-energy particles. In principle, it would be possible to measure the resulting change in conductivity, but these changes would, of course, be minimal. To create a region without free charge carriers (depletion zone), one combines p- and n-doped semiconductors to form a p-n junction, a diode, as seen in Figure 2.4.

A p-n junction has the basic property of conducting well in the forward direction because the depletion zone (region of high resistivity) vanishes. In the reverse direction, the opposite happens: the external electric field "pulls" the charge carriers into the respective opposite region, where they recombine. Thus, the depletion zone grows, and the total resistance of the p-n junction increases dramatically.

Macroscopically, therefore, the diode has two states:

Forward bias: When a diode is forward biased, meaning the positive terminal of a voltage source is connected to the diode's anode (p side) and the negative terminal to the diode's cathode (n side), the current can flow through the diode. In this condition, the diode has a low resistance and is said to be "on" or conducting. The voltage required to overcome the diode's forward voltage drop (typically around 0.6 to 0.7 V for silicon diodes) is known as the forward voltage.

Reverse bias: When a diode is reverse biased, meaning the positive terminal of a voltage source is connected to the diode's cathode (N-side) and the negative terminal to the diode's anode (P-side), the current is almost completely blocked, and the diode has a high resistance. It is said to be "off" or non-conducting. Only a small leakage current, known as reverse leakage current, flows through the diode in this condition.

Therefore, semiconductor detectors are switched into reverse bias to maximize the depletion zone, and this depletion zone forms the active volume of the semiconductor detector. There are almost no free charge carriers in this setting, so the signal-to-noise ratio is maximized for incoming particles.

2.2.1 Capacitance of a diode

In a pn junction, a layer of low charge carrier concentration (depletion zone, space-charge region) resides between two well-conducting layers (undepleted p and n zones). This structure, conductor-

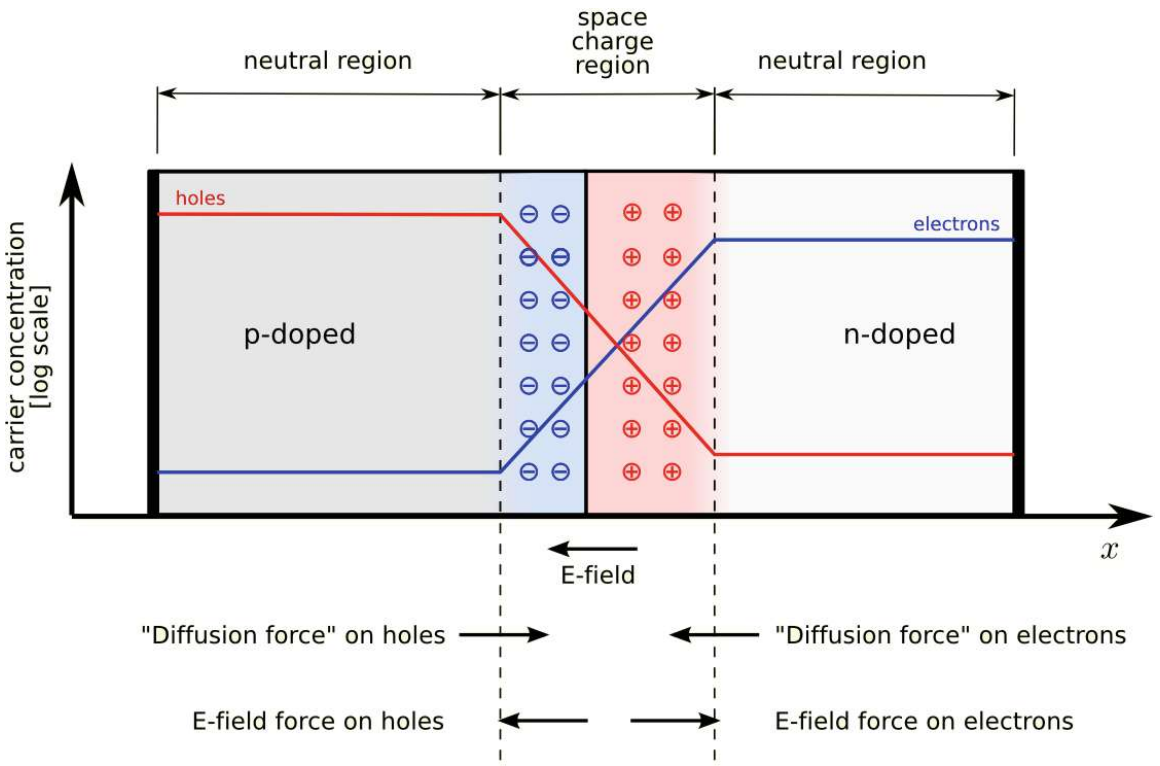

Figure 2.4: This sketch shows a p-n junction with no external applied voltage in thermal equilibrium. The neutral regions contain p- and n-charge carriers, respectively. The red zone has an excess of p-carriers, while the blue zone has an excess of n-carriers. Together they form the depletion zone. The separation of the charge carriers creates an electric field that opposes and balances the diffusion forces. The conduction electrons diffuse from the outside into the space charge zone, while the electric field prevailing in the space charge zone provides the drift. The opposite is true for the holes. The E-field times the thickness of the space charge region form the "built-in voltage" U_{bi}. Image from Wikiversity [82].

insulator-conductor, corresponds to a plate capacitor. To calculate the capacitance of a semiconductor diode, it is therefore apparent to start with the equation for a plate capacitor:

$$C = \epsilon \frac{A}{d} \tag{2.1}$$

where ϵ is the electrical permittivity, A is the area, and d is the thickness of the plate capacitor. ϵ is composed of $\epsilon = \epsilon_0 \epsilon_\mathrm{r}$, where ϵ_0 is the vacuum permittivity and ϵ_r is the relative permittivity of the material.

Now we look at the "built-in voltage" U_bi, which is defined by the shifted Fermi levels (Figure 3.1c) $E_\mathrm{F,p}$ and $E_\mathrm{F,n}$ for the junction of the p-type and n-type silicon. Macroscopically, it is the voltage across the space-charge region without an external electric field (see Figure 2.4) [74]:

$$U_\mathrm{bi} = \frac{E_\mathrm{F,p} - E_\mathrm{F,n}}{q} = \frac{k_\mathrm{B} T}{q} \ln\left(\frac{N_\mathrm{A} N_\mathrm{D}}{n_\mathrm{i}}\right) \tag{2.2}$$

The product qU_bi corresponds to the energy by which the conduction or valence band is shifted with respect to the Fermi level [74]. Now the total width of the depletion zone is given by the sum of the depletion zone thicknesses of p- and n-type zones [74]:

$$d = d_\mathrm{p} + d_\mathrm{n} = \sqrt{\frac{2\epsilon U_\mathrm{bi}}{q(N_\mathrm{A} + N_\mathrm{D})}} \left(\sqrt{\frac{N_\mathrm{D}}{N_\mathrm{A}}} + \sqrt{\frac{N_\mathrm{A}}{N_\mathrm{D}}}\right) \tag{2.3}$$

Because we apply a negative bias voltage to our semiconductor detector (reverse bias), the thickness of the depletion zone increases. Therefore, we substitute $U_\mathrm{bi} \to U_\mathrm{bi} + U$. Furthermore, in our detector, a highly doped region (N_A) is embedded in a region of lower doping concentration (bulk with N_D), thus ($N_\mathrm{A} >> N_\mathrm{D}$) applies. Thus Equation 2.3 can be rewritten as:

$$d \approx \sqrt{\frac{2\epsilon(U_\mathrm{bi} + U)}{qN_\mathrm{D}}} \tag{2.4}$$

Inserting Equation 2.1 into 2.4 yields:

$$C \approx A \sqrt{\frac{q\epsilon N_\mathrm{D}}{2(U_\mathrm{bi} + U)}} \tag{2.5}$$

The squared inverse of this equation is:

$$\frac{1}{C^2} \approx \frac{2(U_\mathrm{bi} + U)}{A^2 q\epsilon N_\mathrm{D}} \approx \kappa_1 + \kappa_2 U \tag{2.6}$$

where all the material constants and quantities that remain constant to a first approximation are consolidated in κ_1 and κ_2.
What is essential about Equation 2.6 is the linearity between the inverse square of the capacitance and the voltage applied to the diode [4]. This means that as long as the bias voltage is below the full depletion voltage, i.e., the depletion zone has not yet fully migrated through the sensor, the inverse square of the capacitance increases linearly with the voltage. When the full depletion zone is reached, this curve makes a sharp bend, which is characterized by the fact that only the "remaining" corners and edges of the sensor are filled with the depletion zone. Once this is achieved, the capacitance remains constant with respect to the voltage since the full depletion zone cannot become larger than the total sensor bulk. Exactly this behavior can be observed in the measurements (Appendix A.16), where the tipping point determines the full depletion voltage.

2.2.2 Shockley ideal diode equation

The Shockley diode equation provides a mathematical relationship between the idealized current flowing through a diode and the voltage across it in forward bias and reverse bias (without breakdown). The equation is given as follows:

$$I(U,T) = I_0 \left[\exp\left(\frac{qU}{nk_\mathrm{B}T}\right) - 1\right] \tag{2.7}$$

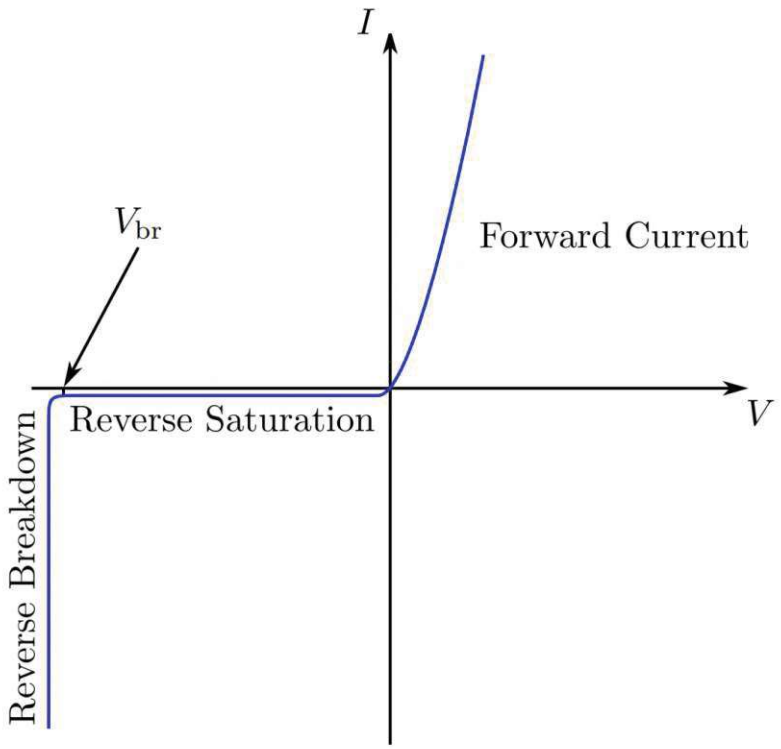

Figure 2.5: Diode characteristic (current-voltage) of an ideal pn junction. According to the Shockley equation 2.7, an increasing forward voltage causes an exponential increase in the diode current. A small leakage current, the saturation current (I_0), runs in the reverse direction. A breakdown in the reverse direction is not described by the Shockley equation but takes place in reality and ends quickly in the destruction of the diode in the absence of electrical power limitation or heat dissipation. Image from [84].

where I_0 is the reverse bias saturation current (the leakage current at reverse bias voltage), q is the elementary charge, k_{B} is the Boltzmann constant, and T is the temperature. n is the "ideality factor" which describes the imperfect junctions observed in real transistors, and typically ranges from 1 (ideal material) to 2. For a complete derivation of the equation from the Fermi levels, refer to Shockley [71]. The Shockley equation is a fundamental equation for diode current that correctly describes the forward current and the reverse bias saturation current. However, it does not describe the reverse breakdown (see Figure 2.5) caused by avalanche multiplication and/or tunneling effect. Since both phenomena occur in a range outside the permissible sensor specification, this will no longer be discussed in this paper.

2.2.3 Temperature dependency of diode currents

In statistical mechanics, the Fermi-Dirac distribution plays a fundamental role in describing the distribution of energy states of particles that obey the Pauli exclusion principle (Fermions). It describes the probability that a system at a given temperature T is in an energy state ε_i in a thermal equilibrium:

$$p_i(\varepsilon_i, T) = \frac{1}{\exp\left(\frac{\varepsilon_i - \mu}{k_B T}\right) + 1} \tag{2.8}$$

whereas p_i is the probability for a system to be in the state i, μ is the total chemical potential and k_B the Boltzmann's constant [45].
In this consideration, we will restrict ourselves only to the charge carriers, since only they contribute to the electrical properties of interest. In the limiting case, where only very few charge carriers are in the conduction band ($p_i << 1$, which is valid for semiconductors), μ being in the center of the

bandgap ($\frac{1}{2}$) and temperatures far from absolute zero ($T >> 0$), the following approximation applies:

$$p_i(\varepsilon_i, T) \approxeq \exp\left(-\frac{\varepsilon_i}{2k_B T}\right) \tag{2.9}$$

whereas p_i is the probability for a system to be in the state i and k_B the Boltzmann's constant [45]. Equation 2.9 is the classical limiting case of the Fermi-Dirac distribution, namely the Maxwell-Boltzmann distribution.
Now that we have derived the Maxwell-Boltzmann distribution for our system, we move on to the next step: The current in a semiconductor is quadratically temperature-dependent since the T^2 dependence corresponds to the thermionic emission of charge carriers with kinetic energies $E_{\text{eff}} = \frac{1}{2} m_{\text{eff}} v^2$ across a barrier:

$$I(T) \propto T^2 \exp\left(-\frac{E_{\text{eff}}}{2k_B T}\right) \tag{2.10}$$

Now we have the proportionality of the current in semiconductors as a function of temperature at the effective energy. If we now relate two currents at different temperatures $I(T_1)$ and $I(T_2)$, the prefactors of the proportionality truncate out, and we obtain the following equation:

$$I(T_2) = I(T_1)\left(\frac{T_2}{T_1}\right)^2 \exp\left[-\frac{E_{\text{eff}}}{2k_B}\left(\frac{1}{T_2} - \frac{1}{T_1}\right)\right] \tag{2.11}$$

With this equation, we can now scale the current at one temperature that we measured to a current at another temperature to obtain a standard measure that ensures comparability. The scaling formula results in a rule of thumb that the current doubles approximately every 7 K increase in temperature.

2.3 Ionizing energy loss and the minimum ionizing particle (MIP)

he Bethe-Bloch equation is a commonly used instrument to describe the energy loss of charged particles for the passage of charged particles through matter. It is derived from semi-relativistic pertubation theory and models the energy loss primarily due to collision-induced electromagnetic interactions (ionization and excitation) with atomic electrons in the material under the premise that incident particle energies are much higher that electron binding energies, so the electrons of the target can be seen as resting in the detector frame of reference. This equation provides a relationship between the kinetic energy loss ($\frac{dE}{dx}$) of a particle per unit length and its velocity, charge, and mass, as well as the microscopic parameters of the target material.
A typical formulation with corrections is given by:

$$-\left.\frac{\mathrm{d}E}{\mathrm{d}x}\right|_{\text{coll}} = Kz^2 \frac{Z}{A}\frac{1}{\beta^2}\left[\underbrace{\frac{1}{2}\ln\frac{2m_{\text{e}}c^2\beta^2\gamma^2 T_{\max}}{I^2}}_{\text{semi-relativistic}} \underbrace{-\beta^2}_{\substack{\text{relativistic}\\ \text{correction}}} \underbrace{-\frac{\delta(\beta\gamma)}{2}}_{\substack{\text{density}\\ \text{correction}}} \underbrace{-\frac{C}{Z}}_{\substack{\text{shell}\\ \text{correction}}}\right] \tag{2.12}$$

where $\beta = \dfrac{v}{c}$, $\gamma = \dfrac{1}{\sqrt{1-\beta^2}}$ the Lorentz factor, Z the target's atomic number, A its relative atomic mass, m_{e} the electron rest mass, z the incident particle's charge number, $T_{\max}$ is the maximum kinetic energy transfer to the electron in a single collision, and I is the mean excitation potential of the target. The Bethe-Bloch coefficient K is a constant derived from other, fundamental constants: $K = 4\pi N_{\text{A}} {r_{\text{e}}}^2 m_{\text{e}} c^2$ with N_{A} being the Avogadro constant, and r_{e} the classical electron radius $e^2/4\epsilon_0 m_{\text{e}} c^2$. The density correction is caused by the polarization effect at higher energies, and the shell correction is important for small energies [35].

The Bethe-Bloch equation is a valid approximation in the energy range from a few MeV up to several GeV for protons. At lower energies, below a few MeV, the energy loss of protons is dominated by energy transfer through elastic collisions with atomic nuclei. The Bethe-Bloch equation is invalid in this energy regime, and other theoretical models are more appropriate. At higher energies, above several GeV, the energy loss of protons may be influenced by different processes, such as radiative

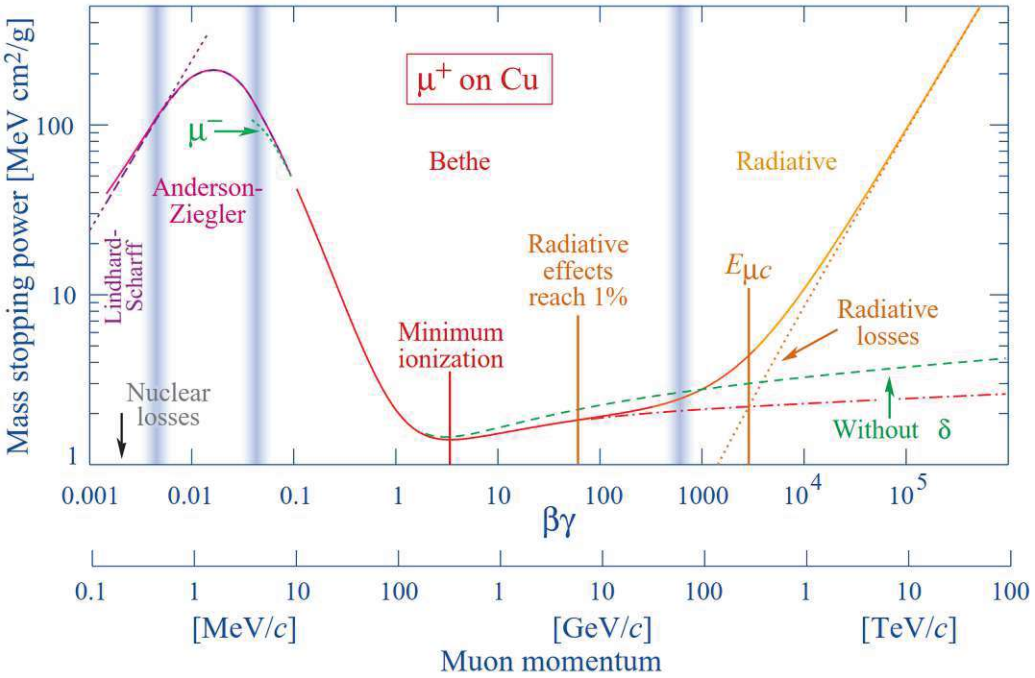

Figure 2.6: Mass stopping power $\frac{dE}{dx}$ for positive muons in copper as a function of $\beta\gamma = pc/m$ up to the TeV/c momentum (TeV energy range). The solid curves indicate the total stopping power, whereas the dashed and dotted lines indicate single effects and models. The Bethe-Bloch equation best approximates the middle energy range, labeled "Bethe" (red line). In the TeV/c range, radiative losses dominate, and the Bethe-Bloch equation is not a valid approximation anymore [35]. Specialized plots of stopping power in silicon exemplified by protons and electrons can be found in the Appendix A.1. Image from [59].

losses.
It is important to note that the Bethe-Bloch equation provides an average description of energy loss and may not capture the full details of energy loss fluctuations and statistical effects like straggling, particularly at low energies. Therefore, additional experimental data and Monte Carlo simulations are often employed in practical applications and experimental studies to better characterize protons' energy loss over a wide range of energy.
The Bethe-Bloch equation does not apply to electrons, as seen in Appendix A.1. The curve shape is quite different. On the one hand, this is due to the quantum mechanical indistinguishability of the incident electrons from the target electrons (for which the Bethe-Bloch equation is not designed); on the other hand, the bremsstrahlung is dominant for electrons.

As can be seen in Figure 2.6, there is a minimum of the mass stopping power $\frac{dE}{dx}$ in the semiclassical range for intermediate particle energies ("Bethe" region). In this region, a particle deposits the smallest energy per path length in the detector, thus the generated signal is the smallest. This point is called "minimum ionizing particle" (MIP), at a kinetic energy corresponding to 2 to 3 times the rest energy. This rule of thumb applies to all electrically charged particles. More easily recognizable plots for protons and electrons can be found in the Appendix A.1.

"The science of today is the technology of tomorrow."

Edward Teller

3 Semiconductor detector technology

Research into semiconductor particle detectors for low and high-energy radiation, such as gamma rays, electrons, protons, and other ionizing particles, has made enormous progress in recent years. The driver of this progression is the great importance of many applications, such as medical imaging, monitoring of industrial processes, national and environmental security, and basic research.
Semiconductor detectors are of particular importance here. A semiconductor particle detector is a device that uses a semiconductor material such as silicon or germanium to detect and measure the presence and properties of charged particles such as protons, electrons, and other particles. The most common detectors, Ge and Si, are used in many different applications. They offer advantages over scintillators and gas detectors concerning their simple, miniaturized design, easy integration into readout electronics, and high spatial and energy resolution.
Semiconductor particle detectors operate on the principle that when a charged particle passes through the sensor, it can knock loose an electron from the atoms in the semiconductor material, creating a charge disturbance that can be detected and measured. Semiconductor particle detectors are widely used in various applications, including particle physics research, medical imaging, and industrial inspection. They are particularly well suited for detecting low-energy charged particles, such as beta particles, due to their high sensitivity and ability to distinguish different particles based on their energy levels. However, because of their low response time and beam hardness, they are also in particular demand in high-energy physics. Many parts of this chapter are considered textbook knowledge and are not referenced separately.

3.1 Basic principles and requirements for semiconductor particle detectors

The working principle of a detector is linked to the structure of the crystal to be studied. The more regular its crystal structure, the better the conduction of electrons in the crystal. The periodic structure of crystalline materials constitutes allowed energy bands (valence and conduction) for electrons that exist in that solid. The energy of any electron within the pure material must be limited to one of these energy bands, which can be separated by "holes" or forbidden energies. The sensitive volume of detectors corresponds to the depletion region formed by the junction of a semiconductor. When the semiconductor is exposed to radiation, electron and hole pairs are created within this region and are then collected, generating the electrical signal.
Semiconductor crystals are widely used for the detection of ionizing radiation because of their advantages over other types of crystal detectors, such as fast response time, small size, and excellent resolution of the radiation energy. These characteristics of semiconductors lead to simplification in the electronic system and lead to an enhanced signal-to-noise ratio (SNR) [44].
One of the significant advantages of semiconductor detectors provided the band gap is high enough, is the low leakage current generated by thermal fluctuations. If the band gap is high enough and the

radiation exposure is low (see Section 4), semiconductor detectors are suitable for operation even without active cooling[44].
Paramount properties of a semiconductor detector for high energy physics are:

- Wide band gap E_g to achieve high resistivity and low leakage current.
  The band gap must be sufficiently large to obtain high resistivity and low leakage current. A high leakage current would inevitably lead to an increased signal-to-noise ratio (SNR) since the desired signal manifests as a current through the detector. The band gap, therefore, directly influences the noise and the minimum possible energy resolution of the detector. In silicon, the average energy needed to create one electron-hole pair is $\approx 3.65\,\text{eV}$ [27].

- High charge carrier mobility μ and lifetime τ.
  High mobility of the charge carriers is desirable, so that incident particles trigger a sufficiently short and high current pulse. The shorter and higher it is, the faster the detector is, so the dead time decreases, and therefore the integration time can also be reduced. The drift length of the charge carriers is given by $l = \mu\tau E$, where μ is the carrier mobility, τ is the carrier lifetime, and E is the applied electric field. How many charge carriers are ultimately collected depends on the ratio of the product of mobility μ times lifetime τ times applied electric field E. The product $l = \mu$ times lifetime τ corresponds to the characteristic drift length. Ideally, this drift length should be longer than the thickness of the detector so that the charges generated by particle incidence are collected as completely as possible. This is usually the case for electrons due to their high mobility, but not for holes. Lower mobility of the holes (as in p-type sensors) requires applying a higher bias voltage to achieve full depletion. The mobility depends on both temperature and doping concentration: A higher temperature leads to the charge carriers being able to scatter at the lattice vibrations in the crystal, lowering the mobility. Impurities (doping) in the crystal lattice lead to disturbed periodicity of the electric field of the lattice atoms, which also reduces mobility. Irradiation of sensors increases the effective doping concentration. Therefore, mobility decreases, and thus the full depletion voltage increases.

- Pure, homogeneous and defect-free bulk material and sufficient detector thickness.
  The purity, homogeneity, and low density of crystal lattices are the basis for adequate transport properties of the charge carriers but also for the lowest possible leakage current. Impurities and crystal defects also interfere with the process of charge collection. The above properties also influence the electric field, which should have the highest possible homogeneity [85]. In the case of calorimeters for high-energy physics, with very penetrating particles, the detector thickness is critical for energy resolution. One wants as much particle energy as possible to be deposited in the detector volume. However, a thick detector would not only cause a high leakage current but would also require too high a voltage for full depletion to be achieved, and this would cause problems with the high-voltage supply. At the same time, one wants calorimeters to have high stopping power so that the incident particles deposit as much energy as possible over a short length. This would require a dense material, which is different from silicon. To circumvent these problems, the HGCAL uses a sandwich configuration, where detector and absorber with high density are placed alternately.

The above fundamental requirements help to ensure that the semiconductor detector ultimately has the properties it needs for subsequent operation in high-energy physics. A detector in modern physics experiments may well receive radiation doses in the range of up to 1.5 MGy, or viewed in particle fluences, $10^{16}\,\text{cm}^{-2}$. To produce semiconductor detectors with enhanced radiation hardness, it is necessary to process the starting material (silicon in the case of this work) with high chemical purity and as free of defects as possible [50].

3.2 Particle interactions and signal generation

3.2.1 Particle interactions

When a charged particle passes through the silicon detector, it interacts with the silicon material's electrons and atomic nuclei. Several interactions may occur depending on the particle's charge and energy, such as ionization, excitation, and pair production. Section 2.3 details the energy loss of charged particles in silicon.

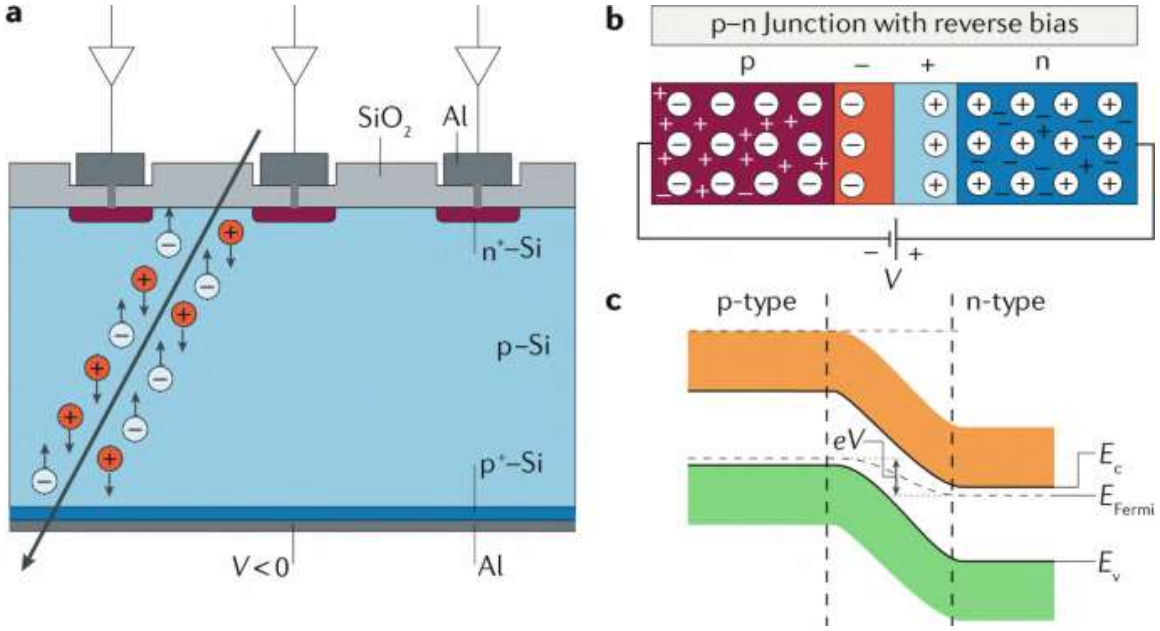

Figure 3.1: Overview of physical processes in semiconductor particle detectors.
(a) Signal generation in a p-type semiconductor detector. High voltage (order of magnitude 600 V) is applied between the aluminum-coated backside and the segmented n-electrodes. Now the bulk is free of free charge carriers (full depletion). When an ionizing particle (black arrow) passes through the detector, it generates free charge carriers by impact and secondary ionization, which flow through the electric field to the electrodes and generate a current pulse.
(b) pn junction with depletion zone. The p-type and n-type materials are in direct contact, so the excess holes from the p-type material will diffuse into the n-type material, and the excess electrons from the n-type material will diffuse into the p-type material. This creates a depletion region at the interface between the two materials where the majority of the charge carriers have been depleted and acts as a barrier to the flow of charge carriers. This depletion zone can be controlled by varying the doping levels or applying a voltage. In case of a semiconductor particle detector, the depletion zone ideally spreads over the whole sensor bulk.
(**c) Deformation of the energy bands at the depletion zone.** In thermal equilibrium, the two Fermi levels of the p- and n-zone must be continuous. Consequently, the energy bands bend across the space charge zone to equalize the energy levels.
Picture taken from [3].

- **Ionization:** The primary interaction mode is ionization, where the charged particle loses energy by colliding with and ionizing the silicon atoms. This process creates electron-hole pairs within the silicon material. The ionization energy of silicon is 3.63 eV, not the same but nearly three times larger than the band gap (1.12 eV at 300 K) because silicon is an indirect semiconductor (see Section 2.1.1).

- **Excitation:** In addition to ionization, the charged particle may also excite the silicon atoms, causing electrons to move to higher energy levels within the atom. These excited electrons eventually return to their ground state, emitting photons. Bulk traps create additional energy transition levels in doped (intentionally or radiation damage-induced) semiconductors.

- **Pair Production, showers, and jets:** Charged particles can create matter-antimatter pairs through high-energy pair production. This process involves converting the particle's energy into a pair of new particles, producing ionization and excitation within the detector material. This process can also repeat itself, which leads to showers. Hadronic interactions may create narrow cascades of secondary particles called "jets" [45][73][74].

3.2.2 Charge collection and signal generation

After the particle interacts with the silicon material and creates electron-hole pairs, the electric field within the depletion zone facilitates the movement of these charge carriers toward the electrodes. The reverse bias voltage applied across the silicon detector creates a strong electric field within the depletion zone. This field causes the electrons and holes to separate, with the electrons drifting toward the positively biased electrode and the holes drifting toward the negatively biased electrode, see Figure 3.1. The electrodes, typically made of metal, are in contact with the silicon material and collect the charge carriers. They are designed to capture the drifting electrons or holes efficiently. There is an additional diffusion in all directions via random walk due to thermal motion. The drift time and diffusion spread determine the spatial resolution of the detector [45][73][74].

3.2.3 Signal amplification and readout

The drift generates an electric current through the sensor. The readout electronics amplify and process these electrical signals, making them measurable and suitable for analysis. This is done in three steps:

- **Signal amplification:** The collected charge is typically very small, so the readout electronics include amplifiers to enhance the signal strength. These amplifiers may use various techniques, such as charge-sensitive amplifiers or voltage amplifiers.
- **Signal processing:** After amplification, the electrical signals are further processed using various techniques such as shaping, filtering, and digitization. This processing helps to improve the signal-to-noise ratio and extract relevant information about the particle interactions.
- **Data acquisition:** The processed signals are digitized and recorded by data acquisition systems. These systems convert the analog signals into digital form, allowing for subsequent analysis, reconstruction, and interpretation of the particle interactions. [45][73][74]

3.3 Production techniques for semiconductor detectors

The semiconductor device fabrication process is highly complex and requires a high degree of precision, as well as advanced equipment and materials. It is a continuous process of improving and perfecting the technology to create smaller, faster, and more efficient electronic devices.
The production of semiconductor particle detectors involves a series of steps to create the desired electronic components on a wafer:

1. Purification of the starting material
2. Photolithography of electrical structures
3. Dicing of the wafer: Cutting it into smaller pieces
4. Passivation and/or encapsulation
5. Bonding and assembly onto carrier structures

Each of these stages affects the crystal quality, introducing defects and imperfections and potentially deteriorating the performance of the detector.

Once the electronic components have been created, the wafer goes through a series of steps to passivize the surface, protect the electronic components, and add metal contacts to connect the electronic components to the outside world. After these steps, the wafer is diced into individual parts, and each chunk is packaged, tested, and then shipped to customers.

3.3.1 Wafer preparation

The silicon semiconductor detector production process starts with the creation of a silicon, poly-crystalline bulk material, which is then refined and purified to produce a mono-crystalline substrate.

This thesis describes the three different wafer processing methods used to fabricate the 8” prototypes (full list: Table A.1), including the test structures (Section 5.6): The Czochralski process, the Float-zone method, and the Epitaxial crystal growth. There are also other processes, such as the Bridgman method (crystallization of the ingot in an enclosed case), but these will not be discussed here in order not to go beyond the scope of this thesis.

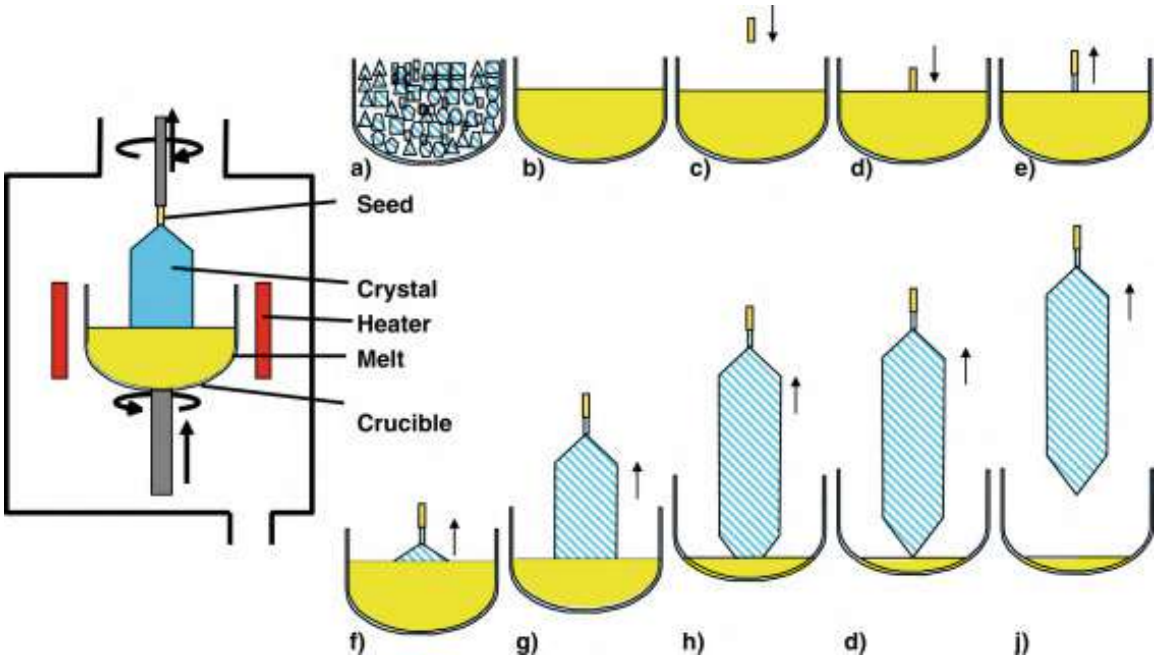

Figure 3.2: Overview of the Czochralski process. It starts by melting a high-purity material in a crucible **a)** and then slowly drawing a seed crystal from the melt **e)**. As the seed is pulled upwards and rotated, the material solidifies and forms a cylindrical ingot **g)** to **j)**.
Picture taken from [32].

Czochralski process

The Czochralski process is a method to grow single-crystal ingots of semiconductors, such as silicon and germanium, as well as some metals and oxides. Polish scientist Jan Czochralski developed the process in 1915. Since the 1950s, the semiconductor industry widely uses this process.
Figure 3.2 illustrates this method. The process begins with a small seed crystal, typically made of the same material as the desired ingot, suspended on the end of a rod or wire. The seed crystal is then dipped into a melt of the desired material, typically held in a quartz crucible. The temperature of the melt is precisely controlled to ensure that it is at the correct temperature for the desired material to be in its liquid phase. The seed crystal is then slowly withdrawn from the melt at a controlled rate while the rod or wire is rotated. As the seed crystal is withdrawn, atoms from the melt adhere to the surface of the seed crystal, forming a single crystal. The rate at which the seed crystal is withdrawn, as well as the rate of rotation, is critical to the success of the process and it is nowadays the main method for commercially grown silicon.
The size and shape of the ingot can be controlled by varying the rate of withdrawal, the temperature of the melt, and the size and shape of the seed crystal. The process can also be modified to produce multi-crystalline ingots using several seed crystals or large-diameter boules using a larger seed crystal. The Czochralski process is widely used in the semiconductor industry due to its ability to produce high-quality single-crystal ingots with a high level of control over their size, shape, and crystal orientation. The process is also relatively simple and inexpensive, making it a cost-effective method for producing semiconductor wafers. The Czochralski process has its limitations, however: It is typically limited to materials with a relatively low melting point, and it can be challenging to produce large-diameter boules without introducing defects [32].
The Czochralski process can also offer advantages for radiation-hard silicon detectors through the inherent impurity of oxygen in the process. While impurities are undesirable in themselves, oxygen has the property of acting as an “intrinsic getter” [56] for metals, aggregating radiation-induced damage and thus partially reducing its effect [66]. Another benefit of oxygen is pinning dislocations, which improve the thermal stability of the silicon.
However, oxygen and other impurities also have a significant disadvantage over float-zone processed material, resulting in low resistivity.

A more advanced method is the Magnetic applied field Czochralski method (MCz). It works the same as the conventional Czochralski method, except that a strong horizontal or vertical magnetic

field is also applied. This field is used for magnetohydrodynamic control of the silicon melt so that convection between the inner region, where the crystal grows, and the outer region in contact with the crucible (the container in which the silicon melt is located) is restricted. This method, therefore, reduces introduced impurities during crystal growth by reducing erosion of the silica crucible. As a result, this method can provide detector-grade silicon with high oxygen concentration [52].

Float-zone method

The Float-zone process, also known as the single-zone or vertical Bridgman process, is used to grow high-purity, single-crystal ingots of semiconductors and other materials. W.H. Zachariasen first developed this process in the 1940s, and since the 1960s, the semiconductor industry has been widely using it.
This technique is based on the spontaneous segregation of desired elements and unwanted impurities in a melt due to their different solubility in solids and liquids. As illustrated in Figure 3.3, the process begins with an already preprocessed polycrystalline rod of the desired material (by the Czochralski method, see Figure 3.2), which is placed in a high-purity quartz or pyrolytic boron nitride (pBN) chamber. The chamber is evacuated to a high vacuum and then filled with inert gas, such as argon or helium, to prevent oxidation of the material. A heating element, typically made of infrared-transparent material such as graphite, is positioned above and below the rod. The rod is heated by passing an electric current through the heating element, which causes the material at the top of the rod to melt. As the material melts, it forms a floating zone that moves down the rod as more material melts. The speed at which the floating zone moves down the rod can be controlled by adjusting the power supplied to the heating element. The rod's temperature and the inert gas atmosphere composition can also be controlled to optimize the growth of the single crystal. As the floating zone moves down the rod, the material in the zone solidifies and forms a single crystal. The single crystal ingot is typically pulled out of the furnace after the floating zone has passed through the entire rod. The process can also be used to grow multi-crystalline ingots using several rods or a unique technique called the modified float-zone process.
This basic process can be carried out more often, i.e., the melt zone can be repeatedly passed through the ingot, which increases the purity at each cycle above what would have been obtained in a conventional solidification process. Since the impurities migrate to one end of the ingot during the float-zone cycle, there is also the possibility of cutting off the end with increased impurities between each float-zone cycle [75].
This basic process can be carried out more often, i.e., the melt zone can be repeatedly passed through the ingot, which increases the purity at each cycle above what would have been obtained in a conventional solidification process. Since the impurities migrate to one end of the ingot during the float-zone cycle, there is also the possibility of cutting off the end with increased impurities between each float-zone cycle. The Float-zone process has several advantages over other growing single-crystal ingots. It can produce high-purity single crystals with a low defect density and is relatively simple and inexpensive. The process is also relatively insensitive to the starting material's impurities, making it well-suited for growing single crystals of materials with high impurity levels.[83]

Epitaxial crystal growth

Epitaxial crystal growth is used to grow a thin layer of single crystal material on top of a substrate material. The process is commonly used to grow semiconductor materials, such as silicon and gallium arsenide, on top of other semiconductor materials. However, it can also be used to grow other types of crystals, such as oxides and metals, on top of various substrates.
The process begins with a substrate, typically a single-crystal material, but it can also be a polycrystalline material or a substrate with a specific crystal orientation. The substrate is cleaned and placed in a high vacuum or controlled atmosphere chamber. The growth process can take several forms, including molecular beam epitaxy (MBE), metalorganic chemical vapor deposition (MOCVD), and chemical vapor deposition (CVD). In MBE, atoms or molecules of the growth material are evaporated in a vacuum chamber and directed toward the substrate surface, where they deposit and form a crystal. In MOCVD and CVD, a precursor gas is introduced into the chamber. The substrate is heated to a high temperature, typically between 600 to 1000 °C, to activate the precursor and deposit the growth material on the substrate. The thickness and quality of the epitaxial layer can be controlled by varying the growth conditions, such as temperature, pressure, and the flow rate of the precursor gas. The process can also be used to grow multi-layer structures, where multiple layers of

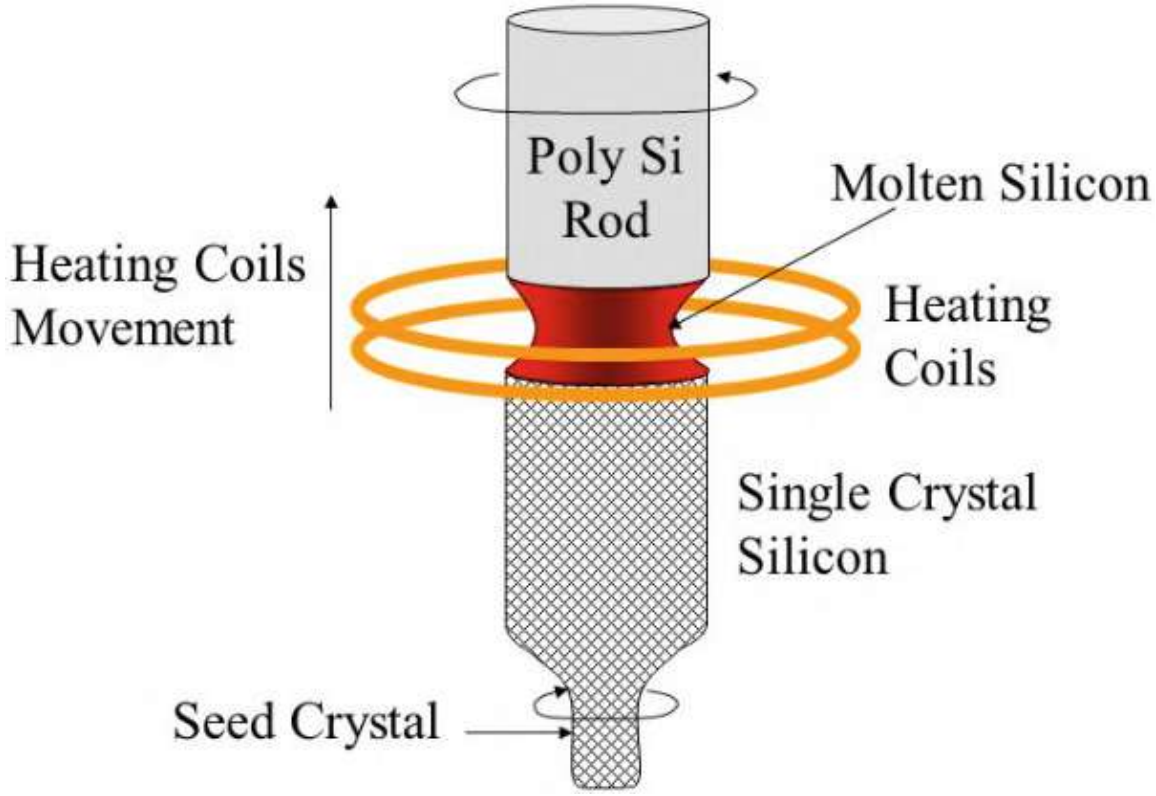

Figure 3.3: Float-Zone method. A prefabricated ingot with a polycrystalline structure is clamped vertically and made to rotate. At one point along the cylindrical ingot, vertically movable heating coils use electromagnetic induction to heat a narrow zone of the ingot above the melting temperature. These coils slowly move vertically across the ingot to allow atoms to cool and settle as a single crystal in the areas that have passed.
Picture taken from [83].

different materials are grown on top of each other.
Epitaxial crystal growth has several advantages over other single-crystal growth methods. The process allows for the growth of single-crystal materials on top of a substrate with a specific crystal orientation, which can improve the electronic and optical properties of the material. The process is also well-suited for growing high-quality thin films, which are essential in many semiconductor devices, such as transistors and solar cells. The process has some limitations as well. Epitaxial growth can be sensitive to impurities, defects, and the quality of the substrate. The process also requires high temperature and high vacuum conditions, which can be challenging to maintain and can limit the choice of substrate materials. Additionally, the cost of the equipment and the precursors used for the growth can be relatively high.

3.3.2 Photolithography

Lithography is a process used to fabricate microelectronic devices and other microstructures. It is a technique for printing tiny structures, such as those found in integrated circuits, onto a substrate using a chemical reaction. There are several different types of lithography, but the most common is photolithography.
The photolithography mask is a vital component of the photolithography process, which serves as a "stamp" to transfer tiny patterns onto the chip. The computer design process for photolithography masks typically involves several steps, including:

1. **Circuit design:** the design of a microelectronic circuit is usually done through computer-aided design (CAD) software. In this process, electrical circuits that will be integrated onto the semiconductor chip are designed on a computer screen.

2. **Creation of the photomask design:** After the circuit has been created, the photomask design is created. This involves converting the circuit into a two-dimensional mask consisting of a layer of photosensitive material.

3. **Transfer of the design to the mask:** The machine design is now transferred to the photomask surface. This is done using special image generation programs that convert the machine design into a vector format compatible with the photomask exposure process.

4. **Design optimization:** in this step, the mask design is optimized to ensure that it accurately and precisely transfers the desired patterns onto the semiconductor chip. This can be achieved by using simulation tools to study the circuit's behavior under different operating conditions.

5. **Photomask fabrication:** after the mask design is complete, the photomask is fabricated. The design is applied to a transparent film and then exposed through a photolithography process.

6. **Testing and verification:** After the photomasks are produced, they are tested for quality and accuracy. This is done through special testing procedures to ensure the mask design transfers the desired patterns to the semiconductor chip.

Once the photomask has been fabricated, tested, and verified, it can be used in the series production of semiconductor devices, as seen in Figure 3.4: Photoresist is applied to a wafer. This wafer is then exposed through the photomask, and the pattern on the photomask is transferred to the wafer surface, similar to a shadowgraph. The photoresist is a light-sensitive material applied to the substrate in a thin layer. When the photoresist is exposed to light, the areas of the photoresist that are exposed to light become more soluble, while the areas that are shielded from light remain less soluble. After the photoresist is exposed to light, it is developed. It involves rinsing the substrate with a chemical developer to remove the areas of photoresist that were made more soluble by the light exposure. This leaves behind a photoresist pattern on the substrate that is the inverse of the way on the mask.
The next step in the lithography process is to use the patterned photoresist as an etch mask, which involves etching away the underlying substrate material to create the desired pattern. Finally, the photoresist is removed to reveal the patterned substrate.
In a few words, the basic principle of photolithography is to protect some areas from dissolution by photoresists. Whether the exposure makes the photoresist sensitive to dissolution (positive photoresist) or insensitive to dissolution (negative photoresist) is a technical detail and does not change the basic principle.

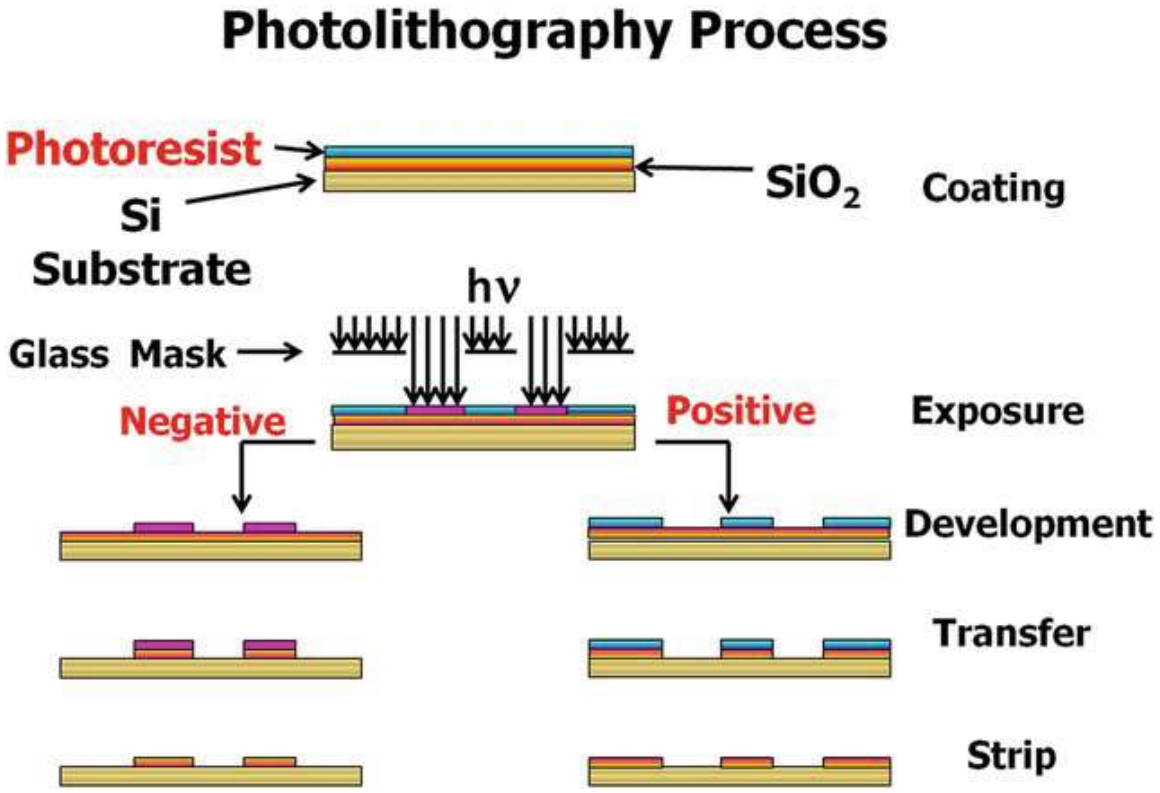

Figure 3.4: Basic principle of photolithography. In the first step, the substance to be applied in a structured manner is deposited over the entire surface of the wafer (in this case, silicon oxide). The photoresist is also spread over the whole surface. In the second step, this photoresist is exposed through a photomask (or "reticle") only at specific locations (similar to the structure to be obtained, as a positive or negative). This exposure changes the chemical properties of the photoresist so that in the next step, it can be dissolved away either only at the exposed (positive) or at the unexposed (negative) areas. Now the silicon oxide is exposed at these places where the photoresist as a protective layer was dissolved and washed away. In a further step, an etchant is applied that etches away only the silicon oxide where no photoresist lies above it. In the final step, all remaining photoresist is etched away, and the processed wafer is ready for a new layer. Picture taken from [80].

Lithography is a critical step in the fabrication of microelectronic devices, as it enables the creation of tiny and complex structures with high precision. It produces various microelectronic devices, including computer chips, solar cells, and medical implants.

3.3.3 Wafer thickness control

In high energy physics, it is important that the sensor thickness is precisely determined because then the active sensor volume is exactly known. Furthermore, the sensor currents scale proportionally with the sensor thickness as the active volume increases, and the capacitance is inversely proportional to the sensor thickness (plate capacitor). For the silicon sensors of the HGCAL, there are two procedures to bring the sensors to the defined thickness (see Figure 3.5):

1. For the 200 µm and 300 µm thick sensors, the wafer is fabricated using a standardized process at a much larger thickness. After cutting, the backside is mechanically ground to the desired thickness. Since grinding results in crystal lattice damage around the ground surface, the backside must have a backside implant with high doping (p++) to bring the electric field applied under the p-bulk close to zero. Otherwise, early breakdowns could occur in this zone.

2. For the 120 µm thick sensors, a diametrical approach is taken: A thin wafer is fabricated, and an epitaxial process is used to grow the silicon layer more and more until the desired thickness is achieved. However, for mechanical stability reasons, the overall thickness of these sensors is still about 300 µm. To further bring the active sensor thickness to 120 µm, these sensors receive a thick backside implant of high doping (p++) where the electric field is close to zero.

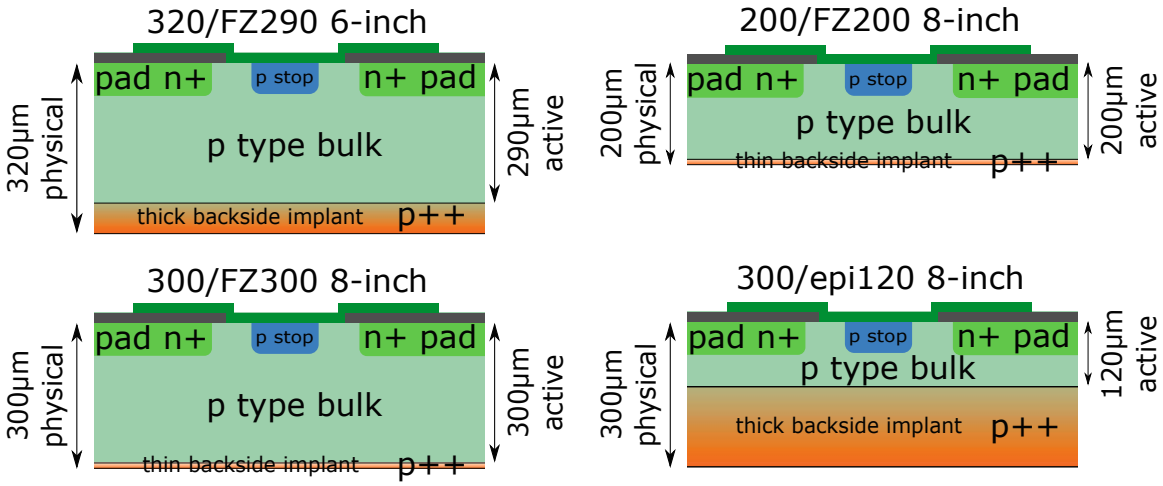

Figure 3.5: Cross-section of the sensor structures of the HGCAL. The layer thicknesses in the image are not to scale. The upper right (**200/FZ200 8-inch**) and lower left (**300/FZ300 8-inch**) images represent the cross-section of the 200 µm and 300 µm thick sensors. The wafers are mechanically ground from a much thicker wafer to the desired thickness. The 200 µm sensor is actually 1/3 thinner, which requires special care during handling.
On the bottom right picture, in contrast, the 120 µm thick sensors take (**300/epi120 8-inch**) thin starting wafers and apply an epitaxial crystal growth process to bring them to the desired active thickness. However, since the overall thickness is again 300 µm, the active thickness is limited by introducing a thick backside implant of high doping (p++) into the backside, which keeps the electric field in this region close to zero.
The upper left sensor cross-section (**320/FZ290 6-inch**) is used for comparison with the sensors of the CMS Tracker, which are manufactured in the 6" process.
Picture from [61].

"Have no fear of perfection - you'll never reach it."

Salvador Dali

4 Radiation damage mechanisms

4.1 Crystallographic properties of silicon

Silicon is a chemical element with the symbol Si and atomic number 14. Silicon and Germanium crystallize in the diamond lattice structure (Figure 4.1), GaAs, CdTe, and other compound semiconductors in the zinc blende structure or the zinc sulfide structure (hexagonal).
Unlike metals, semiconductors do not form dense sphere packings, so the number of immediate neighbors per atom is comparatively small, with a typical lattice spacing of about 5.5 Å. The diamond lattice structure can be thought of as two interpenetrating face-centered cubics (fcc) cells arranged along the diagonal of the cube by one-quarter of the diagonal length. Each atom is covalent bonded to four neighboring atoms that are equally spaced around it. These bonds are very stable and result in a high melting and boiling temperature. All atoms are identical, whereas, in the zinc-blende structure, each one of the fcc cells consists of the other atoms of the compound. The packing density is only half that of the body-centered cubic lattice (bcc). Figure 4.1 shows the unit cell of the diamond cubic crystal. The cubic crystal structure of silicon also has a vital role in its electronic

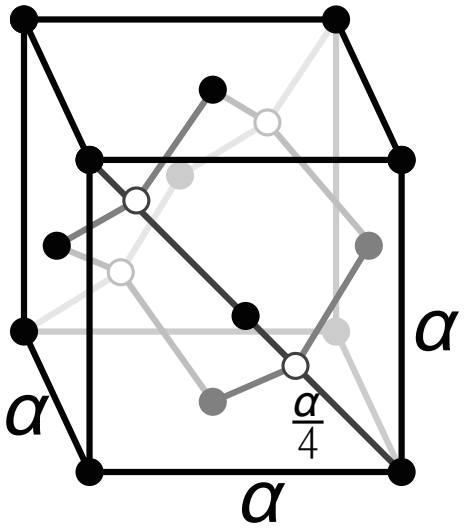

Figure 4.1: Unit cell of the diamond cubic crystal structure of silicon and germanium. The lattice atoms are located at the eight corners; the six cube faces, and at the centers of those four of the eight octants that are not directly adjacent. In simple words, it is two intersecting, cubic face-centered structures. Image from [42].

properties, allowing it to be used effectively as a semiconductor material. Silicon is a fundamental

building block in the semiconductor industry and is used in various applications, including solar cells, transistors, and integrated circuits.
Necessary for some applications is at which cutting directly through the crystal obtains the densest packing of atoms at the surface. To describe the crystal orientation, the "Miller indices" represent lattice planes which define a plane orientation in the crystal by a triplet of numbers. The (111) plane is the plane with the densest packing of lattice atoms in an fcc lattice [45].

4.2 Microscopic high energy radiation damage mechanisms in silicon

There are now several ways to classify the effects of radiation on a solid-state detector:

- **Surface damage** vs. **bulk damage**: Photons (no rest mass, therefore hardly any energy transfer to heavy atomic nuclei) cause primarily surface damage. Bulk damage, on the other hand, is induced mainly by hadrons (due to the higher rest mass).
- **Non-permanent** vs. **permanent**: Many lattice damages, e.g., Frenkel pairs, can heal in the short term, e.g. by immediate recombination. Lattice excitations (phonons) are also not permanent lattice damage. Some other types of lattice damage, such as cluster defects, do not heal immediately and tend to be persistent. However, these can be partially healed by annealing; see Section 4.4.
- **Pattern**: Vacancies, Interstitials, Frenkel pairs, see Section 4.2.1.
- "**Multiplicity**": This denotes the dimensionality of the lattice damage. One-dimensional would be point defects, and three-dimensional would be cluster defects. Two-dimensional lattice damage (e.g., dislocations) is more relevant for considering mechanical effects and is not dealt with here.
- **Causing particles**: Charged hadrons typically cause nuclear scattering and EM scattering, which lead to point and cluster defects. Neutral hadrons usually impart their energy to a primary knock-on atom, which then causes further lattice damage, see Figure 4.3.

In the case of silicon, two types of radiation damage must be distinguished concerning reduced detector performance:

- **Surface damage**, specifically in the oxides and silicon oxide transitions caused by **direct and indirect ionizing** radiation. Typically these are **charge carrier traps**.
- **Damage in the bulk material** caused by **non-ionizing energy loss (NIEL)**. Typically, these are **crystal lattice defects**.

A particle can cause both types of radiation damage in a single pass: For example, a proton can first damage the surface oxide of the detector by impact ionization (ionizing energy loss) and then knock a lattice atom in bulk out of its location by inelastic impact (non-ionizing energy loss).
The summation of all energy contributions yields:

$$E_{\text{loss,total}} = E_{\text{loss,ionization}} + \underbrace{E_{\text{loss,displacement}} + E_{\text{loss,nuclear}}}_{\text{non-ionizing energy loss (NIEL)}} \tag{4.1}$$

4.2.1 Non-ionizing energy loss (NIEL) radiation damage hypothesis

If a particle entering a crystal has sufficient energy and momentum, it can dislodge a lattice atom from its regular location. This takes place by inelastic collision under energy exchange; the heavier the incident particle is compared to the lattice atom (energy and momentum relation of inelastic collisions) The maximum energy transfer can be achieved when the incident particle has the same rest mass as the crystal atom. Since the minimum energy required to release the atom from the lattice (20 eV for silicon [40]) is far less than typical energy losses in high energy physics, only inelastic collisions are relevant here. Below this energy, no dislocation, i.e., crystal lattice damage, takes place, but the energy is transferred to the crystal as phonons. Phonons, although by definition part of the NIEL, do not cause damage to the crystal lattice and are dissipated as heat.

Crystal lattice defects are disturbances in the perfect arrangement of atoms in a crystal. These defects can also be caused by other factors than radiation, including mechanical stress, thermal treatment, and other environmental conditions. Some zero dimensional crystal lattice defects (point defects, see Figure 4.2) are:

Interstitials occur due to gaps or voids in the crystal lattice caused by an uneven arrangement of atomic nuclei in the lattice or by the introduction of atoms from a foreign substance.

Frenkel defects or more precise, Frenkel pairs [28], are a type of crystal lattice damage caused by the absence of an atom (vacancy) at its normal position in the crystal lattice. Instead, the atom is located at a different place in the lattice (interstitial). So it is a combination of an interstitial and a missing atom.

Center-of-mass defects, also known as translational or displacement defects, are a type of crystal lattice damage in which a group of atoms is displaced as a unit in the lattice rather than a single atom at a different location in the lattice, as in Frenkel defects. This results in a shift in the center of gravity of the affected atoms and, thus, a change in the center of gravity of the overall crystal lattice. These defects are related to cluster defects, see Figure 4.3.

Nuclear transmutation refers to the transformation of atomic nuclei by nuclear reactions in the presence of hadron radiation, especially neutron radiation. One possibility is the transformation of silicon[a] into other isotopes or phosphorus:

$$^{28}\mathrm{Si} + {}^{1}\mathrm{n} \longrightarrow {}^{29}\mathrm{Si} + {}^{1}\mathrm{n} \longrightarrow {}^{30}\mathrm{Si} + {}^{1}\mathrm{n} \longrightarrow {}^{31}\mathrm{Si} \xrightarrow{2.62\,\mathrm{h}} {}^{31}\mathrm{P}^{+} + \mathrm{e}^{-} + \bar{\nu}_{\mathrm{e}} + 1.492\,\mathrm{MeV} \tag{4.2}$$

Here, a silicon atom captures one or more neutrons to eventually become ^{31}Si, which decays by beta decay with a half-life of 2.62 h to the stable phosphorus isotope ^{31}P.

This circumstance can produce n-doped silicon (neutron transmutation doping) very homogeneously. For this purpose, silicon is irradiated with neutrons; neutron capture yields ^{31}Si and ^{31}P. The radiation damage strongly disturbs the crystal lattice, so it is cured in a subsequent annealing step.

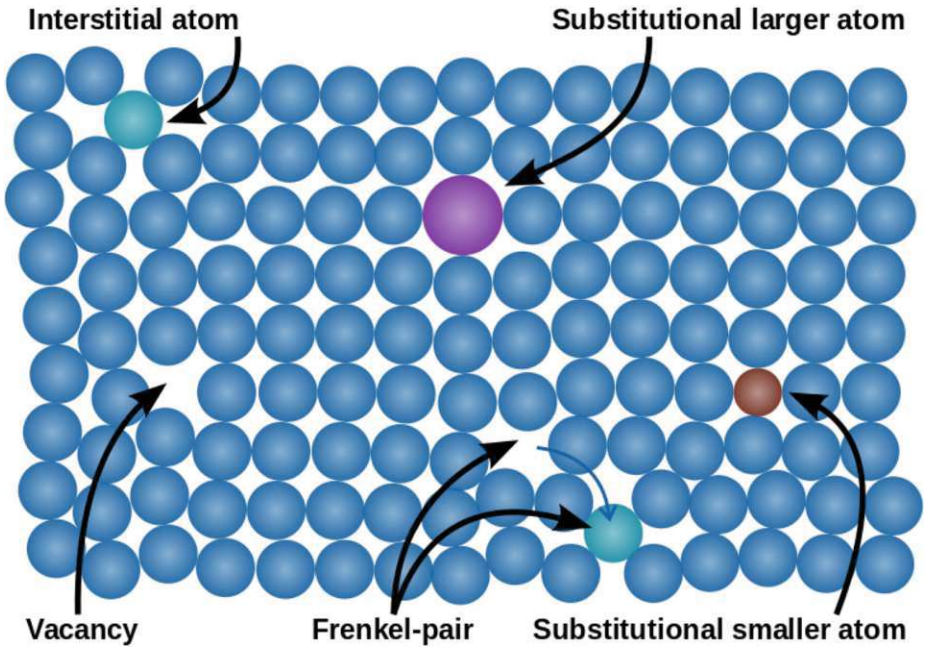

Figure 4.2: Point defects (zero dimensional) in crystals. All these defects contribute to radiation damage in crystalline solids. Image from [a].

There are still many multidimensional crystal damages, but they play only a minor role in radiation hardness considerations regarding semiconductor particle detectors. Crystal lattice damage can affect both the electronic and mechanical properties of materials, and its effect can vary depending on the type and density of the defects. A high density of crystal lattice damage can lead to a reduction

[a] ^{28}Si is the most common isotope with ≈92 % occurrence, ^{29}Si with ≈4.7 %, and ^{30}Si with ≈3.1 %.

[a] https://www.differencebetween.com/difference-between-point-defect-and-line-defect/, accessed 2023-01-07

in the strength and hardness of the material. In contrast, a lower density of defects can often have a positive effect on electronic properties, such as in semiconductors. It is essential to understand how crystal lattice damage occurs and how it affects the properties of materials, as it plays a critical role in the development and optimization of materials and devices [45].
Since neutrons do not lose energy through direct ionization in solids, energy transfer through non-ionizing collisions is the typical radiation damage caused by neutrons. Therefore, studies on bulk damage caused by neutron irradiation from nuclear reactors or other neutron sources are carried out. Since the neutron spectrum in nuclear reactors depends on many factors (location in the core, moderation type, fuel type and enrichment, burn-up) and is given in a vast range (meV to MeV), it has proven beneficial to normalize the spectrum to an equivalent, mono-energetic neutron radiation of 1 MeV energy, abbreviated throughout the work with n_{eq} [68]. For proton irradiation, the damage function is also normalized to the equivalent damage of 1 MeV neutrons to create comparability. Since the fluence ϕ is just normalized to 1 MeV neutrons, each particle must be brought to a mono-energetic, NIEL-equivalent fluence:

$$\Phi_{\mathrm{eq}} = \sum_i \kappa_i(E_i) \cdot \Phi_i(E_i) \tag{4.3}$$

where $\Phi_i(E_i)$ is the non-normalized fluence of the i-th particle of energy E_i, and $\kappa_i(E_i)$ is the hardness factor for the i-th particle of energy E_i. In other words, κ describes the severity of crystal lattice damage of a given particle at a given energy. Other hadrons, such as pions, are not practicable for large-scale sensor irradiation studies. Also, the massless photons can cause displacement damage provided their energy is high enough [31], and additionally through secondary effects, e.g. Compton scattering [14] and photodisintegration [26].

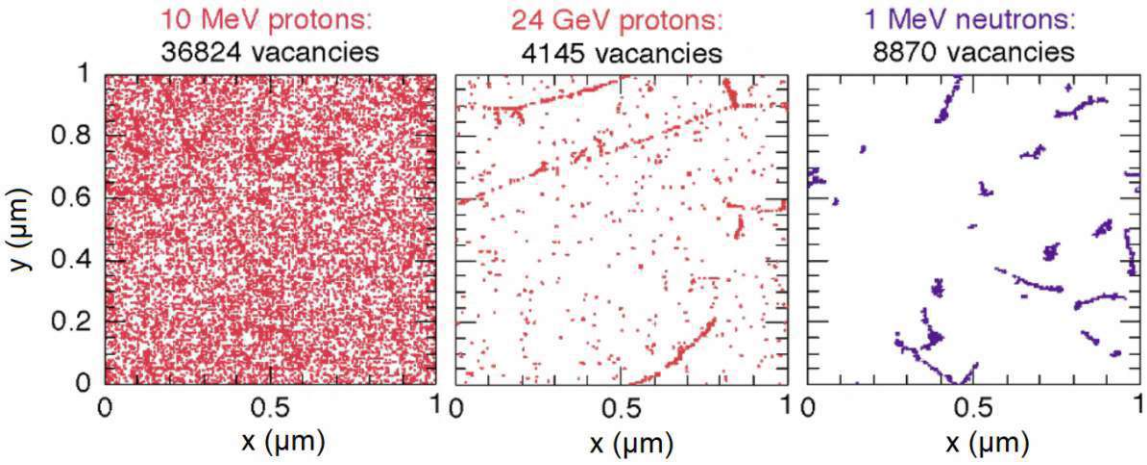

Figure 4.3: Simulation of crystal lattice defects in a silicon cube of 1 µm^3 by particle irradiation with a fluence of 10^{14} cm^{-2} particles. These plots represent a two-dimensional projection of the distribution of crystal lattice defects for protons with 10 MeV and 24 MeV and neutrons with 1 MeV kinetic energy. Since 10 MeV protons have a significantly higher displacement damage cross-section than 24 MeV protons according to Figure 4.4, significantly more lattice defects (≈37 000 versus ≈4000) are observed. Further, neutrons exhibit different behavior than protons, with fewer individual defects (due to lack of Coulomb interaction), and the defects are clustered more frequently. Image from [40].

4.2.2 Displacement damage function $D(E)$ and damage function α

The displacement damage function $D(E)$ and the damage function α are both key concepts in the field of radiation damage in materials, particularly within the context of how energetic particles such as neutrons, ions, or electrons cause damage to the crystal lattice of a material.
The displacement damage function $D(E)$ describes the amount of damage caused by an incident particle with energy E. It quantifies the number of displaced atoms (Figure 4.2) created by the interaction of the energetic particle with the material. This function considers the energy transferred to atoms in the material and the probability of displacement events. The damage function α is related to the macroscopic effects of the displacement damage on the material properties. It typically

describes the relative damage efficiency of different types of radiation or the effect of radiation on specific material properties, such as electrical conductivity or mechanical strength. $D(E)$ links fundamentally to α through the process of integrating the microscopic damage events over the energy spectrum of the incident radiation to predict the macroscopic damage in the material:

$$\text{Displacement per atom dpa} = \int_{E_{\text{min}}}^{E_{\text{max}}} \Phi(E) \cdot D(E)\, dE \tag{4.4}$$

whereas the Displacement per atom dpa is an auxiliary function, E_{min} and E_{max} are the minimum and maximum energies of the incident particles that can cause displacement damage, $\Phi(E)$ the fluence of particles, and $D(E)$ the displacement damage function [79]. Note that $\Phi(E)$ is not normalized to 1 MeV [68]. To normalize the fluence, one needs the hardness factor κ.

$$\Phi_{\text{neq}} = \kappa \cdot \Phi \tag{4.5}$$

κ in turn can be expressed by the damage function $D(E)$, the fluence Φ, and a unit normalization[b] by integrating over the energies:

$$\kappa = \frac{\text{dpa}}{95\,\text{MeVmb} \cdot \int_{E_{\text{min}}}^{E_{\text{max}}} \Phi(E)\, dE} = \frac{\int_{E_{\text{min}}}^{E_{\text{max}}} \Phi(E) \cdot D(E)\, dE}{95\,\text{MeVmb} \cdot \int_{E_{\text{min}}}^{E_{\text{max}}} \Phi(E)\, dE} \tag{4.6}$$

α is then related to the dpa through empirical or semi-empirical relationships. These relationships can vary depending on the specific property being studied and the material in question. In general, α can be expressed as a function of dpa: $\alpha = f(\text{dpa})$, where $f(\text{dpa})$ is a function that encapsulates the dependence of the material property on the number of displacement events. The exact form of $f(dpa)$, $D(E)$, and α as well as their normalizations often requires experimental calibration [57]. This involves irradiating the material with known spectra and measuring the resulting property changes to establish the empirical relationship [68]. Figure 4.4 shows $D(E)$ of silicon for neutrons, protons, electrons and pions.

[b] 95 MeVmb is standard for silicon, see https://rd50.web.cern.ch/niel/

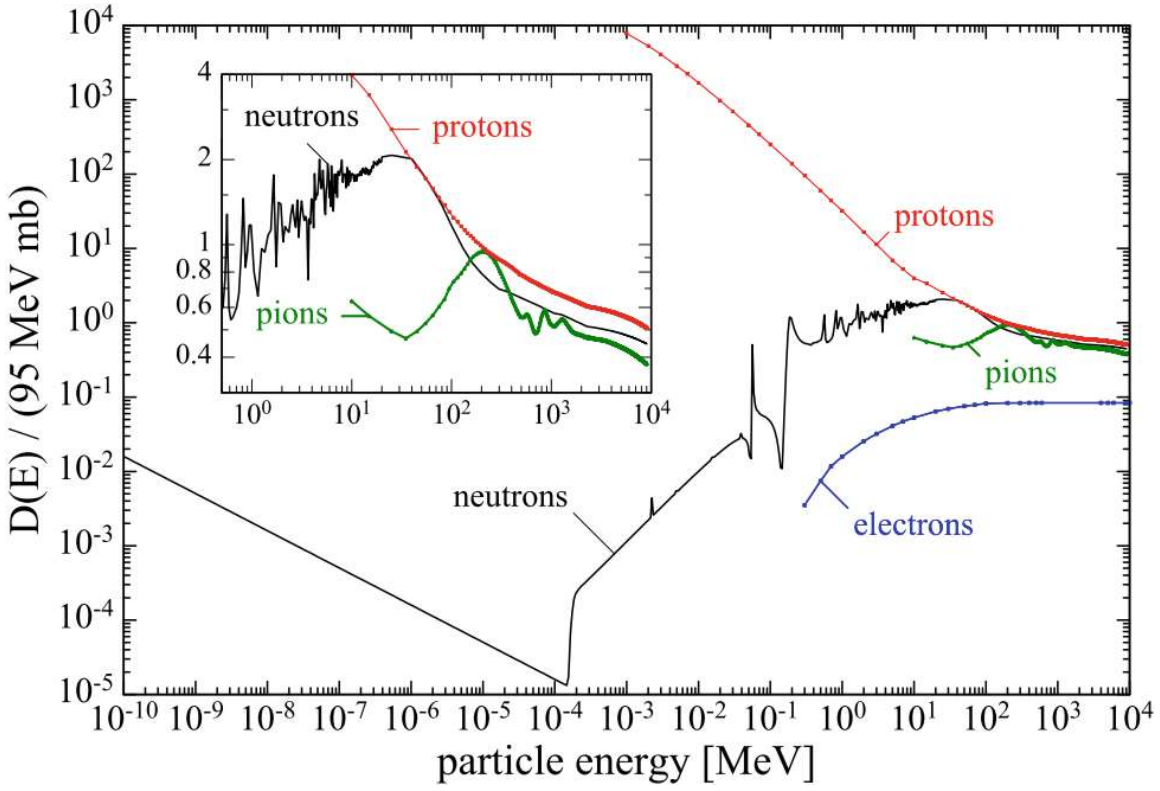

Figure 4.4: Displacement damage cross sections of protons, neutrons, pions and electrons over various energies in silicon. The displacement damage function $D(E)$ is normalized to 95 MeV mb. Data from [54].

4.3 Effects of NIEL damage on electrical characteristics

The micro-scale crystal lattice defects discussed in Section 4.2 also impact the macroscopic properties of the sensors. Apart from the change in the mechanical properties, which are irrelevant here, the changes in the electrical properties are interesting. Since this work investigated mainly bulk damage, this description focuses on it and leaves out surface damage. This chapter will focus on the relevant mechanisms, the change in effective doping concentration, and the consequent changes in leakage current and full depletion voltage.

4.3.1 Effective doping concentration N_{eff}, charge carrier mobility μ, and resistivity ρ

During irradiation, crystal lattice defects that behave like acceptors or donors are created. Both defects are generated during irradiation, leading to a change in the doping concentration of the silicon bulk material. It is recommended to introduce the effective doping concentration after irradiation, N_{eff}, to include the generation of radiation-induced acceptors and donors.
Charge carrier mobility refers to the ability of charge carriers (electrons or holes) to move through a semiconductor material in response to an electric field. It is a critical parameter affecting electronic devices' speed and efficiency. Mobility is influenced by various factors, including the material's crystal structure, defects, temperature, and external influences, such as irradiation.
Irradiation introduces defects into the crystal lattice of a semiconductor, which can act as scattering centers for charge carriers. As charge carriers move through the lattice, they interact with these defects, causing deviations from their ideal trajectories. This scattering leads to a reduction in the overall mobility of charge carriers. The greater the concentration of defects introduced by irradiation, the stronger the scattering effect and, consequently, the lower the mobility.
Resistivity measures a material's opposition to the flow of electric current, the inverse of conductivity. The resistivity of a semiconductor is closely related to its charge carrier concentration and mobility. Irradiation-induced defects have a significant impact on resistivity. As discussed earlier, defects act

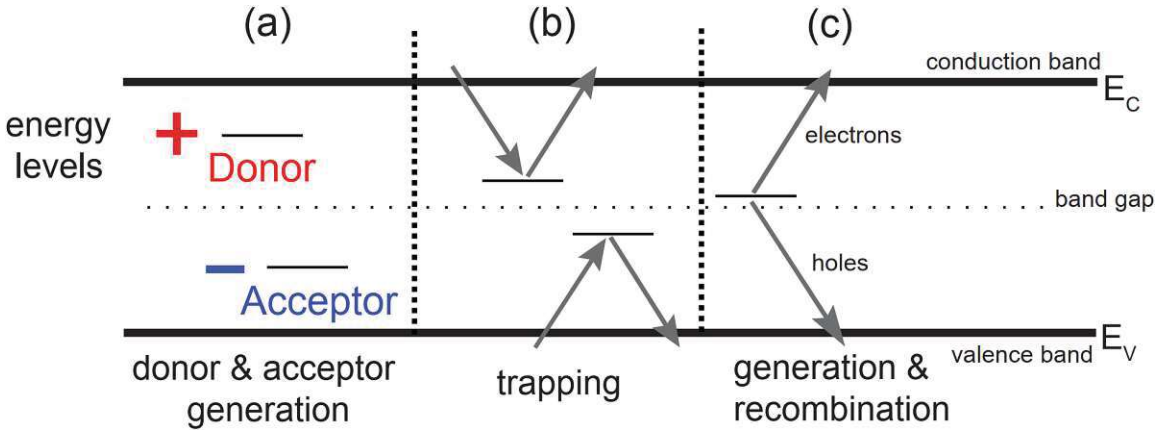

Figure 4.5: Radiation-induced defect levels in the band gap of a semiconductor.
(a) Insertion of additional charge carriers (donors and acceptors) increases the effective doping concentration. **(b)** Defective sites can trap electrons or holes, which reduces charge collection efficiency (CCE) or **(c)** increase currents since charge carriers can be generated or recombined more easily. Image from [43].

as scattering centers that hinder the movement of charge carriers. This scattering increases the resistance charge carriers encounter as they travel through the material, resulting in higher resistivity. In other words, the presence of defects introduced by irradiation increases the material's opposition to current flow.
Resistivity is also influenced by the effective charge carrier concentration, which is altered by irradiation by generating donors and acceptors in the band gap or changes in doping profiles. Increased carrier concentration due to donor and acceptor generation can contribute to lower resistivity, while carrier trapping and recombination at defects can reduce the effective carrier concentration and increase resistivity. The resistivity is given by:

$$\rho = \frac{1}{\mu \cdot e \cdot N_{\text{eff}}} \tag{4.7}$$

where μ is the mobility, e the elementary charge and N_{eff} the effective charge carrier concentration.

4.3.2 Effects on leakage current

Leakage currents are an issue in reverse-biased semiconductors. These currents flow through the depletion zone despite the reverse direction (without breakdowns). The leakage current is linearly dependent on voltage as well as on defects. Furthermore, it shows an exponential temperature dependence due to the Fermi-Dirac statistics (see Equation 2.11).
The reason for the increased leakage currents due to radiation damage is that crystal lattice damage (NIEL, see Section 4.2.1) leads to additional energy levels in the bandgap, as can be seen in Figure 4.5. Shallow defects, i.e., defects close to the edge in the forbidden area of the band gap, resulting in additional donors at the upper edge or acceptors at the lower edge, see Figure 4.5a. Defects closer to the center of the band gap at the Fermi level are called deep defects. These cause traps for electrons or holes (Figure 4.5b), which worsen the charge collection efficiency or serve as centers for generation-recombination processes which increase the leakage current.
The radiation-induced microscopic defects induce macroscopic influences, like an increase of the effective doping concentration.
The following equation gives the defect and voltage dependence of the change in leakage current:

$$\Delta I = I_{\text{irrad}} - I_{\text{unirrad}} = \alpha(T,t) \cdot \Phi \cdot {}_{\text{neq}} \cdot V \tag{4.8}$$

Where here I_{irrad} is the current of the irradiated diode, I_{unirrad} is the current of the unirradiated diode, V is the reverse voltage, Φ_{neq} is the fluence normalized to 1 MeV neutrons, and α is the so-called "damage factor" or in other words, the current related damage rate (see Section 4.2.2). α is temperature and time dependent, and can lower over time, which means that the sensor's radiation damage partially recovers, the so-called "annealing" (see Section 4.4).

It is essential in this equation that the currents I_{irrad} and I_{unirrad} are measured at the same temperature since the leakage current also depends on the temperature, as already mentioned. If this is impossible, the currents must be scaled to the same temperature using Equation 2.11.
Experimental data reveals that the particle fluence Φ_{neq} and the radiation-induced current change ΔI follow a linear relationship over a wide range, as Figure 4.6 illustrates.

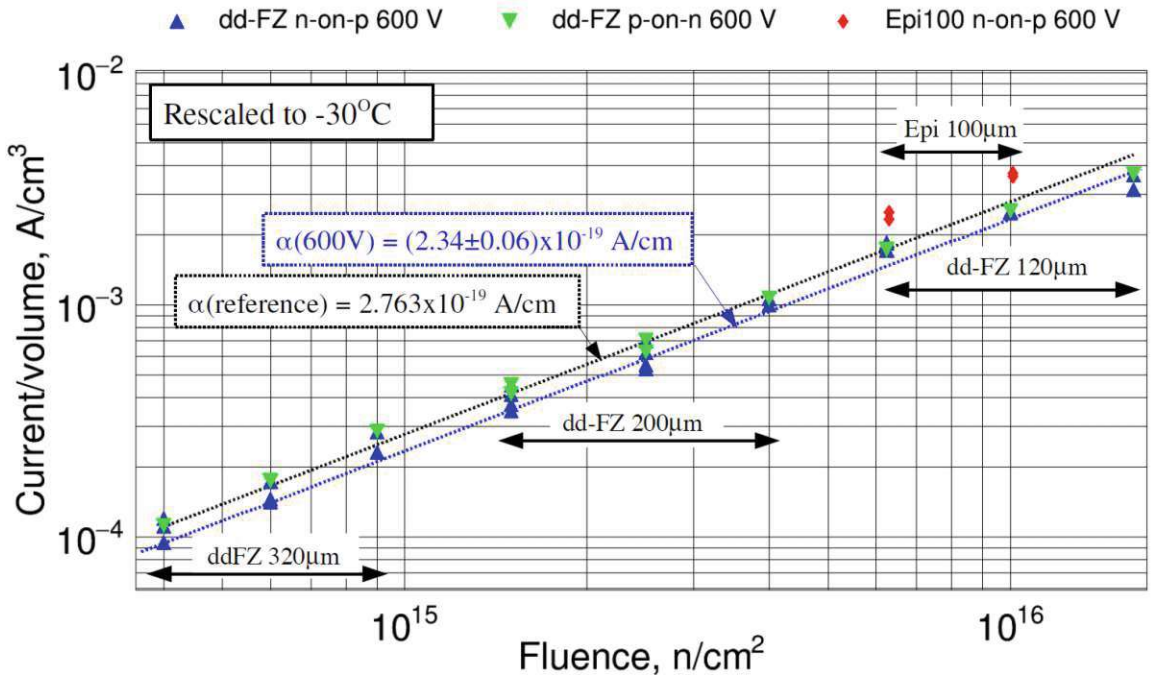

Figure 4.6: In this plot of experimental data, one can see the leakage current density as a function of neutron fluence for different sensor types and thicknesses. Measurements were made at −20 °C, and the results were scaled to −30 °C using the Boltzmann factor (2.11). The applied bias voltage was 600 V. It can be seen that the leakage currents increase linearly with fluence in this range relevant to HGCAL, which greatly facilitates the interpolation and extrapolation of measurements. The linearity represents the NIEL hypothesis. Figure from [1].

4.3.3 Effects on full depletion voltage

The full depletion voltage U_{fd} is one of the critical parameters for semiconductor particle detectors. To maximize the detector volume, extending the depletion zone as far as possible to the entire detector volume is essential. With increasing voltage (reverse bias), the depletion zone grows increasingly from the electrodes into the detector volume. The point at which the depletion zone reaches the opposite electrodes, i.e., the depletion zone has spread over the entire volume, is called full depletion voltage: the sensor completely depletes charge carriers. Now, the slope with which the growth of the depletion zone depends on the voltage depends on the effective doping concentration N_{eff}.
Irradiation using collision products from hadron colliders produces acceptor-like states in the shallow defects and removes donor-like ones [49]; one could say that the hadron radiation makes the sensor more and more “p-like”. In the case of n-type bulks, this reduces the effective doping concentration to zero until an inversion occurs at a certain fluence: The n-type becomes p-type, and the effective doping concentration increases again (type inversion). However, this also means that the space-charge region grows from the opposite side, which can be problematic for the sensor bias voltage supply.
In the present work, only p-type sensors are treated experimentally, which do not show this type of inversion, as they are already “p-type”. However, this also means the effective doping concentration increases with increasing irradiation. The higher N_{eff}, the more charge carriers work against the external field, thus the slower the depletion zone grows (see Equation 2.6. Irradiation increases the effective doping concentration, so the depletion zone grows more slowly, which means that the full depletion voltage shifts towards higher voltages. A higher voltage means a higher leakage current, which is already increased by irradiation (see Section 4.3.2).

From Equation 2.4 we get:

$$U_{\text{fd}} \approx \frac{e}{2 \cdot \epsilon \cdot \epsilon_0} N_{\text{eff}} \cdot d^2 \tag{4.9}$$

where e is the elementary charge, ϵ the electrical permittivity, ϵ_0 the vacuum permittivity, N_{eff} the effective charge carrier concentration and d the active thickness of the detector [53].

4.4 Partial repairing of radiation damages: Annealing

Annealing of radiation damages refers to the process of repairing or mitigating the effects of radiation damage to a material by heating it to a high temperature. The purpose of annealing is to restore the material's crystal structure and properties, which may be damaged by exposure to radiation.
Radiation damage can occur when a material is exposed to high-energy particles such as protons, neutrons, or even lighter particles as electrons (see Figure 4.4). These types of radiation can ionize atoms in the material, breaking chemical bonds and creating defects in the material's structure. Other damage types are dislocations of atoms or altering them by nuclear reactions. These defects can also form stable compounds called "clusters". These can result in various adverse effects, including changes in the material's electrical, mechanical, and chemical properties and degradation of its performance or functionality. Annealing is a common technique used to repair or mitigate the effects of radiation damage. It involves heating the material to a high temperature, which can help "heal" defects in the structure and restore its original properties. Nevertheless, not only beneficial annealing occurs, but the radiation damage can also deteriorate the desired properties (reverse annealing). Typically, in the case of semiconductors, beneficial annealing occurs first. However, if the annealing is too long, it changes at a transition point into reverse annealing, where the electrical properties deteriorate again (see Figure 4.7).

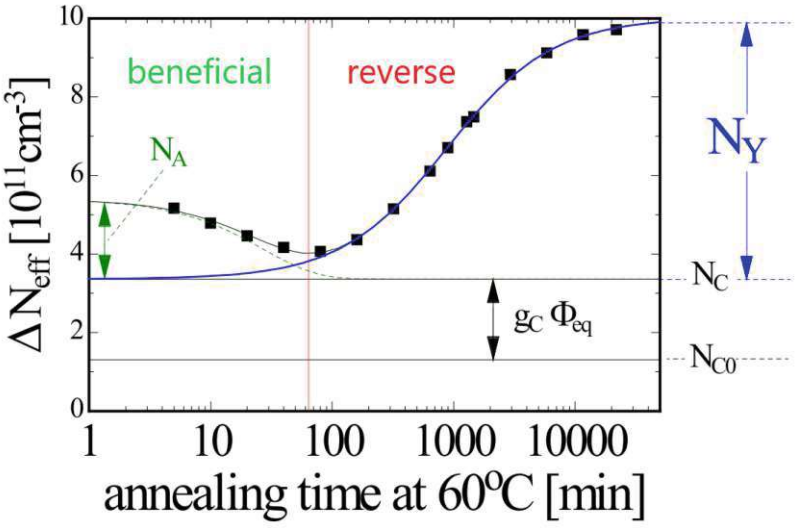

Figure 4.7: A typical course of an annealing curve. Initially, the effective carrier concentration N_{eff} decreases, resulting in a net improvement of the electrical properties (beneficial annealing). After about 100 min at 60 °C, this goes into saturation, and the detrimental annealing processes begin to dominate (reverse annealing). Figure from [54].

In this work, we restrict ourselves to the partial restoration of *electrical* properties by annealing. Here, point defects (see Figure 4.2) are essential, generating new energy levels in the bandgap, see Figure 4.5. Point defects are fundamentally mobile and can migrate or diffuse by thermal motions following Fick's diffusion law. This migration rate depends exponentially on temperature, in terms of the Boltzmann factor, because as the temperature increases, the point defects have more kinetic energy and thus can more easily and thus more often overcome the energy barrier of the crystal lattice. Now there are several possibilities for what happens when a point defect in the crystal lattice migrates:

- A defect migrates in the crystal lattice and settles at another previously defect-free site. This migration does not affect the electrical properties, so it is neither beneficial nor reverse annealing.
- A defect migrates in the crystal lattice and encounters another defect. These defects may form a stable junction called a cluster defect for energy minimization reasons.
- An interstitial migrates and meets a vacancy, a quasi-particle. Since a vacancy is exactly a missing interstitial atom and an interstitial is exactly an excessive one, these two defects reunite at this point to form a perfect crystal. It is the reverse of the formation of a Frenkel pair, the recombination. This type of annealing is beneficial because it restores the electrical properties.

Although there are phenomenological models, such as the NIEL hypothesis, no existing physical model from derived first principles describes the quantitative effects of radiation damage in solids. The reason is that although all the processes involved are each understood on an elementary level, the multifaceted interaction of these in many-particle systems, such as solids, has not yet proven modelable.
The longer annealing takes place, the greater the chance that a defect will be annealed or that clusters will form. The formation and grow of clusters as well as the reintroduction of already annealed defects is understood to be the main contributor to reverse annealing. The exact temperature and duration of the optimal annealing process will depend on the type of material and the severity of the radiation damage [53].
As a best approximation for the relevant time scale of this work, the effective modeling of the damage function is given by:

$$\alpha(t,T) = \underbrace{\alpha_0(T)}_{\text{constant}} + \underbrace{\alpha_1(T)\cdot\exp\left(\frac{-t}{\tau(T)}\right)}_{\text{long-term annealing}} - \underbrace{\beta(T)\cdot\ln\left(\frac{t}{t_0}\right)}_{\text{short-term annealing}} \tag{4.10}$$

whereas $\alpha(t,T)$ is the damage function, depending on time t and temperature T, the time constant $\tau(T)$ which describes how fast the annealing process happens, and a constant t_0 which is used to adjust the units. The different contributions of annealing are described by: $\alpha_0(T)$, which describes the best possible annealing at a given temperature, $\alpha_1(T)$ for the long-term annealing contribution and $\beta(T)$ for the short-term contribution [53].

"Simplicity is the ultimate sophistication."

Leonardo da Vinci

5 Sensor design

5.1 Basic concept

Geometry is often the crucial element driving design choices. The hexagon is the largest, seamlessly tileable, regular shape on a circular silicon wafer. As for the HGCAL, the demonstrative feature is therefore the hexagonal shape. This feature has extensive effects on the whole hierarchy of detector design and operation and economic considerations. Using a hexagonal shape maximizes the wafer-area usages, resulting in a reduction of necessary sensor tiles, hence decreases costs. One sensor segments into smaller cells; each of it has its analog readout channel. Consequently, these active sensing elements also have a regular, hexagonal shape (see Figure 5.7), except for some irregular cells at the sensor edges and corners. These edge and corner cells are necessary to fill the otherwise unused area between the regular pattern and the sensor edges. This is depicted in Figures 5.6a and 5.6b.
To better understand the schematics of this chapter, each design screenshot[a] depicts a legend with the different materials and the corresponding color code. One has to note that a passivation layer (SiO_2) covers the whole upper surface of the sensor. Only the areas with a "passivation window" (which means that there is no passivation layer) provide contact to the underlying metal.

Compensation of diffusion effects

In semiconductor production, during the ion implantation process, the bombardment by high-energy ions damages the silicon crystal lattice. For repairing this damage, one crucial step is annealing after ion implantation. Annealing is done at temperatures up to 100 °C for a few seconds. The heat increases the mobility of the dopants, leading to a lateral spread of the implant (see Figure 5.1). For the HGCAL sensors, this additional lateral spread is about 1 µm. For mitigation, the photolithography masks have to be corrected. All structures containing implants have to be shrunk by 1 µm to have the correct physical dimensions at the end of the production process. Table 5.1 shows the difference between the designed dimensions and actual dimensions. Note that widths have a difference of 2 µm because the difference adds up on both ends of the structure.

5.2 p-stop designs: common and individual

With n-in-p sensors (analogous to n-in-p, of course), the following problem arises after irradiation: The oxide covering the sensor (passivation) forms positive charge carriers when irradiated with ionizing radiation. These charge carriers are formed from electrons knocked out of the oxide, while the positive atoms rest at their lattice position. Due to the insulating nature of the oxide, these are immobile. At the oxide-bulk interface, the negative charge carriers in the p-bulk move towards the excess of positive charges in the oxide. They accumulate in a thin layer close to the interface

[a] The software "KLayout" (https://klayout.de), a tool for creating photolithography mask layouts, was used to construct the sensor design. The design screenshots originate from this software.

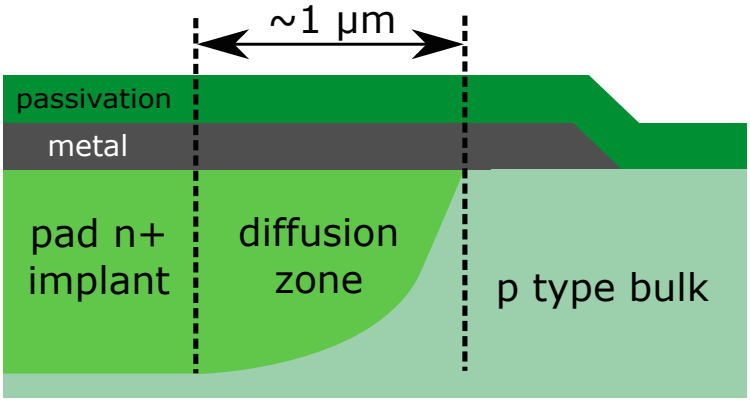

Figure 5.1: This sketch outlines the cross-section of the implant at the beginning of an active sensor cell. After all processing steps, including thermal annealing, the implant still diffuses outward by about one µm, resulting in an arc-shaped path. Sizes are not to scale but to better illustrate the existing structures.

Table 5.1: Intercell dimensions of both p-stop types "common" and "individual" (2021 prototypes)

Parameter	**p-stop common**		**p-stop individual**	
	real	design	real	design
No. p-stop implants	1	1	2	2
p-stop width	6 µm	4 µm	6 µm	4 µm
Inter p-stop distance			6 µm	8 µm
p-stop to cell implant	37 µm	39 µm	31 µm	33 µm
Interpad distance	80 µm	82 µm	80 µm	82 µm
Metal overhang	12.5 µm	13.5 µm	12.5 µm	13.5 µm

(accumulation layer). This forms a conductive channel between the n-implants and short-circuits the cells/strips, which must be insulated for functioning operation see Figure 5.2a. [78]
The "p-stop" method interrupts this channel: An additional p-implant is inserted between the active n-implants, which cuts the conductive channel of accumulated p-charges (Figure 5.2a). Another method is the "p-spray", where p-type ions are evenly applied to the surface. In the present sensors, only the "p-stop" method was used in two different geometries: common and individual, see Figure 5.3. [78]

With p-stop common (Figure 5.3a), there is a single, contiguous p-stop implant between the active cells, which is also connected to the p-stop of the sensor edge. With p-stop individual (Figure 5.3b), each active cell has its own isolated p-stop implant. At the time this thesis was completed (2024), the HGCAL collaboration decided to use the p-stop common design for the final production of the sensors.

5.3 Extensions for guard ring and edge ring

A guard ring in silicon sensors serves several essential purposes, primarily aimed at improving the performance and reliability of the device. Here are the most critical functions:
Uniform electric field distribution: The guard ring helps create a more uniform electric field across the sensor's active area. This uniformity is essential to ensure consistent sensor performance and accurate measurement over the entire active area. [74]
As a shield, it protects the sensor from high-voltage breakdown at the edges. The guard ring acts as a guardian, controlling the distribution of the electric field near the edges, preventing premature breakdown, and enhancing the sensor's robustness and reliability in high-voltage operations. [74]
Attenuation of surface conditions: The surface of silicon sensors can exhibit conditions that trap charges and cause instabilities in sensor performance. The Guard ring can help avoid the effects of these surface states by providing a controlled path for all surface currents, stabilizing the sensor's behavior. [74]

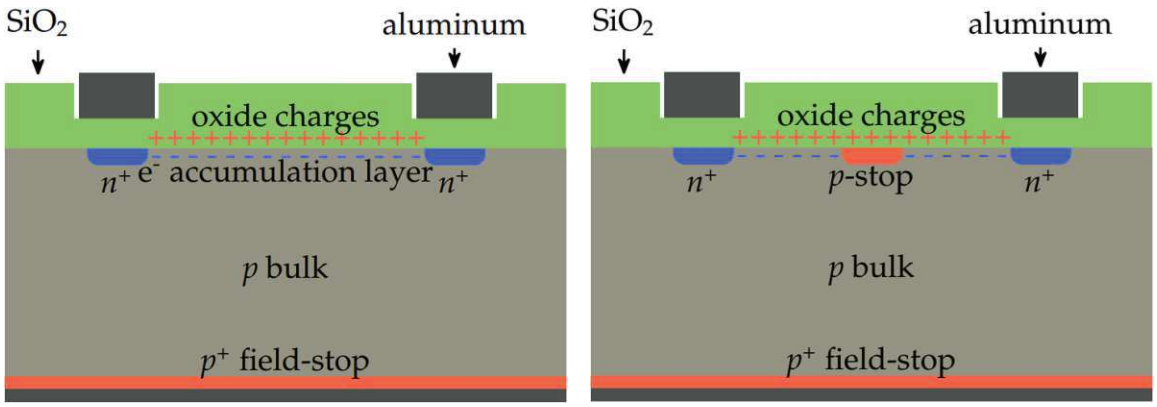

(a) Without a p-stop implant, the electrons of the negative accumulation layer connects the n-implants of the sensing elements.

(b) With a p-stop implant, the negative accumulation layer is interrupted by a small depletion zone, and the n-implants are insulated.

Figure 5.2: Schematic drawing of the principle of the p-stop. Incident radiation knocks electrons out of the oxide, leaving positive charges behind. These attract negative charges (electrons) from the bulk, which form a thin accumulation layer under the oxide and short-circuit the n-implants (a)). This accumulation layer can be interrupted by a p-stop element (b)), and the n-implants are isolated again. Figure from [38]

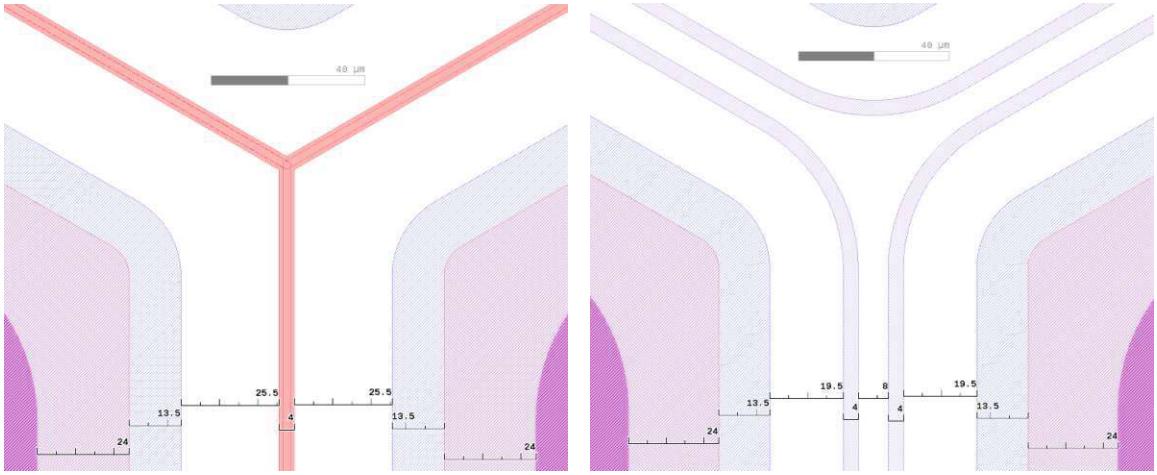

(a) **p-stop common**. All p-stop elements of the active sensor area are interconnected.

(b) **p-stop individual**. Each sensing cell has its own p-stop element.

Figure 5.3: Design of interpad nexus of neighboring cells (2021 prototypes). All values are given in µm. Be aware of the extra µm of implants given by diffusion processes (see Section 5.1).

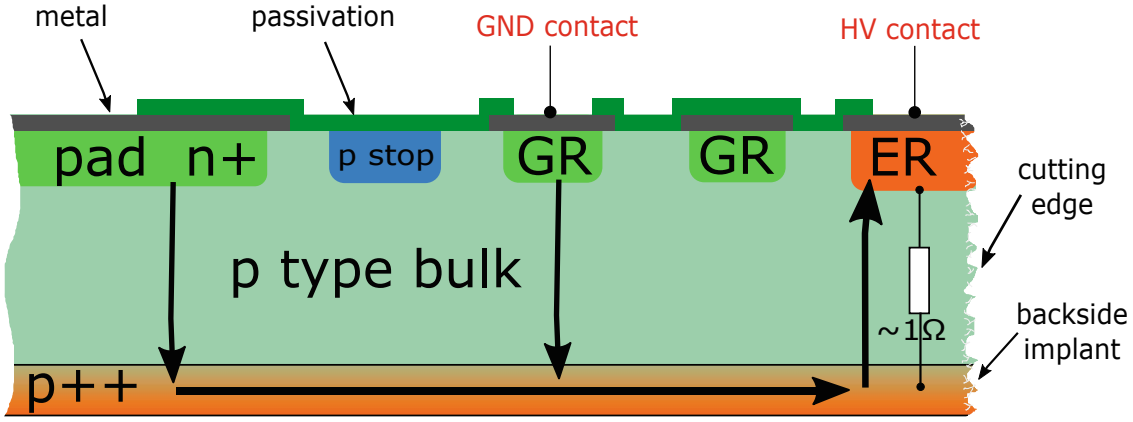

Figure 5.4: Principle of the current flow at the edge region:
Black arrows indicate the current flow. Because of the crystal lattice damage at the cutting edge of the sensor, the Ohmic resistance is meager (in the range of a few ohms), so there is effectively a connection between the backside and the edge ring, and they are at the same electrical potential. This allows, in addition to the high voltage resistance, the edge ring to contact HV instead of the sensor backside. This can then be placed on a special rubber pad to avoid scratches. Figure from [61].

These rings are typically made of a highly conductive material, such as aluminum. They are designed to have a low resistance to ensure that they can effectively dissipate excess current. In this design prototype, there is a floating outer guard ring and an inner guard ring on ground potential, see Figure 5.5b. Both rings are from the "Metal overlap' type, where the surface metal extends laterally over the underlying guard ring implant, see Figure 5.4.

An edge ring surrounds the whole active sensor region (see Figure 5.5a), serving the following purpose:
Crucially, the edge ring keeps the depleted zone of the sensor region away from the physical edge of the sensor. This reduces the field strengths in the edge regions where wafer dicing (see Figure 5.4 and Section 3.3) create many defects in the crystal lattice, fracture edges, and other weaknesses. Enclosing the active area with an edge ring significantly reduces the elevated leakage current that typically occurs at the sensor's edges.

As mentioned in Section 6.3.4, the frontside biasing concept needs dedicated structures to ease wire bonding for mass production. Trapezoidal extensions of the edge ring were the chosen shape (see Figure 5.5a). We chose the same angles (30°) as in the corners of the full sensor to avoid sharp corners, as they may lead to regions with high electric fields. Since it is known from experience with the sensor corners that this small curvature does not lead to any measurable influence on the electrical performance. When designing the geometry, care was taken to balance minimizing the required area on the one hand (to keep the active sensor area as large as possible) and creating enough space to contact two pogo pins per position.
The contact pads of the guard ring (see Figure 5.5b) are designed according to the same geometric concept as the high voltage pads. While the high-voltage pads are only used for test purposes (i.e., frontside biasing), the guard ring pads are also suitable for regular sensor operation.

5.4 Low-density (198 channel) and High-density (444 channel) design

For the 200 µm and 300 µm thick sensors, the CMS collaboration has chosen the so-called "Low-density" (LD) design with 198 full-size channels, see Figure 5.6a. The vendor will produce these sensors in a float-zone process. Note the hexagonal shape of the main cells, the irregular shapes of the corner and edge cells. One full hexagonal cell has an active area of approximately 126 mm^2. Table 5.2 shows an overview of essential differences between the Low-density and High-density designs.

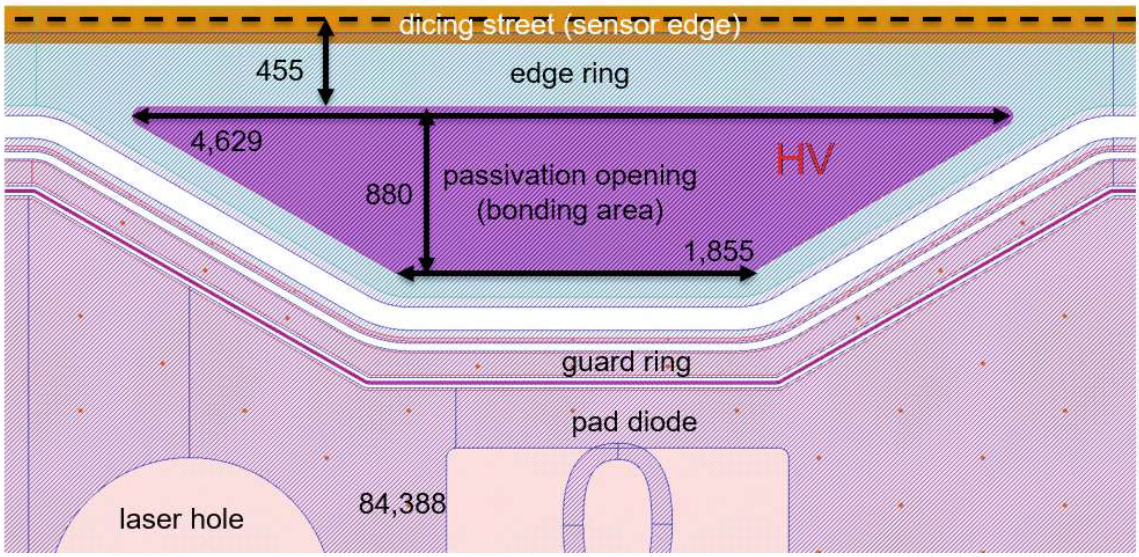

(a) **Edge ring extension**. The purple pad, embedded in the Edge ring, is at high voltage potential.

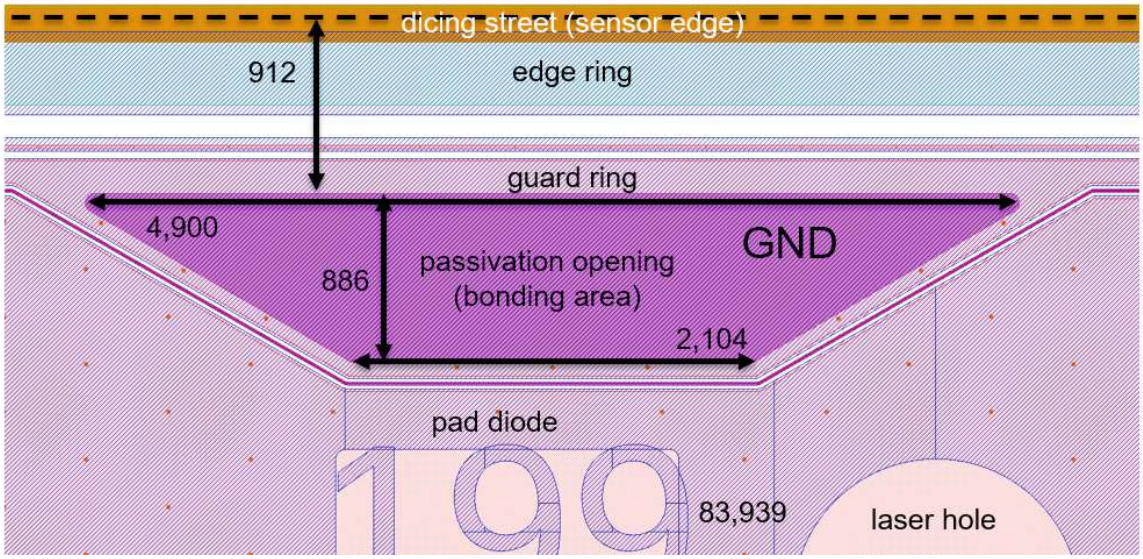

(b) **Guard ring extension**. The purple pad, embedded in the guard ring, is at ground potential.

Figure 5.5: Screenshots of the edge- and guard rings designs (2021 prototypes). All dimensions are in micrometers. In these pictures, it is easy to see that there is no isolated metallization on the surface. An isolated floating piece of metal could negatively affect the high voltage stability. Therefore, the author put a special focus on metallization during the design.

5.5 Selection of processing techniques

For the selection of processing methods (see Section 3.3.1), several methods were considered: Epitaxial (epi), Float Zone (FZ), and Magnetic Czochralski (MCz).
The HGCAL Collaboration selected thin (120 µm), epitaxially grown substrates (epi) for the areas of highest radiation exposure due to their outstanding radiation hardness [24]. MCz was also considered initially, as it can be enriched with more oxygen than FZ [66]. However, it was impossible to determine with certainty whether the vendor could also produce a sufficient number of wafers in MCz. FZ processing was chosen for all other areas with lower radiation hardness requirements, as this material is widely used in high-energy physics, with which there is much understanding [30]. The vendor has many years of experience processing large quantities. The HGCAL Collaboration

[b]The calculated values of the active areas are measured up to the edge of the p-stop common, which is considered the best approximation.

Table 5.2: Specifications of the sensor types LD and HD. Here only values are shown which differ between the sensor types.

Parameter	Low-density (LD)	High-density (HD)
Total number of cells	198	444
No. cells excluding calibration cells	192	432
Number of calibration cells	6	12
Number of edge cells	33	51
Number of corner cells	12	18
Total active[b] sensor area	23 258 mm^2	23 249 mm^2
Active area of one full-size cell	126 mm^2	56.1 mm^2
Active area of one calibration cell	29.2 mm^2	13.1 mm^2

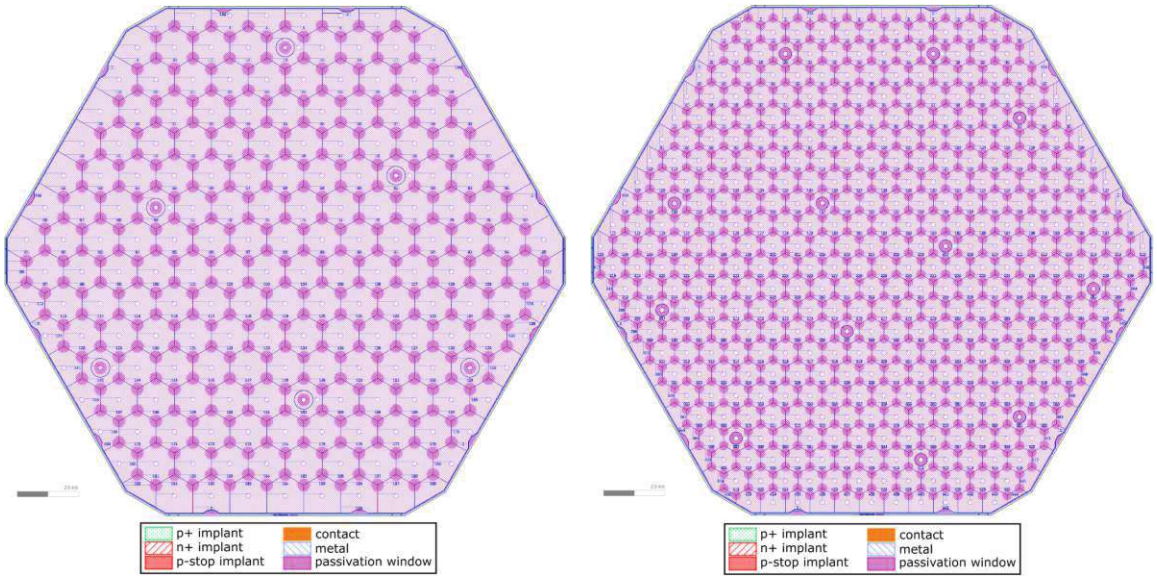

(a) **Low-density design** with 198 active channels. (b) **High-density design** with 444 active channels.

Figure 5.6: Design of the full sensor prototypes (2021 prototypes). Larger images can be found in Appendix A.2 and A.3.

Figure 5.7: Screenshot of the design file (2021 prototypes) of the sensor design. Depicted is a single cell of the high-density sensor. The violet sectors at the corners are contact areas where it is possible to contact and apply a bias voltage to the cell. The circle in the center means no metal, which allows testing the sensing element by a laser. The small orange circles are contact holes, which connect the metal layer to the underlying silicon. The lower rectangle is a placeholder for cell labels, which are visible in the full sensor design.

determined that the requirements of areas with low radiation doses can also be sufficiently met with FZ. Therefore, there was no compelling reason to use the superior MCz processing. Nevertheless, two prototypes of this material were produced, and one was available for our experiments.

5.6 Design of the test structures

Experience with previous CMS sensors showed that test structures are a valuable tool for complementing prototype sensor tests. One does not always want to do electrical measurements on full 8-inch sensors for various reasons. The large capacitance of sensors means that one has large charging currents between voltage steps, leading to longer waiting times. Test structures are also part of the so-called Process Quality Control (PQC) strategy, which defines complementary actions during the series production process. They comprise specialized structures like metal-oxide-semiconductor (MOS) elements, van-der-Pauw contacts, and gate-controlled diodes (GCD), see Figure 5.8. One can find a detailed overview of the PQC strategy and its elements in [38]. During series production, they help to monitor production, spot deviations from specifications. They provide the ability to test more wafers compared to other quality assurance processes. Besides series production, PQC offers various advantages for the prototype phase: It makes it possible to observe parameters that would not be as easy to investigate using full-size sensor prototypes. Furthermore, these small test structures are easier to handle and therefore have a more negligible risk to break.
As mentioned before, the CMS Tracker utilizes semiconductors manufactured in the 6-inch process, whereas the HGCAL uses 8-inch. Both wafer layouts use the same set of test structures (except the Ministrip-Sensors, see Section 5.7). This standardization is effective in spotting differences between these processes, as well as the implications for radiation hardness. The placement of these test structures is in the areas between the hexagonal sensor and the edge of the circular wafer.

5.7 Design of the Ministrip sensors

The wafers for HGCAL include two additional types of test structures, designed in the shape of strip sensors: Regarding the design choicees, one as close as possible to the CMS Tracker strips (“TrackerStrip”, or “Microstrip”), and one like the HGCAL (“HGCALStrip”, or “Ministrip”). The choice for the TrackerStrip (Figure 5.9b) is its geometrical similarity to the full-scale Tracker, featuring

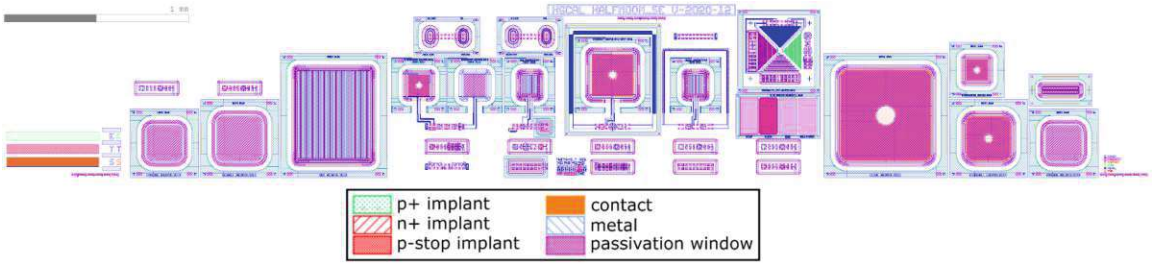

Figure 5.8: Test structures from Process Quality Control (PQC) as they are placed in the lower right and upper left area outside the large main sensor. For a detailed description, please refer to [38].

similar interstrip geometry and dimensions as of the PS-s Tracker sensor [7]. This requirement leads to the fact that the TrackerStrip features only the p-stop individual type. For the HGCALStrip (Figure 5.9a), the intention was to use strips because it eases contacting the neighbor strips of one test strip. If one wants to test one strip, only the two neighboring strips must set to ground potential. This geometry made it possible to study interpad/interstrip properties without employing full-size sensors. In a hexagonal pattern, one must contact six adjacent cells, increasing the number of contact needles, effort, and time expenditure.
The small physical size of the Ministrip sensors gives an additional advantage for irradiation. Many research reactors feature just small irradiation ports, not suitable for 8-inch sensors. Using Ministrip sensors also allow the application in smaller irradiation ports, accelerating the irradiation campaign.

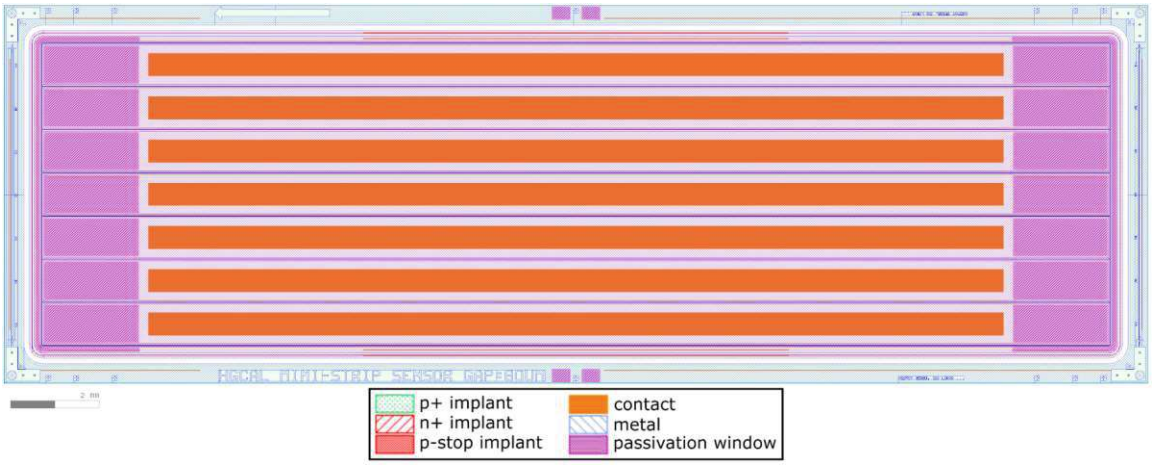

(a) **HGCAL Ministrip, HGCALStrip**. This Ministrip sensor inherits the interpad dimensions from the HGCAL. As for the corresponding full sensor, the Ministrip has both p-stop common and p-stop individual versions. The strip pitch is 950 µm, the active area of a strip is 0.212 cm^2.

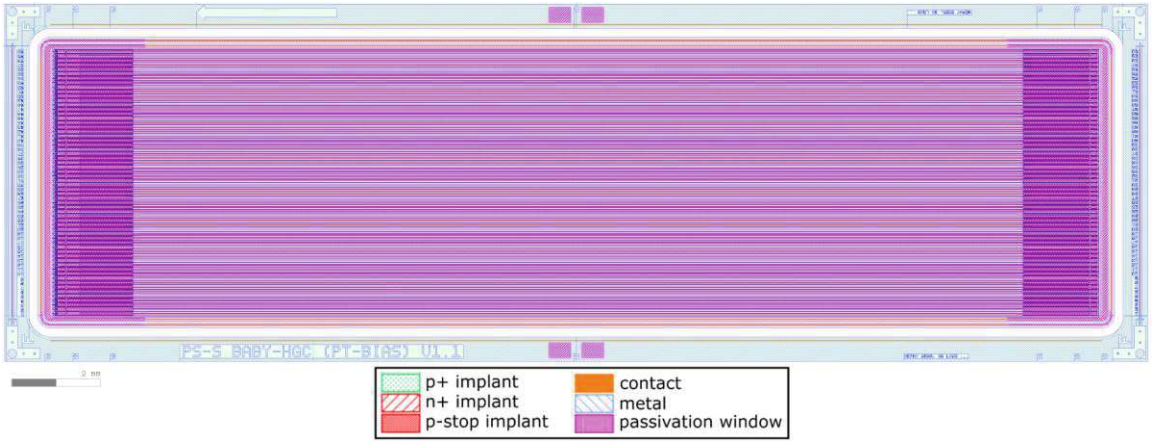

(b) **Tracker Microstrip, TrackerStrip**. This Ministrip sensor inherits the interstrip dimensions from the PS-s Tracker sensor [7]. The TrackerStrip features only the p-stop individual type, strip pitch is 100 µm.

Figure 5.9: Design of the Ministrip/Microstrip sensors

"What we observe is not nature itself, but nature exposed to our method of questioning."

Werner Heisenberg

6 Physical measurements and methods

6.1 Sensor qualification

This chapter describes the test setups at the Institute of High Energy Physics (HEPHY). A distinction is made between measurements on full sensors (LD and HD design, see Section 5.4) and measurements on test structures (see Section 5.6). Only electrical measurements (current-voltage characteristics and capacitance measurements) and microscopy were performed on full sensors. At the same time, the test structures, according to their name, offer a wider range of measurement possibilities.
Figure 6.1 depicts the overall process control and assurance strategy of HGCAL: The vendor produces the sensors and test structures. There is already a first step of quality control on the vendor side. CERN takes over the distribution, and the individual HGCAL institutes test about 10 % of the entire sensors in the sensor quality control (SQC) in batches. At the same time, the institutes test around 10 % of the test structures using process quality control (PQC) for the manufacturer's process quality. Table 6.1 gives an overview of the relevant parameters and qualification criteria.

Table 6.1: Quality criteria of the unirradiated HGCAL sensors. These criteria define the overall performance of the CMS experiment and are therefore essential for vendor selection. "Scaling" in this context means a transformation of the current from −30 °C to 20 °C by the Boltzmann factor, see Equation 2.11.

Parameter	HGCAL quality specification
Thickness (active/physical) d_{ac}/d_{ph}	120/300, 200/200, 300/300 µm
Thickness tolerance	± 10 µm
Full depletion voltage U_{fd}	120 µm: < 70 V
	200 µm: < 160 V
	300 µm: < 370 V
Breakdown voltage U_{bd}	> 800 V
Cell current at 600 V I_{600}	≤ 100 nA
Cell current at 800 V I_{800}	$< 2.5 \times I_{600}$
Total current at 600 V, scaled to 20 °C $I_{600,tot}$	≤ 100 µA
Total current at 800 V, scaled to 20 °C $I_{800,tot}$	$< 2.5 \times I_{600,tot}$
Bulk resistivity ρ	> 3 kΩ cm
Intercell resistance at 20 °C and $U_{fd} + 50$ V R_{int}	> 100 MΩ
Intercell capacitance at 20 °C and $U_{fd} + 50$ V C_{int}	< 1.5 pF cm^{-1}
Number of faulty cells	≤ 8 per sensor
Clustering of faulty cells	≤ 2 adjacent

It is noticeable that some of the quality criteria refer to currents, either related to individual cells or the sensor as a whole. These are deliberately set low and do not allow an excessive number of

"hot" cells, i.e., cells that break down early due to material defects or areas with too high current consumption. The current is restricted by two fundamental limitations for the silicon sensors in the finished HGCAL:

1. The electrical power input is ultimately converted into heat, which the HGCAL cooling system must dissipate to maintain the operating point at −30 °C. The leakage currents increase significantly with increasing particle fluence. The innermost HGCAL sensors are expected to draw up to 4 mA at 800 V bias voltage per sensor, but most will draw about 4 mA current [1].
2. The electrical power of the detectors must be maintained by the power supply, which takes up space and generates waste heat. The total power consumption of the HGCAL (sensors and electronic signal chain) is 110 kW per endcap, with the cooling system designed for 300 kW or 150 kW per endcap. Thus, during normal operation, the cooling system runs at approximately 75 % of its cooling capacity [1].

In order to find the optimum processing method for the silicon sensors on the part of the manufacturer, numerous process variations were made for the different batches. Process variations embrace

- **Active sensor thickness:** 120 µm, 200 µm and 300 µm
- **Silicon crystal growth technique:** One 300 µm in Magnetic Czochralski, all other Float-Zone (200 µm and 300 µm) and epitaxial (120 µm), see Section 5.5
- **Oxide type:** Referred[a] as "Standard" and "Type A" to "Type E"
- **Flatband voltage:** −2 V and −5 V, see [38]
- **p-stop geometry:** Common and individual, see Section 5.1
- **p-stop doping concentration:** "Standard", 0.5 fold, 2.5 fold, and 5 fold, see Section 6.2

6.2 Complementary methods for quality assurance

6.2.1 Spreading resistance profiling (SRP)

Spreading Resistance Profiling (SRP) is a semiconductor characterization technique that determines electrical properties, particularly resistance and charge carrier concentration. It is a destructive method for obtaining depth profiles of dopant concentrations and understanding the doping distribution within a semiconductor sample in the sub-micrometer range. Figure 6.2 illustrates this method: The semiconductor specimen is cut at an oblique angle to project the surface onto a large area. Two electrodes with metal tips are contacted to this cut surface, and a small voltage is applied between them. The current flow is then measured. This measurement is repeated at several points over the surface so that the resistance of the semiconductor can be determined throughout the beveled cut surface, from which the local doping concentration can be calculated. This provides a profile of the doping concentration over the depth profile.
By measuring the spreading resistance as a function of the position of the probe tips, one can construct a depth profile of the charge carrier concentration along a cross-section of the semiconductor material. This provides information about the dopant distribution and allows for evaluating dopant diffusion, activation, and other process-related effects. It is essential to note that SRP is a contact-based technique, and the results can be influenced by the probe geometry and the semiconductor's surface condition.

For the study of HGCAL sensors, SRP is suitable as a qualitative and quantitative analysis in terms of the penetration depth of doping profiles, as shown in Figure 6.3. To some extent, the values obtained are suitable for comparison with other microscopic (SEM, see Section 6.2.3) and macroscopic, electrical (see Section 6.4.2) investigations, as well as verification of the validity of the CMS specifications, see Appendix A.4.
One of the key values for assessing the production quality is the effective charge carrier concentration N_{eff} of the bulk material. In this SRP measurement, a value of $1.36 \pm 0.04 \times 10^{12}\,\text{cm}^{-3}$ [b] was determined.

[a] Hamamatsu did not provide detailed information about the process variations regarding oxide types
[b] The uncertainty is the standard deviation, the measurement series ranges from depths of 0.25 to 3.4 µm.

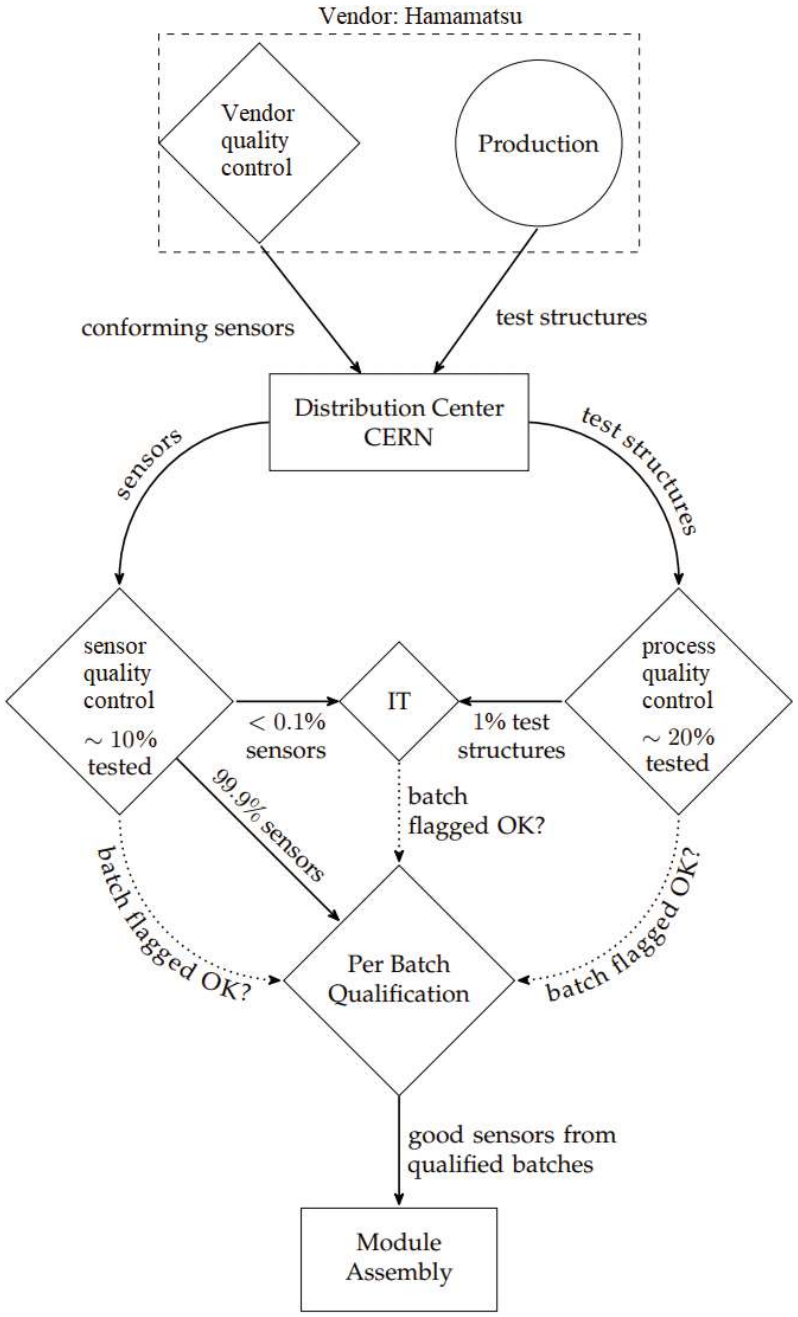

Figure 6.1: Flow chart of the sensor quality assurance strategy of HEPHY sensors and test structures. The exact values for the splitting have yet to be decided (as of 2021). Each sensor will be electrically tested by the vendor Hamamatsu before being delivered to the distribution center at CERN. The participating institutes will test approximately 3000 sensors (equivalent to 10 %) to qualify each sensor in batches. Around 6000 test structure sets (equal to 20 %) will also be tested to investigate and qualify the stability of the production process. All sensors or batches found to be in order are ultimately fed into module production. Approximately 30 sensors (corresponding to 0.1 %) and 300 test structures (corresponding to 1 %) are irradiated in parallel [38].

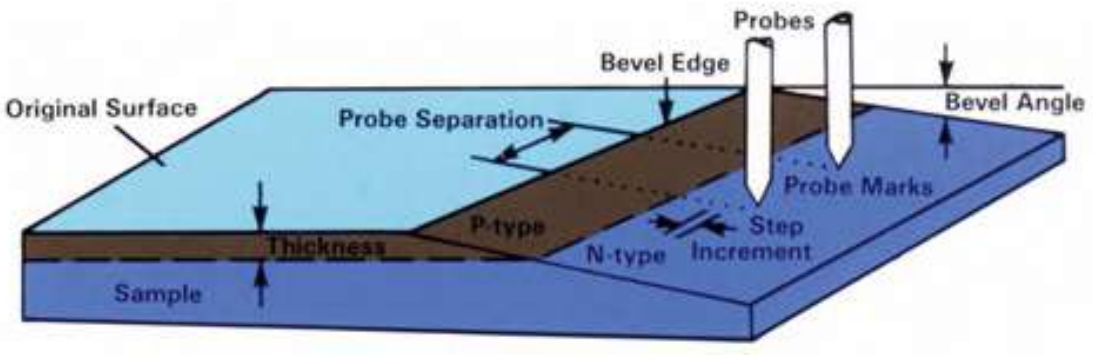

Figure 6.2: Operating principle of SRP. Two metal probe tips are brought into contact with the sharply beveled surface of the specimen. A small voltage is applied between the probe tips, creating a current flow through the semiconductor specimen. The probe tips are then scanned across the surface, and the current is continuously monitored. As the bevel is moved, the spreading resistance of the semiconductor material beneath the probe changes, and this variation in resistance provides information about the local doping concentration. Picture from [29].

6.2.2 Secondary ion mass spectrometry (SIMS)

Secondary Ion Mass Spectrometry (SIMS) is an analytical technique used in materials science, surface chemistry, and other scientific fields to determine solid materials' elemental and isotopic composition at high sensitivity and spatial resolution.
SIMS, at its core, involves shooting a solid sample with a beam of high-energy primary ions (here cesium at 15 keV) to sputter secondary ions from the surface. These secondary ions are then extracted, accelerated, and focused into a mass spectrometer for analysis. The mass spectrometer separates the ions based on their mass-to-charge ratios (m/q), and a detector records the number of ions at each m/q value. This data provides information about the elemental and isotopic composition of the sample.
For the HGCAL sample examined, the SIMS method discovered no increased concentration of dopants such as boron, phosphorus, or arsenic in the bulk material outside the detection limits of (see Figure 6.4).

6.2.3 Scanning electron microscopy (SEM)

A scanning electron microscope (SEM) is an electron microscope in which an electron beam is passed (rasterized scanning) in a specific pattern over the object to be magnified, and interactions of the electrons with the object are used to produce an image of the object. The images typically produced by a scanning electron microscope are images of the object's surfaces and have a high depth of field. (SEM) allows the surface structure and composition of samples to be studied at high resolution and provides a wealth of information about the sample's spatial structure, layer thickness, porosity, and other properties.
For the investigation of the HGCAL prototypes, an SEM from the supplier Fresenius [29] in Dresden, Germany, was used, so the samples were examined there. The particle energy of the electrons was 2.5 eV and 5 eV. In preparation, the samples were cut vertically so that a measurement of the structures in cross-section could be made, see Figure 6.5. Various etching processes can be used to modify the solid structure specifically. Not only do different compositions react differently, but also regions with crystal lattice defects. This makes it possible for the areas where implants are located (relatively high crystal lattice defect density) to obtain a certain contrast, as can be seen in Figure 6.6.

6.2.4 Confocal Laser Scanning Microscopy (CLSM)

Confocal laser scanning microscopy (CLSM) is an imaging technique used to produce high-resolution surface images of samples. Unlike conventional microscopy methods, CLSM enables layer-by-layer image acquisition through a coherent laser beam that shines on the sample point-by-point and picks

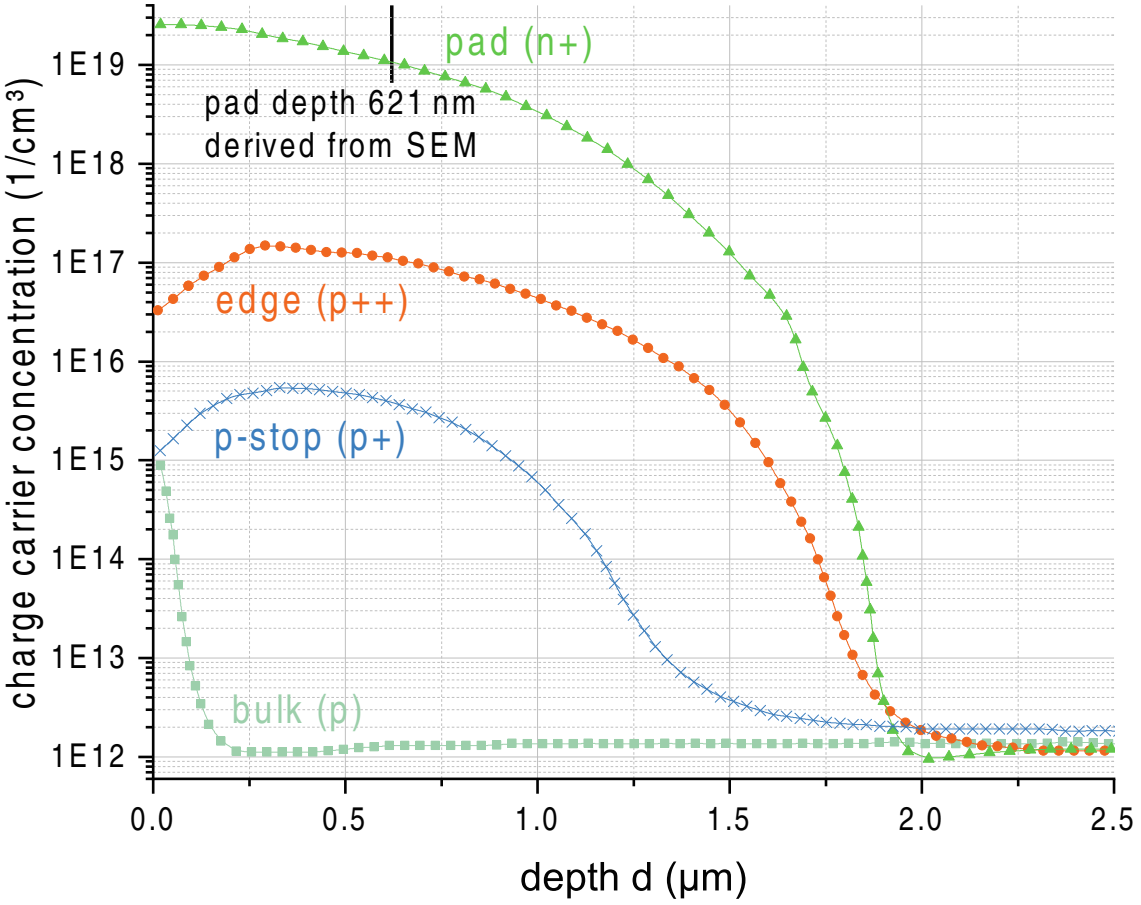

Figure 6.3: Results from the SRP measurements. The resistance R between the needles is measured. We can deduce the resistivity (Figure A.4) from the known distance between the needles. More meaningful, however, is the microscopic size of the effective charge carrier concentration, which derives from the resistivity and is plotted here. Looking at the concentration depth of the p-stop - implant, we see that this reaches about 1 to 1.5 µm deep. This is in good agreement with the SEM images of the etched material, Figure 6.6, in which the p-stop was measured at 0.6 µm. The discrepancy is explained by the fact that only the highest concentrations can be made visible by etching. Of course, for the bulk radiation damage measurement, it is interesting to compare the bulk with the concentrations of the unirradiated bulk material, which is at $1.36 \pm 0.04 \times 10^{12}\,\mathrm{cm}^{-3}$ [c] was determined.. In addition, the location of how deep the pad implant penetrates the bulk according to SEM measurements is marked; see Section 6.2.3. The actual penetration depth, however, is significantly deeper, although with an approximately exponential decay.

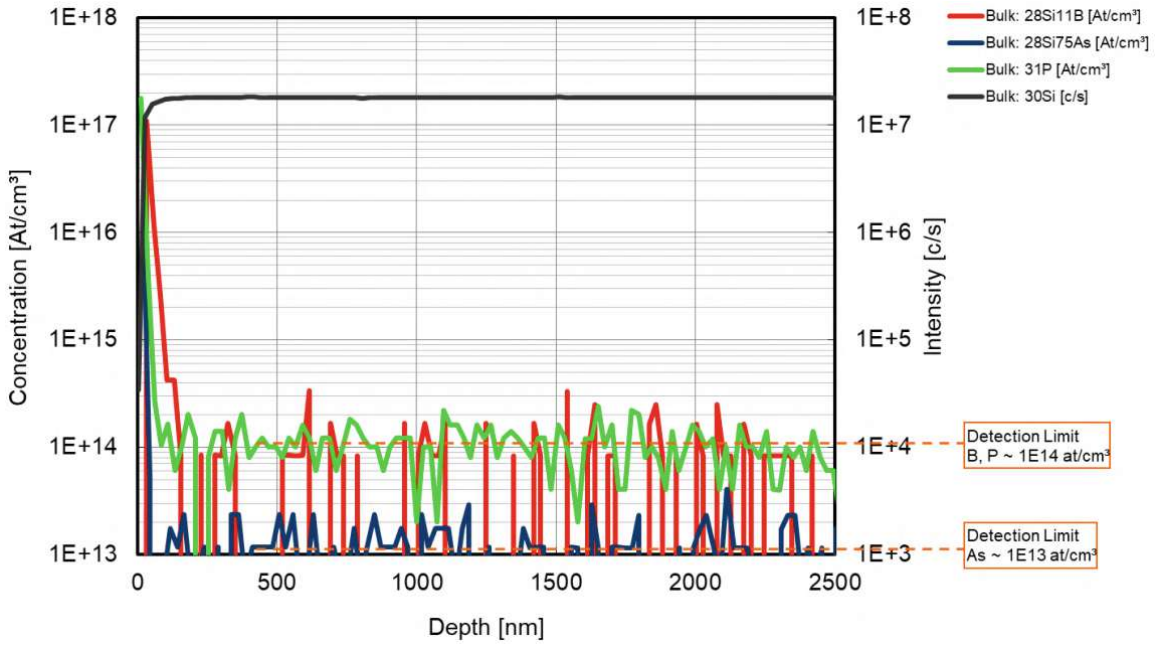

Figure 6.4: SIMS image of the bulk structure near the surface. With the exception of surface contamination, which is carried into the depths by the sputtering process during SIMS, none of the dopants mentioned can be detected in the examined structure within the detection limits of B and P of $10^{14}\,\mathrm{cm}^{-3}$ and for As of $10^{13}\,\mathrm{cm}^{-3}$. This test result is therefore interpreted as negative in terms of the achievable accuracy.

up light reflected from the sample. Special optics, the confocal aperture, block light originating outside the focal plane, allowing higher resolution and depth of field. The resulting data is processed to produce a three dimensional image that provides a detailed understanding of the spatial structure of the sample. CLSM is a valuable tool in research and diagnostics because the technique is fundamentally non-destructive and enables high image resolution [48].
Since the processing of the silicon detectors creates differences in height due to the principle, electrically active structures (for example, metallizations) can be detected. Auxiliary layers added during processing can even detect where underlying bulk regions have been equipped with implants, for instance, the n+ implant of the active zone or the p-stops. For silicon detectors with silicon oxide surface passivation, a limitation arises because SiO_2 (glass) is transparent in the visible light range and therefore imaging this layer is not necessarily unproblematic. For the detection of the passivation layer, this method is, therefore, only suitable to a limited extent.
The CLCM is a valuable tool to complement the light microscopic incoming inspection of the sensors. In the case of the HGCAL prototypes, we used the Leica DCM8[d] primarily to determine and assess surface damage from transport, handling, and electrical flashover, as well as for checking the implant geometries and dimensions (see Section 6.3.5). Figure 6.7a shows an example of the intercell geometry at the nexus of three cells of a HGCAL full sensor.

6.3 Test station for large area silicon sensors

The institutes[c] participating in HGCAL sensor tests maintain test stations for sensor quality checks during series production. For the prototype phase, these working groups are constantly improving it. Table 6.1 gives an overview of the qualification specifications. For acceptance by HGCAL, all sensors, irradiated or not, must fulfill these quality criteria.
In general, irradiation tests are time-consuming and require adequate infrastructure, and measuring the irradiated sensors is more complex and challenging and requires a specially designed test station. Therefore, only some prototypes were subjected to irradiation tests, and a much more significant proportion was irradiated with the test structures (see Section 6.4).

[d] https://www.leica-microsystems.com/products/digital-microscopes/p/leica-dcm8/

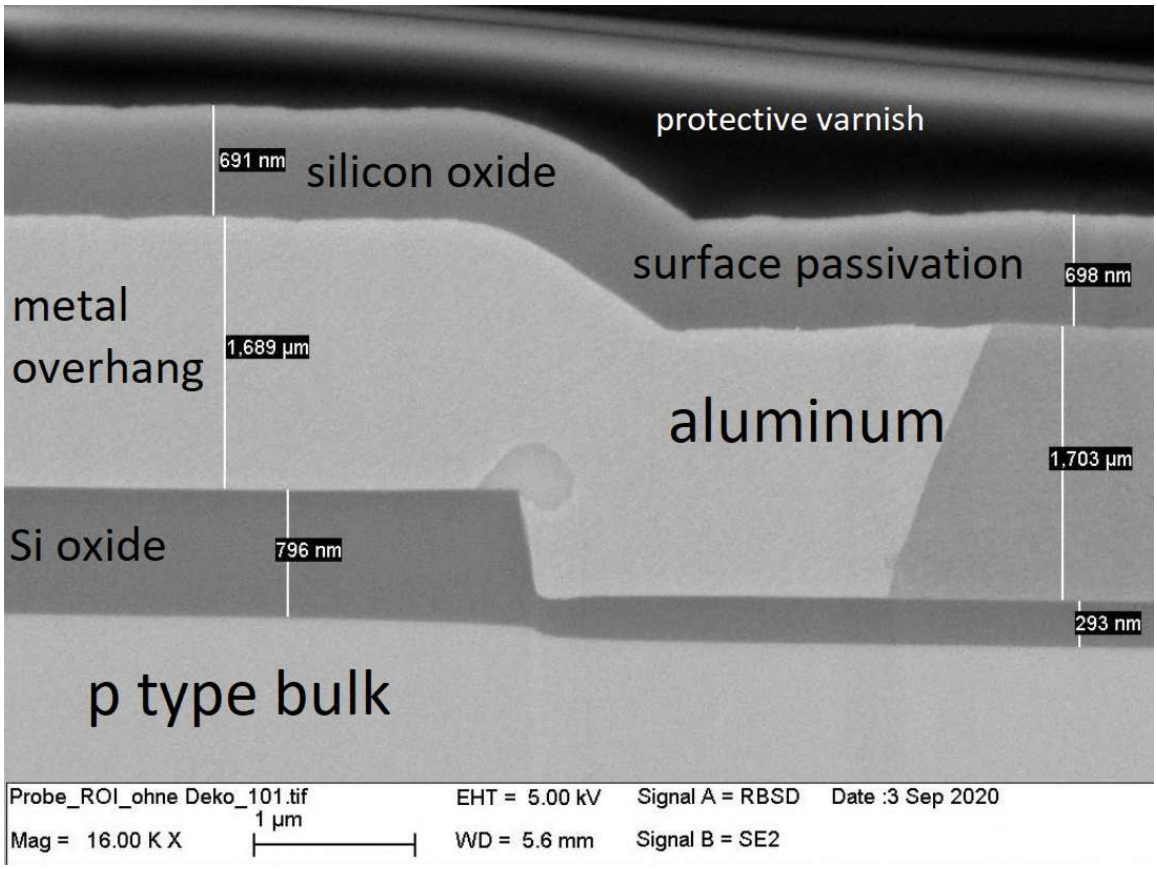

Figure 6.5: Scanning electron microscope image of the surface structure of a test structure of a 6-inch HGCAL prototype wafer (2019 version). The sample was cross-sectioned to obtain a cross-sectional image of the surface structures. The measured layer thicknesses are drawn in the image. In this context, it may be useful to compare this image with Figure 5.1 in Chapter 5. It must be added that the processing of 6-inch wafers can differ significantly compared to 8-inch wafers, and therefore the results cannot be transferred 1:1 to the new 8-inch HGCAL. Picture from [29].

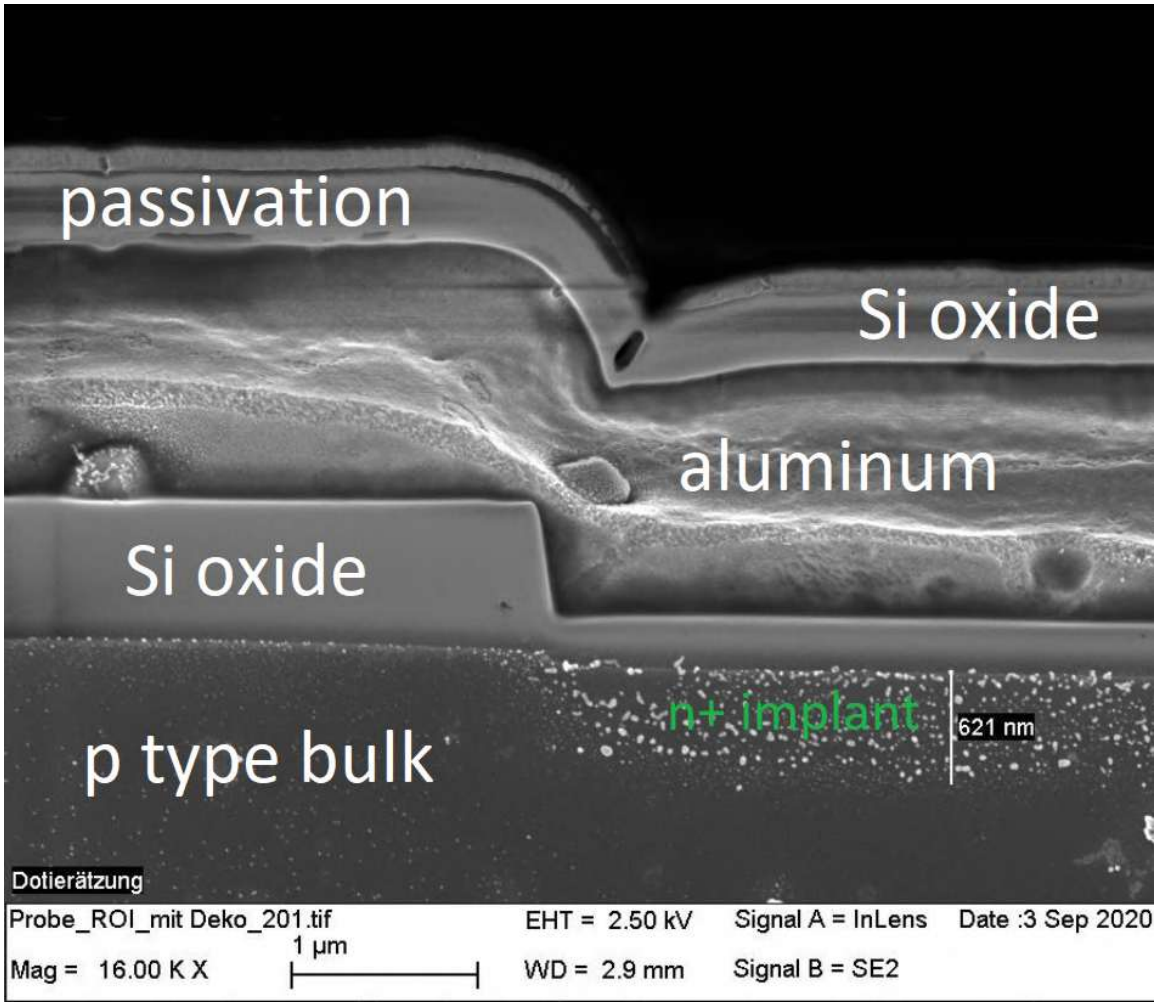

Figure 6.6: Scanning electron microscope image of the same part, but now prepared with etchants to reveal substructures. Now the altered crystal structure of the silicon is revealed where the n^+ implant was introduced. Thus, the implant's thickness can be measured at approximately 620 nm. The arc-shaped termination at the lateral end of the implant is also clearly visible.

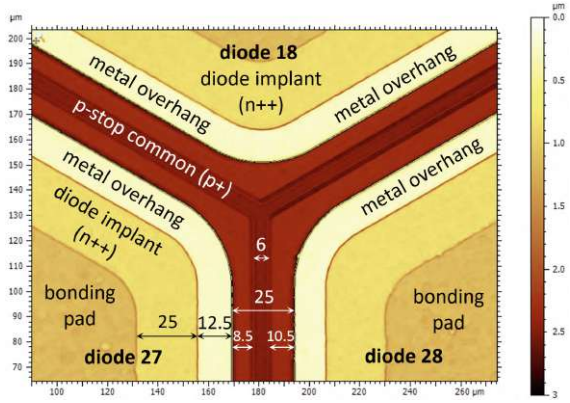

(a) Pseudo color image of an interpad nexus between three neighboring cells, with p-stop common structure. The color scale indicates the height of the structures. A mask misalignment of 1 µm led to a horizontal shift of the p-stop mask, resulting in a p-stop not centered between the cells.

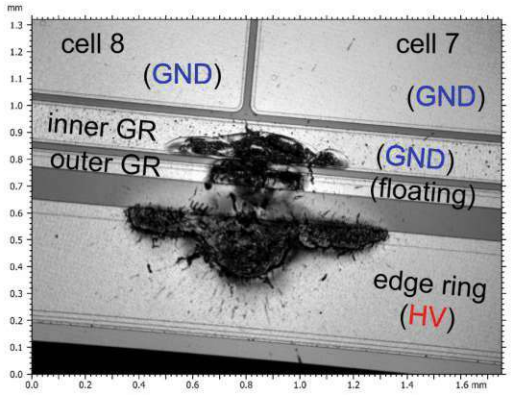

(b) Burn mark, caused by spark-over between the edge ring on high voltage and the inner guard ring on ground potential. These earlier prototypes had multiple passivation openings on the inner guard ring (as at this location), which provided potential pathways for sparking.

Figure 6.7: Confocal laser microscopy images of sensor prototypes (2019 prototype run), with added descriptions of visible structures. These images are an export from the Software "Leica Mountain View".

The HGCAL institutes rely on custom-made test stations for fast, reproducible, safe, and automated measurements. These test stations must be automated as much as possible to meet the requirements of the large quantities of (~ 3000) sensors used for quality control.

An essential component of the HGCAL test station (Figure 6.9) at HEPHY consists of a cold chuck, which is responsible for temperature control (see Section 6.3.2) of the HGCAL sensor and uses a vacuum system to secure the sensor against slipping. The cold chuck is mounted on a movable stage, which allows the sensor to be positioned and pressed against the probecard, see Chapter 6.3.1. A dedicated positioner can be used to contact additional contact areas. This additional contact option was used several times during prototype design since specialized probecards were unavailable for some prototype iterations. The changes very often affected the edge and guard regions of the sensor (see Section 5.3). This setup is in a dry air box where dry air is constantly blown in for irradiated sensors to keep the dew point well below the sensor temperature to prevent condensation and ice formation. A microscope is used to inspect the sensor surface for any surface damage and accurately position the probecard over the sensor for contacting. The dry air box, in turn, is located together with the microscope in a light-tight black box to prevent photon-induced currents, see Figure 6.8.

6.3.1 Probecard system

To measure the large-area sensors quickly, reproducibly, and automatically, HGCAL institutes use a probecard system [20] the so-called "ARRAY" (switching mAtRix pRobecArd sYstem) system [8], see Figure 6.10. It is a switching matrix connected to the measuring instruments, with exchangeable probecards adapted to the respective sensor. To contact a sensor, the height-adjustable chuck is moved upwards against the probecard until the spring-loaded pins (called "pogo pins", see Figure 6.12) press on the corresponding contact regions of the sensor.

Figure 6.11 provides an overview of the electrical wiring of the switching system. The switchcard consists of three levels of 8-to-1 semiconductor multiplexers (MAX328), which switch the channels to the measuring devices. The three levels of multiplexers allow in total $8^3 = 512$ channels. An additional multiplexer is used to switch between IV and CV measurements. The multiplexers MAX328 were chosen because they have an acceptable series resistance of 1.5 kΩ and a leakage current of only a few pA. One 10 kΩ resistor is connected in series as standard in the original design

[c]Brown University, University of California, Fermi National Accelerator Laboratory, Florida State University, and Texas Tech University in the US; CERN in Switzerland; Karlsruhe Institute of Technology in Germany; and the Institute of High Energy Physics (HEPHY) in Austria.

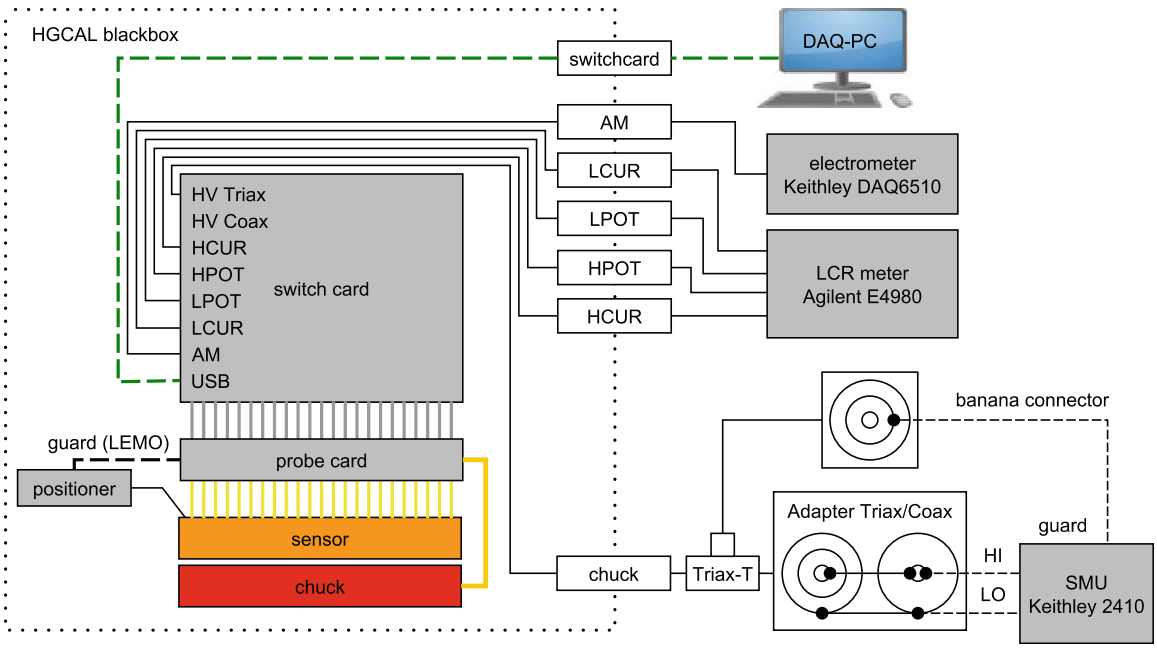

Figure 6.8: HGCAL test setup at HEPHY for full sensor tests. The main components are the cooled chuck with the sensor on top and the probecard system, located in a light-tight black box. Outside, the measuring instruments and control computer are connected.

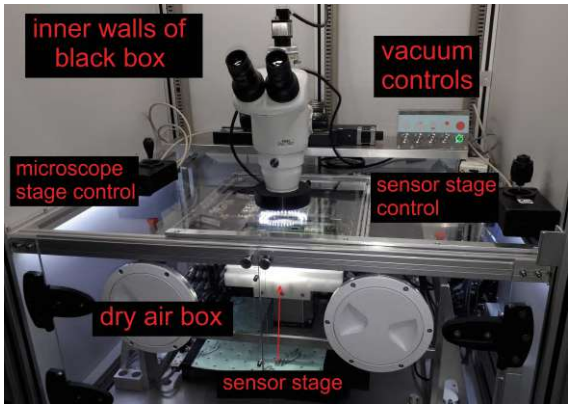

(a) An overview of the inside of the test station. The HGCAL sensor itself is located in a dry air box into which dried air is constantly blown to prevent condensation on the cooled sensor. Both the sensor stage (joystick on the right) and the microscope (joystick on the left) can be moved in three degrees of freedom. The vacuum system sucks the sensors at the cold chuck to prevent them from slipping. The control switches for this can be switched between different sensor sizes (e.g. full sensor and Ministrip).

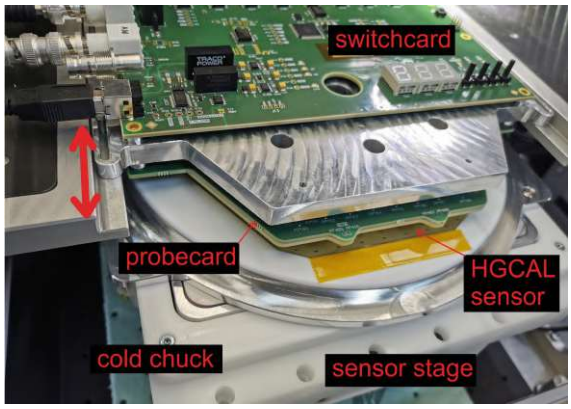

(b) The probecard system consists of a holding plate that can be moved (back and forth) on a movable carriage to position the probecard over the sensor. Fine positioning is performed via the sensor stage. Below the holding plate, the probecard is screwed with the pogo pins, against which the HGCAL sensor is pressed to establish contact. Above the holding plate the switchcard is fixed, which is connected to the probecard, and also to the measuring devices outside the black box.

Figure 6.9: Photos of the inside of the black box of the HGCAL test station at HEPHY.

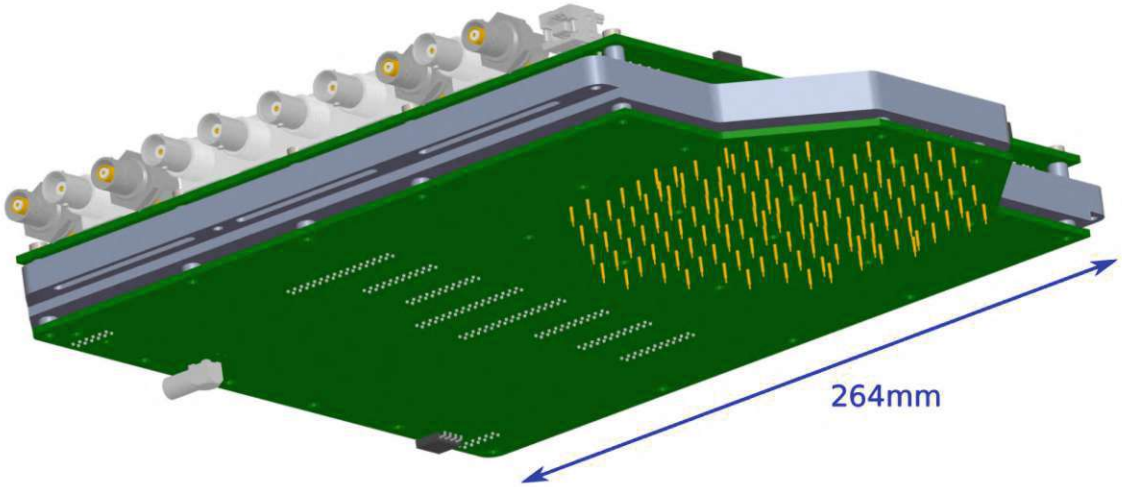

Figure 6.10: A CAD drawing of the probecard system [20]. One can spot the contacts of the switchcard, which connect to measurement devices outside the black box (Figure 6.8). On the bottom, this sketch depicts the pogo pin contacts (Figure 6.12).

to protect the multiplexer from higher currents. In the process of this work, we reduced this value to 1 kΩ for measurements of irradiated sensors to limit the voltage drop over this resistor. The probecard system is designed to switch the cells to ground potential by default via the switching matrix, so there are never floating cells. All cells are, therefore, always switched to ground via 1 kΩ or 10 kΩ resistors or connected to the respective measuring device. This serves the uniform field distribution in bulk to prevent unwanted currents ("punch through") across several cells.
Each channel can be shorted to ground potential using ADG1414 switches to ensure a stable ground potential for all cells not under measurement. The switchcard connects to the measurement devices with five coaxial BNC connectors and one Triax connector. A DAQ computer controls these instruments, the switchcard, and the cooling system [8][20][62].

6.3.2 Cooling system

One of the significant challenges of the HGCAL system is cooling. This applies not only to the finished calorimeter but also to the test station for the irradiated sensors. Before the test station at HEPHY was certified for HGCAL, the cooling system was designed for a temperature of −20 °C, which was considered sufficient for sensor tests. Over the years, it became apparent that this specification was not strict enough, as the currents of the irradiated sensors require a temperature of −30 °C.
The cooling system for HEPHY's test station includes the following main components (see Figure 6.13):

- The cold chuck with the cooling plate on which the sensor is placed. This contains resistance-based temperature sensors to measure and consequently control the temperature.
- Under the cold plate are three Peltier elements that serve two purposes: First, they provide a temperature gradient of ΔT up to 30 K to avoid running the chiller's cooling lines below freezing. This could lead to short electrical circuits due to condensation. Second, the Peltier elements are capable of fast and accurate temperature control.
- Underneath the Peltier elements is the heat exchanger to which the chiller's cooling lines are connected. The cooling capacity and the waste heat of the Peltier elements are dissipated via this heat exchanger.
- The chiller works with an alcohol-based cooling liquid and dissipates the waste heat to the environment.

[d] LCR: inductance (L), capacitance (C) and resistance (R) measuring device

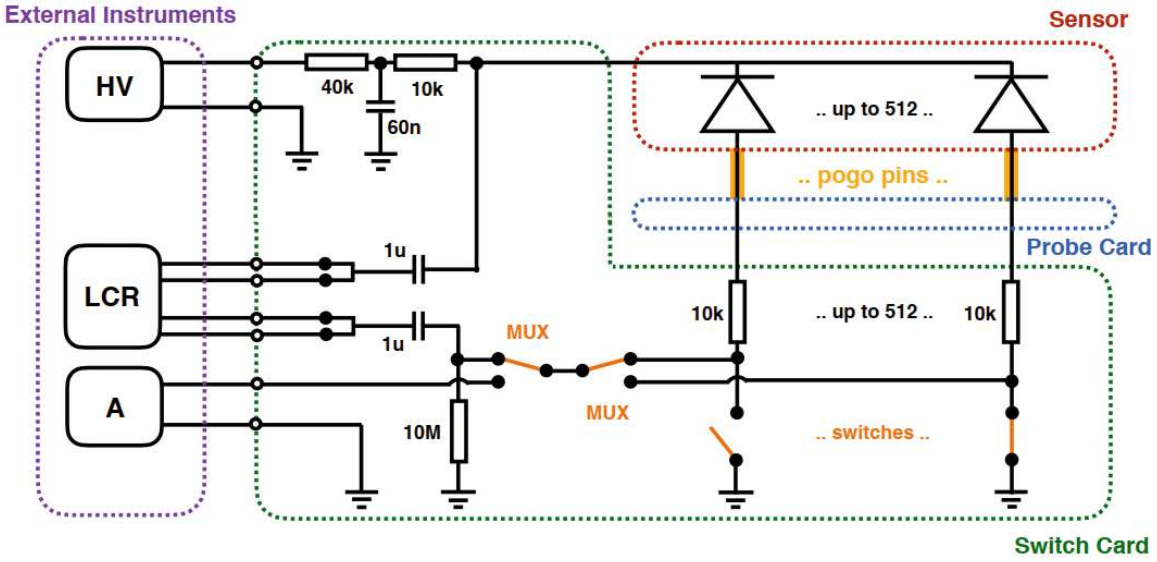

Figure 6.11: Circuit diagram of the switching matrix of the ARRAY system [8][20].
There are two modes to operate the probecard: In the IV measurement mode, the amperemeter ("A") is connected to the measuring cell. The amperemeter ("A") is connected to the measuring cell in IV measurement mode. In CV measurement mode, the cell under test is switched to ground via a 10 MΩ resistor to decouple the LCR[d] meter to high impedance, i.e., to achieve a pull-down effect of the potential. In addition, the test leads are decoupled via capacitors (1 µF) to prevent the LCR meter from high voltage DC forwarding. The LCR meter is rated only for small bias voltages.

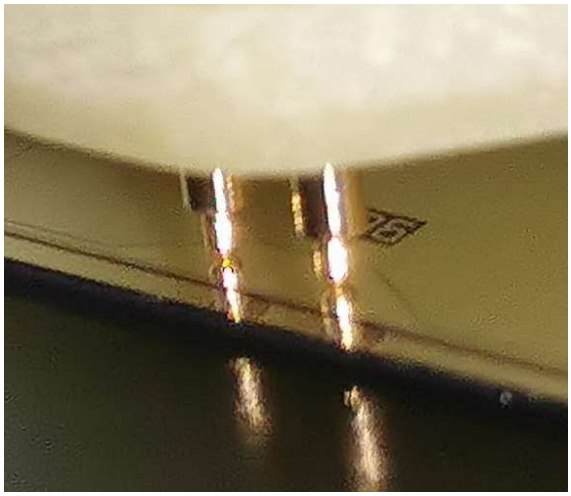

(a) Pogo pin pair contacting the guard ring. This makes a separate contact needle unnecessary.

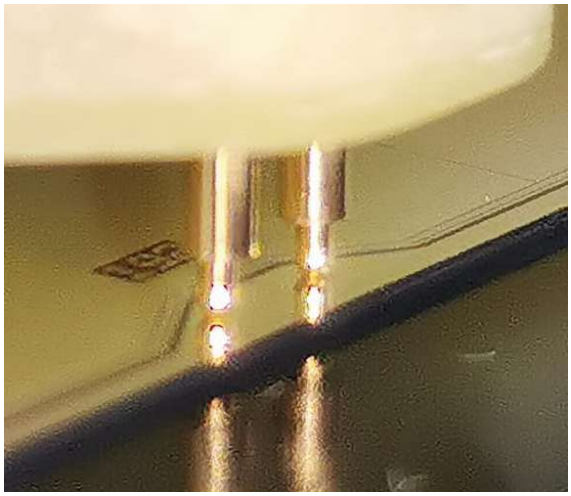

(b) Pogo pin pair contacting the high voltage extension (Only for front side biasing).

Figure 6.12: Photos of pogo pins of the probecard, pressed on the sensor. For redundancy, these pins are duplicated per contact position.

- All active systems are centrally managed by a micro controller, connected to the same DAQ computer that controls the electrical sensor tests.

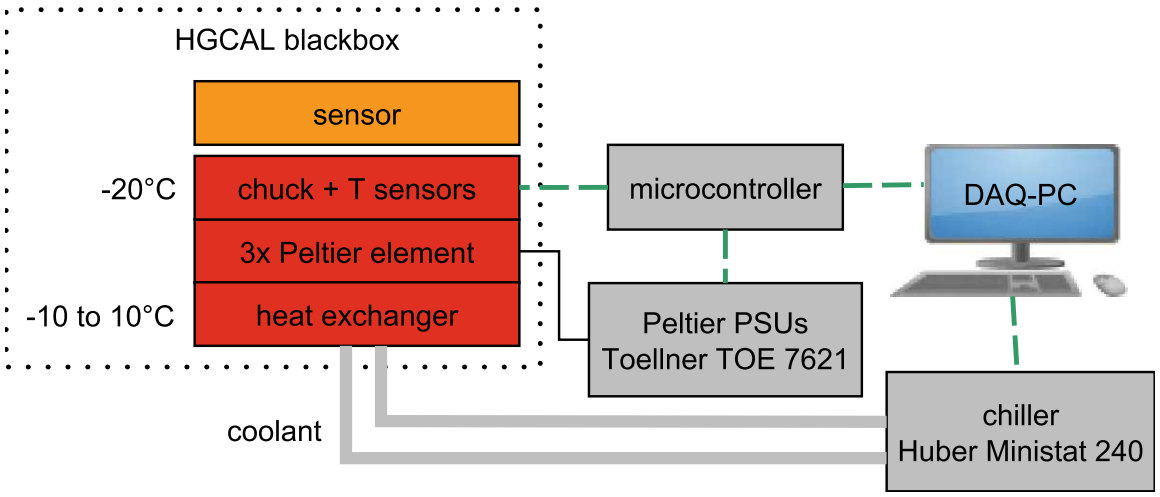

Figure 6.13: The cooling system at HEPHY. The sensor is on a cooling plate, cooled to the target temperature utilizing Peltier elements. The chiller dissipates the heat from the Peltier elements using a heat exchanger. The coolant lines are colored in gray, the voltage supply cables are in black, and the data lines are in dashed green.

To be able to reach the −30 °C mentioned at the beginning of the section, tweaks of the system were tried:

a) Cooling of the injected dry air

The injected dry air has room temperature, which means a considerable heat load on the cold chuck. A simple and inexpensive solution is a vortex tube (Ranque-Hilsch tube [39]), which separates the air flow of a compressed gas into a hot and cold stream due to enthalpy conservation. Only the cold air was extracted from the vortex tube and blown into the housing. The experiments showed a cooling of the air stream by about 10 K but on the cost of a substantially reduced air mass flow. This system would have require a much higher mass flow, higher pressures, and sufficiently dimensioned supply lines to bring this system to a reasonable temperature. Due to the effort required, this idea was therefore rejected.

b) Improving the effectiveness of the cooling system

Another approach tried is multi-staged:

1. The heat input of the Peltier elements is reduced. This can only be achieved if the Peltier elements have to dissipate a lower heat flow since Ohmic losses are lower at lower heat load:

$$P_{trans} = \pi I \qquad \text{and} \qquad P_{waste} = RI^2 \tag{6.1}$$

   where P_{trans} is the heat transported through the Peltier element, P_{waste} the Ohmic losses, π the Peltier coefficient R the Ohmic resistance and I the electrical current through the Peltier element. Less thermal load means less temperature difference. Another effect is the transportation of heat back from the hot side to the cold side, which of course increases with higher temperature difference. Thus the power loss decreases the smaller the temperature difference between the hot and cold sides of the Peltier elements.

2. Consequently, the temperature of the heat exchanger must be lowered. However, this also means that the chiller must dissipate a higher temperature difference and thus a more increased heat flow. The problem is shifted away from the Peltier elements to the chiller.

3. Now, however, the chiller's cooling capacity depends on the temperature difference of the cooling liquid to the environment, as Figure 6.14 shows. Therefore the ambient temperature

must be lowered.

The approach of lowering the ambient temperature was tried by reducing the temperature setting of the clean room air conditioner by 5 K: No stable behavior was observed at −20 °C chiller temperature and −22 °C ambient temperature, while 17°C ambient temperature resulted in settling to a stable point at −30 °C chuck temperature.

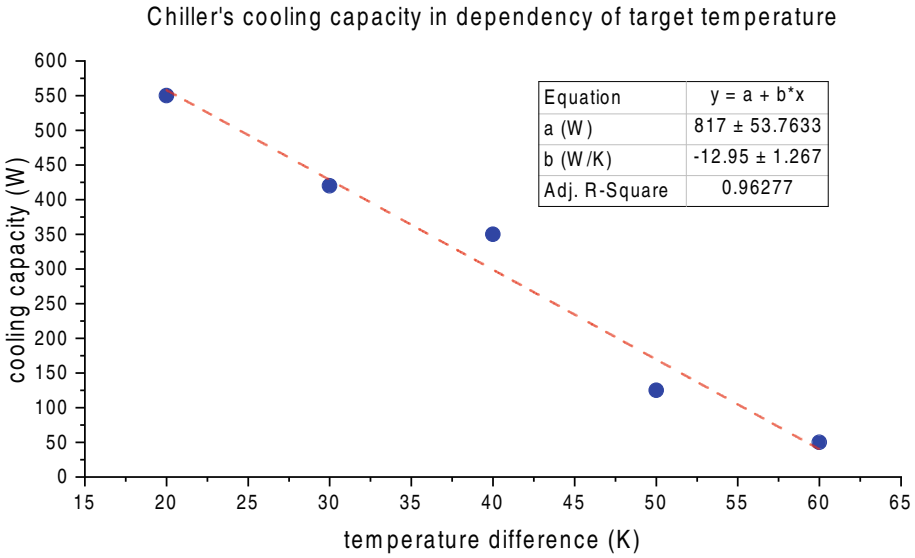

Figure 6.14: This graph plots the chiller's cooling capacity depending on the temperature difference (environment - chiller). One can see that the cooling capacity decreases rapidly as the temperature difference increases. This behavior led to the attempt to lower the room temperature to achieve the desired chiller temperature of −30 °C with the help of the thermoelectric coupling.

Why were these tweaks not implemented? Although the second approach of lowering the room temperature led to a stable −30 °C, this method was not established for sensor testing. One reason is that when the sample station is opened, there is inevitably a heat input, and this quickly overloads the cooling system, which is operated close to the limit, which in turn results in long cooling times, which would have significantly lengthened the entire measurement time, and reduced the number of possible measurement points to about three per day. Another reason is that lowering the room temperature by 5 K is also not a suitable permanent solution, leading to an uncomfortable working environment. Thus, all measurements of irradiated sensors were performed at −20 °C, which made it impossible to measure the large-area full sensors using the probecard system.

6.3.3 Current and capacitance measurements of unirradiated sensors

Only unirradiated full sensors of the 2019 prototypes were electrically tested at HEPHY. This was due to the under-design of the cooling system (see Section 6.3.2) combined with the difficulties of measuring high currents with the probecard system (see Section 6.3.1). Nevertheless, these measurements provided valuable feedback for improving the manufacturing process. At higher currents (up to 1 mA), the original series resistor of 10 kΩ (see Section 6.3.1) becomes non-negligible. It leads to a drop in the voltage applied to the sensor. According to the voltage divider rule, the following voltage is now present at the sensor:

$$U_{\text{sensor}} = U - I \cdot R_{\text{series}} \tag{6.2}$$

whereas U_{sensor} is the resulting voltage on the sensor, U is the supplied voltage, I the current through series resistor and sensor, and R_{series} is the series resistor.
Because the HEPHY has lowered the series resistor from 10 kΩ to 1 kΩ, at a maximum current of 1 mA allowed for the multiplexers, the voltage drop is now at 1 V instead of 10 V volt. It follows that the error at the first applied bias voltage (25 V) is at most 4 % instead of 40 %. This error decreases from 1 % (10 kΩ series resistor) to 0.1 % (1 kΩ series resistor) at higher applied bias voltages up to

1000 V and is thus negligible in these ranges. Nevertheless, the author has chosen to factor out this known systematic error and report only voltages corrected for the voltage drop across the series resistor.

Optical, sanity and contact checks before measurements

As an incoming inspection, each sensor was first examined under an optical microscope for visually apparent damage to the surface. Typical damage includes scratches, chipping, craters, and etching defects, and these do not necessarily result in electrical defects, especially if they occur in the outer edge region (see Figure 6.15). However, the investigation of surface damage has shown a correlation with early breakdowns [61]. These findings can be explained by field spike effects at the fracture sites: Cracks typically have sharp, angular edge regions where electric fields become very large according to $E \propto r^{-2}$. These field extrema then provide electrical paths for early breakdowns. So, if there is a bottleneck in sensor inspection during production, those sensors that show minimal damage after optical inspection should be electrically tested first.
Before the automated measurement programs were started, the total current through the sensor was measured manually in reverse bias and then in the forward direction as a sanity check. In the reverse direction, a few volts should not yet lead to a significant current increase, while in the forward direction, it should already increase in the range of about one volt.
First automated electrical tests were performed for each sensor under the probecard to qualify the basic functionality, trustworthiness, and repeatability of the measurements. These were to ensure that the pogo pins were pressed sufficiently and centered on the contact surfaces. Similar to the manual sanity checks, the sensor was switched into forward bias of one volt, see Figure 6.16.

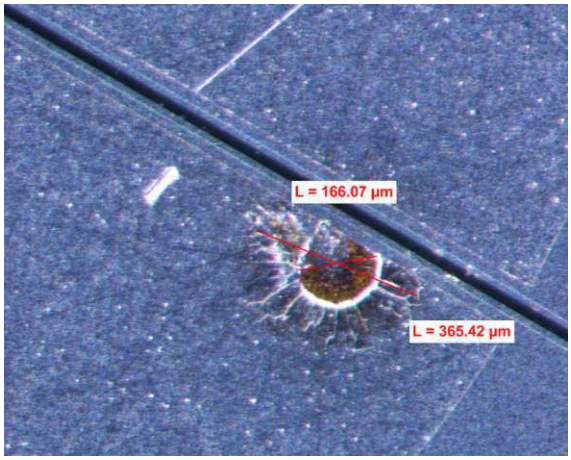

(a) Light microscope image of excavation on an aluminum contact pad at the cell boundary. The structure of the damage identifies a faulty sensor handling tool. This sensor (Z3415_11) suffered from a very early electrical breakdown at 200 V.

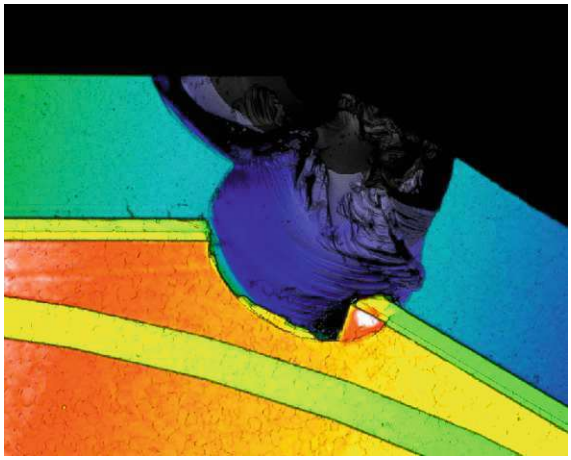

(b) Confocal laser microscopy (Section 6.3.3) of the sensor Z3415_06. This is the chipping of a corner, which is visible by the fracture edges. Utmost care is required when handling the sensors to avoid such damage.

Figure 6.15: Examples of damage found on surfaces. This batch Z3415 of 2019 prototypes suffered considerable processing and transport damages and correspondingly poor electrical performance.

Current measurements of unirradiated full sensors

After completion of the optical pre-controls and the preparatory measurements, the cell currents of the full sensors (see Figure 6.18), as well as their total currents (Figure 6.19) and guard ring currents (Figure 6.20), were measured. The guard ring current is subject to the same quality criteria as a single cell, namely <100 nA at a voltage <600 V. All measured currents were scaled to 20 °C because the quality criteria (Table 6.1) are valid only for this temperature.
The measurements revealed noticeable differences in quality between the individual sensor prototypes: According to the HGCAL quality criteria, four of the 11 sensors tested met all specifications, which corresponds to a yield of 36 %. Table 6.2 summarizes the results of these quality criteria.

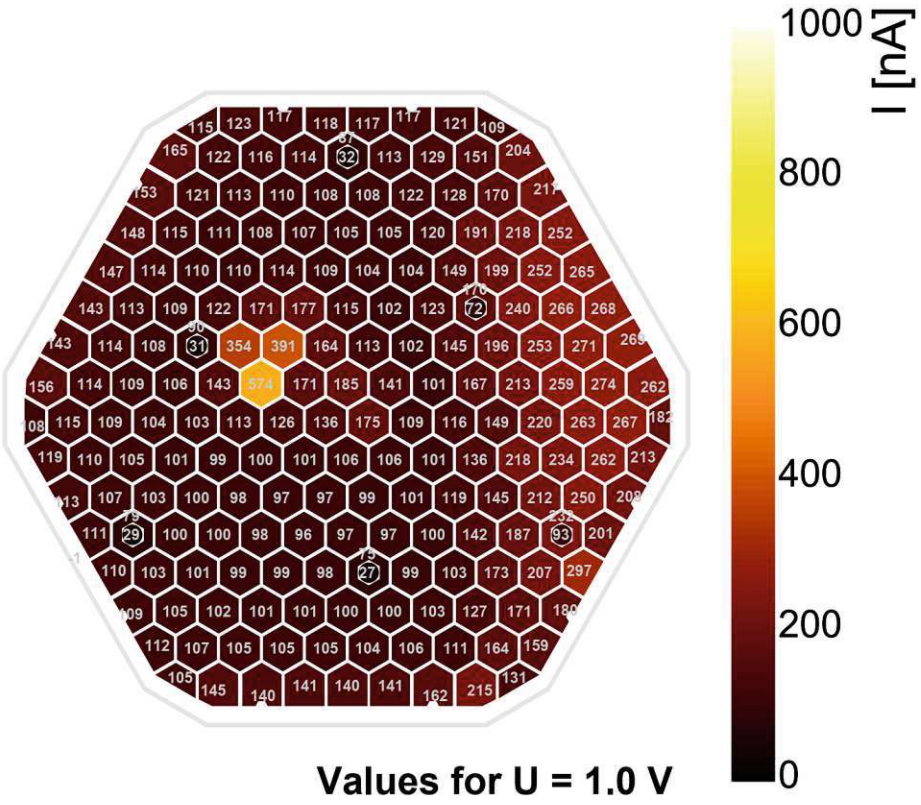

Figure 6.16: Test results on pogo pin contacting, specimen 1013 (300 µm, float-zone, individual p-stop, standard p-stop concentration, and standard oxide). Testing in the forward direction ensures that all cells have good electrical contact with the switchcard via the pogo pins. Each cell's forward current (nA) is measured at a voltage of 1 V. All cells had sufficient contact in this sample, and there were no breakdowns in the forward direction. It should be added that this measurement does not provide any conclusions about any defective cells in the reverse direction.

Table 6.2: This table presents an overview of the tested sensor prototypes (2019 batch). The quality criteria, according to Table 6.1, are applied. The table cell is colored green or red depending on a pass or fail. The last two columns are not hard quality criteria, so there is no limit for the number of cells. According to the HGCAL quality criteria, out of 11 sensors, only four passed completely (yield 36 %), while six failed (reject 54 %). One sensor was just above two criteria, which gave it a "partially passed". All sensors had standard oxide type. The max bias voltage was determined without voltage correction and unscaled, where $I_{\text{tot}} < 1\,\text{mA}$. The total current at 600 V, I_{600}, was scaled to 20 °C.

IV grading	no.	p-stop geo	d_{ac}	U_{fb}	p-st con.	proc.	max bias	total I_{600} < 100 µA	total $\frac{I_{800}}{I_{600}}$ < 2.5	cells I_{600} > 100 nA	cells where $\frac{I_{800}}{I_{600}}$ > 2.5 max 8 cells	> 2 neigh. bad	cells I_{600} > 10 nA	cells I_{600} >1 nA
			(µm)	(V)			(V)	(µA)						
failed	1005	ind.	300	-5	2.5	FZ	100							
failed	1006	ind.	300	-5	5.0	FZ	50							
passed	1013	ind.	300	-2	1.0	FZ	1000	0.21	1.57	0	0	0	1	191
passed	1014	ind.	300	-5	1.0	MCz	1000	0.32	1.25	0	0	0	GR	172
failed	1105	com.	300	-5	1.0	FZ	500							
failed	1106	com.	300	-5	2.5	FZ	500							
failed	1107	com.	300	-5	5.0	FZ	75							
failed	1114	com.	300	-2	1.0	FZ	800	407	1.47	85	0	failed	194	194
passed	2004	ind.	200	-5	1.0	FZ	1000	0.59	1.50	0	0	0	GR	196+GR
partially	2105	com.	200	-5	1.0	FZ	900	2.14	2.88	3	12	0	18+GR	198+GR
passed	2114	com.	200	-2	1.0	FZ	1000	0.34	1.49	0	0	0	GR	196+GR

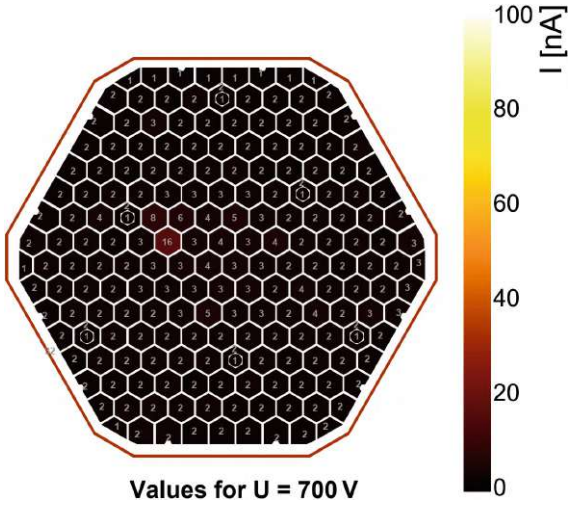

(a) Cell number 86 shows a slightly higher current but within tolerance.

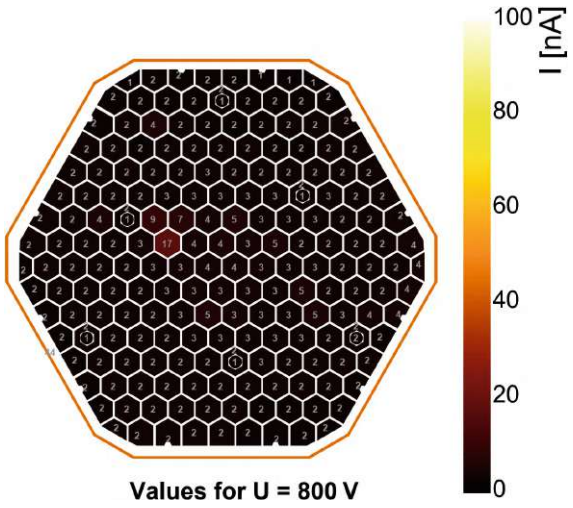

(b) No qualitative differences from the previous voltage step.

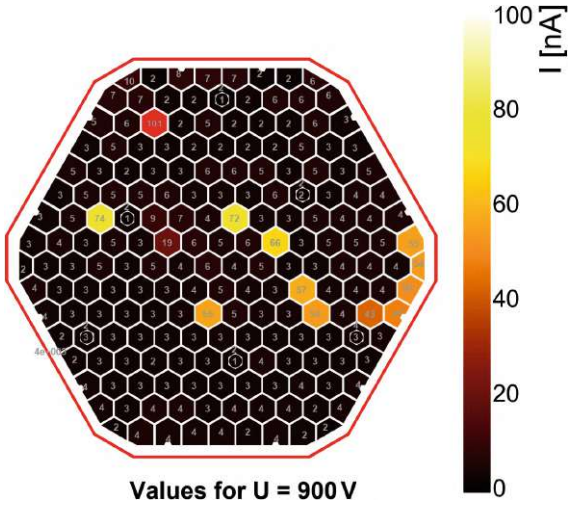

(c) The breakdown begins to develop, and individual, previously inconspicuous cells rise rapidly in the current. At the same time, the current in the guard ring increases.

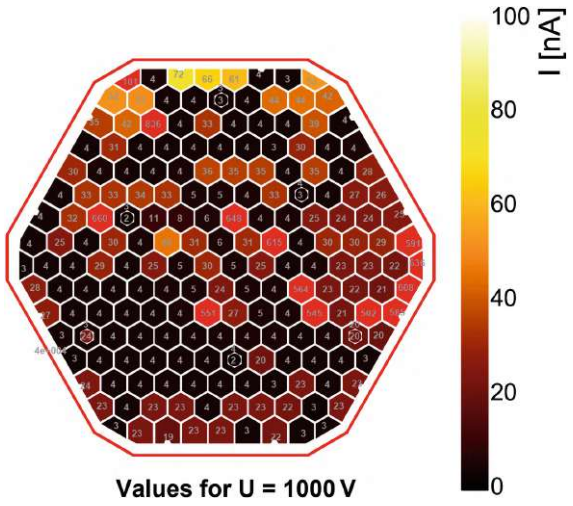

(d) Now cells adjacent to the breakdown cells also increase strongly in current. The guard ring current is 10x larger than in the previous voltage step.

Figure 6.17: Development of a late voltage breakdown of the sensor prototype 1014 (2019 prototypes batch) in the range from 700 V to 1000 V. This measurement was performed using the frontside bias concept. The characteristics of the sensor are an active thickness of 300 µm, p-stop individual, −5 V flat ban-d voltage, with standard p-stop and standard oxide concentration. This sensor was the only one available of Magnetic Czochralski (MCz) processing.

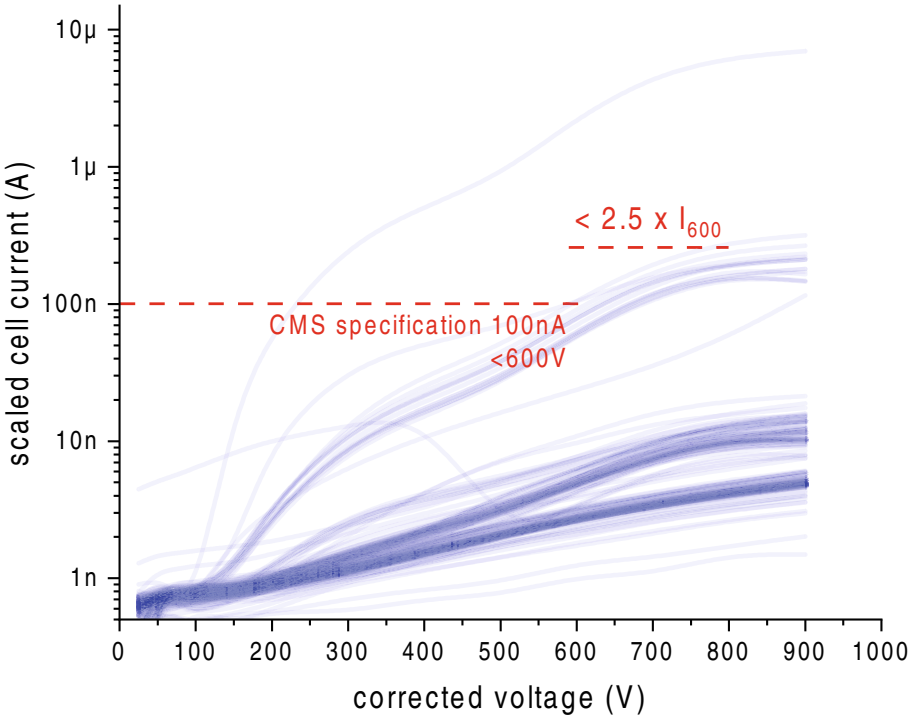

Figure 6.18: Curve plot of all cell currents of sensor 2105, 20 °C. This sensor was qualified as "partially passed" because it only slightly overlaps two quality criteria (see Table 6.1). From this set of curves, the careful observer can see that while the majority of cells are below the <100 nA criterion, one cell is clearly above it, and two cells very slightly exceed the limit. One of the cells that passes the <100 nA limit at 600 V fails at the second limit, where the current at 800 V may be no more than 2.5 times the current at 600 V. The currents of the defect-free cells split into bands because not all cells have the same size: The full cells in the center have the largest area (and therefore the largest current), and the cells at the edge and in the corners are smaller, therefore, have a smaller current. B-splines interpolate the areas between the measurement points for more convenient viewing of the curves. Two examples of other IV-curve arrays are in the Appendix A.5 and A.6.

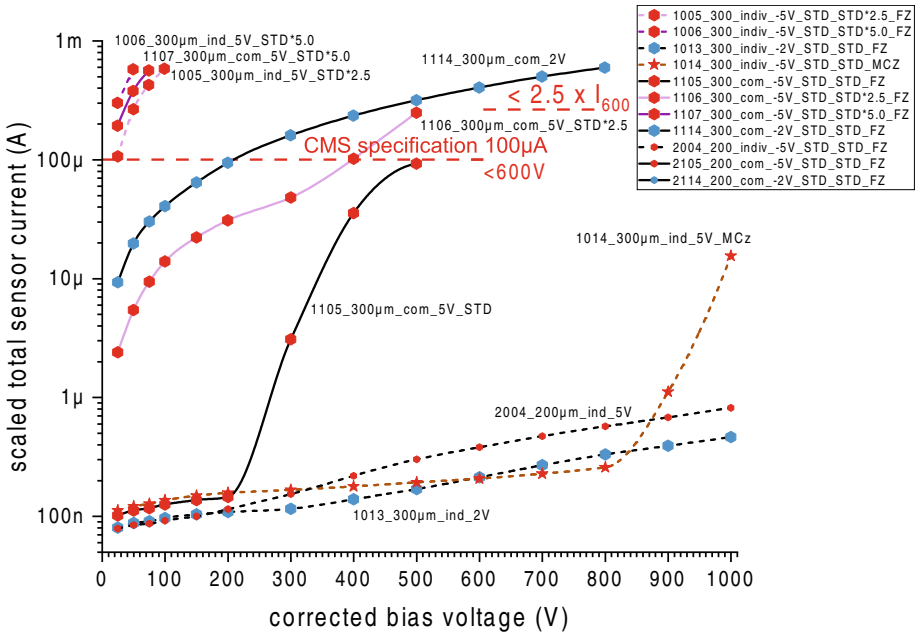

Figure 6.19: Results of all measured total sensor currents of the prototypes (design of 2019) over increasing bias voltage, scaled to 20 °C. Nominal voltage was applied to the sensors up to 1000 V, and according to Equation 6.2, the nominal voltage was corrected by the voltage drop across the series resistor to obtain the actual voltage applied to the sensor. 300 µm (1000-series, large symbols) and 200 µm (2000-series, small symbols) thick sensors were measured. Sensors with common p-stop geometry are shown in solid lines, and those with individual p-stop with dashed lines. −2 V flatband voltage is indicated with blue symbols, −5 V with red symbol. The standard p-stop doping concentration is shown with black lines and the others (2.0 and 5.0) with pink lines. There is one sensor that was not manufactured in Float-Zone processing (FZ, Section 3.3.1), but in Magnetic Czochralski (MCz, Section 3.3.1). This sensor is shown with a brown line and a star symbol. The quality criterion for total sensor current is maximum 100 µA up to 600 V bias voltage, indicated by the horizontal red dashed line. This limit was exceeded by all sensors with increased p-stop doping concentration (1005, 1006, 1007, 1106) and by two sensors with standard concentration (1105 due early breakdown, and 1114). All other sensors passed this test, but some failed other extended quality criteria. The results are summarized in Table 6.2.

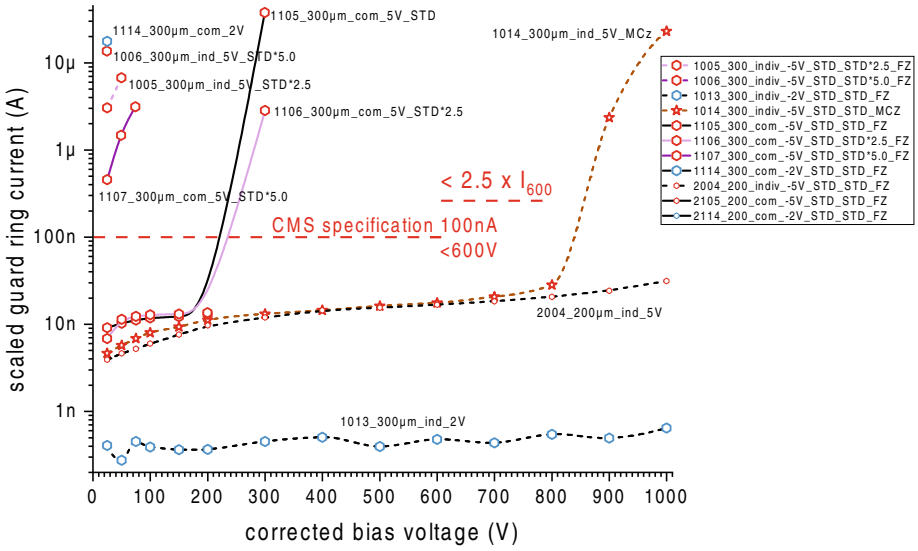

Figure 6.20: Results of all measured guard ring currents of the prototypes (design of 2019) over increasing bias voltage, equivalent to the measurement of the total currents in Figure 6.19. All currents are scaled to 20 °C Nominal voltage was applied to the sensors up to 1000 V, and according to Equation 6.2, the nominal voltage was corrected by the voltage drop across the series resistor to obtain the actual voltage applied to the sensor. 300 µm (1000-series, large symbols) and 200 µm (2000-series, small symbols) thick sensors were measured. Sensors with common p-stop geometry are shown in solid lines, and those with individual p-stop with dashed lines. −2 V flatband voltage is indicated with blue symbols, −5 V with red symbols. The standard p-stop doping concentration is shown with black lines and the others (2.0 and 5.0) with pink lines. There is one sensor that was not manufactured in Float-Zone processing (FZ, Section 3.3.1), but in Magnetic Czochralski (MCz, Section 3.3.1). This sensor is shown with a brown line and a star symbol. The quality criterion for guard ring current is maximum 100 nA up to 600 V bias voltage, indicated by the horizontal red dashed line. This limit was again exceeded by all sensors with increased p-stop doping concentration (1005, 1006, 1007, 1106) and by two sensors with standard concentration (1105, 1114). All other sensors passed this test, but some failed other extended quality criteria. The results are summarized in Table 6.2.

The IV measurements showed a similar, apparent pattern of cells breaking down prematurely on four sensors shortly before the typical large-area voltage breakdown (see Figure 6.21). All these sensors are 300 µm thick; otherwise, they differ in processing. These observations indicate a common cause in a process step, discussed with the supplier according to the Sensor Quality Control scheme (SQC, see Section 6.1), and contribute to improving sensor quality.

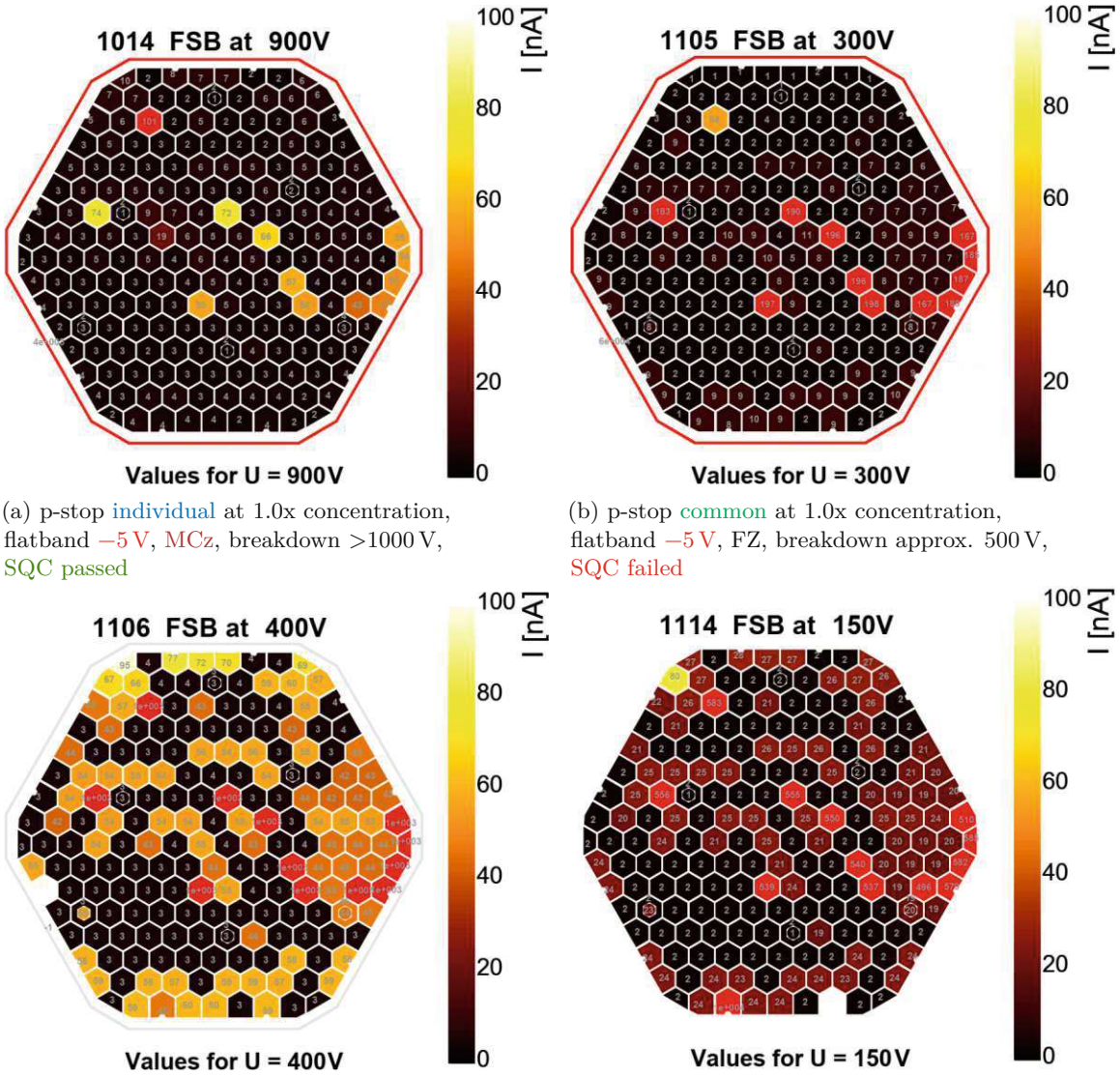

(a) p-stop individual at 1.0x concentration, flatband −5 V, MCz, breakdown >1000 V, SQC passed

(b) p-stop common at 1.0x concentration, flatband −5 V, FZ, breakdown approx. 500 V, SQC failed

(c) p-stop common at 2.5x concentration, flatband −5 V, FZ, breakdown approx. 500 V, SQC failed

(d) p-stop common at 1.0x concentration, flatband −2 V, FZ, breakdown approx. 800 V, SQC failed

Figure 6.21: This collection of plots of four full sensors at different bias voltages shows a similar pattern on cells with high currents. This pattern can be observed particularly well on plots (a) and (b), but on closer inspection, the careful observer will also find it on plots (c) and (d). All these sensors are 300 µm thick but were otherwise manufactured with different processing variants.

Of these sensors, only one (number 1014, MCz) passed all quality criteria. This pattern may also be observed on other sensors but is not perceptible in these measurements. The reason for this is that the applied voltage steps for the sensors are 50 V or 100 V, but this premature appearance of the characteristic pattern could occur between these steps and fade into the background noise of the large-area breakdown of the sensor at the next higher voltage step: One can see the typical development of a large-area breakdown in Figure 6.17. It would have been possible to select smaller voltage steps, but this would significantly increase the measurement time required for a sensor.

6.3.4 Sensor backside protection

The backside of the sensors with the thin p++ implantation (see Figure 3.5) is sensitive to scratches, as shown in [61]. For this reason, HEPHY assembled a Teflon chuck (see Figure 6.22a), which also provides the possibility to hold a protective rubber mat. It is also possible to place sensors that have not yet been diced directly on the chuck together with the dicing frame; see Figure 6.22b. However, these insulating materials make biasing via the backside impossible. Therefore, the author developed and tested [61] a frontside biasing concept, see Section 5.3. There were no discrepancies regarding electrical properties between backside and frontside biasing, so the author views the concept as qualified.

(a) (b)

Figure 6.22: Teflon chuck and dicing frame on the HGCAL test station at HEPHY.

6.3.5 High voltage stability

In an earlier irradiation study (2019, for the later one see Section 6.5) there was a full sensor (number Z3415_06, 300 µm, p-stop common) that was irradiated at the RINSC with a fluence almost 2.5 times higher than planned: $1.23 \times 10^{15}\,\mathrm{cm}^{-2}$ instead of $5 \times 10^{14}\,\mathrm{cm}^{-2}$. It was annealed for about one week (approx. 170 h) at room temperature 22 °C.
This fluence overshoot was used to test the high-voltage resistance. At this high fluence and annealing time in the reverse annealing region, the full depletion voltage U_{fd} was expected to be more than 1.3 kV. The tests showed a creeping breakdown at 1.2 kV when the power supply went into compliance at 50 mA.
The sensor was then biased again and now showed the 50 mA compliance already at 500 V. The reduced breakdown voltage was the first indication of permanent damage caused by a high-voltage breakdown. The examinations under the confocal laser microscope[e] showed burn marks on several regions:

- From the sensor edge to the edge ring, see Figure 6.23a
- From the edge ring to the guard ring, see Figure 6.23b
- From the guard ring to the cells 9, 28, and 190, see Figures 6.23c and 6.23d

These findings suggest a multi-stage breakdown, from the sensor edge via the edge ring onto the guard ring and from these on to the individual cells, which corresponds precisely to the course of the high voltage on the sensor edge to the cells at ground potential. Based on this experience, the sensor design for the next prototype was improved to eliminate these weak points affecting high voltage stability.

[e] Leica DCM8

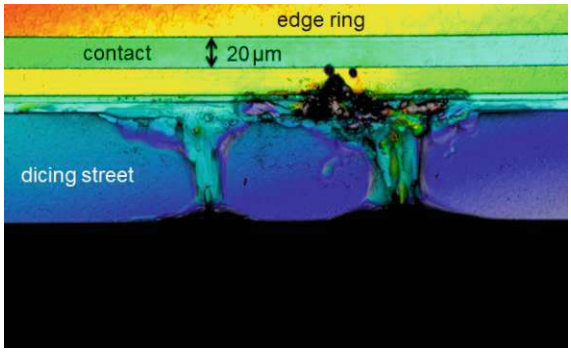

(a) Burn mark from the sensor edge (chuck) to the edge ring

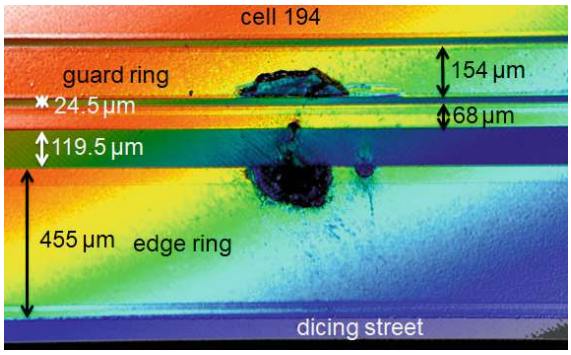

(b) Burn mark from the edge ring to the guard ring

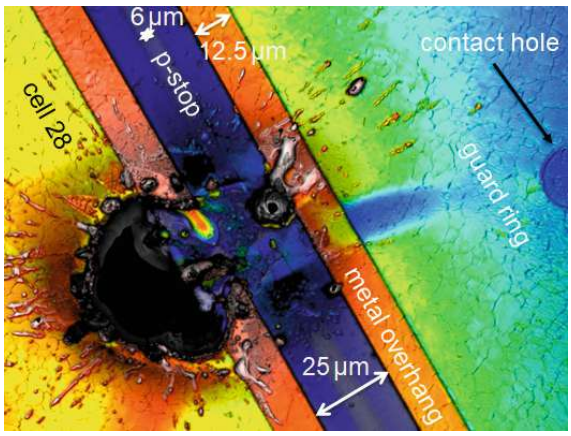

(c) Burn mark from the guard ring to cell 28

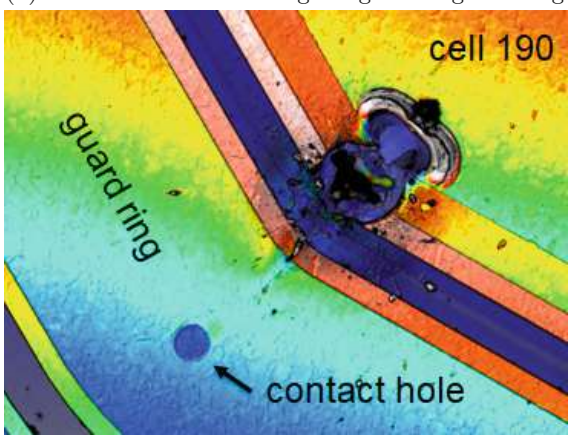

(d) Burn mark from the guard ring to cell 190

Figure 6.23: Burn marks on different sensor regions. Burn marks on different sensor regions caused by a high voltage breakdown at 1.2 kV. The sensor number is Z3415_06 (early prototype), 300 µm, p-stop common irradiated by $1.23 \times 10^{15}\,\mathrm{cm}^{-2}$ and annealed for approx. 170 h. Images taken by Leica DCM8 [48] confocal laser microscope.

6.4 Test structures

6.4.1 Ministrip sensor concept

The Ministrip test structures provide an idealized test environment for electrical measurements. Their size makes them easy to handle, fit into all irradiation equipment used, and the low currents resulting from their tiny dimensions make measurements less complicated compared to the large-area, full HGCAL sensors on 8-inch wafers.
Electrical measurements were made in the form of current-voltage sizes, capacitance-voltage measurements, and interstrip measurements (capacitance and resistance). The direct quantities mentioned above were analyzed, but also derived quantities such as the damage function (see Section 4.2.1, full depletion voltage, electrical fields, effective doping concentrations, charge carrier mobilities, and bulk resistivities.
For a complete list of all 76 Ministrip sensors measured (unirradiated and irradiated), refer to the Annex A.1.

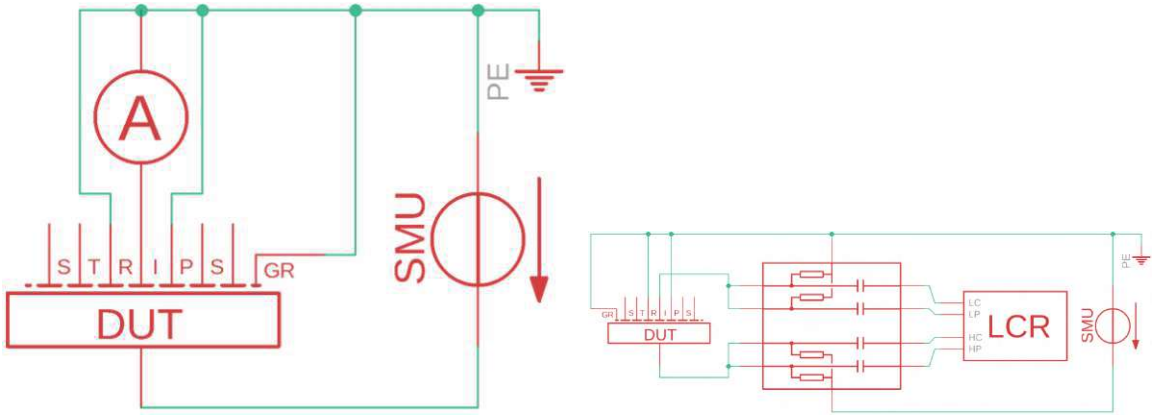

(a) Single strip current measurements.
An electrometer (denoted as "A") measures the current through a single strip. The current measurements are more robust than the capacitance measurements.

(b) Single strip capacitance measurements.
A LCR[g] meter measures the capacitance of a single strip. The LCR meter is decoupled from high voltage by a decouple box (red square in the middle).

Figure 6.24: Schematics of the setups for single strip measurements of the Ministrip sensors. The Ministrip sensor is denoted as "DUT", [e]. A SMU[f] supplies the bias voltage. Both neighboring strips to the measured strip, as well as the guard ring, are directly connected to ground potential.

6.4.2 Electrical characterization of unirradiated Ministrip sensors

Before and parallel to the irradiation studies, the Ministrip sensors were also tested without irradiation. On the one hand, this is important to establish comparability with the irradiated Ministrip sensors. On the other hand, it is significantly faster to measure the non-irradiated sensors because cooling is not necessary, see Section 6.3.2. Therefore, a total of 76 sensors could be measured; for a list of their properties, see Appendix A.1. Current-voltage characteristics (IV, see Figure 6.24a), capacitance-voltage characteristics (CV, see Figure 6.24b), and the interstrip properties (see Figure 6.26) were measured at random.
The focus of this paper is on IV and CV measurements. For the IV measurements, the author used the CMS specifications (see Table 6.1), the author defined a maximum permissible current density $i = \frac{I_{\max}}{A_{\mathrm{SD}} \cdot d_{300}}$, with i the current density, $I_{\max}$ the maximum permissible cell current of 100 nA, A_{SD} the area of an SD cell, and d_{300} the thickness of the 300 µm sensors. This choice of parameters results in an upper bound for the current density. To simplify the evaluation, the author has defined here that no Sensor may exceed this current.
Figure 6.27 shows a set of curves of the strip currents of three exemplary Ministrip sensors. Qualitatively, those with higher currents show the typical diode characteristic in the reverse direction. One

[e]DUT: device under test
[f]SMU: source measurement unit
[g]LCR: inductance (L), capacitance (C) and resistance (R) measuring device

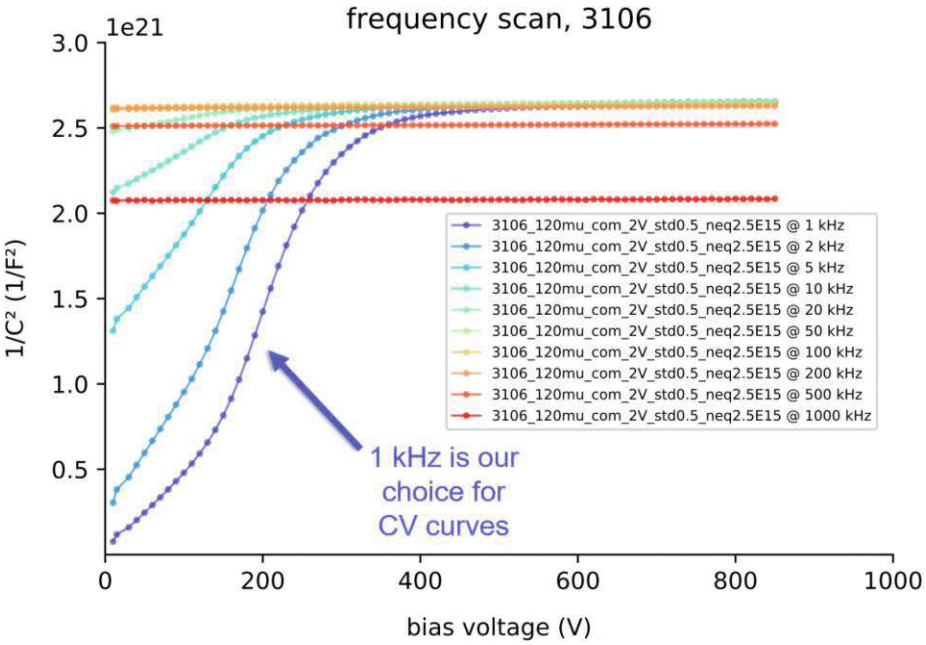

Figure 6.25: To determine the optimum frequency at which the capacitance determination of the Ministrip sensors should take place, we measured C^{-2}/U curves of sensor 3106 at various frequencies. As shown in this figure, we decided to use 1 kHz for the following measurements since the effects of the propagation of the full depletion zone were most clearly visible here. This resulted in the most reliable determination of full depletion.

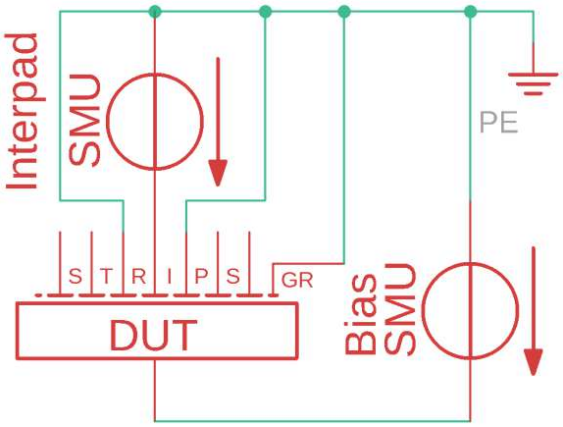

(a) Interstrip resistance measurements. Three adjacent strips, as well as the guard ring, are connected to ground potential. An additional voltage is applied to the middle strip via an SMU[f], resulting in a current to the neighboring strips. A second SMU supplies the bias voltage.

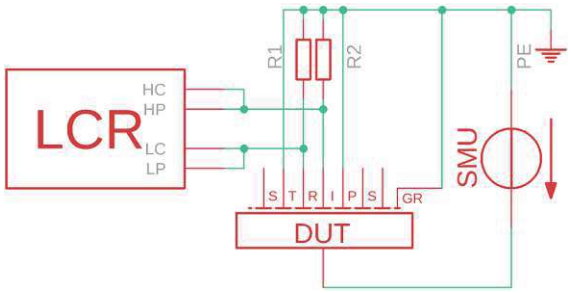

(b) Interstrip capacitance measurements. Four adjacent strips, as well as the guard ring, are connected to ground potential. The two middle strips are connected to an LCR[g] meter, which is protected by resistors R1 and R2. An SMU[f] supplies the bias voltage.

Figure 6.26: Schematics of the setups for interstrip measurements of the Ministrip sensors. The Ministrip sensor is denoted as "DUT"[e].

sensor has quite low strip currents in the lower pA range, which is close to the achievable accuracy of the measurement setup. Therefore, This measurement is quite noisy initially but then shows a qualitatively cleaner curve towards higher bias voltages. The currents are about one or more orders of magnitude below the limit the author defines.
In contrast to the full sensors, the maximum tolerable limit for the currents of the full sensors is not defined for the Ministrip sensors due to their different geometry. The corresponding plot is found in the Annex A.7.

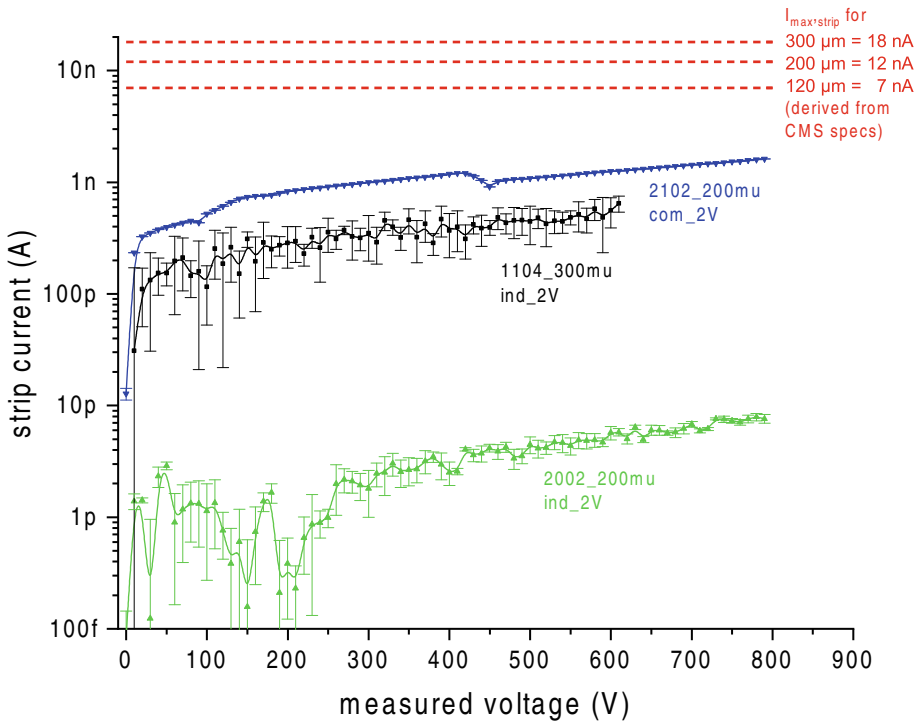

Figure 6.27: Sample of single strip currents of the unirradiated Ministrip sensors. The three dashed red lines for the maximum strip currents are derived from the CMS specifications via the maximum tolerable current density and are not binding. They are only used to estimate the quality of the respective sensors. The currents at low voltages appear noisy because, on the one hand, the system settles slowly (rapid and extensive changes in the electrical field configuration take place in the lower voltage range). At low sensor currents in the lower pA range, the lower limit of the accuracy of the electrical measurement setup becomes visible. The only decisive factor here is that there are several orders of magnitude below the maximum tolerable strip currents.

The bulk capacitance measurements of the non-irradiated Ministrip sensors showed some anomalies in five specimens (1007, 1108, 2006, 2108, 2109), see Figure 6.28. Some sensors did not follow the expected steady drop in capacitance with the point of highest curvature at full depletion voltage (for description, see Section 2.2.1, for expected values, see Annex A.6), these were numbers 1007 and 2109. The sensors 2006 and 2108 reached the full depletion voltage too late, while 1108 with 3.8 pF had a significantly higher final capacitance than the other 300 µm sensors, which are on average at 2.15 pF. This final capacitance is 1.8 times higher. The properties of the five peculiar sensors are:

- **1007**: 300 µm, p-stop individual, −5 V U_{fb}, standard p-stop conc., oxide Type A
- **1108**: 300 µm, p-stop common, −5 V U_{fb}, standard p-stop conc., oxide Type A
- **2006**: 200 µm, p-stop individual, −5 V U_{fb}, 5x p-stop conc., standard oxide
- **2108**: 200 µm, p-stop common, −5 V U_{fb}, standard p-stop conc., oxide Type A
- **2109**: 200 µm, p-stop common, −5 V U_{fb}, standard p-stop conc., oxide Type B

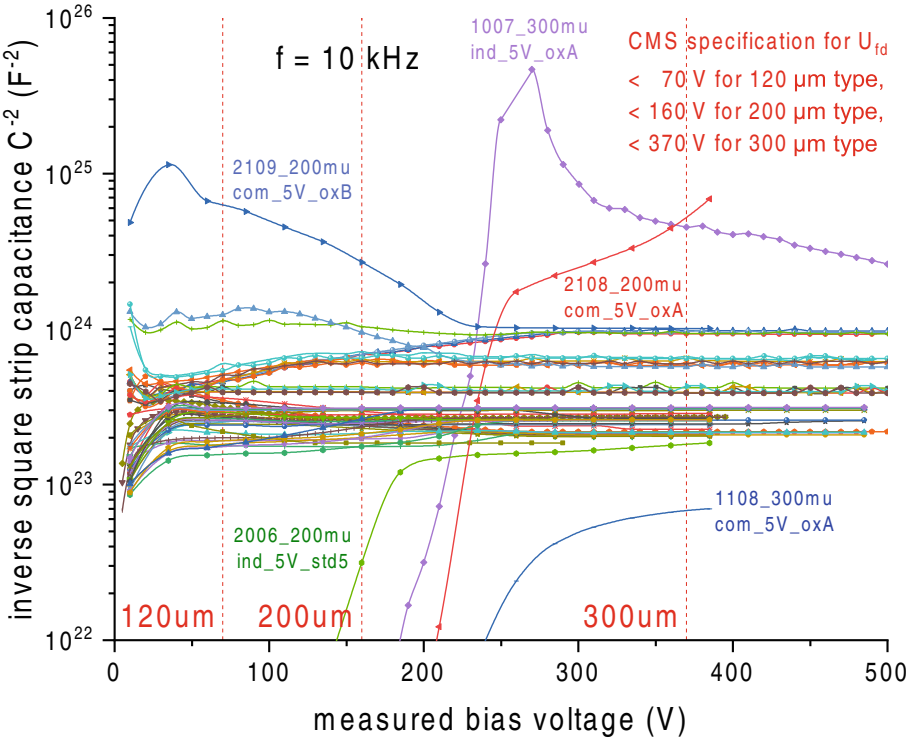

Figure 6.28: Capacitance of unirradiated Ministrip sensors. This plot graphs the inverse square capacitance (see Equation 2.6) because the capacitance increase up to the full depletion voltage can be traced as a linear increase. For most sensors that can be evaluated, even the thicker ones, the full depletion voltage is below 70 V, which is within the specification of CMS. However, as can be seen here, the qualitative progressions of the curves do not always follow the increase with subsequent constant region after the full depletion voltage expected from theory. For such sensors, the full depletion voltage cannot be determined without doubt using this method. The frequency used for measuring the capacitance was 10 kHz.

According to Equation 2.4, for a given sensor, U_{fd} is approximately proportional to effective space charge N_{eff}, according to:

$$U_{\text{fd}} = \frac{q|N_{\text{eff}}|d^2}{2\epsilon_{\text{Si}}\epsilon_0} \tag{6.3}$$

whereas d is the sensor thickness, q is the elementary charge, ϵ_{Si} is the relative permittivity of silicon, and ϵ_0 is the vacuum permittivity, values from Table 6.3. By converting the equation to the effective space charge N_{eff}, this can be approximated from the full depletion voltage U_{fd}. For a more sophisticated and more precise model, refer to [4], but the approximation above only differs by less than 0.05 % in the relevant temperature range of −30 to 30 °C.

Table 6.3: Parameters for the calculation of the effective doping concentration N_{eff}. All parameters and calculations were done in SI units.

Parameter	symbol	value
elementary charge	q	$1.602 \times 10^{-19}\,\text{C}$
vacuum permittivity	ϵ_0	$8.854 \times 10^{-12}\,\text{F m}^{-1}$
relative permittivity of silicon	ϵ_{Si}	11.68

Figure 6.29 shows the results of the calculated effective doping concentrations N_{eff} split down by active sensor thickness and processing. It shows a large scatter of results in a range of 5.74×10^{11} to $4.27 \times 10^{12}\,\text{cm}^{-3}$, with only the median of 200 µm Ministrip sensors with $1.45 \times 10^{12}\,\text{cm}^{-3}$ close to the SRP measurements (Section 6.2.1) of $1.38 \pm 0.02 \times 10^{12}\,\text{cm}^{-3}$ (Figure 6.3). The author trusts the SRP more since determining the full depletion voltage employing a two straight lines fit is not always successful, and many CV curves show an anomalous course. They are, therefore, not included in the calculation. Furthermore, with this measurement method, it is difficult to assess whether the space charge region remains limited to the strip under investigation or whether it expands into the neighboring regions or punches through.

Four of the five conspicuous Ministrip sensors also show irregularities:
The interstrip measurements (capacitance vs. bias voltage and resistance vs. bias voltage) are eligible for finding early problems with individual process variations, especially concerning the oxide layers (see Section 6.1). These process variations should influence the interpad properties. However, no correlation could be found through these measurements, as almost all sensors behaved similarly, regardless of their process variation, and there were only a few outliers. These, in turn, could not be systematically assigned to a specific process variation. The corresponding plots are in the Annex under Figure A.10 and Figure A.13. Further studies on the interpad/interstrip properties are required to optimize these process parameters, with separate irradiation studies on the oxide layers. However, the same four Ministrip sensors (1007, 1108, 2006, 2108) show peculiarities in both measurement methods.

6.5 Annealing studies of irradiated Ministrip sensors

Parallel to the irradiations of the full sensors, the Ministrip sensors were also irradiated. Concerning the irradiations with neutrons in the reactor, the Ministrip sensors also have advantages for the measuring apparatus (see the following paragraph). Another practical advantage: The small dimensions. While the 8-inch sensors could only be irradiated at the RINSC reactor[h], as this was the only one with an irradiation tube large enough for these sensors, the Ministrip sensors can also be irradiated in other reactors, such as the TRIGA reactors[i]. This shortens the transport distances, thus making it easier to ensure proper cooling of the irradiated sensors, and is, of course, also a cost factor.

The irradiated Ministrip sensors were used for the annealing studies because their current consumption was decisively lower than the large-area full sensors (see Section 5.7). Also, their

[h] Rhode Island Nuclear Science Center reactor [65], 2 MW thermal power, Rhode Island, USA
[i] TRIGA Mark II, 250 kW thermal power, from the Atominstitut [77] of the Vienna University of Technology and the Institute "Jožef Stefan" [72] in Ljubljana, Slovenia.

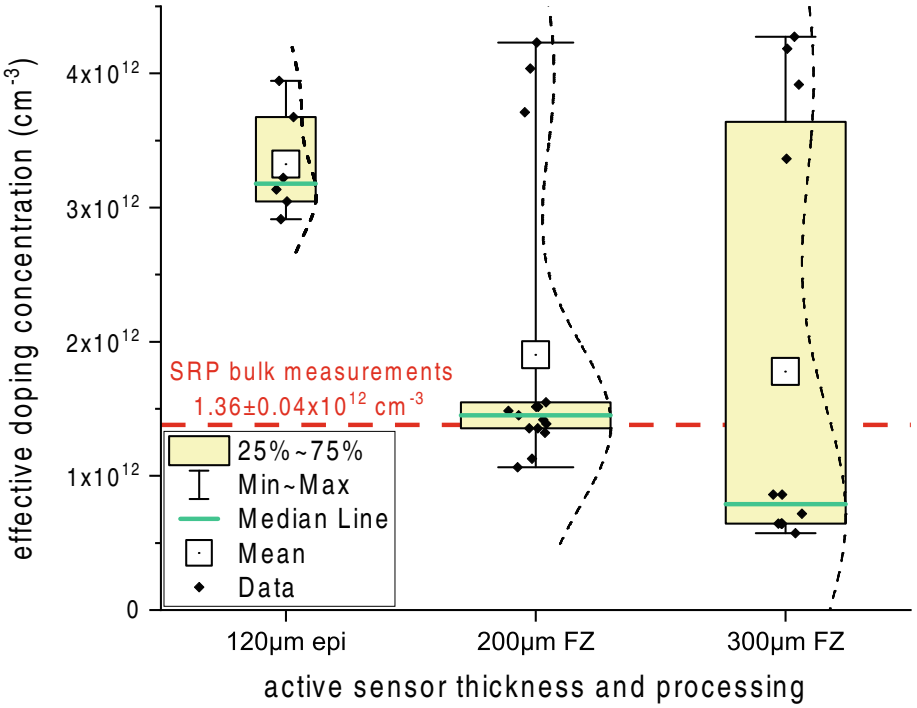

Figure 6.29: N_{eff} determined from full depletion voltage U_{fd} of the unirradiated Ministrip sensors. This boxplot illustrates the results for the respective processings (epi and FZ) and active sensor thicknesses (120 µm, 200 µm, and 300 µm). The data points are the black diamonds. The beige box indicates the percentiles 25 to 75 %, the whiskers the minima and maxima. The green line expresses the median, and the small white box with a dot stands for the arithmetic mean. In addition, weighted moving average fits are placed over the distributions, indicated by the vertical dashed lines. For comparison, the result of the SRP measurement of the bulk is visible as a dashed, horizontal, red line at $1.38 \pm 0.02 \times 10^{12}\,\text{cm}^{-3}$. The uncertainty is the standard deviation, the measurement series ranges from depths of 0.25 to 3.4 µm. One can see that only the 200 µm FZ Ministrips with a median of $1.45 \times 10^{12}\,\text{cm}^{-3}$ are close to the value determined using SRP, the 300 µm FZ are already slightly below it. The fact that the 120 µm epi sensors have a significantly higher doping concentration with a median of $1.36 \pm 0.04 \times 10^{12}\,\text{cm}^{-3}$ can be explained by the different processing (higher doping!) of the epitaxial process used. This plot only shows the Ministrip sensors that show a typical $1/C^2$ curve and where the fit of the two-straight line method worked. The author declared all others as not determinable by this measurement method.

Table 6.4: Properties of Ministrip sensors used in annealing studies. It is important to note that not all sensors reached the full depletion voltage at all annealing times. In addition, in some cases, the measured data was too noisy or showed irregular behavior. These inconclusive data were excluded.

ID	thickness (µm)	process	oxide type	flatband voltage	p-stop type	p-stop conc.	target fluence Φ ($n_{eq}\,cm^{-2}$)
1003	300	FZ	STD	-2V	individual	STD	1.0×10^{15}
1013	300	FZ	STD	-2V	individual	STD	6.5×10^{14}
1114	300	FZ	STD	-2V	common	STD	6.5×10^{14}
2003	200	FZ	STD	-2V	individual	STD	1.0×10^{15}
2103	200	FZ	STD	-2V	common	STD	1.0×10^{15}
2105	200	FZ	STD	-5V	common	STD	1.0×10^{15}
3103	120	epi	STD	-2V	common	STD	1.0×10^{16}
3107	120	epi	STD	-2V	common	STD	2.5×10^{15}

susceptibility to effective manufacturing defects is lower because of the smaller surface area. This allowed reproducible and extrapolated measurements without accessing the probecard system ("ARRAY" system, see Section 6.3.1). When the data was taken (2020), the electronics of the probecard system were not suitable for the high total sensor currents up to the mA range that occurs at −20 °C. As described in Section 6.3.2, it was not yet reliably possible to achieve lower temperatures so as not to overload the ARRAY's electronics.
Annealing was performed by removing each irradiated Ministrip sensor from the cooling compartment and placing it in a climate chamber at 60 °C for a defined time. The sensors were measured electrically between the heating periods: current-voltage and capacitance-voltage. Annealing steps were performed, each at 60 °C at intervals of 10 or 20 min, up to 160 min. One sensor, number 2103, was measured only at 0 min (unannealed), 80 min, and 160 min.
A second series of measurements was started after my time at HEPHY and included 180 minutes of annealing, 200 min, and 2000 min. These data were not recorded by the author but are included in this thesis to show the further course of the annealing.
Due to the intermediate steps (taking out of the cooling compartment, transport to the measuring station, and return transport) and the resulting heating and cooling times, there is an uncertainty in the determination of the exact annealing time, estimated at 1 min.
The phenomenon of annealing (Chapter 4) was quantified and analyzed in four ways during the measurements:

1. Development of total sensor currents at fixed voltage over the annealing duration.
2. Shift of the full depletion voltage over the annealing duration.
3. Interstrip resistance (one strip to the neighboring two) over the annealing duration.
4. Interstrip capacitance (one strip to the neighboring two) over the annealing duration.

Of all the irradiated Ministrip sensors, annealing studies were performed only on selected ones. The full range of irradiated sensors was not available (because most of them were located at other institutes), and there would not have been time for all of them. An annealing series for a single sensor takes about three days. Table 6.4 gives an overview of all annealed Ministrip sensors and their crucial properties.

6.5.1 Ministrip sensor currents during annealing

The first step to quantify the radiation damage at the crystal lattice (see Chapter 4.2.1) by neutron radiation was the measurement of the Ministrip currents. For this purpose, as shown in Figure 6.24a, the measured strip, its two neighbors, and the guard ring were switched to ground potential, and the sensor backside was connected to the bias voltage. The current through the central stripe, as well as the total current, was measured. Only the strip current was used for the analysis since it represents

Table 6.5: Parameters of the annealing model at relevant annealing times. There is a distinction between the constant annealing parameter α_0, the parameter for long-term annealing α_1, and the parameter for short-term annealing β. The constant t_0 is a fit parameter to calibrate the time to the unit minutes [53].

T (°C)	α_0 ($\mathrm{A\,cm^{-1}}$)	α_1 ($\mathrm{A\,cm^{-1}}$)	β ($\mathrm{A\,cm^{-1}}$)	τ (min)	t_0 (min)
21	7.07×10^{-17}	1.23×10^{-17}	3.29×10^{-18}	14 000	1
60	4.87×10^{-17}	1.26×10^{-17}	3.16×10^{-18}	94	1
80	4.23×10^{-17}	1.13×10^{-17}	2.83×10^{-18}	9	1

a defined system due to the grounding of its two neighbors. Figures 6.30e to 6.30b show the results over several annealing times (dark red to yellow). As known from the literature, the sensor current decreased steadily over the annealing duration.

For further analysis, a defined point, in this case, 800 V, is selected, and the current density (current/volume) is determined. Figure 6.31 shows the results of this normalization, with all measured annealing steps.

Now we want to determine the damage function α. For this, we consider Equation 6.4, which describes the proportionality between bulk damage, the equivalent neutron fluence, and the current density:

$$\begin{aligned} \alpha \Phi_{\mathrm{neq}} V = \Delta I = I_{\mathrm{irrad}} - I_{\mathrm{unirrad}} \approx I_{\mathrm{irrad}} \qquad \text{with} \qquad I_{\mathrm{irrad}} >> I_{\mathrm{unirrad}} \\ \alpha \approx \frac{I_{\mathrm{irrad}}}{\Phi_{\mathrm{neq}} V} \end{aligned} \tag{6.4}$$

whereas I_{unirrad} is the leakage current before, I_{irrad} the leakage current after irradiation, Φ_{neq} the 1 MeV neutron equivalent fluence, V the active detector volume, and α the damage factor, which describes the proportionality between fluence and current increase. Since I_{irrad} is larger than I_{unirrad} by a factor of about 100, the error made by equating $\Delta I \approx I_{\mathrm{irrad}}$ is only about one percent, which is considered negligible for the present work.

The damage function is defined in the publication of M. Moll [54] at 21 °C, but the irradiated sensors were measured at −20 °C. This means that the measured currents must be scaled back to 21 °C according to Equation 2.11 in order to compare them to the literature values. Conversely, therefore, to quantify and assess the effects of radiation damage on the final sensors in the CMS experiment, again, the data has to be scaled to the operating temperature of −30 °C there. Conveniently, the ambient temperature in the cavern of the CMS experiment is also 21 ± 1 °C [58]; therefore, the comparison with the scaled measurement results is possible at a glance.

As described in more detail in Section 4.4, the damage function is given by using the experimentally determined parameters from Table 6.5:

$$\alpha(t, T) = \alpha_0(T) + \alpha_1(T) \cdot \exp\left(\frac{-t}{\tau(T)}\right) - \beta(T) \cdot \ln\left(\frac{t}{t_0}\right) \tag{6.5}$$

In the literature [1][46][53] a standard annealing step of 80 min at 60 °C is usually chosen. The Ministrip data is also available after this annealing step in this work. This results in a value of the damage function α of $2.60 \pm 0.29 \times 10^{-19}\,\mathrm{A\,cm^{-1}}$, see Figure 6.32. This is consistent with literature values that are in the range of $2.34 \pm 0.06 \times 10^{-19}\,\mathrm{A\,cm^{-1}}$ and $2.763 \times 10^{-19}\,\mathrm{A\,cm^{-1}}$, see Figure 4.6.

Determining the damage function alpha fits qualitatively well to the model of M. Moll [53] in the range of beneficial annealing, scaled to 21 °C. The 200 µm sensor fits the prediction best (about 7 % deviation), the 120 µm sensors are about 18 % above, the 300 µm sensors about 18 % below. For the quantitative difference in the beneficial annealing region, the uncertainty of the fluence could play a role and explain the discrepancies. The inaccuracy of the determination of fluence may result from the following uncertainties:

1. The **residence time** of the sensors in the reactor (ATI [77], Ljubljana [72], RINSC [65]) or the opening and closing times of the shutter.

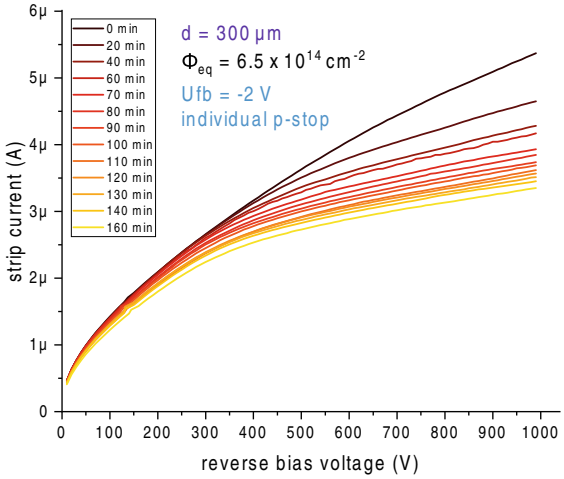

(a) Ministrip sensor number 1013:
300 µm active thickness, float zone processing, −2 V flatband voltage, p-stop individual.
Irradiated with 6.5×10^{14} n_{eq} neutrons.

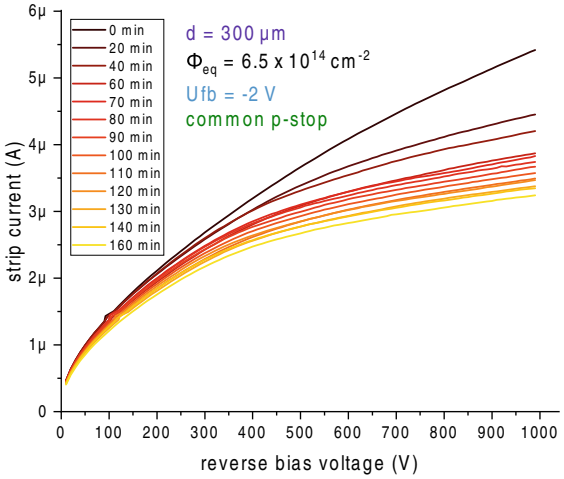

(b) Ministrip sensor number 1114:
300 µm active thickness, float zone processing, −2 V flatband voltage, p-stop common.
Irradiated with 6.5×10^{14} n_{eq} neutrons.

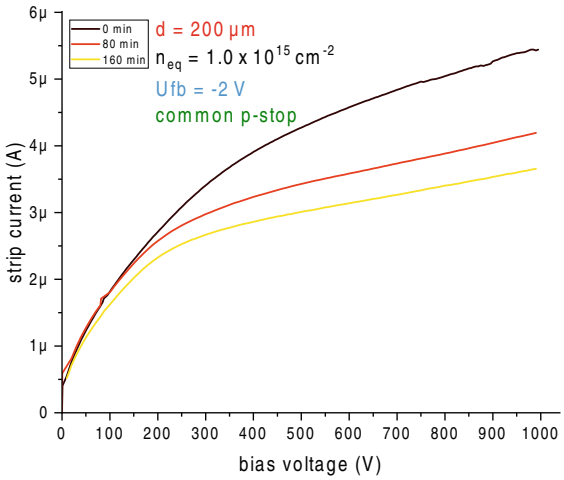

(c) Ministrip sensor number 2103:
200 µm active thickness, float zone processing, −2 V flatband voltage, p-stop common.
Irradiated with 1.0×10^{15} n_{eq} neutrons.

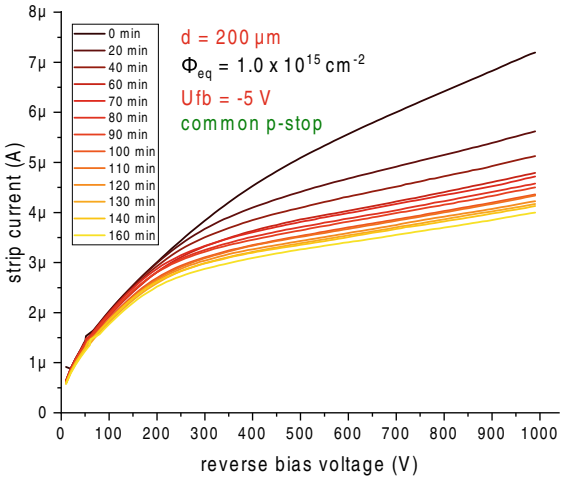

(d) Ministrip sensor number 2105:
200 µm active thickness, float zone processing, −5 V flatband voltage, p-stop common.
Irradiated with 1.0×10^{15} n_{eq} neutrons.

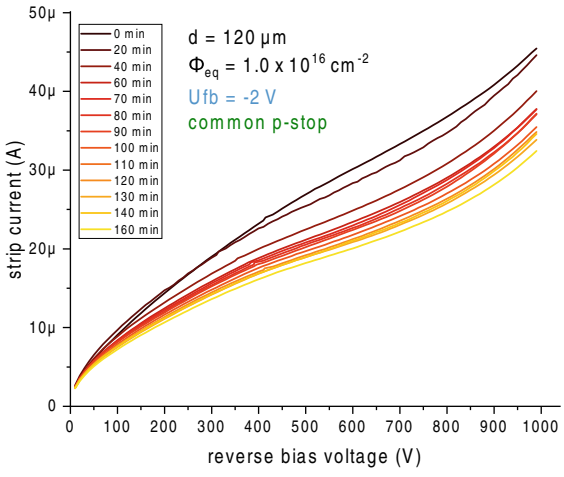

(e) Ministrip sensor number 3103:
120 µm active thickness, epitaxial processing, −2 V flatband voltage, p-stop common.
Irradiated with 1.0×10^{16} n_{eq} neutrons.

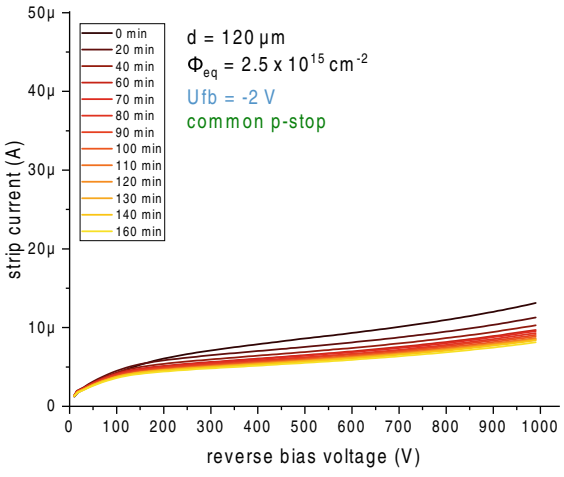

(f) Ministrip sensor number 3107:
120 µm active thickness, epitaxial processing, −2 V flatband voltage, p-stop common.
Irradiated with 2.5×10^{15} n_{eq} neutrons.

Figure 6.30: The IV curves between the annealing steps of the irradiated Ministrip sensors. The measured annealing steps range between 0 min (no annealing) and 160 min. The respective Ministrip sensors with the same active thickness are in the same row and have the same current scale. All the sensors feature standard oxide and standard p-stop concentration.

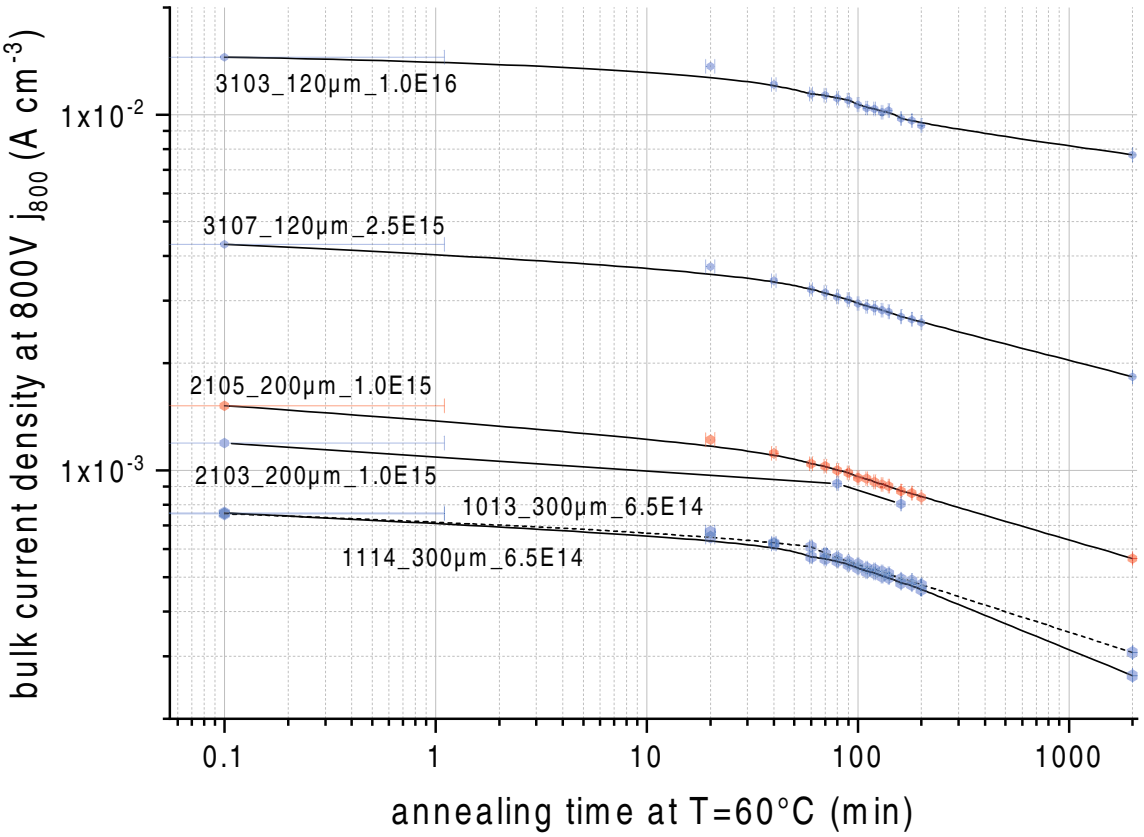

Figure 6.31: Leakage current densities (current per detector volume) of all annealed Ministrip sensors over the respective annealing times. It should be clear that higher fluences lead to higher leakage current densities, according to the NIEL hypothesis (Section 4.3). One can observe how the bulk current density decreases with increasing annealing time. These data feed to calculating the damage function α, see Equation 6.4 and Figure 6.33.

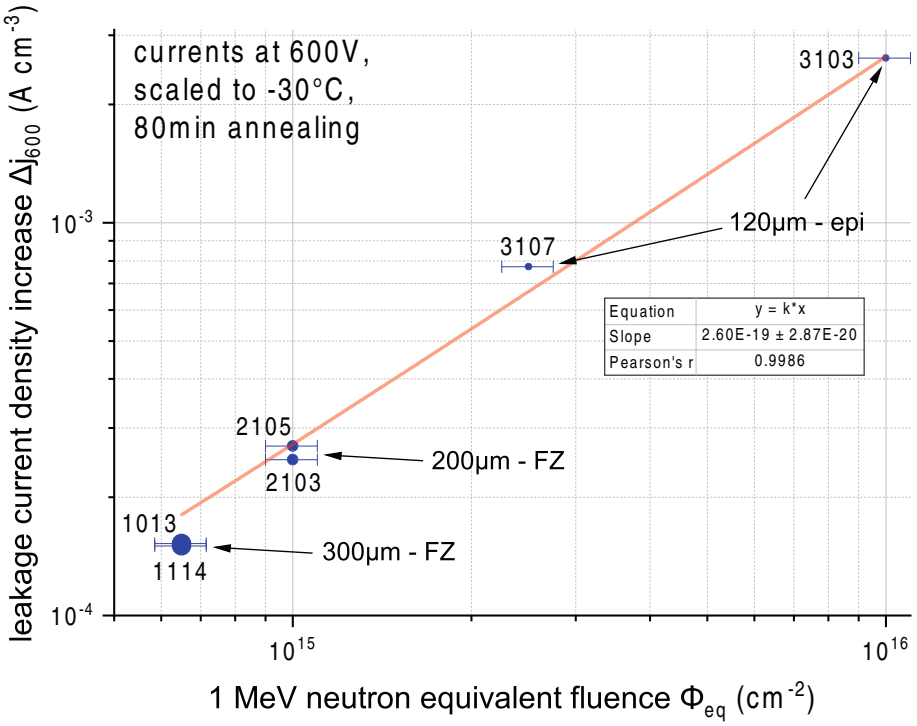

Figure 6.32: Linearity of the Ministrip sensor current density Δj (difference of irradiated to unirradiated sensors) to the neutron fluence normalized to 1 MeV. In contrast to Figure A.15, only data with a standard annealing step (80 min at 60 °C) were included in this plot to provide comparability with literature values [46][54]. Because annealing studies of not all but six 2019 prototype series Ministrips were performed at HEPHY (see Table 6.4), this dataset constrains in contrast to Figure A.15. The large circles represent the 300 µm thick Ministrip sensors, the medium ones represent the 200 µm, and the small ones represent the 120 µm.

2. The **position** of the sensors in the irradiation tube. In the case of lateral irradiation tubes , the neutron flux through the irradiation tube is not homogeneous and can lead to a location-dependent neutron fluence.

3. A foil **dosimeter** measured the dose during irradiation. The dose is proportional to neutron fluence at constant reactor power. This dosimeter is subject to some uncertainty.

4. **Annealing during irradiation**. Although dry ice cooled the sensors during irradiation and an enclosed temperature sensor logged the temperature, it cannot be ruled out with absolute certainty that there were local hot spots. Nevertheless, the author considers this point somewhat hypothetical, given the high-temperature difference between the boiling point of dry ice and the necessary temperatures that would lead to significant annealing.

Points 1 to 3 would lead to a vertical shift of the annealing curves and point 4 to a horizontal shift.

As can be seen in Figure 6.33, the value of the damage function α decreases with increasing annealing time, up to a point at 40 ± 20 min. Then, the damage function decreases faster than before. This behavior corresponds qualitatively to the results from the literature of Moll [53], but there, this kink would only occur at about 2000 min. Therefore the new 8" sensors may show significantly better annealing behavior regarding the current.

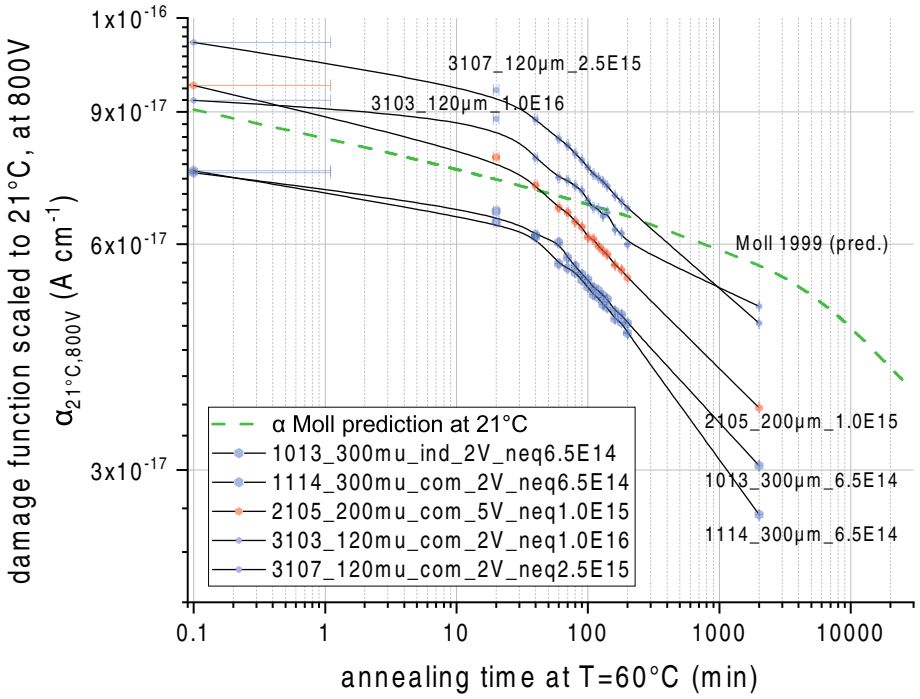

Figure 6.33: Damage function α, temperature scaled to 21 °C at 800 V. The definition of the damage function α (see Equation 4.10) determines a normalization of the sensor current densities to the neutron fluence Φ. Therefore, in contrast to Figure 6.31, the values of the sensors move closer together and form a common band. Within the distribution of this band is the prediction of the radiation damage model of Moll [53] with a deviation of about ± 40 %, at least until the range of about 100 min. After that, the measured sensors show significantly better beneficial annealing than Moll's prediction. One can also observe that a kink in the annealing curves of the measured sensors occurs at about 40 ± 20 min. According to the model assumption, this kink should occur much later, at about 2000 min (green dashed curve).

6.5.2 Ministrip capacitance and full depletion voltage during annealing

To determine the full depletion voltage, it is useful to take the quadratic inverse of the capacitance, since the increase of the capacitance up to the full depletion voltage is then ideally linear, which

results from the Equation 2.6 already derived in Chapter 2.2:

$$\frac{1}{C^2} = \kappa_1 + \kappa_2 V \tag{6.6}$$

which shows the proportionality between $\frac{1}{C^2}$ and V.
Using this transformation, the full depletion voltage can be determined by using following methods: The method of **maximum curvature** and the method of the **intersection of straight lines**.
The **maximum curvature** method takes advantage of the fact that at the full depletion voltage, the growing depletion region "bumps" against the inner end of the bulk of the semiconductor. This means that the change in capacitance slows down. Therefore, the full-depletion voltage can be found by finding the maximum of the first derivative, that is, by setting the second derivative to zero. The disadvantage of this theoretically ideal finding method is that the measured data is discrete and noisy, so it requires filtering and interpolation functions, which has a negative effect on the robustness of the method in general and the fitting in particular.
Due to the geometry of the ideal capacitance/voltage curve, this point can also be found by fitting a straight line into the rising part ($U < U_{\mathrm{fd}}$) where the depletion zone grows towards the other pole, and the constant region where the depletion zone has its maximum extension, and thus, the capacity does not decrease any further, independent of additional increase in voltage ($U > U_{\mathrm{fd}}$), respectively (see Appendix A.16). The intersection point of these two consecutive lines then lies in the area of the full depletion voltage. This **intersection method** was used for the following results because it does not require an interpolation function and is robust.
Now the full depletion voltage after each annealing step was determined (see Figure 6.34) and plotted

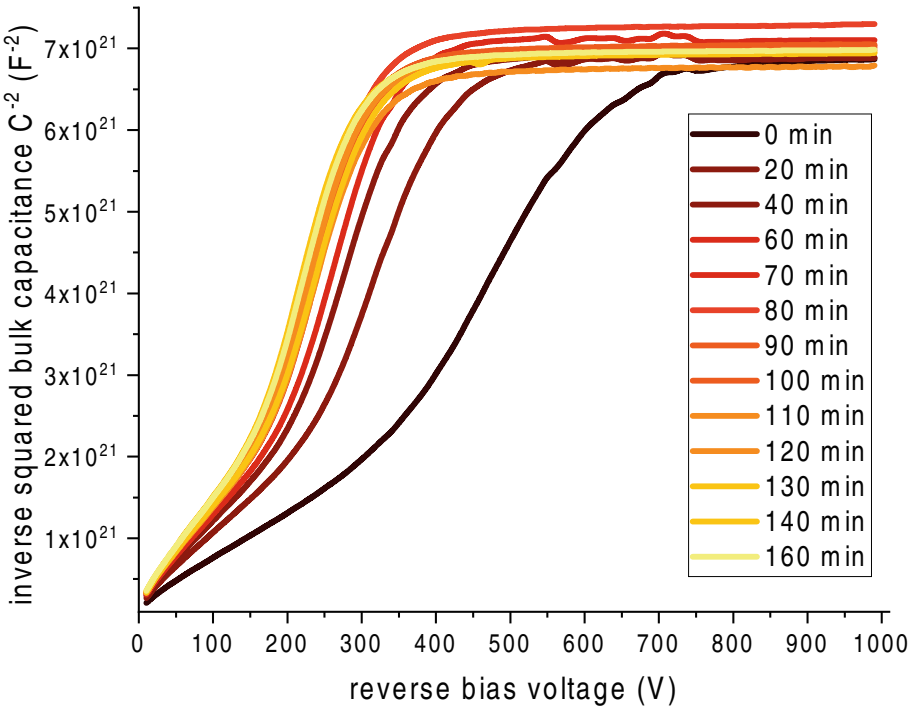

Figure 6.34: Transformed ($1/C^2$) CV curves of a Ministrip sensor over consecutive annealing times: A CV curve was measured at each annealing step. One can see that the capacitance decreases rapidly (increasing from $1/C^2$) until a maximum is reached. This is the point of full depletion voltage. As annealing time increases, the full depletion voltage decreases, indicating beneficial annealing through partial repair of crystal structure damage. The parameters of the Ministrip sensor 2105 are: 200 µm active thickness, float zone processing, −5 V flatband voltage, p-stop common, standard p-stop concentration, and it was irradiated with 10^{15} n_{eq} neutrons.

in an annealing (time-vs-voltage) plot, see Figure 6.35. Of course, the fitting method introduces errors that are accounted for in the plot. In the time dimension, errors result from the warm-up and cool-down times and from the transport of the Ministrip sensors from the freezer to the measurement station. These errors were also taken into account in the plot. The minimum of the full depletion voltage is found in the range of 100 ± 10 min (see Figure 6.35), which is in good agreement with

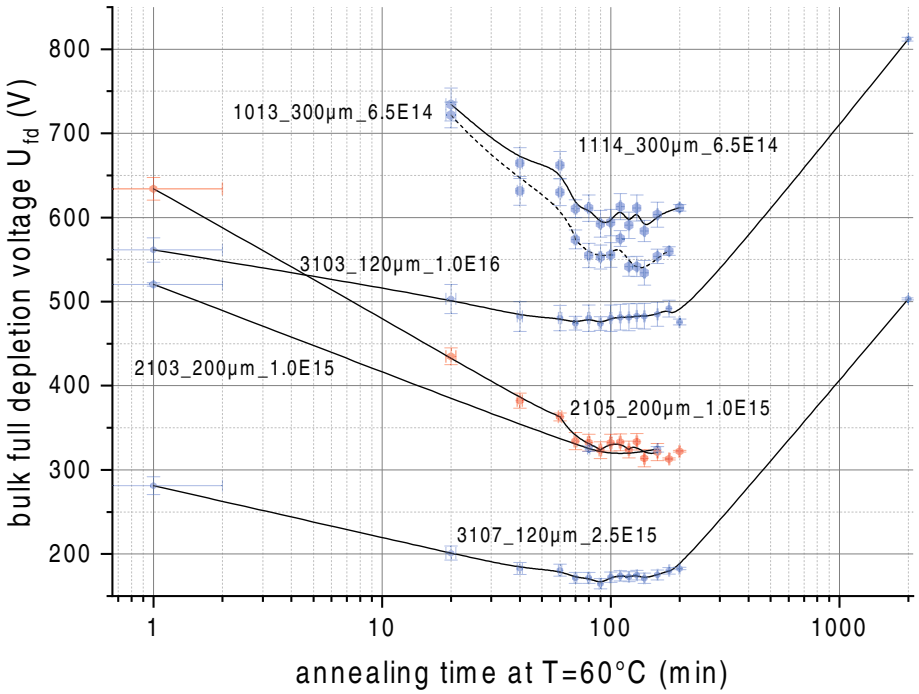

Figure 6.35: This plot shows the extraction of the full depletion voltage U_{fd} from the CV curves. An entire CV curve was measured at each annealing time. The full depletion voltage was determined as the intersection of two straight lines into the rising part and the constant region (see Figure 6.34 and Appendix A.16). The measurement error in the time dimension is determined by the sensors' transport, heating, and cooling times.

comparative measurements of the past, see PhD theses by Axel König [46] and Michael Moll [53]. Since the plot of the full depletion voltage already shows the minimum at 100 ± 10 min minutes, it is interesting to take a look at the microscopic variables derived from the data. The full depletion voltage U_{fd} is a macroscopic quantity, i.e., it depends on external parameters such as the active thickness of the sensors. To resolve this dependence, the next step is to determine the electric field strength of the full depletion by simply dividing by the active sensor thicknesses. The result can be seen in Figure A.17. Now it can be seen that the annealing function (electric field versus time) follows the same function, only with a constant additive factor.
Now it must be taken into account that the sensors were not all irradiated with the same fluence. Further, the full depletion electrical field E_{fd} is divided by the fluence Φ for normalization. The basic assumption here is that the fluence is linearly related to the increase in full depletion voltage to a first approximation. The result can be viewed in Figure A.8. Now it can be seen that the annealing curves split into three bands, each band groups into a sensor thickness. The sensors with the highest active thickness (300 µm) show the highest normalized electric field E_{fd}/Φ, whereas the lowest active thickness (120 µm) need the lowest normalized electric field to reach full depletion. This is an indication that thinner sensors generally have increased radiation hardness. For comparison, the SRP measurements of the unirradiated sensors resulted in an effective doping concentration of $1.38 \pm 0.02 \times 10^{12}\,\text{cm}^{-3}$, so the neutron irradiation increased it by 1 to 1.5 orders of magnitude.
Now, analogous to Section 6.4.2, we can again determine the effective charge carrier concentration N_{eff} from the full depletion voltage E_{fd} according to Equation 6.3. The results are plotted in Figure 6.36. The careful observer sees that the effective doping concentration N_{eff} of the bulk increases with the neutron fluence, visualized in Figure 6.37. This linearity between N_{eff} and neutron fluence Φ is one of the predictions of the NIEL hypothesis (see Section 4.2.1) and this constant increase is compatible with the fact that these are p-type sensors (no type inversion).

6.5.3 Interstrip resistance during annealing

The resistance is an essential parameter of the interpad/interstrip/intercell region. This resistance should be as high as possible so that these elements are well insulated. So the next step for the

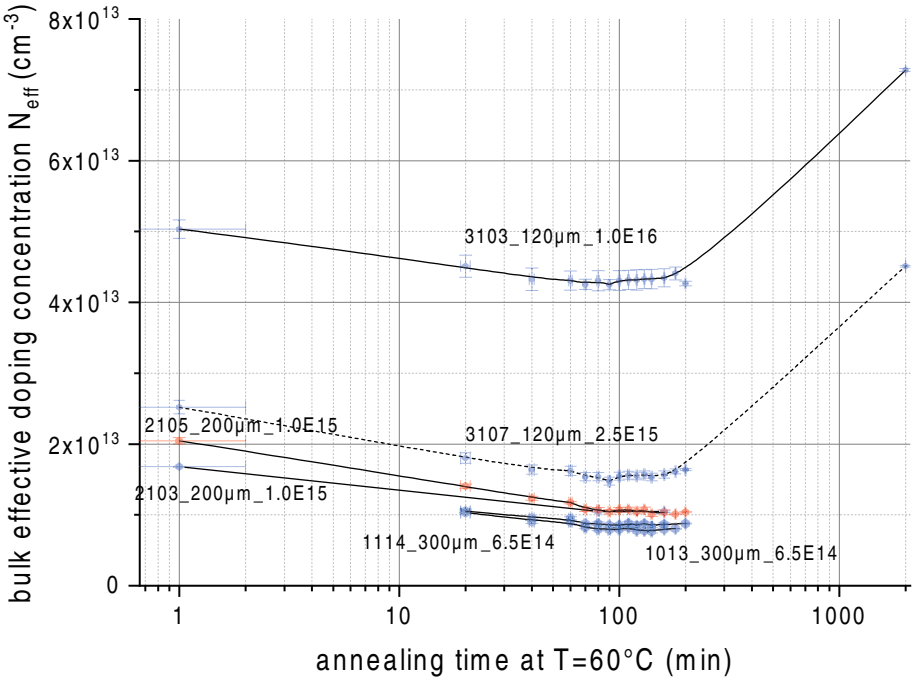

Figure 6.36: The effective doping concentration of irradiated Ministrip sensors plotted against annealing time. The effective doping concentration is one of the most meaningful parameters, as it directly quantifies microscopic effects such as the accumulation of crystal lattice damage and its healing. Since it is a p-type detector, the effective doping concentration increases with radiation damage caused by hadronic radiation.

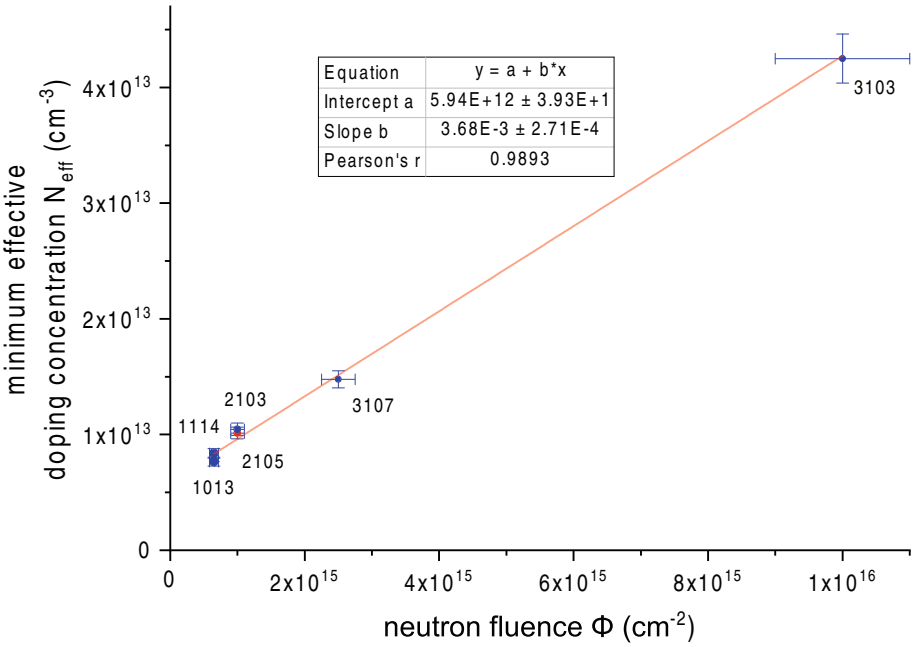

Figure 6.37: The effective doping concentration N_{eff} of irradiated Ministrip sensors plotted against neutron fluence Φ. The data was taken from the corresponding minimum of Figure 6.36. We see a linearity between fluence and effective doping concentration, one of the predictions of the NIEL hypothesis. The SRP measurements of the unirradiated sensors resulted in an effective doping concentration of $1.38 \pm 0.02 \times 10^{12}\,\text{cm}^{-3}$, so the neutron irradiation increased it by 1 to 1.5 orders of magnitude.

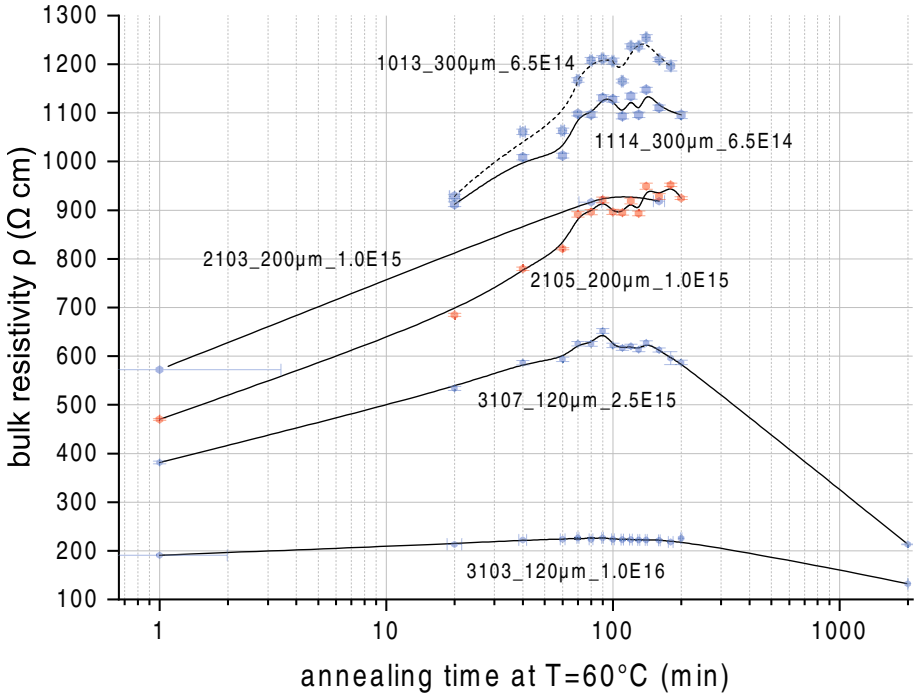

Figure 6.38: Bulk resistivity of the Ministrip sensors over annealing time. The resistivity can be calculated from the full depletion voltage, mobility, and active thickness of the Ministrip sensors [4]. As can be seen, the resistivity increases with the annealing time to reach a maximum at the reversal point between beneficial and reverse annealing (100 ± 10 min). This then drops again significantly in the reverse annealing region. Furthermore, it can be observed that four bands are formed, one for each applied fluence. The higher the fluence, the lower the resistivity. This is consistent with the microscopic theory that NIEL radiation damage increases conductivity or decreases resistivity by introducing additional crystal lattice defects.

annealing studies was to investigate the changes between the active cells. Interstrip measurements were specifically performed on the Ministrip sensors. The first type of measurement was the insulation of the strips from each other, or in other words, interstrip resistances. For this, three adjacent strips and the guard ring were connected to ground potential (see Figure 6.26a). Now a small voltage against ground potential was applied to the middle strip, in the range of 0 to 5 volts, and the measured differential current was recorded. This was repeated at various bias voltages, typically in the range of 10 to 490 V.

Three methods were tried to ultimately determine the resistance:

1. A straight line was fitted into the IV curve. This method proved not too robust and was subject to large fluctuations, especially since the fitting was very sensitive to outliers.

2. The differential of the current, i.e., the increase of the current regarding the voltage, represents the resistance. The numerical differentiation was problematic since the step size of 0.5V was too large due to the measurement times. So this method was also discarded as not robust.

3. It was realized that simply dividing the interstrip voltage by the interstrip current to obtain the resistance gave a very stable result. This was repeated for all voltage steps and arithmetically averaged within each bias voltage step. Figure 6.39 shows the result for sensor 1013. The author still tried to find a suitable and physically arguable algebraic expression for the function $R_{\text{int}}(V_{\text{bias}})$ but did not find any.

The next step was to extract a single resistance value from the set of curves. To ensure that the Ministrip sensors reached the full depletion voltage, the highest applied bias voltage was used for the evaluation in each case, namely 490 V. Thus, the averaged resistance value at 490 V bias voltage was taken in each case and evaluated for all measured annealing times for each sensor. Figure A.11 is an example for one sensor, and Figure 6.39 shows the aggregated results for all analyzed sensors. As readily seen, the interstrip resistance increases with increasing annealing time, which is a desired effect. After all, the strips should be insulated from each other as well as possible. A bend in the curve can also be observed: From about 100 ± 10 min, the effect of annealing increases sharply. In contrast to the annealing studies on bulk capacitance (see Chapter 6.5.2), this, therefore, does not represent the maximum of beneficial annealing, but only a point from which annealing becomes only the more effective for interstrip resistance.

In all cases, the interstrip resistance was in a range between 0.4 kΩ cm and 65 kΩ cm, which is about 1-2 orders of magnitude below the CMS criterion of 100 kΩ cm for non-irradiated sensors, see Table 6.1. With longer annealing times, the author expects significant increases in the interstrip resistance, making future annealing studies attractive. As seen in Figure A.12, similar to the CV curves, we normalized to fluence to work out systematics. Again, analogous to the normalization in Figure A.8, we see that the measured interstrip resistances group into bands, depending on the active thickness of the sensors. The 300 µm sensors (numbers 1013 and 1114) irradiated with the same fluence are close (<3 % deviation). Number 1013 has a p-stop individual, and number 1114 has a p-stop common; otherwise, their properties are identical. The 120 µm sensors (numbers 3103 and 3107) are further apart (<24 %) but got different fluences, which may indicate a non-linearity concerning resistance and neutron fluence. Their properties are otherwise identical. However, the 200 µm sensors (numbers 2103 and 2105) show an enormous discrepancy of a factor of up to 4.6. Sensor number 2103 has a flatband voltage of −2 V, number 2105 one of −5 V, the only one of the annealed Ministrip sensors. Nevertheless, the author considers number 2103 an exceptional case since the rest of the sensors show scaling with thickness and fluence. Number 2105 is between the 120 µm sensors and the 300 µm sensors in both fluence and thickness, and 2103 is not. Hence, attributing this discrepancy to the different flatband voltages would be a premature conclusion.

6.5.4 Interstrip capacitance during annealing

The interstrip capacitance measurements were analogous to the bulk capacitance measurements (see Figure 6.26b). Here, however, four adjacent strips were biased. The two outer ones were connected directly to ground potential, and the two inner ones were connected to the LCR meter with a series resistor each as over-voltage protection. Several measurement frequencies were tried, as in the bulk capacitance measurements, in a range from 500 Hz to 1 MHz. The finding was that the frequency of

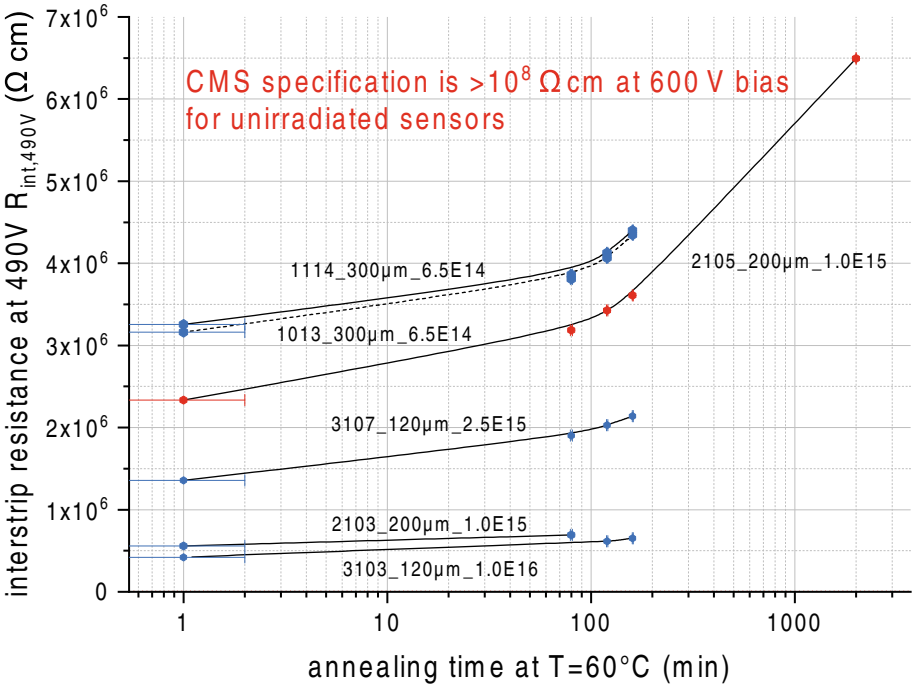

Figure 6.39: Calculated interstrip resistances of the Ministrip sensors at a bias voltage of 490 V at different annealing times. This voltage was the highest bias voltage applied to all sensors. It can be seen that the interstrip resistance also increases with increasing annealing time, indicating positive effects due to annealing. It is equally noteworthy that in the range around 100 ± 10 min, the effectiveness of annealing increases sharply. The temporal location of the inflection point is the same as for the bulk CV curves. The careful observer also can see that the interstrip resistance becomes smaller with increasing fluence, which meets the expectation since radiation damage also occurs in the oxide and the region between the strip implants, affecting the interstrip insulation. This motivates normalization to fluence, as in Figure A.12. One can see that in the range of the measured annealing time of up to 2000 min, the interstrip resistance is, in any case, about 1-2 orders of magnitude below the CMS specification of $>10^8\,\Omega\,\mathrm{cm}$, which, however, applies to non-irradiated sensors. This is, therefore, not an exclusion criterion per se.

100 kHz shows the most stable results.
Figure 6.40 summarizes the results of the interstrip capacitance measurements. Interestingly, the capacitances split quantitatively into two bands: One is within the CMS specification of <3.53 pF with values of about 1.8 pF to 2.6 pF. The other band is well above this with values of around 44 pF to 47 pF. These bands show slight variation over the entire annealing time. The author concludes that this is not a random fluctuation but is subject to systematics. The author cannot recognize any correlation between processing split, neutron fluence, active thickness, and affiliation to one of these bands.
As with the previous bulk capacitance measurements, a trend reversal occurs in the range 100 ± 10 min, see Annex A.20: The full depletion voltage shows a maximum after it drops again more or less sharply, so the qualitative trend is the same. Of course, the full depletion voltage is much lower in absolute terms than for bulk capacitance because the geometry is different. Now, again analogous to the bulk capacitance measurements, one can normalize the full depletion voltage to the thickness and to fluence, see Annex A.21. Again, the curves split into three bands containing sensors of equal thickness.

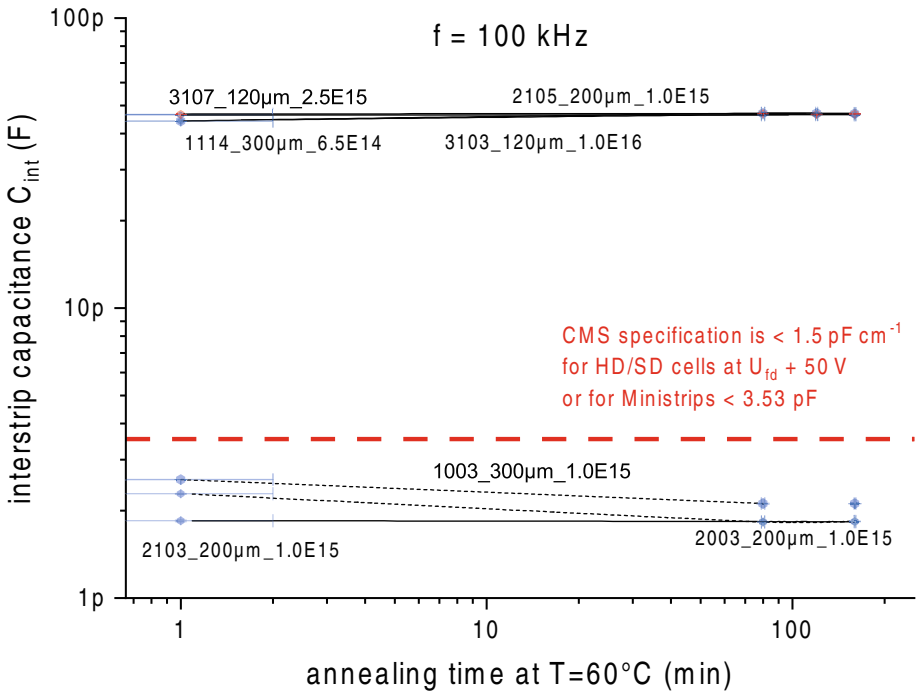

Figure 6.40: Interstrip capacitances over annealing. The final capacitance that the system had at the last voltage point of 490 V was plotted. Interestingly, the data split into two bands, one of which is well within the CMS specification of <3.53 pF, the other well above. The author can find neither a connection nor systematics of these two bands about the processing differences. The interstrip capacitance remains stable over the annealing time. This property is primarily due to the geometric configuration of the strips (their width, spacing, and length) and the dielectric properties of the material between the strips, as shown in [64]. Irradiation and subsequent annealing do not alter the physical layout or spacing of the strips, which are primary factors in defining the capacitance. This stability ensures the reliability of our semiconductor wafers in various conditions.

"Physics is like sex: sure, it may give some practical results, but that's not why we do it."

Richard Feynman

7 Summary and outlook

The current Run 3 of the LHC is expected to operate until the end of 2025 [37]. After that, the installation of the High-Luminosity LHC will begin [1] during the Long Shutdown 3, starting in 2026. Parallel to the upgrade of the LHC, the upgrade of experiments such as the CMS [19] are planned to meet the requirements of the 10 fold increased spontaneous luminosity. This upgrade is called CMS Phase-2 upgrade and mainly concerns the Inner and Outer Tracker [21] and the calorimeter HGCAL [20]. This upgrade is necessary because the current installations will be at the projected end of their material life time in 2025 and cannot continue to be operated without a significant loss of efficiency. The High-Luminosity upgrade also poses new requirements, namely unprecedented cumulative fluences up to $10^6\,\mathrm{n_{eq}cm^{-2}}$ and 2 MGy of absorbed doses. The increased luminosity environment will result in pileups of up to 200, which demands higher spatial and temporal resolution. As a result of these demands, the entire detector volume of the calorimeter will be rebuilt and new technologies will be established in high-energy physics. One such technology is the use of 8-inch wafer material for the silicon sensors. The purpose of this thesis is to establish the feasibility and quality of this new semiconductor process.

Sensor design

To ensure that the sensor geometry meets the requirements of the HGCAL upgrade, the author developed the sensor design for the prototypes based on previous work [64]. The sensor's basic shape is hexagonal, which means the least material loss on the circular wafers. The sensor elements, called "cells", are therefore also hexagonal. The p-stop architecture separates these from each other and the periphery. There are two basic designs: "common" and "individual". Depending on the required beam hardness and spatial resolution, there are two design choices concerning the number of active sensing elements: The "Low-density" with 198 cells per sensor and the "High-density" with 444 cells per sensor.
A guard ring surrounds the sensor periphery ring, which is contacted separately at several points. The guard ring conforms the electric field on the one hand and diverts currents in the event of overvoltage or breakdown on the other. This structure is, in turn, surrounded by an edge ring, which keeps the depleted zone away from the physical edge of the sensor in order to reduce the field strengths in the edge region.
The design features distinctive test structures located on the wafer's remaining regions for quality and process controls and studies on material properties such as annealing behavior. In particular, the Ministrip sensors can be used flexibly in irradiation studies due to their small size. They also have only a few contacts and draw low currents, simplifying and accelerating testing. The Ministrip sensors played an outstanding role in the annealing studies of this thesis.

Test station

The already existing test station and testing concept, without which the measurements and quality controls would not have been feasible, was improved in essential points, such as developing the frontside biasing concept. Complementary to the frontside biasing, there were tweaks like applying a chuck design with a protective mat to not damage the sensitive back of the sensors. Furthermore, the cooling system and the ventilation with dry air were optimized. The author enhanced the electrical measurement system as complementary measures to improve precision and signal-to-noise ratio and wrote and optimized associated measurement scripts.
In addition to the previously mentioned measurements, optical input checks were made by microscopy and electrically by forward biasing at low voltages to test the contact quality. Each sensor was subjected to a complete series of measurements before irradiation to investigate the same parameters studied after irradiation. Specialized measurement series were made, among others, to calibrate the measurement system, which was especially relevant for the capacitance-voltage measurements, to find the optimal imposed frequency. The test station setup was very flexible for measuring full sensors and using needles on positioners for the specially designed Ministrip sensors. Nevertheless, the complete measurement of an irradiated Ministrip sensor, namely current-voltage, capacitance-voltage, and inter-strip measurements, took about half a working day. Including annealing steps, it could take several days. The continuous cooling times and the removal of sometimes occurring icing are time-consuming and require careful handling to prevent damaging the sensors by voltage flash-overs. Possible debugging was an additional time-consuming factor in the case of a full sensor, where all cells have to be switched sequentially, about twice the time is to be expected.

Quality control and auxiliary measurements

The quality controls were extended by complementary methods, such as scanning electron microscope imaging (performed by an external company) and confocal laser microscopy, to check the geometry of the sensors, both laterally and in-depth. Due to the unsuitability of the test station for cooled full sensors at the time of the measurements (2020 and 2021), it was only feasible to measure the unirradiated full sensors. However, this was sufficient to verify the Sensor Quality Control (SQC) scheme and to test eleven of the first sensors of the 2019 prototype. The following observations were made: Of the eleven sensors, four passed all HGCAL quality criteria (yield 36 %), and one sensor was so close to the criteria that it was classified as “partially passed”. All sensors with higher p-stop concentrations (2.5x and 5.0x) were found to have significantly lower breakdown voltages, between 75 V and about 500 V. Only one of the sensors with standard p-stop concentration failed the SQC (breakdown at about 500 V), all others had breakdowns ranging from 800 V to above 1000 V, see Table 6.2. Therefore, the author concludes that a lower p-stop concentration for full sensors leads to higher breakdown voltages and is advantageous. The author suspects that the conductivity of high p-stop concentration (2.5x and 5.0x) is too high, and therefore, the insulation of the cells from each other and the guard ring is no longer sufficient. This would explain the observation of premature breakdowns. Furthermore, a characteristic pattern appeared on four sensors in the voltage range shortly before the breakdown voltage, which affected the same cells in these sensors. This indicates a common cause in a manufacturer’s processing step.

Annealing studies

The main goal of this thesis, to study the effects of radiation damage on the silicon bulk and the insulation between the cells, was carried out and achieved using the Ministrip sensors. For the bulk currents, a point of rapid improvement is observed at around 40 ± 20 min, from which the damage function improves at an accelerated rate. This contrasts M. Moll’s model used for comparison, in which this point is expected around 2000 min. Consequently, the present sensors show a significantly better annealing behavior concerning bulk currents than predicted by the literature models. The author regards this improvement as being due to more suitable processing methods from the sensor manufacturer. The author found that the observed effects of radiation damage, precisely the current-related alpha factor of $2.60 \pm 0.29 \times 10^{-19}\,\mathrm{A\,cm^{-1}}$ (see Figure 6.32) is well within the range of the comparative values found in the literature. Over the annealing duration, the alpha factor initially behaves quantitatively and qualitatively like M. Moll’s model. However, there is a kink in the function at about 40 ± 20 min, where the damage function drops significantly faster than before. According to M. Moll, however, this kink should occur much later, at around 2000 min, see

Figure 6.33. From this, the new 8" sensors indicate a significantly more advantageous annealing behavior than predicted by the model. However, the author points out that this behavior, although identical for all sensors, is based on only five series of measurements. Further studies are needed to verify and quantify this observation and pinpoint the cause of this improvement.
The measured full-depletion voltages range from low annealing times of up to 730 V, then show a rapid improvement with increasing annealing until the minimum is reached at around 100 ± 10 min. The full depletion voltage then increases again, which can be seen as reverse annealing concerning this variable, as a lower full depletion voltage means less sensor current and less heat dissipation.
The effective doping concentrations N_{eff} derived from the full depletion voltage show an increase (in the range $10^{13}\,\text{cm}^{-3}$) compared to the non-irradiated sensors, which are at around $1.36 \times 10^{12}\,\text{cm}^{-3}$ (Figure 6.3), proportional to the neutron fluence (see Figure 6.37). This is consistent with the predictions of the NIEL hypothesis.
The interstrip resistances show, qualitatively similar to the bulk currents, a steady improvement over the entire annealing time. There is again a distinct point at 100 ± 10 min, from which the resistances increase disproportionately quickly as annealing progresses, i.e., the properties concerning interstrip resistance improve significantly. Nevertheless, the resistances over the measured annealing time of up to 2000 min are about 1 to 2 orders of magnitude below the CMS specification of $>10^8\,\Omega\,\text{cm}$ for non-irradiated sensors. Reduced interstrip or intercell resistances can lead to increased cross talk.
With the interstrip capacitances, it indicates that the inflection point of the curves is again at about 100 ± 10 min, analogous to the measurements of the full depletion voltage of the bulk material (Figure 6.40). The interstrip capacitances split into two bands. Four of the Ministrip sensors are about a factor of 10 above the CMS specification for non-irradiated sensors, but three are significantly below.
In summary, the determined sensor parameters and their behavior after annealing are comparable to already established silicon semiconductor sensor technologies in high energy physics (e.g., 6-inch and n-type) but with improvements in annealing behavior. The logical step for future studies is to optimize the process parameters concerning material properties such as bulk doping and implant concentration. The geometry may also be optimized; for example, it cannot be determined from the data of this work whether the common p-stop or individual p-stop is more suitable. Further studies specifically designed for this purpose are therefore recommended.

Bigger picture and outlook

What do these annealing studies mean for the planned HGCAL upgrade of the CMS experiment? The CO_2 cooling system will keep the sensors at $-30\,°\text{C}$ during operation. The desired effect is to keep the leakage current low, which puts less strain on the power supply, inherently requiring less cooling power. However, we have seen that the annealing is "frozen" at a temperature of $-30\,°\text{C}$; in other words, it does not effectively occur during the relevant timescale. Now, it is to be noted that the temperature in the cavern where CMS is located is $21 \pm 1\,°\text{C}$ [58]. When the cooling system is not operating, the transition point between beneficial annealing and reverse annealing regarding full depletion voltage is therefore reached after around 10 days (1.4×10^4 min, see Table 6.5) for already irradiated but uncooled sensors. Therefore, the short maintenance intervals of the CMS experiment of a few days are advantageous, as on the one hand, they reduce the full depletion voltage of the irradiated silicon sensors (which enables smaller bias voltage and thus lower leakage current), but on the other hand, directly reduces the leakage current. After these 10 days, at least the full depletion voltage turns to reverse annealing while the pure leakage current continues to anneal positively. According to the model assumption [53], at CMS cavern conditions, this reverse annealing of the full depletion voltage approaches saturation after around 617 days (10^6 min). This thesis demonstrated the suitability of the sensors for the increased radiation exposure of the HL-LHC using the Ministrip sensors. The author recommends using the Ministrip concept for future irradiation studies due to the aforementioned flexibility.

Acknowledgments

Special gratitude goes out to all staff at the Academy, particularly Florian Pitters and Manfred Valentan, to explain the underlying physics and teach me how to use the required devices and software. They showed exceptional patience, endurance, and topical expertise. Without them, I would not have been able to perform that well during the last six years. Florian and Manfred deserve the greatest gratitude. They have provided me with knowledge and emotional support during obstructive problems and essential phases, without which the completion of this thesis would never have been possible. As postdoctoral researchers they have mastered the long step of understanding strategic foresight but also understand typical problems of PhD students, and provided the right help at the right time. Florian's keen eye for proofreading gets special attention here. In addition to their outstanding professional knowledge and skills, these Postdocs are also people of extraordinary character, the likes of which you only meet a few in the course of a lifetime. I would like to thank also my head supervisor, Jochen Schieck of the Austrian Academy of Sciences. He consistently allowed this paper to be my own work but steered me in the right direction when I left the path of scientific precision. His encouragement, perception, empathy, and immediate help with emerging problems made it possible to finally master this thesis. Jochen is an upright, helpful and also understanding person, for whose qualities every colleague can be grateful. Furthermore to Bernhard Arnold, Andreas Bauer, Thomas Bergauer, Dominic Blöch, Wolfgang Brandner, Florian Buchsteiner, Suman Chatterjee, Marko Dragicevic, Klaus-Dieter Fischer, Natalie Fortin, Markus Friedl, Viktoria Hinger, Christian Irmler, Stefanie Kaser, Axel König, Simone Krüger, Martin Kurz, Margit Oberegger, Markus Oderits, Josef Pirker, Elias Pree, Benjamin Redl, Stefan Schultschik, Christoph Schwanda, Patrick Sieberer, Felix Ulrich-Pur, Barbara Weber, and Hao Yin who assisted me with useful tips, clear explanations, auxiliary work and administrative support. Christoph, Dominic, Felix, Markus and Viktoria deserve additional mention: they excelled not only in professional skills, but also in humanity. I would like to emphasize this quality in particular, as this should be an exemplary effect on us people in everyday life.

Without the help of bachelor's and master's students, finishing this thesis in time would not have been possible. So, I want to give special thanks to Maximilian Babeluk, Florian Meier, and Peter Salajka. They attracted attention with their bold, pragmatic solutions, such as cooling irradiated sensors in a Chinese restaurant.

I wish to show my appreciation to other members of the HGCAL Collaboration, in particular Nural Akchurin, Pedro Almeida, Paul Aspell, David Barney, Philippe Bloch, Erica Brondolin, Pedro Dias de Almeida, Zoltan Gecse, Karl Gill, Ulrich Heintz, Nick Hinton, Joseph Incandela, Susanne Kyre, Emilia Leogrande, Don Lincoln, Ronald Lipton, Marcello Mannelli, Timo Peltola, Thorben Quast, Eva Sicking, Jim Strait, Tommaso Vergine, Mateus Vicente Barreto Pinto, Tejinder Virdee, and Rachel Yohay. I would especially like to mention the professional and cognitive help of Eva, Marcello, Ron, and Zoltan, who exceeded my expectations with their friendly nature and exemplary organizational skills. These are the kind of people a PhD student needs in a scientific collaboration. Not to mention the hospitality of Joseph, as well as the great YouTube videos[a] by Don, which I had enjoyed watching for many years.

I want to express my gratitude to my close friend Roland Rittchen for proofreading. I would also like to thank my family, in detail my sister Andrea Paulitsch-Buckingham for her proofreading and my parents Marina Paulitsch and Peter Paulitsch, for providing financial and motivational support to ensure the completion of this thesis. These people are not only family and friends, but also admirable characters in many aspects.

Additional support like biochemicals can help complete a PhD thesis more efficiently and effectively. I want to emphasize alkaloids such as caffeine, and vitamin D supplements, which help survive the so-called "test beam collapse" and weeks of work in clean rooms almost without permanent damage.

Last but not least, I would like to thank all scientists, engineers, and teachers for providing the knowledge and tools which are the foundation of this thesis. Life on earth can only survive through the steady progress of humankind.

This project has received funding from the call "Forschungspartnerschaften" of the Austrian Research Promotion Agency (FFG), Austria, under grant no. 868296.

[a] https://www.youtube.com/@fermilab

Bibliography

[1] O. Aberle et al. *High-Luminosity Large Hadron Collider (HL-LHC): Technical design report*. CERN Yellow Reports: Monographs. CERN, Geneva, 2020. URL https://doi.org/10.23731/CYRM-2020-0010.

[2] M. Ackermann et al. Updated search for spectral lines from Galactic dark matter interactions with pass 8 data from the Fermi Large Area Telescope. *Phys. Rev. D*, 91:122002, Jun 2015. URL https://doi.org/10.1103/PhysRevD.91.122002.

[3] P. Allport. Applications of silicon strip and pixel-based particle tracking detectors. *Nature Reviews Physics*, 1:567–576, 2019. ISSN 0168-9002. URL https://doi.org/10.1038/s42254-019-0081-z.

[4] N. Arora, J. Hauser, and D. Roulston. Electron and hole mobilities in silicon as a function of concentration and temperature. *IEEE Transactions on Electron Devices*, 29(2):292–295, Feb 1982. ISSN 1557-9646. URL https://doi.org/10.1109/T-ED.1982.20698.

[5] D. Barney. Overview slide of CE with main parameters. Technical Report CMS Document 13251-v9, CERN, Jun 2019. URL https://cms-docdb.cern.ch/cgi-bin/PublicDocDB/ShowDocument?docid=13251.

[6] R. Bernabei et al. The DAMA/LIBRA apparatus. *Nuclear Instruments and Methods in Physics Research Section A: Accelerators, Spectrometers, Detectors and Associated Equipment*, 592(3): 297–315, 2008. ISSN 0168-9002. URL https://doi.org/10.1016/j.nima.2008.04.082.

[7] D. Blöch. *Development of a measurement infrastructure for the qualification of silicon strip sensors for the CMS Phase-2 Upgrade*. PhD thesis, Technische Universität Wien, 2021. URL https://doi.org/10.34726/hss.2021.47402.

[8] E. Brondolin et al. ARRAY: An open source, modular and probe-card based system. *Nuclear Instruments and Methods in Physics Research Section A: Accelerators, Spectrometers, Detectors and Associated Equipment*, 940:168–173, 2019. ISSN 0168-9002. URL https://doi.org/10.1016/j.nima.2019.06.007.

[9] O. Brüning and L. Rossi. *The High Luminosity Large Hadron Collider*, volume 24. CERN, 2015. URL https://doi.org/10.1142/9581.

[10] CDF Collaboration. Observation of Top Quark Production in $\overline{p}p$ Collisions with the Collider Detector at Fermilab. *Phys. Rev. Lett.*, 74:2626–2631, Apr 1995. URL https://doi.org/10.1103/PhysRevLett.74.2626.

[11] CERN. LHC Guide. *Education, Communications and Outreach Group*, March 2017. URL https://cds.cern.ch/record/2255762.

[12] CERN. Facts and figures about the LHC, October 2021. URL https://home.cern/resources/faqs/facts-and-figures-about-lhc.

[13] S. Chang, R. Edezhath, J. Hutchinson, and M. Luty. Effective WIMPs. *Phys. Rev. D*, 89:015011, Jan 2014. URL https://doi.org/10.1103/PhysRevD.89.015011.

[14] S. Chen, D. Bernard, and C. De Saint Jean. Calculation and analysis of gamma-induced irradiation damage cross section. *Nuclear Instruments and Methods in Physics Research Section B: Beam Interactions with Materials and Atoms*, 447:8–21, 2019. URL https://doi.org/10.1016/j.nimb.2019.03.035.

[15] W. Chen, D. Qi, X. Gao, and A. T. S. Wee. Surface transfer doping of semiconductors. *Progress in Surface Science*, 84(9):279–321, 2009. ISSN 0079-6816. URL https://doi.org/10.1016/j.progsurf.2009.06.002.

[16] CMS Collaboration. The CMS experiment at the CERN LHC. *CERN-CMS*, August 2008. URL https://cds.cern.ch/record/1129810.

[17] CMS Collaboration. CMS Technical Design Report for the Pixel Detector Upgrade. Technical report, CERN, September 2012. URL http://cds.cern.ch/record/1481838.

[18] CMS Collaboration. Observation of a new boson at a mass of 125 GeV with the CMS experiment at the LHC. *CERN-CMS*, September 2012. URL https://doi.org/10.1016/j.physletb.2012.08.021.

[19] CMS Collaboration. Technical Proposal for the Phase-II Upgrade of the CMS Detector. Technical report, CERN, Geneva, Jun 2015. URL https://cds.cern.ch/record/2020886.

[20] CMS Collaboration. The Phase-2 Upgrade of the CMS Endcap Calorimeter. Technical report, CERN, Geneva, Nov 2017. URL https://cds.cern.ch/record/2293646.

[21] CMS Collaboration. The Phase-2 Upgrade of the CMS Tracker. Technical report, CERN, July 2017. URL https://cds.cern.ch/record/2272264.

[22] CMS Collaboration. Constraints on anomalous Higgs boson couplings to vector bosons and fermions in production and decay in the $H \to 4\ell$ channel. Technical report, CERN, Geneva, 2020. URL http://cds.cern.ch/record/2725543.

[23] R. H. Cyburt, B. D. Fields, and K. A. Olive. Primordial nucleosynthesis in light of WMAP. *Physics Letters B*, 567(3):227–234, 2003. ISSN 0370-2693. URL https://doi.org/10.1016/j.physletb.2003.06.026.

[24] T. V. Eichhorn. *Development of Silicon Detectors for the High Luminosity LHC*. Dissertation, Universität Hamburg, 2015.

[25] F. Englert and R. Brout. Broken Symmetry and the Mass of Gauge Vector Mesons. *Phys. Rev. Lett.*, 13:321–323, Aug 1964. URL https://doi.org/10.1103/PhysRevLett.13.321.

[26] D. J. S. Findlay and D. H. J. Totterdell. Photonuclear transmutation doping of semiconductors. *Semiconductor Science and Technology*, 3(4):388, apr 1988. URL https://doi.org/10.1088/0268-1242/3/4/018.

[27] G. Fraser, A. Abbey, A. Holland, K. McCarthy, A. Owens, and A. Wells. The X-ray energy response of silicon Part A. Theory. *Nuclear Instruments and Methods in Physics Research Section A: Accelerators, Spectrometers, Detectors and Associated Equipment*, 350:368–378, 1994. ISSN 0168-9002. URL https://doi.org/10.1016/0168-9002(94)91185-1.

[28] J. Frenkel. Über die Wärmebewegung in festen und flüssigen Körpern. *Zeitschrift für Physik*, 1926. URL https://doi.org/10.1007/BF01379812.

[29] Fresenius. Measuring and Analysis Methods, 2023. URL https://www.institut-fresenius.de/en/material-failure-analysis/measuring-analysis-methods.

[30] E. Fretwurst, M. Kuhnke, G. Lindstroem, and M. Molla. Radiation hardness of silicon detectors for applications in high-energy physics experiments. *Journal of Optoelectronics and Advanced Materials*, 01 2000.

[31] E. Fretwurst, G. Lindström, J. Stahl, I. Pintilie, Z. Li, J. Kierstead, E. Verbitskaya, and R. Röder. Bulk damage effects in standard and oxygen-enriched silicon detectors induced by 60Co-gamma radiation. *Nuclear Instruments and Methods in Physics Research Section A: Accelerators, Spectrometers, Detectors and Associated Equipment*, 514(1):1–8, 2003. ISSN 0168-9002. URL https://doi.org/10.1016/j.nima.2003.08.077. Proceedings of the 4th International Conference on Radiation Effects on Semiconductor Materials, Detectors and Devices.

[32] J. Friedrich. Methods for Bulk Growth of Inorganic Crystals: Crystal Growth. *Reference Module in Materials Science and Materials Engineering*, 2016. URL https://doi.org/10.1016/B978-0-12-803581-8.01010-9.

[33] G. Hinshaw et al. Five-year WMAP observations. *The Astrophysical Journal Supplement Series*, 180(2):225–245, 2009. URL https://doi.org/10.1088/0067-0049/180/2/225.

[34] G. Kane and S. Watson. Dark matter and the LHC: What is the connection? *Modern Physics Letters A*, 23:2103–2123, 200. URL https://doi.org/10.1142/S0217732308028314.

[35] D. Groom and S. Klein. Passage of particles through matter. *Particle Data Group*, 2023. URL https://pdg.lbl.gov/2023/reviews/rpp2022-rev-passage-particles-matter.pdf.

[36] P. Higgs. Broken symmetries, massless particles and gauge fields. *Physics Letters*, 12(2):132–133, 1964. ISSN 0031-9163. URL https://doi.org/10.1016/0031-9163(64)91136-9.

[37] High Luminosity LHC Collaboration. LS3 schedule change, March 2023. URL https://hilumilhc.web.cern.ch/article/ls3-schedule-change.

[38] V. Hinger. *Silicon Sensor Process Quality Control for the CMS Phase-2 Upgrade*. PhD thesis, Technische Universität Wien, 2021. URL https://cds.cern.ch/record/2766455.

[39] Z. Hu, R. Li, X. Yang, M. Yang, R. Day, and H. Wu. Energy separation for Ranque-Hilsch vortex tube: A short review. *Thermal Science and Engineering Progress*, 19:100559, 2020. ISSN 2451-9049. URL https://doi.org/10.1016/j.tsep.2020.100559.

[40] M. Huhtinen. Simulation of non-ionising energy loss and defect formation in silicon. *Nuclear Instruments and Methods in Physics Research Section A: Accelerators, Spectrometers, Detectors and Associated Equipment*, 491(1):194–215, 2002. ISSN 0168-9002. URL https://doi.org/10.1016/S0168-9002(02)01227-5.

[41] IceCube Collaboration. Limits on a Muon Flux from Neutralino Annihilations in the Sun with the IceCube 22-String Detector. *Phys. Rev. Lett.*, 102, May 2009. URL https://doi.org/10.1103/PhysRevLett.102.201302.

[42] V. H. Ingre. Unit cell of the diamond cubic, face-centered, 2023. URL https://commons.wikimedia.org/wiki/File:Diamond_cubic_crystal_structure.svg.

[43] A. Junkes. *Influence of radiation induced defect clusters on silicon particle detectors*. PhD thesis, Universität Hamburg, 2011. URL https://inspirehep.net/literature/940715.

[44] G. Knoll. *Radiation detection and measurement*. John Wiley, 1989. ISBN 978-0-470-13148-0.

[45] H. Kolanoski and N. Wermes. *Teilchendetektoren, Grundlagen und Anwendungen*. Springer Spektrum, 2016. ISBN 978-3-662-45349-0.

[46] A. König. *Planar Silicon Strip Sensors for the CMS Phase-2 Upgrade*. Phd thesis, Technische Universität Wien, 2017. URL https://repositum.tuwien.at/handle/20.500.12708/158652.

[47] P. Laube. Semiconductor Technology from A to Z, 2022. URL https://www.halbleiter.org/.

[48] Leica Microsystems GmbH. Leica DCM8, February 2023. URL https://www.leica-microsystems.com/products/digital-microscopes/p/leica-dcm8/.

[49] G. Lutz. *Semiconductor Radiation Detectors*. Springer-Verlag Berlin Heidelberg, 2007. ISBN 978-3-540-71678-5. URL https://doi.org/10.1007/978-3-540-71679-2.

[50] D. McGregor and H. Hermon. Room-temperature compound semiconductor radiation detectors. *Nuclear Instruments and Methods in Physics Research Section A: Accelerators, Spectrometers, Detectors and Associated Equipment*, 395(1):101–124, 1997. ISSN 0168-9002. URL https://doi.org/10.1016/S0168-9002(97)00620-7. Proceedings of the Fourth International Workshop on GaAs Detectors and Related Compounds.

[51] MedAustron. MedAustron EBG GmbH, October 2021. URL https://www.medaustron.at.

[52] S. Meroli. Czochralski process vs Float Zone: Two growth techniques for mono-crystalline silicon, February 2023. URL https://meroli.web.cern.ch/Lecture_silicon_floatzone_czochralski.html.

[53] M. Moll. *Radiation Damage in Silicon Particle Detectors*. Phd thesis, Universität Hamburg, 1999. URL https://mmoll.web.cern.ch/thesis/pdf/moll-thesis.pdf.

[54] M. Moll. Displacement Damage in Silicon Detectors for High Energy Physics. *IEEE Transactions on Nuclear Science*, 65(8):1561–1582, 2018. URL https://doi.org/10.1109/TNS.2018.2819506.

[55] National Institute of Standards and Technology. Physical measurements laboratory, 2023. URL https://physics.nist.gov/PhysRefData/Star/Text/intro.html.

[56] V. Neimash, T. Sagan, V. Tsmots, V. Siratskii, V. Shakhovtsov, and V. Shindich. Intrinsic Gettering of Radiation Defects in Silicon Caused by High-Temperature Oxygen-Containing Defects. *Solid State Phenomena*, 19:87–94, 1 1991. URL https://doi.org/10.4028/www.scientific.net/SSP.19-20.87.

[57] Nordlund et al. Improving atomic displacement and replacement calculations with physically realistic damage models. *Nature Communications*, 9, 2018. URL https://doi.org/10.1038/s41467-018-03415-5.

[58] L. M. Pant. Effect of environmental parameters on the performance of resistive plate chambers. *DAE Symp. Nucl. Phys.*, 55:680–681, 2010. URL https://inspirehep.net/files/43ae6b91f8e4b16cd4f911178502418b.

[59] C. Patrignani. Review of Particle Physics. *Chinese Physics C*, 40(10), oct 2016. URL https://dx.doi.org/10.1088/1674-1137/40/10/100001.

[60] P. Paulitsch. Performance Studies of Silicon Strip Sensors for the Phase-II Upgrade of the CMS Tracker, 2018. URL https://cds.cern.ch/record/2316709.

[61] P. Paulitsch. The silicon sensors for the High Granularity Calorimeter of CMS. *Nuclear Instruments and Methods in Physics Research Section A: Accelerators, Spectrometers, Detectors and Associated Equipment*, 978:164428, 2020. ISSN 0168-9002. URL https://doi.org/10.1016/j.nima.2020.164428.

[62] F. M. Pitters. Silicon Detector Technologies for Future Particle Collider Experiments, 2019. URL http://cds.cern.ch/record/2714709.

[63] Planck Collaboration. Planck 2013 results. I. Overview of products and scientific results. *Astronomy and Astrophysics*, 571:A1, 2014. URL https://doi.org/10.1051/0004-6361/201321529.

[64] E. Pree. *Development of large area silicon sensors for the high granularity calorimeter at CMS*. PhD thesis, Technische Universität Wien, 2018. URL https://repositum.tuwien.at/handle/20.500.12708/6976.

[65] Rhode Island Nuclear Science Center Commission. Rhode Island Nuclear Science Center, Oct 2022. URL http://www.rinsc.ri.gov/research/.

[66] A. Ruzin, G. Casse, M. Glaser, and F. Lemeilleur. Studies of radiation hardness of oxygen enriched silicon detectors. *Nuclear Instruments and Methods in Physics Research Section A: Accelerators, Spectrometers, Detectors and Associated Equipment*, 426(1):94–98, 1999. ISSN 0168-9002. URL https://doi.org/10.1016/S0168-9002(98)01476-4.

[67] T. Sakuma and T. McCauley. Detector and event visualization with SketchUp at the CMS experiment. *Journal of Physics: Conference Series*, 513(2):022032, Jun 2014. URL https://doi.org/10.1088/1742-6596/513/2/022032.

[68] P. Salajka. Irradiation of silicon detectors for HEP experiments in the Triga Mark II reactor of ATI. Diploma thesis, Technische Universität Wien, 2021. URL https://doi.org/10.34726/hss.2021.92420.

[69] J. Schechter and J. W. F. Valle. Neutrino masses in SU(2) ⊗ U(1) theories. *Phys. Rev. D*, 22: 2227–2235, Nov 1980. URL https://doi.org/10.1103/PhysRevD.22.2227.

[70] J. Schieck et al. Direct Dark Matter Search with the CRESST II Experiment. *PoS*, ICHEP2016: 217, 2016. URL https://doi.org/10.22323/1.282.0217.

[71] W. Shockley. The theory of p-n junctions in semiconductors and p-n junction transistors. *The Bell System Technical Journal*, 28(3):435–489, 1949. URL https://doi.org/10.1002/j.1538-7305.1949.tb03645.x.

[72] B. Smodiš and L. Snoj. The JSI TRIGA Mark II Reactor, Slovenia, Jul 2016. ISSN 0074-1914. URL http://www-pub.iaea.org/MTCD/Publications/PDF/SupplementaryMaterials/D482/Europe.pdf.

[73] H. Spieler. *Semiconductor Detector Systems*. Oxford Science Publications, 2005. ISBN 978-0-19-852784-8.

[74] S. Sze. *Semiconductor Devices - Physics and Technology*. John Wiley and Sons, 2 edition, 1981. ISBN 0-471-33372-7.

[75] I. Tarján and M. Mátrai. *Laboratory manual on crystal growth*. Akademiai Kiado, 1972.

[76] Thomson, W., 1st Baron Kelvin. Baltimore lectures on molecular dynamics and the wave theory. *Cambridge University Press*, page 274, 1904. URL https://babel.hathitrust.org/cgi/pt?id=ien.35556038198842.

[77] TRIGA Center. The TRIGA Mark-II Reactor, Austria, Oct 2022. URL https://www.tuwien.at/en/trigacenter/trigareactor/technical-data.

[78] Y. Unno, Y. Ikegami, T. Kohriki, S. Terada, K. Hara, K. Yamamura, and S. Kamada. P-stop designs for reducing electric field strength at implant edges. pages 2507–2512, 2008. URL https://doi.org/10.1109/NSSMIC.2008.4774864.

[79] A. Vasilescu and G. Lindstroem. Notes on the fluence normalisation based on the NIEL scaling hypothesis. *CERN RD48 Technical Reports*, June 2000. URL https://rd48.web.cern.ch/technical-notes/rosetn.htm.

[80] A. Verma, J. Jennings, R. Johnson, M. Weber, and K. Lynn. Fabrication of 3D charged particle trap using through-silicon vias etched by deep reactive ion etching. *Journal of Vacuum Science Technology B: Microelectronics and Nanometer Structures*, 31, 05 2013. URL http://doi.org/10.1116/1.4799662.

[81] Wikipedia. Standard Model, 2023. URL https://upload.wikimedia.org/wikipedia/commons/0/00/Standard_Model_of_Elementary_Particles.svg.

[82] Wikiversity. Materials Science and Engineering/Diagrams/Semiconductor Devices, 2022. URL https://en.wikiversity.org/wiki/Materials_Science_and_Engineering/Diagrams/Semiconductor_Devices.

[83] H. Xiao. *Introduction to Semiconductor Manufacturing Technology*. SPIE–The International Society for Optical Engineering, 2 edition, 2012. ISBN 978-1510616530.

[84] E. Young. *Ultrafast acoustic strain generation and effects in semiconductor nanostructures*. PhD thesis, University of Nottingham, 2014. URL http://eprints.nottingham.ac.uk/27666/.

[85] A. Zaiour, J. Charara, B. Hamdoun, A. Hamié, and M. Hage-Ali. Electrical Properties Study of Three Highly Purified CdTe Ingots. *Physics Procedia*, 55:470–475, 2014. ISSN 1875-3892. URL https://doi.org/10.1016/j.phpro.2014.07.068. 8th International Conference on Material Sciences, CSM8-ISM5.

[86] F. Zwicky. Die Rotverschiebung von extragalaktischen Nebeln. *Helvetica Physica Acta*, 6: 110–127, Jan. 1933. URL https://ui.adsabs.harvard.edu/abs/1933AcHPh...6..110Z.

List of Figures

List of Tables

Declaration

I hereby affirm that this present thesis was composed by myself and that the work herein is my own except where explicitly stated otherwise in the text. This work has not been submitted for any other degree or professional qualification except as specified, nor has it been published elsewhere. Where other people's work has been used (either from a printed source, internet, or any other source), this has been carefully acknowledged and referenced.
During the preparation and correction of this thesis, I have used AI-based software based on the *Classic language model*[b], *GPT-3*[c], and *GPT-3.5*[d] to assist me in the writing process to improve text structure, text flow, and readability. After using these tools and services, I reviewed and edited the content as needed, and I am taking full responsibility for the content of the whole thesis.

Vienna, 22.10.2024

Peter Paulitsch

[b] https://deepl.com/
[c] https://grammarly.com/
[d] https://chatgpt.com/

A
Appendix

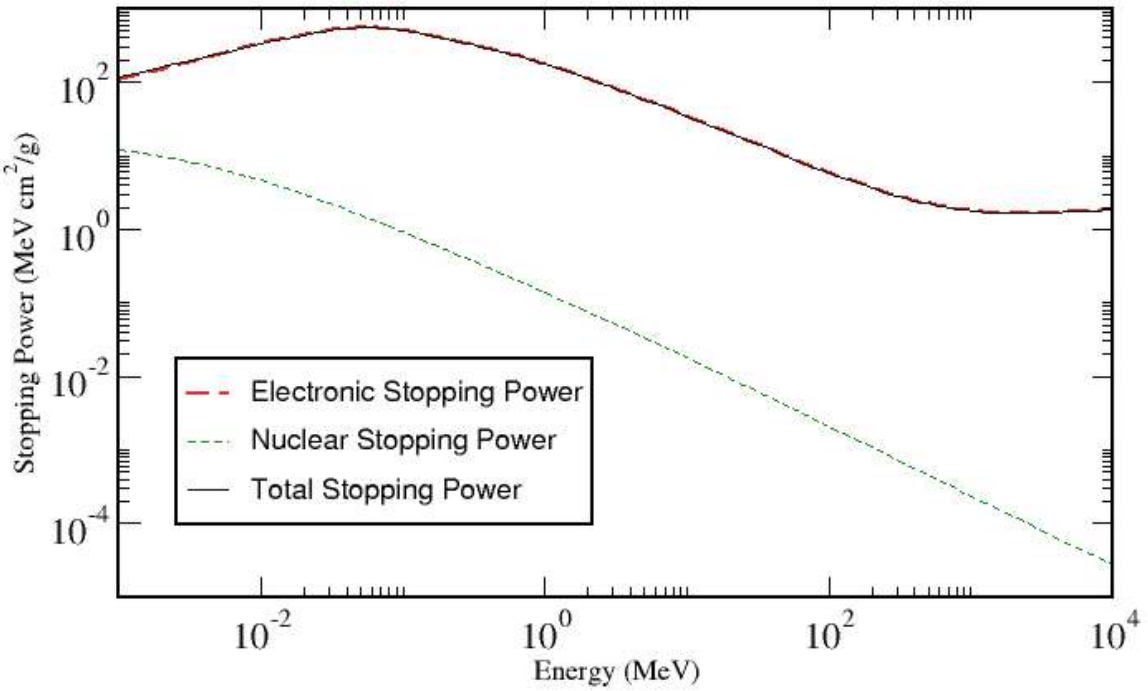

(a) For protons, the energy of the MIP is about 2 to 3 GeV, corresponding to 2 to 3 times the proton's rest mass. The shell electrons of the silicon target dominate the stopping power in this range.

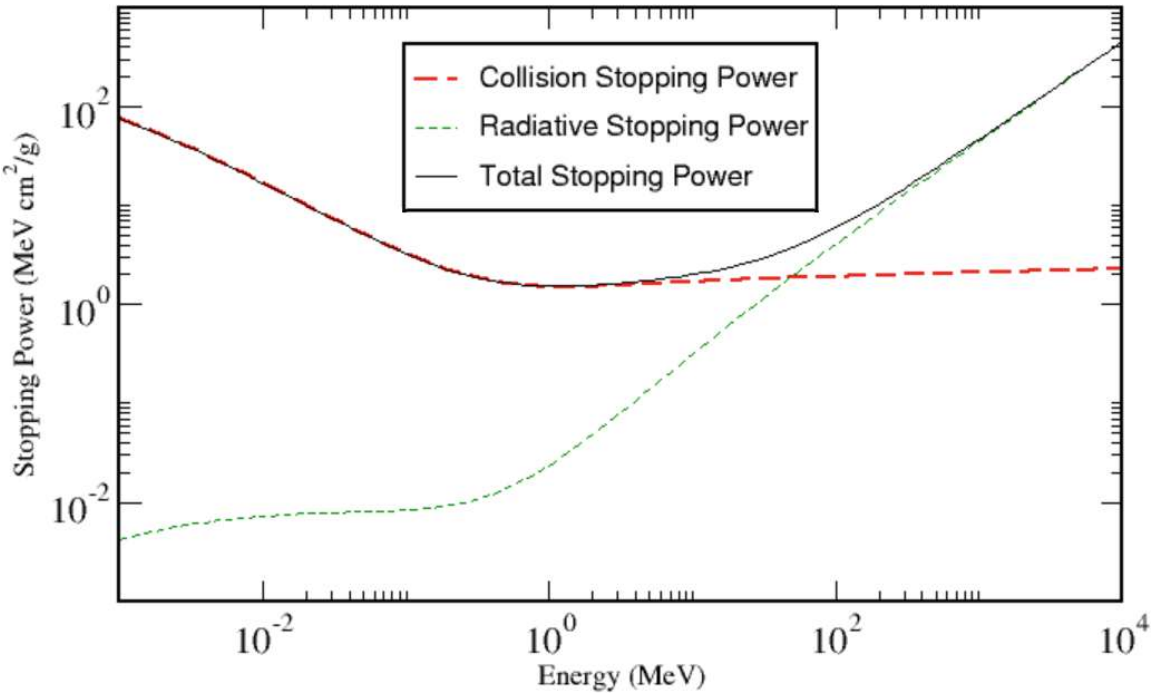

(b) For electrons, the energy of the MIP is about 1 to 1.5 MeV, corresponding to 2 to 3 times the electron's rest mass. In this region, deceleration is dominant due to collisions with the shell electrons. At higher energies, radiative losses due to bremsstrahlung and pair production dominate.

Figure A.1: Mass stopping power $\frac{dE}{dx}$ of charged particles in silicon. The energy range shown here goes from 1 keV to 10 GeV and includes the respective point of energy of a minimum ionizing particle (MIP). Data from [55].

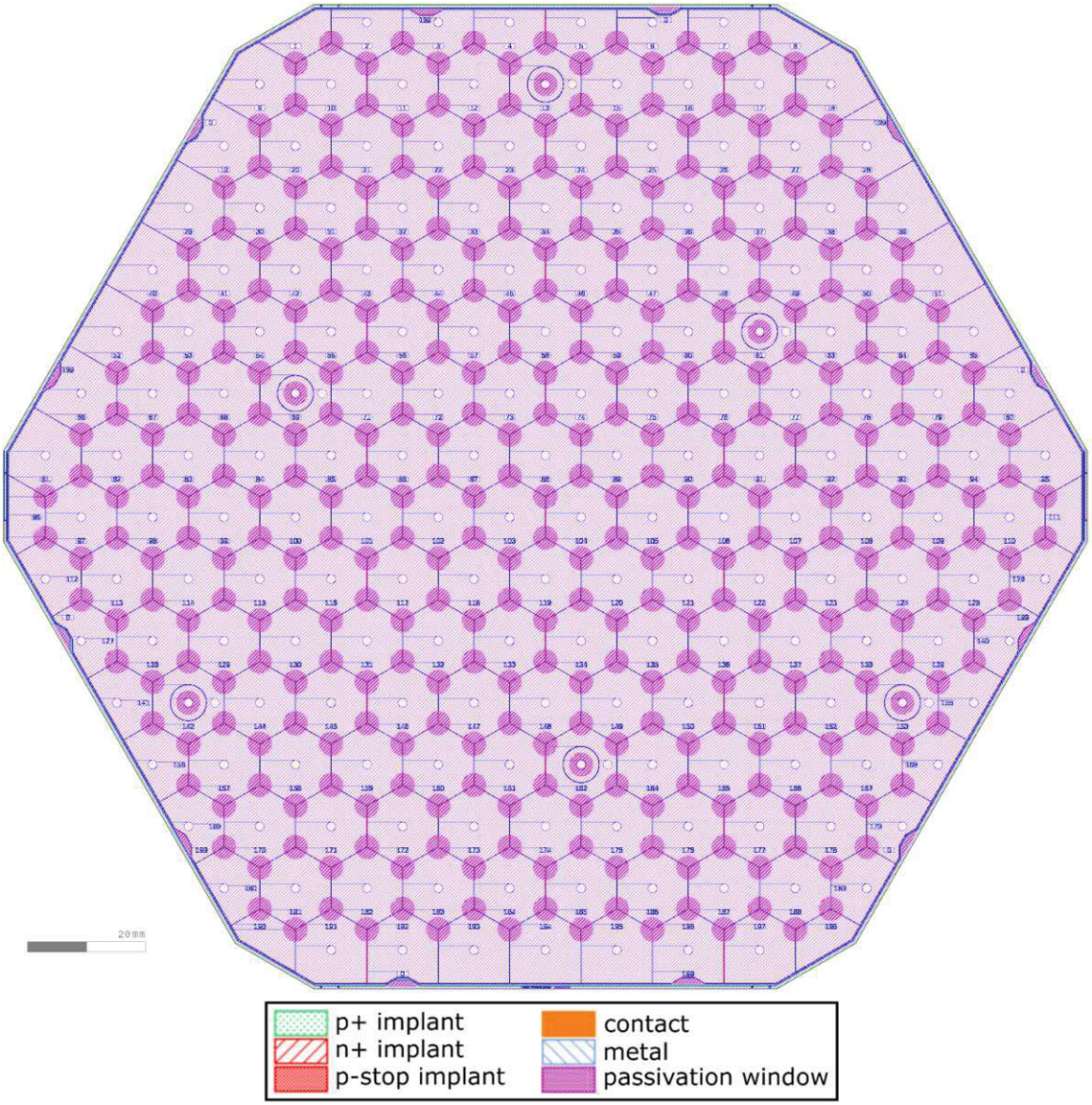

Figure A.2: This is a screenshot from the design file (January 2021) of the Low-density sensor design. One can find a detailed description in Section 5.4.

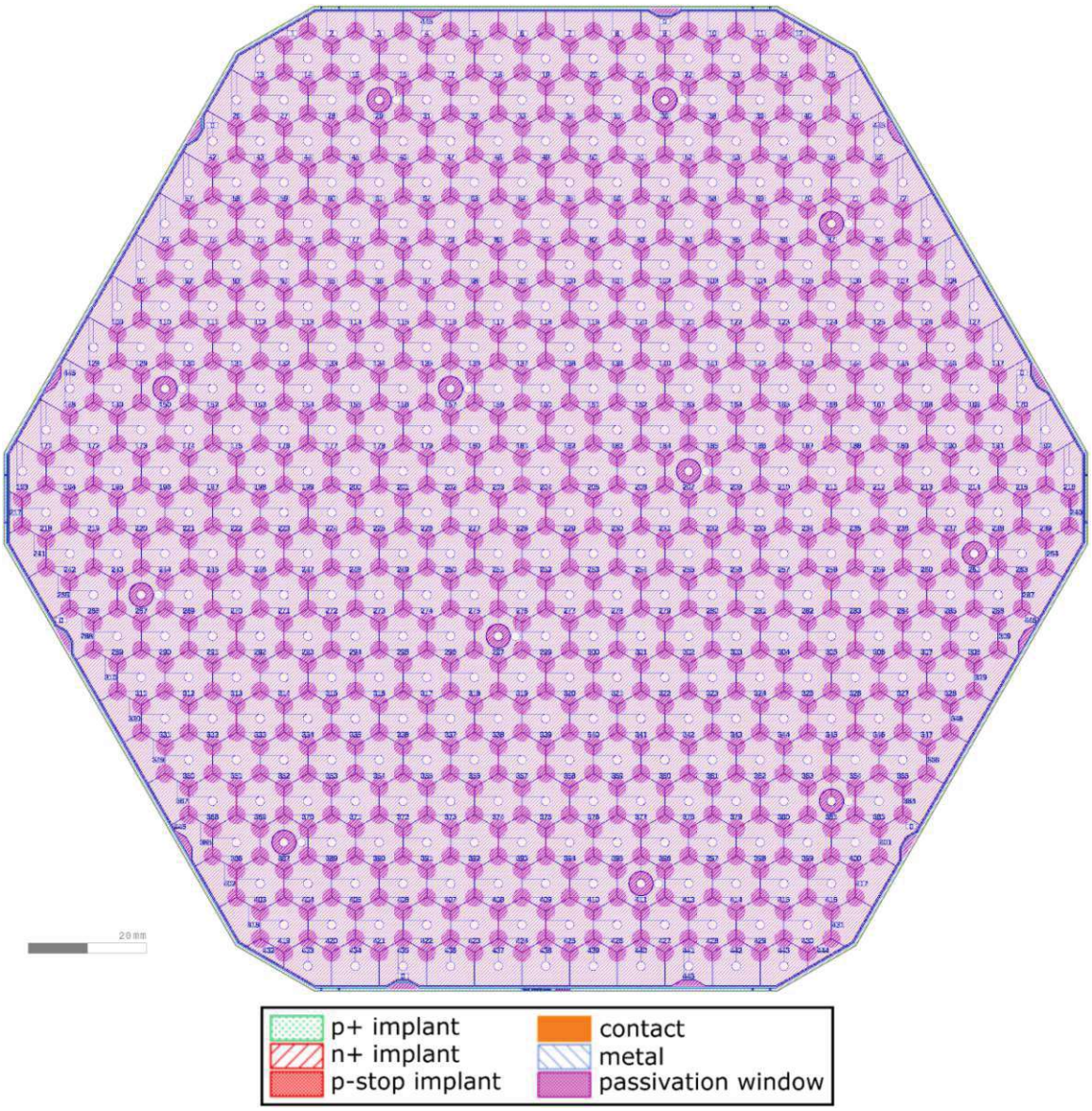

Figure A.3: This is a screenshot from the design file (January 2021) of the High-density sensor design. One can find a detailed description in Section 5.4.

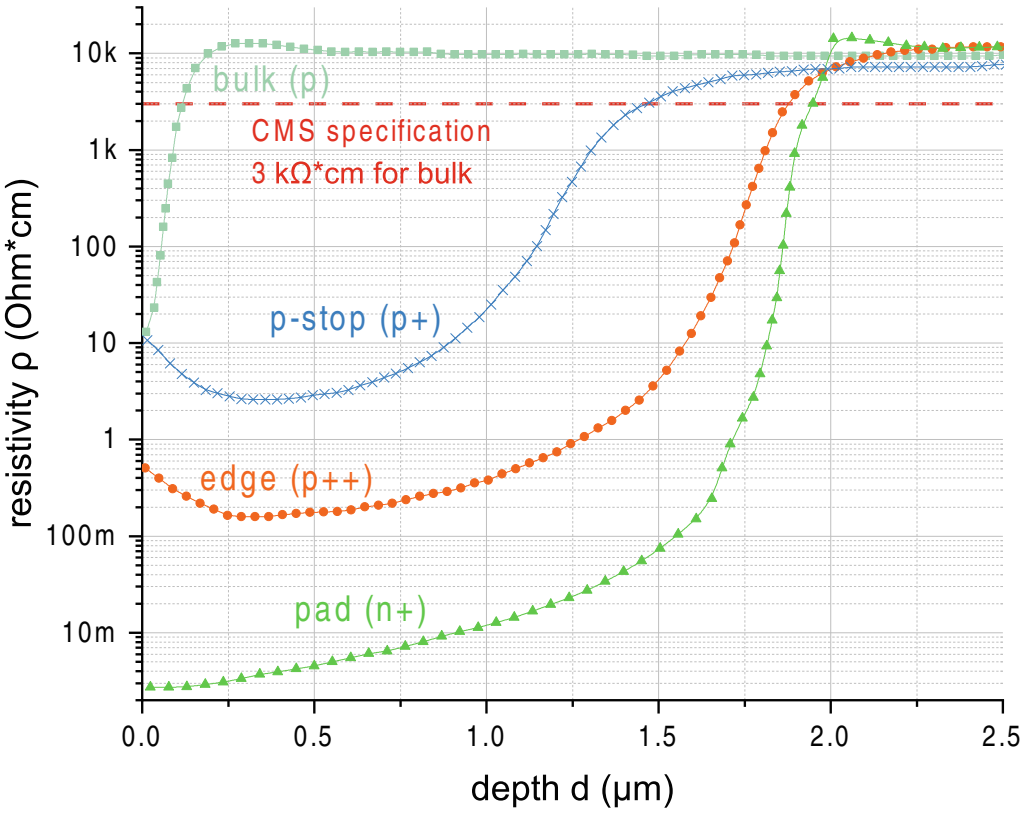

Figure A.4: Results from the SRP measurements. The resistance R between the needles is measured. By knowing the distance between the needles, we can deduce the resistivity, which is plotted. The measured bulk resistivity is well above the minimal CMS specification of 3 kΩ cm

Table A.1: Properties of all measured Ministrip sensors

ID	thickn. (µm)	process	oxide type	flatband voltage	p-stop type	p-stop conc.	target fluence Φ (n_{eq} cm^{-2})
1002	300	FZ	STD	-2V	ind.	STD	1.0×10^{15}
1004	300	FZ	STD	-5V	ind.	STD	1.0×10^{15}
1005	300	FZ	STD	-5V	ind.	STD*2.5	1.0×10^{15}
1006	300	FZ	STD	-5V	ind.	STD*5.0	1.0×10^{15}
1007	300	FZ	Type A	-5V	ind.	STD	
1008	300	FZ	Type B	-5V	ind.	STD	
1009	300	FZ	Type C	-5V	ind.	STD	
1010	300	FZ	Type D	-5V	ind.	STD	
1011	300	FZ	Type E	-5V	ind.	STD	
1013	300	FZ	STD	-2V	ind.	STD	6.5×10^{14}
1104	300	FZ	STD	-2V	com.	STD	
1105	300	FZ	STD	-5V	com.	STD	1.0×10^{15}
1106	300	FZ	STD	-5V	com.	STD*2.5	1.0×10^{15}
1107	300	FZ	STD	-5V	com.	STD*5.0	1.0×10^{15}
1108	300	FZ	Type A	-5V	com.	STD	
1109	300	FZ	Type B	-5V	com.	STD	
1110	300	FZ	Type C	-5V	com.	STD	
1111	300	FZ	Type D	-5V	com.	STD	
1112	300	FZ	Type E	-5V	com.	STD	
1114	300	FZ	STD	-2V	com.	STD	6.5×10^{14}
2003	200	FZ	STD	-2V	ind.	STD	1.0×10^{15}
2004	200	FZ	STD	-5V	ind.	STD	1.0×10^{15}
2005	200	FZ	STD	-5V	ind.	STD*2.5	1.0×10^{15}

Table A.1: Properties of all measured Ministrip sensors

ID	thickn. (µm)	process	oxide type	flatband voltage	p-stop type	p-stop conc.	target fluence Φ (n_{eq} cm^{-2})
2006	200	FZ	STD	-5V	ind.	STD*5.0	1.0×10^{15}
2007	200	FZ	Type A	-5V	ind.	STD	
2008	200	FZ	Type B	-5V	ind.	STD	
2009	200	FZ	Type C	-5V	ind.	STD	
2010	200	FZ	Type D	-5V	ind.	STD	
2011	200	FZ	Type E	-5V	ind.	STD	
2012	200	FZ	STD	-2V	ind.	STD	2.5×10^{15}
2013	200	FZ	STD	-2V	ind.	STD	1.5×10^{15}
2014	200	MCZ	STD	-5V	ind.	STD	
2103	200	FZ	STD	-2V	com.	STD	1.0×10^{15}
2104	200	FZ	STD	-2V	com.	STD	
2105	200	FZ	STD	-5V	com.	STD	1.0×10^{15}
2106	200	FZ	STD	-5V	com.	STD*2.5	1.0×10^{15}
2107	200	FZ	STD	-5V	com.	STD*5.0	1.0×10^{15}
2108	200	FZ	Type A	-5V	com.	STD	
2109	200	FZ	Type B	-5V	com.	STD	
2110	200	FZ	Type C	-5V	com.	STD	
2111	200	FZ	Type D	-5V	com.	STD	
2112	200	FZ	Type E	-5V	com.	STD	
2113	200	FZ	STD	-2V	com.	STD	2.5×10^{15}
2114	200	FZ	STD	-2V	com.	STD	1.5×10^{15}
3001	120	epi	STD	-5V	ind.	STD	1.0×10^{16}
3002	120	epi	STD	-2V	ind.	STD*0.5	1.0×10^{16}
3003	120	epi	STD	-2V	ind.	STD	1.0×10^{16}
3004	120	epi	STD	-5V	ind.	STD	
3005	120	epi	STD	-2V	ind.	STD*0.5	
3006	120	epi	STD	-2V	ind.	STD*0.5	2.5×10^{15}
3007	120	epi	STD	-2V	ind.	STD	2.5×10^{15}
3008	120	epi	STD	-2V	ind.	STD	1.5×10^{15}
3009	120	epi	STD	-2V	ind.	STD	
3010	120	epi	STD	-2V	ind.	STD	
3011	120	epi	STD	-2V	ind.	STD	
3012	120	epi	STD	-2V	ind.	STD	
3013	120	epi	STD	-2V	ind.	STD	
3014	120	epi	STD	-2V	ind.	STD	
3015	120	epi	STD	-2V	ind.	STD	
3016	120	epi	STD	-2V	ind.	STD	
3101	120	epi	STD	-5V	com.	STD	1.0×10^{16}
3102	120	epi	STD	-2V	com.	STD*0.5	1.0×10^{16}
3103	120	epi	STD	-2V	com.	STD	1.0×10^{16}
3104	120	epi	STD	-5V	com.	STD	
3105	120	epi	STD	-2V	com.	STD*0.5	
3106	120	epi	STD	-2V	com.	STD*0.5	2.5×10^{15}
3107	120	epi	STD	-2V	com.	STD	2.5×10^{15}
3108	120	epi	STD	-2V	com.	STD	1.5×10^{15}
3109	120	epi	STD	-2V	com.	STD	
3110	120	epi	STD	-2V	com.	STD	
3111	120	epi	STD	-2V	com.	STD	
3112	120	epi	STD	-2V	com.	STD	
3113	120	epi	STD	-2V	com.	STD	
3114	120	epi	STD	-2V	com.	STD	
3115	120	epi	STD	-2V	com.	STD	
3116	120	epi	STD	-2V	com.	STD	

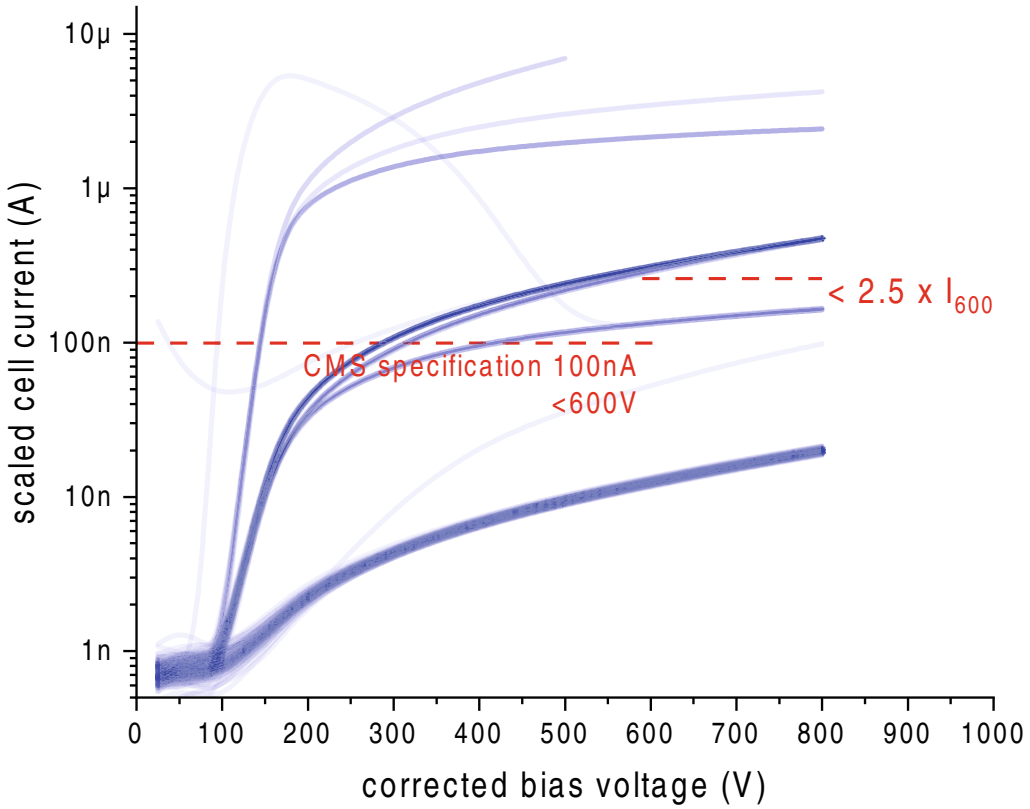

Figure A.5: Curve arrays of the cell currents of the unirradiated sensor 1114. This sensor did not pass the quality control (see Table 6.1) because, on the one hand, the total current is too high (407 µA at 600 V, the limit is 100 µA). Furthermore, as can be seen on this set of curves, there are too many currents above the limit of 100 nA in the number 84.

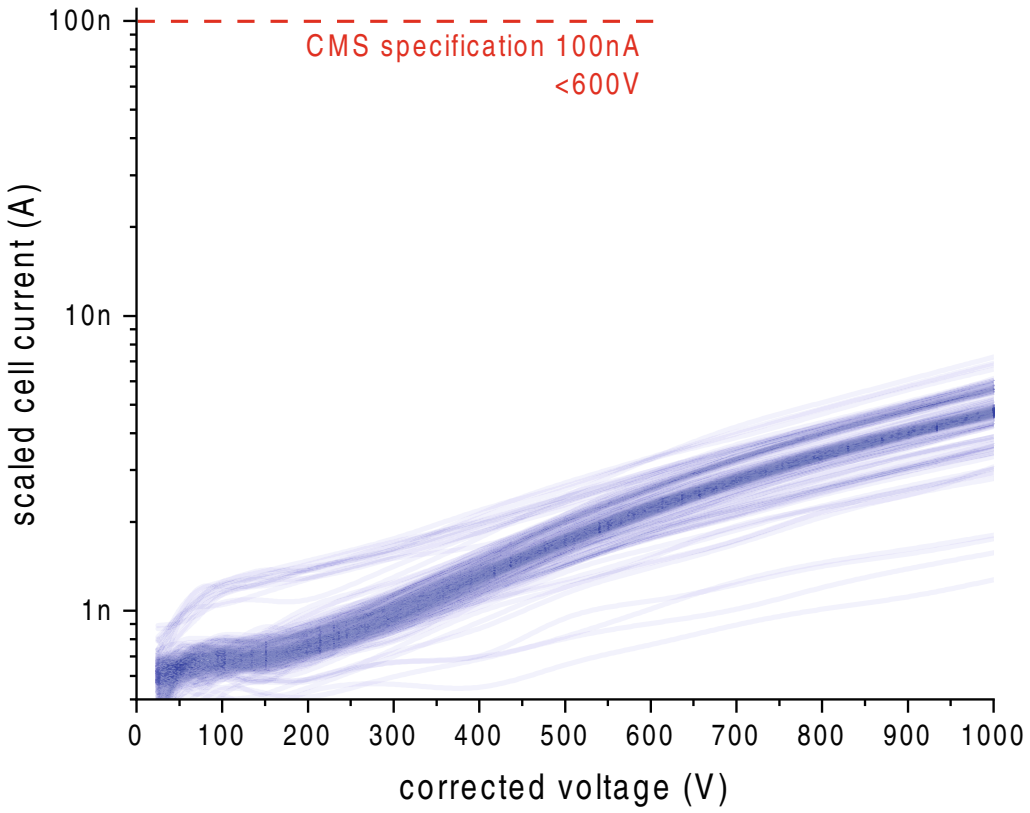

Figure A.6: Cell currents of the unirradiated sensor 2114. This sensor passed the quality control; it is characterized by extraordinarily low currents, 1.5 orders of magnitude of ten below the limit.

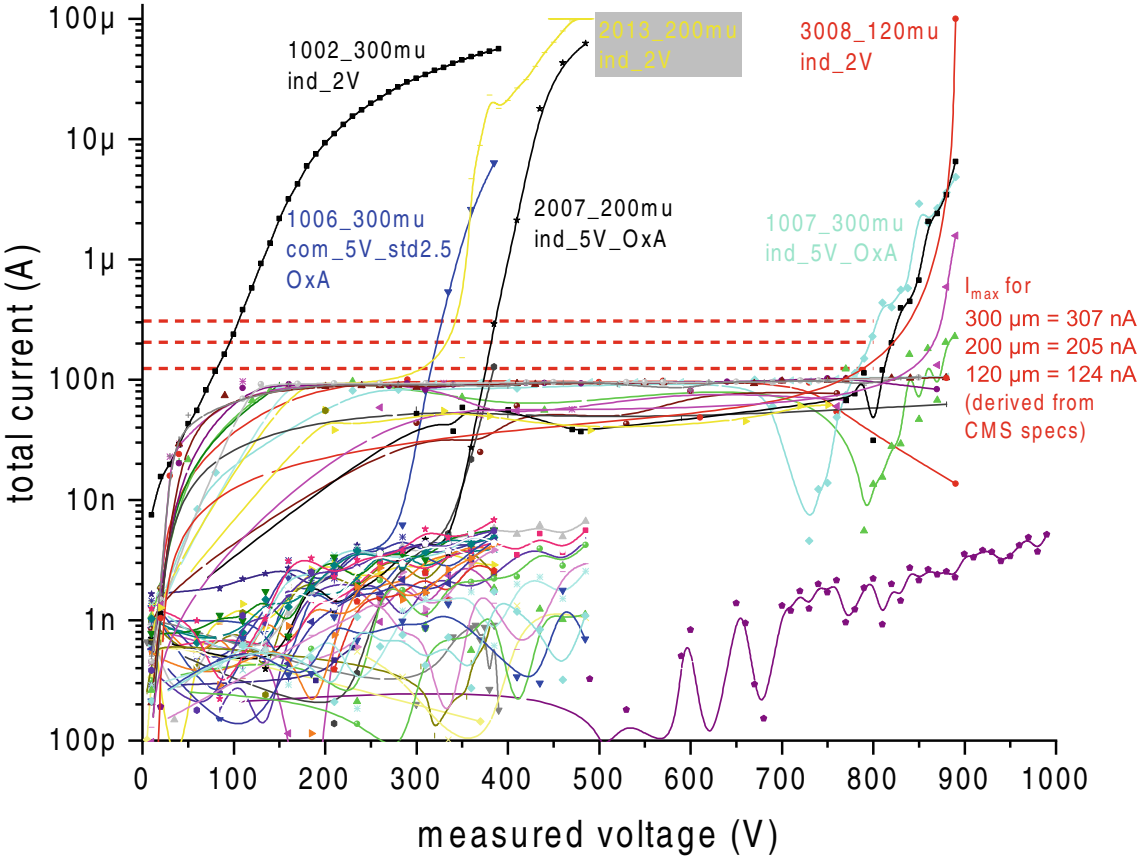

Figure A.7: Total sensor currents of the unirradiated Ministrip sensors. The three dashed red lines for the maximum sensor currents are derived from the CMS specifications via the maximum permissible current density and are not binding. They are only used to estimate the quality of the respective sensors.

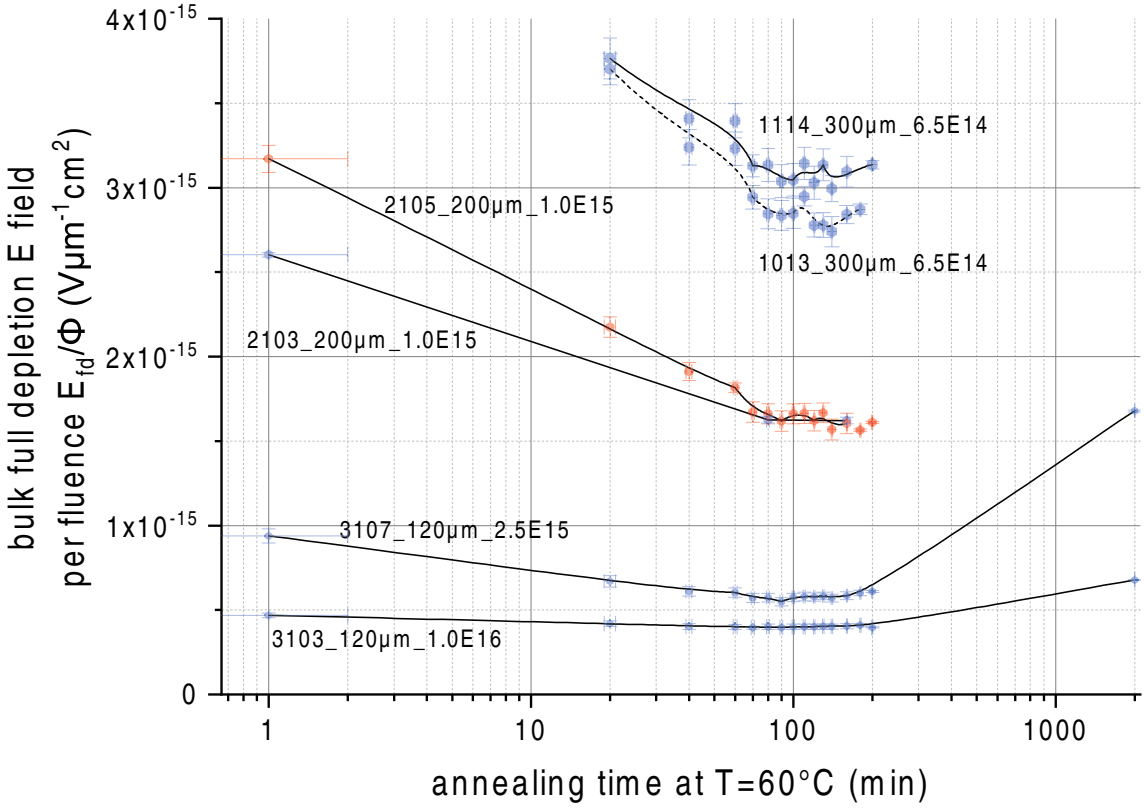

Figure A.8: If we normalize the electric field E by division to the fluence Φ, the annealing curves split into bands, one for each sensor thickness (120 µm, 200 µm, 300 µm). This is an indication of the higher radiation hardness of thinner sensors.

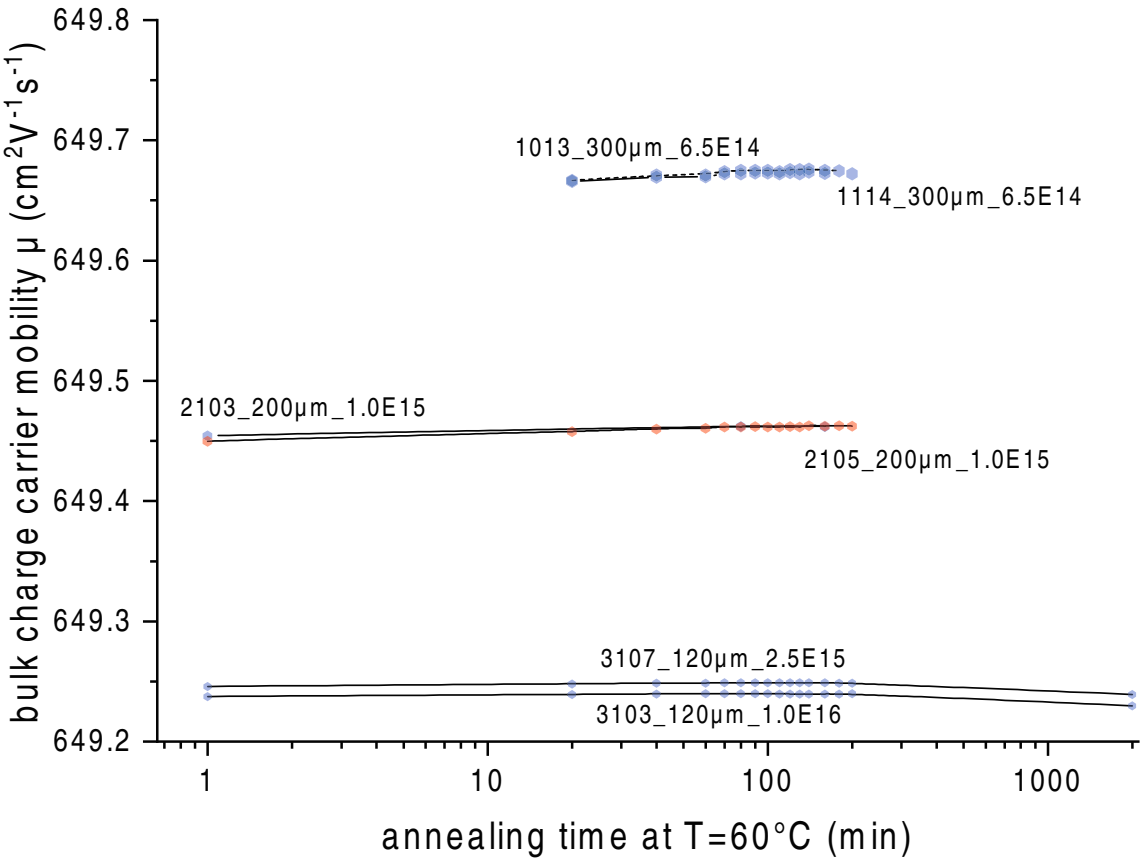

Figure A.9: Charge carrier mobility of the Ministrip sensors over annealing time. The effective charge carrier mobility can be calculated from the Ministrip sensors' full depletion voltage, temperature, and active thickness [4]. It is worth noting that the mobility remains constant over the entire annealing time and splits into bands corresponding to the applied fluences. However, the differences between the bands are marginal and range in differences of ±0.03 %.

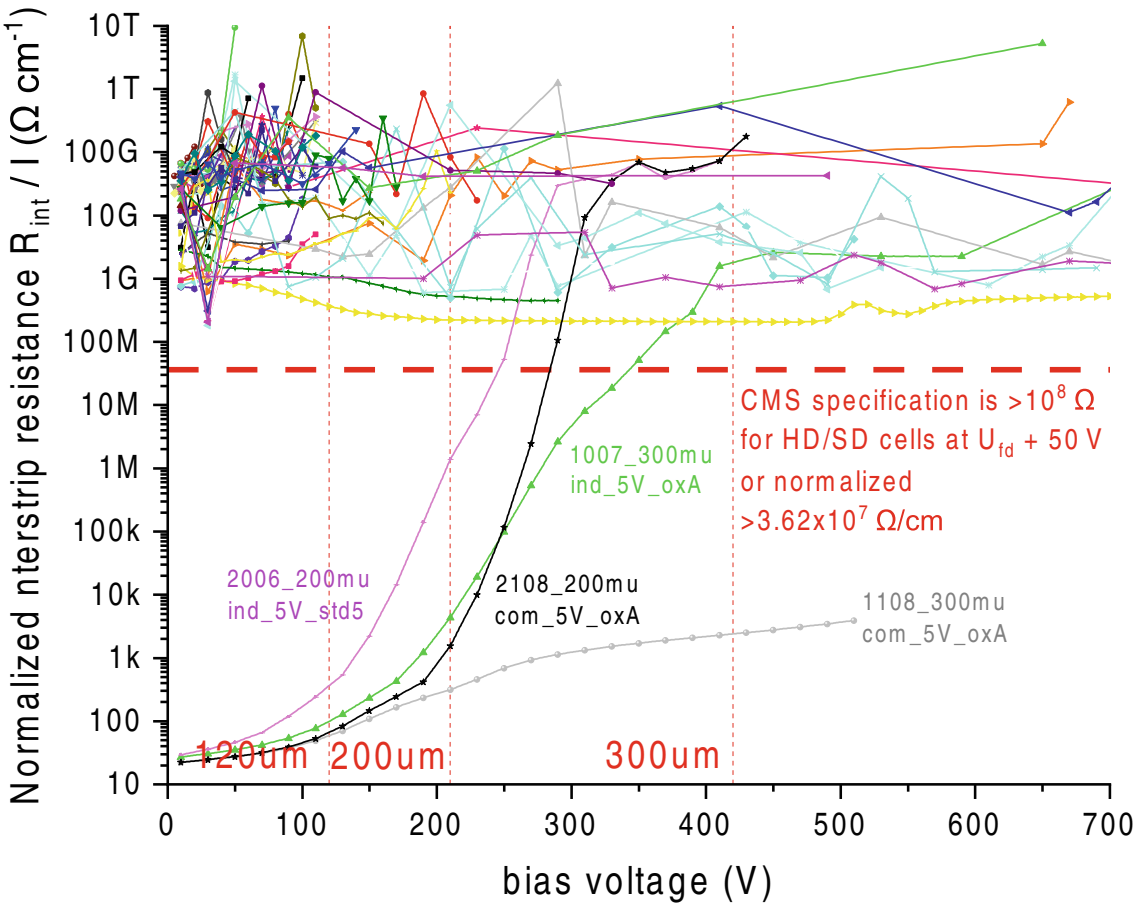

Figure A.10: Normalized to page length interstrip resistance of the unirradiated Ministrip sensors over the bias voltage curve. The specification of CMS is >100 MΩ per cell for HD and LD sensors, which corresponds to >2.18 MΩ normalized to the side length. Almost all measured Ministrip sensors conform to this specification, above specification at every bias voltage. One 300 µmsensor, 1108, does not meet this specification at any bias voltage. Two 200 µm sensors, 2006 and 2108, reach this specification only at too high a bias voltage. The 300 µm sensor 1007 passed this test by achieving the necessary interstrip resistance at 340 V, but the specification only applies at 420 V and above. These four peculiar sensors also show odd behavior with interstrip capacitance (see Figure A.13). It notes that the noise of the measured values above about 1 GΩ is caused by minimal measured currents. Therefore, the noise of the measurement setup takes a dominant part of the measured value.

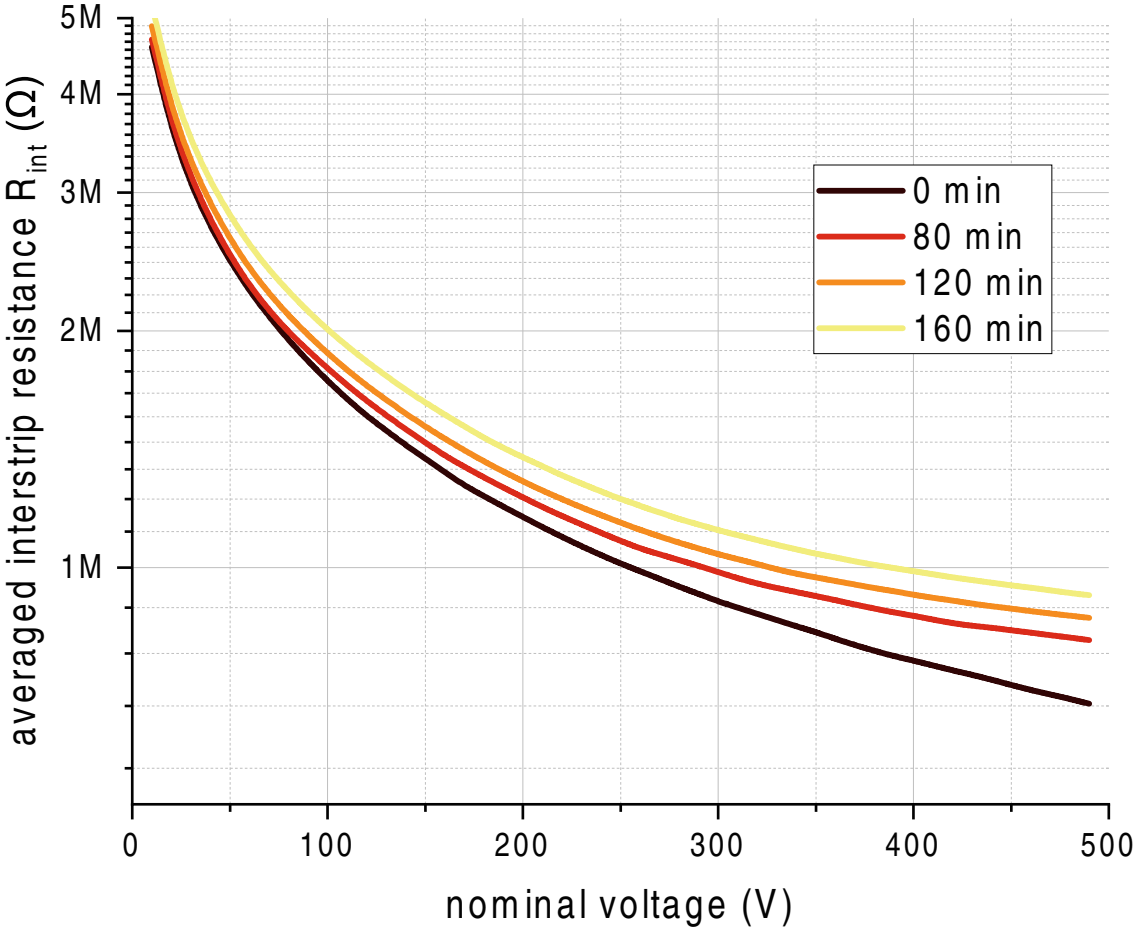

Figure A.11: A plot of the interstrip resistance behavior of the Ministrip sensor number 1013. Its key data are 300 µm active thickness, individual p-stop, 2 V flatband voltage, irradiated with an equivalent neutron fluence of $6.5 \times 10^{14}\,\mathrm{cm}^{-2}$. One can see that the interstrip resistance also increases with increasing annealing time, indicating positive effects due to annealing. The author examined the curves, also for the other measured sensors, for suitable modeling but found none. Thus, for the further analysis (Figures 6.39 and A.12), the voltage at 490 V was used since this was closer to the full depletion voltage (Figure 6.35), giving a result closer to the operating point used in the final CMS experiment.

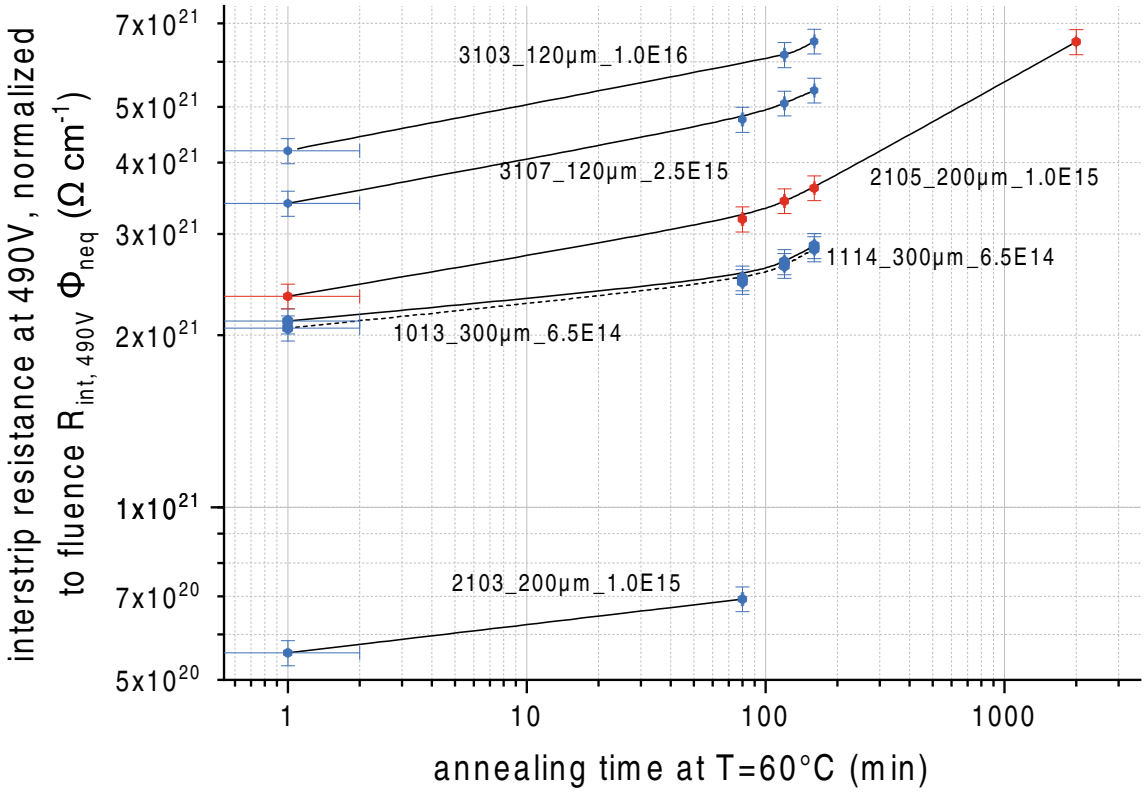

Figure A.12: This plot represents the electrical resistance between the Ministrip strips at a bias voltage of 490 V. Unlike the CV curves, it has been normalized to the electrical fluence by multiplying on it (at higher fluence, the resistance decreases, hence the multiplication). The attentive observer may see that the measured values again split into bands with same thicknesses, with Ministrip 2103 as the outlier, far from the expected band where 2105 lies. The author has not found an explanation for this behavior.

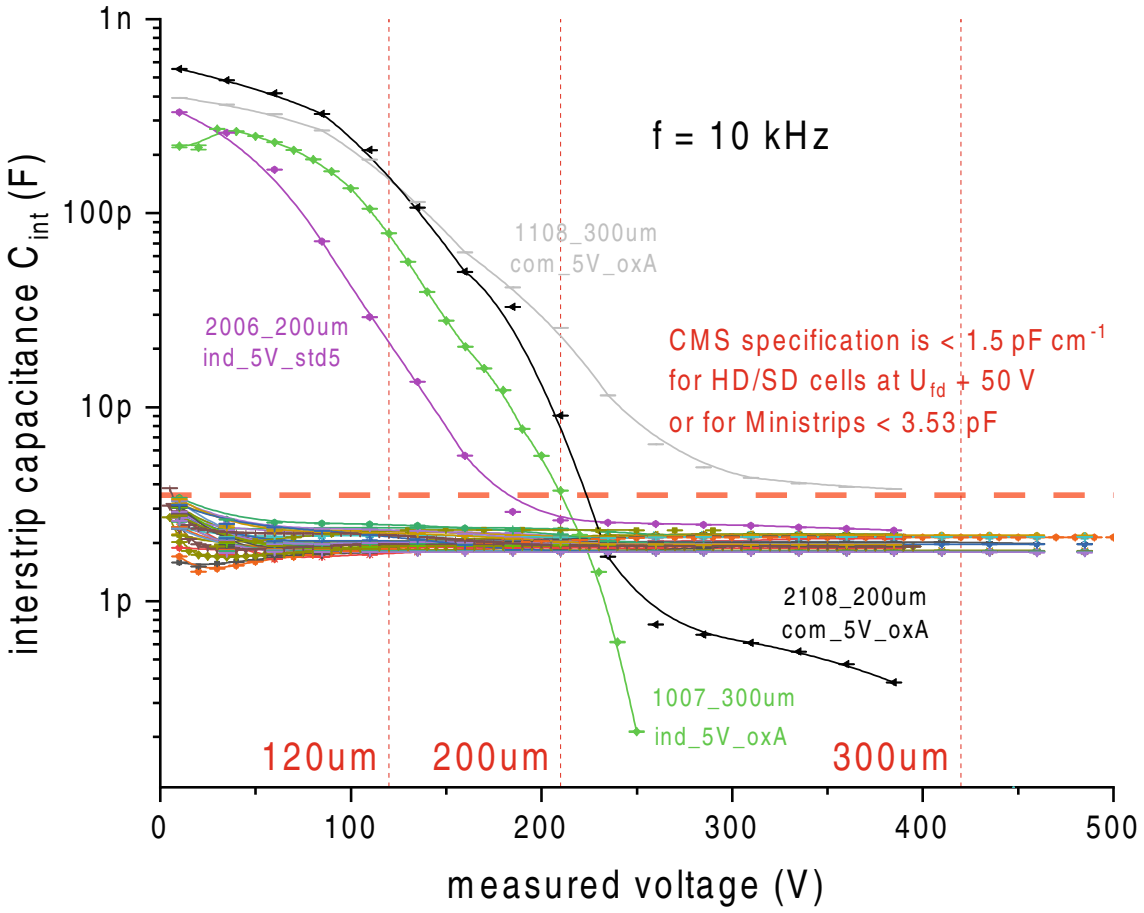

Figure A.13: Interstrip capacitance of the unirradiated Ministrip sensors over the bias voltage curve. The specification of CMS is <1.5 pF per cell for HD and LD sensors, which corresponds to <3.25 pF for the side length of the Ministrips (3.53 cm). Nearly all measured Ministrip sensors conform to this specification, yet they are below specification at every bias voltage. One 300 µm sensors, 1007, is out of specification at the beginning but then falls below the bias voltage threshold of 420 V for 300 µm sensors in time. The other peculiar 300 µm Ministrip sensor, 1108, approaches the limit approximately asymptotically and is declared as passed. One 200 µm sensor, 2006, reaches this specification at a bias voltage of 150 V, which puts it within specification. Another 200 µm sensor, 2108, falls very just short of the specification, reaching it only at 215 V instead of 210 V. These four conspicuous sensors also show an unusual behavior at the interstrip resistance (Figure A.10). The frequency used for measuring the capacitance was 10 kHz.

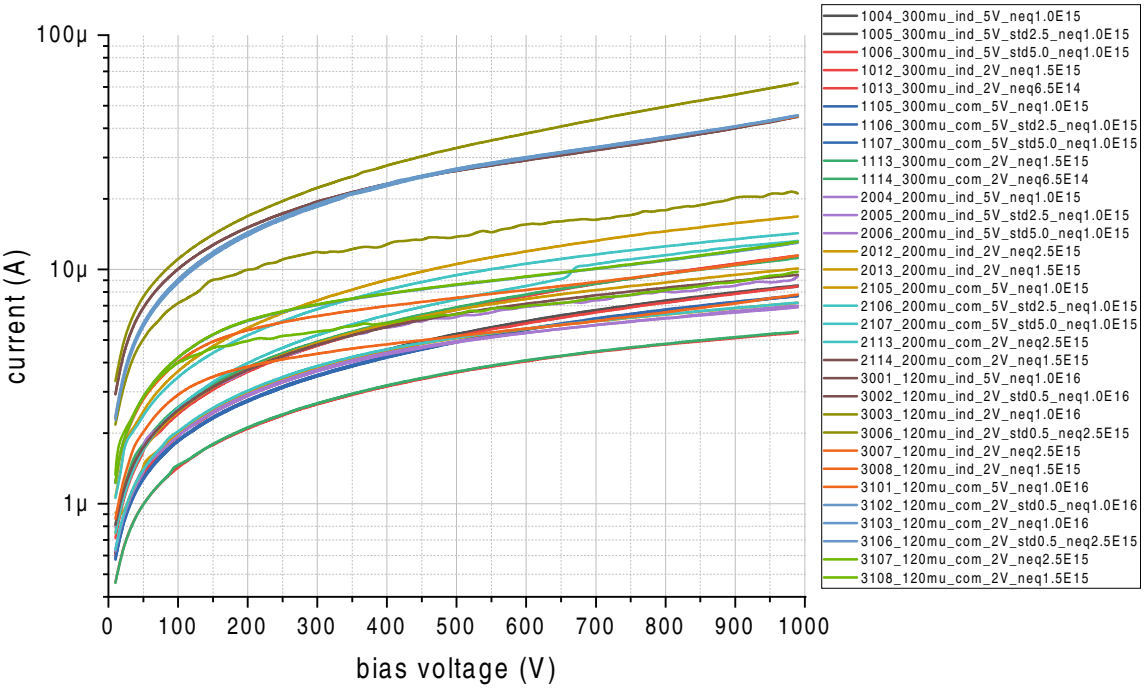

Figure A.14: Family of total currents of all 32 irradiated Ministrip sensors. These total current IV curves serve as a sanity check to determine if the values are trustworthy, in respect to early breakdowns and other irregularities. Note that the current of the Ministrips in this form is not subject to the HGCAL quality specification (Table 6.1), since the geometry of the Ministrip sensors is different from that of the hexagonal sensors.

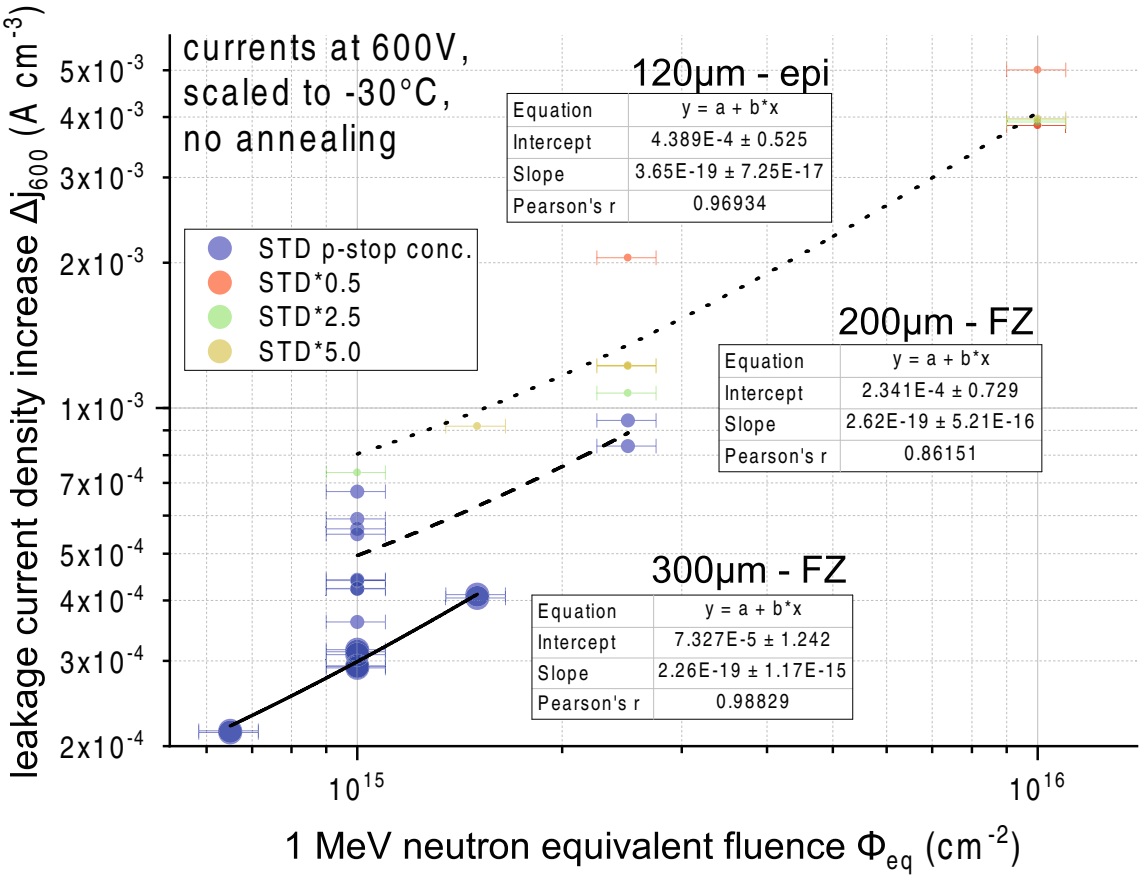

Figure A.15: Comparison of Ministrip sensor current density Δj (difference from unirradiated sensors) to neutron fluence normalized to 1 MeV. The current at 600 V was taken because here the sensors all exceeded the full depletion voltage, see Figure A.14. The currents are scaled to a temperature of −30 °C. Strikingly, although the different sensor types are normalized to the same volumetric current density (A cm^{-3}), the sensor current densities split into three bands, with the 120 µm thick epitaxially processed sensors (thin dots) as the highest current increase, twice as much as those with 300 µm (thick dots) and float-zone processing. However, this splitting into bands is indeed qualitatively consistent with other measurements, such as the full-depletion E-field (Figure A.8), and derived quantities such as the bulk charge carrier mobility (Figure A.9) and the bulk resistivity (Figure 6.38). No MCz Ministrip was tested in the irradiation studies. The author assumes based on existing literature that the oxide configurations (measurable by flatband voltage) and the p-stop properties (doping concentration and geometry common vs. individual) do not significantly affect the bulk currents. Therefore, all sensor types with the same thickness were combined and fitted, independent of their oxide and p-stop configuration.

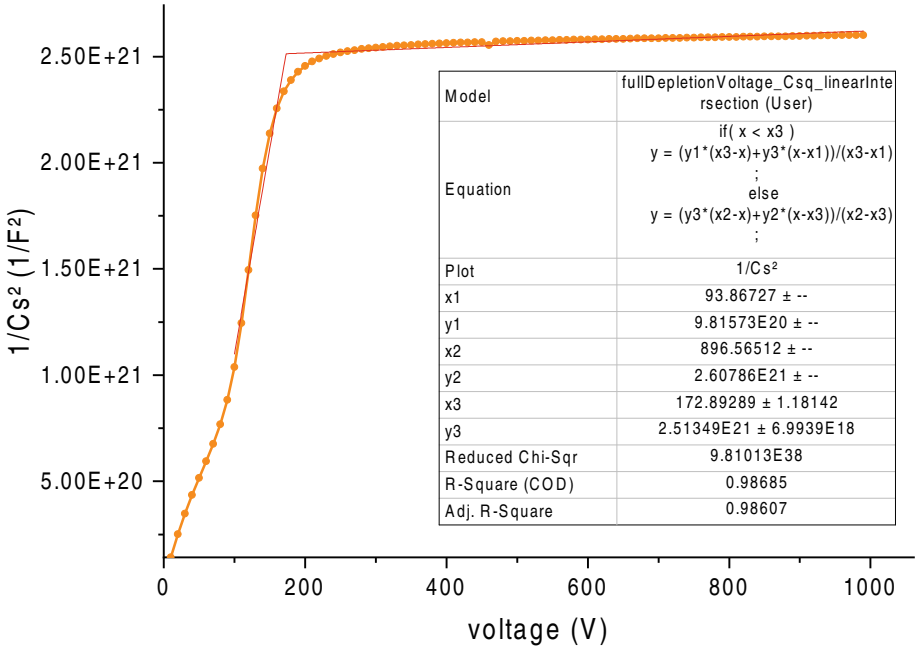

Figure A.16: This is an example of the fit method using two intersecting straight lines to determine the full depletion voltage of a CV curve. The reciprocal of the capacitance C squared is plotted against the bias voltage. The sensor has number 3107, and is processed in 120 µm, epitaxial, standard oxide, −2 V flat band voltage, p-stop common, standard p-stop concentration, irradiated at a fluence of $2.5 \times 10^{15}\,\mathrm{n_{eq}\,cm^{-2}}$. The relevant point is located at x3, y3, which indicates the full depletion voltage and the full depletion capacitance. The results of this fit method are plotted on Figure 6.35 in the annealing studies.

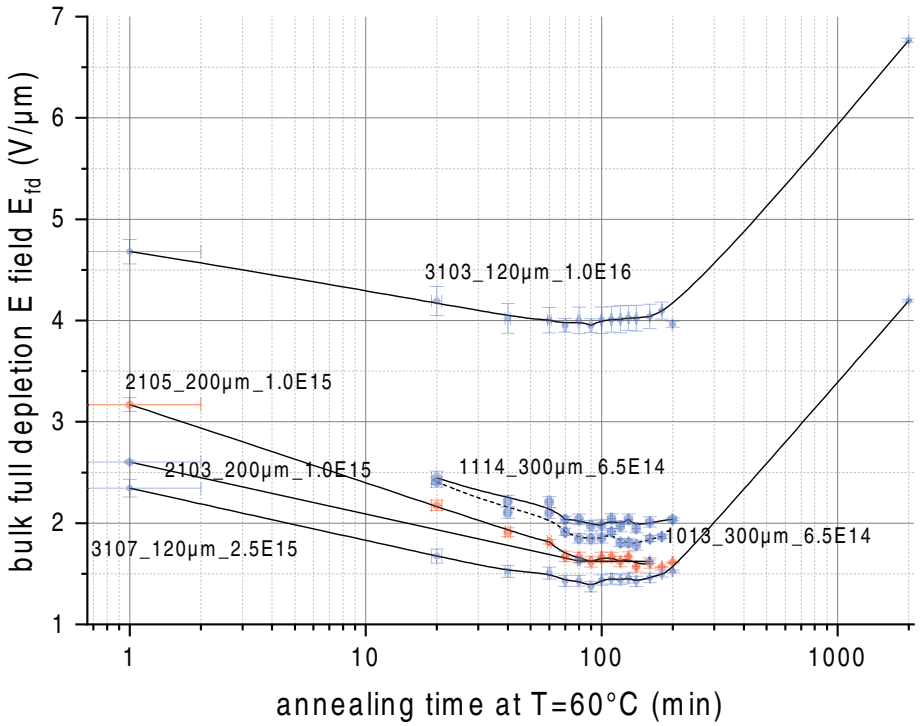

Figure A.17: This plot shows the same data as Figure 6.35, but by dividing by the thickness of the sensor, the electric field strength at full depletion E_{fd} is plotted. This partially resolves the relationship between the individual sensors, which needs to be clarified at first glance. Now we see that the sensors, independent of fluence and thickness, follow approximately the same function over the annealing time, only with a vertical shift.

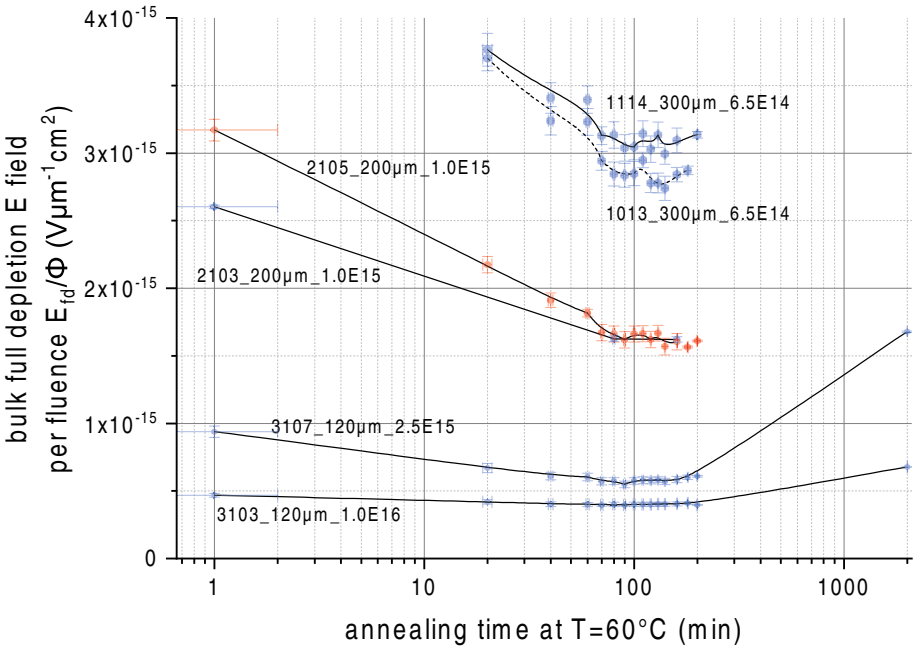

Figure A.18: If we now normalize by division to the fluence Φ, the annealing curves split into bands, one for each sensor thickness (120 µm, 200 µm, 300 µm). This is an indication for the higher radiation hardness of thinner sensors.

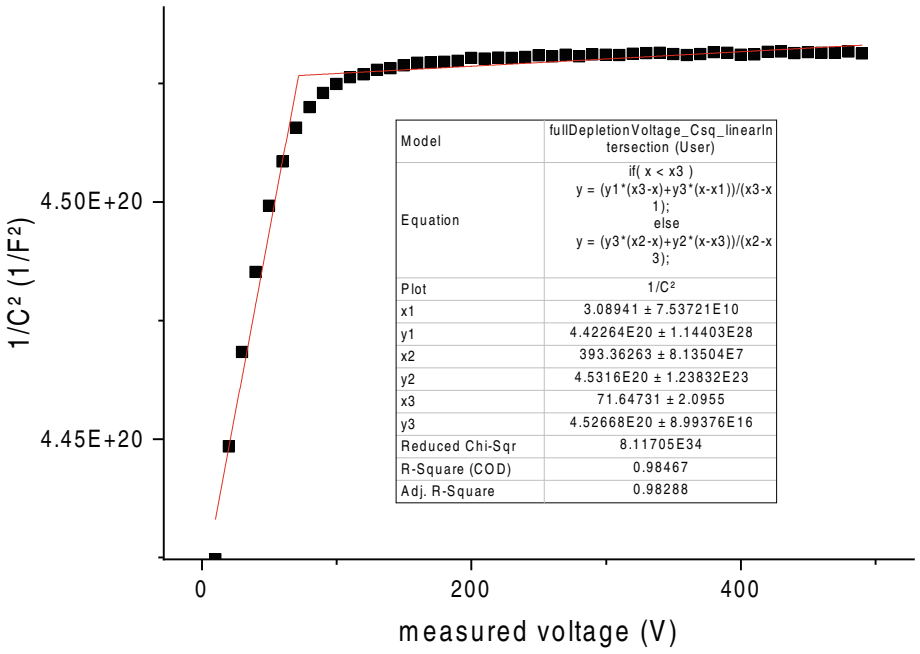

Figure A.19: This is an example of the fit method using two intersecting straight lines to determine the full depletion voltage of an interpad CV curve. The reciprocal of the capacitance C squared is plotted against the bias voltage.
The sensor is 1114, 300 µm, float-zone, standard oxide, −2 V flat band voltage, p-stop common, standard p-stop concentration, irradiated at a fluence of 6.5×10^{14} n_{eq} cm^{-2}. The relevant point is located at x3, y3, which indicates the full depletion voltage and the full depletion capacitance.

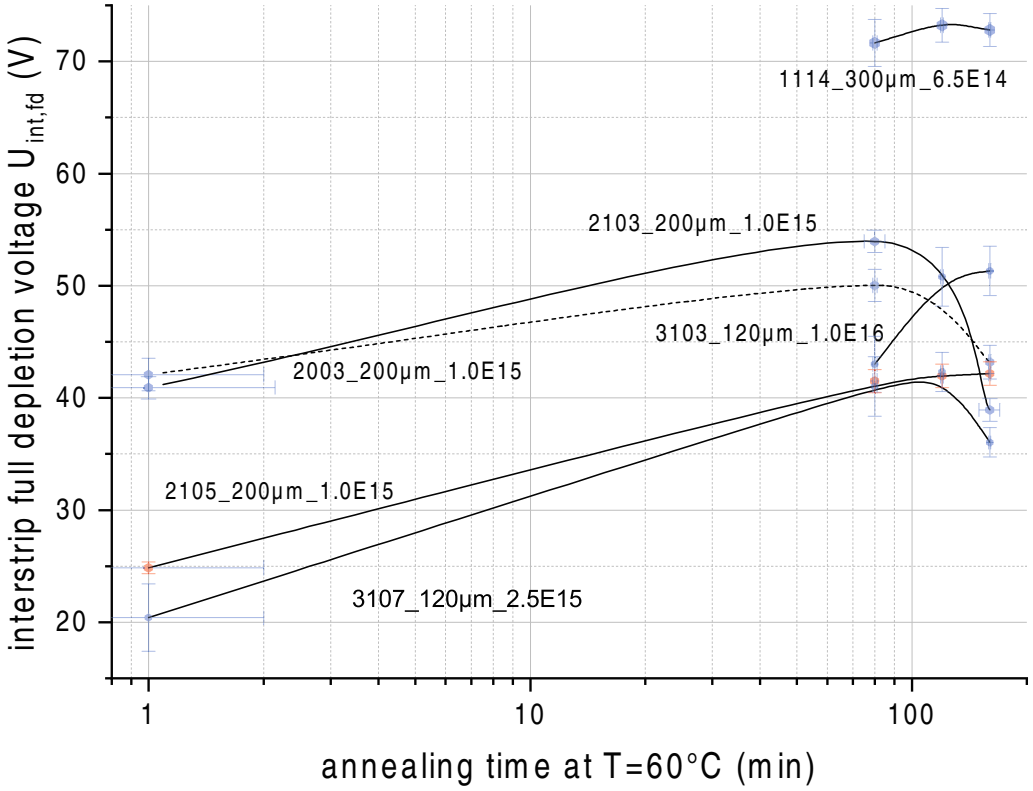

Figure A.20: Plot of the interstrip capacitance full depletion voltage of the Ministrip sensors over the annealing time. One can see that the inflection point of the curves is again at about 100 ± 10 min, analogous to the measurements of the full depletion voltage of the bulk material (Figure A.8).

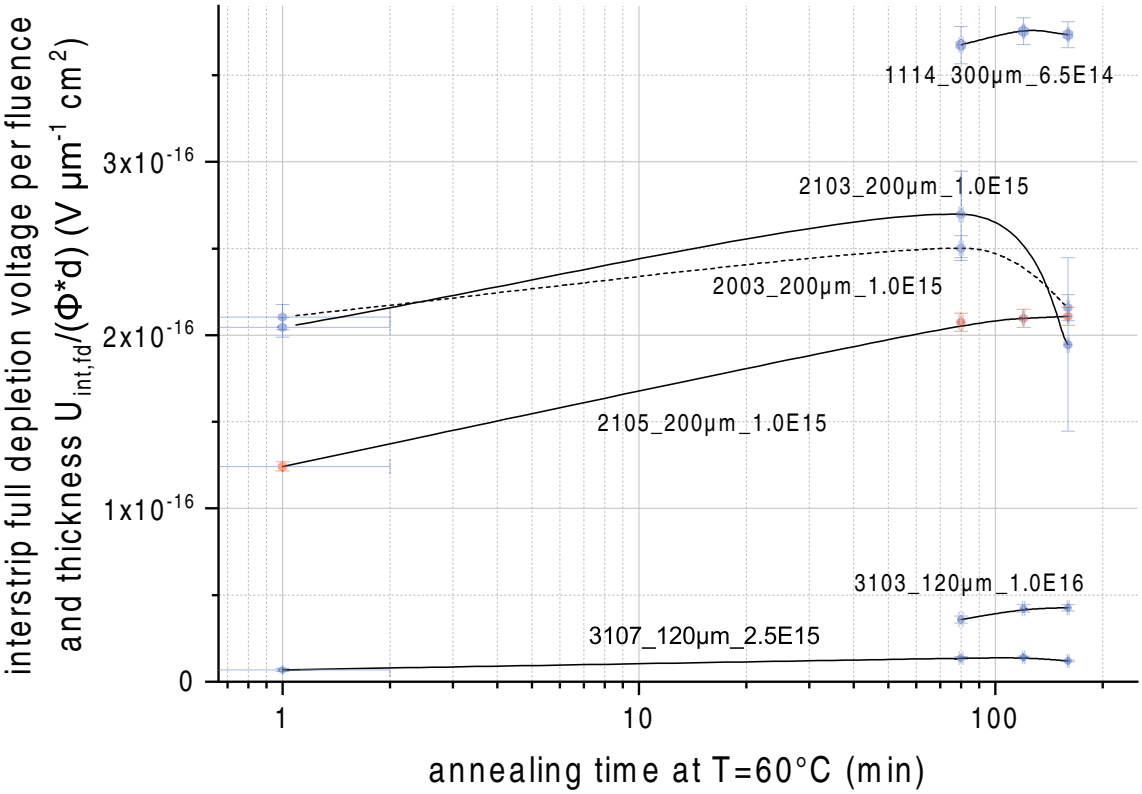

Figure A.21: Interstrip capacitance U_{fd} of the Ministrip sensors over annealing time, normalized to fluence Φ and thickness d of the sensor. Note that the division by the sensor thickness, although the same physical dimension as in Figure A.17, does NOT result in an electric field strength here, but is a normalization by the area of the imaginary plate capacitor. It was omitted to divide by the side length as well, since this was the same for all Ministrip sensors.